CARRIER TRANSPORT IN OPTICAL-EMITTING AND PHOTODETECTING DEVICES BASED ON CARBON-NANOTUBE FIELD-EFFECT TRANSISTORS

A Dissertation
Presented to
The Academic Faculty

by

Chi-Ti Hsieh

In Partial Fulfillment
of the Requirements for the Degree
Doctor of Philosophy in the
School of Electrical and Computer Engineering

Georgia Institute of Technology
August 2010

CARRIER TRANSPORT IN OPTICAL-EMITTING AND PHOTODETECTING DEVICES BASED ON CARBON-NANOTUBE FIELD-EFFECT TRANSISTORS

Approved by:

Dr. David S. Citrin, Advisor
School of Electrical and Computer Engineering
Georgia Institute of Technology

Dr. P. Paul Ruden, Co-advisor
Department of Electrical and Computer Engineering
University of Minnesota

Dr. Albert Bruno Frazier
School of Electrical and Computer Engineering
Georgia Institute of Technology

Dr. Bernard Kippelen
School of Electrical and Computer Engineering
Georgia Institute of Technology

Dr. William Russ Callen Jr
School of Electrical and Computer Engineering
Georgia Institute of Technology

Dr. Phillip First
School of Physics
Georgia Institute of Technology

Date Approved: May 17, 2010

Dedicated to
my father and mother,
Tien-Chih Hsieh and Chun-Mei Chen

ACKNOWLEDGEMENTS

My deepest thanks go to my advisor, Professor David Citrin, and co-advisor, Professor Paul Ruden, for their support, encouragement and patience at every stage of this dissertation.

My thanks and honors to my former advisor, Professor Kevin Brennan, for his support and teaching contributing to the important working of this research.

I would like to thank Professors Bruno Frazier, Bernard Kippelen, Russ Callen, and Phillip First for taking the time out of their busy schedule to read this dissertation.

I would like to thank all the members of Professor Citrin's group and Professor Brennan's group, especially to thank Dr.Tsung-Hsing Yu and Prof. Amit Verma, for many discussions related to this dissertation.

My greatest thanks and gratefulness go to my father and mother whose love, support and assistance were very important for the completion of this dissertation.

I would like to express my thanks and appreciation to my grandmother, uncle, aunt, and many relatives for their support and patience.

I would like to thank a lot of friends for helping me to contribute to this research.

TABLE OF CONTENTS

LIST OF TABLES

Page

LIST OF FIGURES

Page

SUMMARY

A theory of the carrier transport, optical emission, and photoconductivity from optoelectronic devices based on ambipolar long-channel carbon-nanotube (CNT) field-effect transistors (FETs) is presented in this dissertation. In optical emitters based on ambipolar long-channel CNT FETs, an analytic diffusive-transport model for various recombination mechanisms is provided for the first time. The relationship and the scaling of emitted light-spot size and emitted optical power are clearly depicted for the first time as well. We also implement a numerical diffusive-transport approach for the light emission, in which the focus is on the effects of radiative and nonradiative recombination in the channel, with the movement of the spatial recombination profile in response to the gate and drain voltages. For the first time, we find that the emitted light-spot size and the emitted optical power depend sensitively on the operative nonradiative recombination mechanisms. We implement a numerical diffusive-transport approach including exciton photogeneration as well for photoconductors based on ambipolar long-channel CNT FETs with uniform and near-field photoexcitation. We show that the photocurrents are typically much smaller than the dark currents, and explain some possible reasons. Moreover, the exciton densities in CNTs are calculated and the effect of exciton diffusion is presented.

CHAPTER 1

INTRODUCTION

1.1 Problem Definition

The objective of the proposed research is to study theoretically the properties of the carrier transport, optical emission, and photoconductivity from optoelectronic devices based on ambipolar long-channel carbon-nanotube (CNT) field-effect transistors (FETs). In ambipolar CNT FETs electrons and holes can be simultaneously injected at the opposite ends of the CNT channel. The transport and optical properties of CNT FETs are investigated in the framework of a diffusive-transport model due to the long conduction channel in optoelectronic devices.

CNT light emitters are solid-state, electrically driven devices. Interestingly, an optical emitter based on ambipolar long-channel CNT FETs is a light source, in which the location of the light emission along the channel can be controlled; therefore, the spatial dependence of the recombination profile on the gate and drain voltages is explored. The emitted light-spot size and optical power are predicted by both analytic and numerical approaches to exhibit sensitive dependence on the nonradiative recombination mechanism.

CNT light detectors are solid-state, electrically driven devices as well. For strong binding of excitons in CNTs, most of the optical absorption is associated with

photogeneration of excitons. The photoconductivity of CNT FETs including exciton generation is investigated with both uniform and near-field photoexcitation.

1.2 History and Motivation of Optoelectronic Devices Based on Carbon-Nanotube Field-Effect Transistors

A carbon nanotube has a diameter of a few nanometers and a length ranging from nanometers to microns. The aspect ratio of length to diameter is as large as 10^3~10^5, so a CNT can be considered as a quasi-one-dimensional nanostructure. Excellent thermal conductivity, chemical inertness, and high mechanical strength make them excellent candidates for a future nanoelectronic technology [1-3]. The list below shows many advantages for carbon-nanotube field-effect transistors (CNT FETs) [4, 5]. (1) The one-dimensional character of CNTs reduces the phase space for scattering and leads to large "on" currents in semiconductor CNT FETs. (2) Unlike a conventional semiconductor channel, in CNTs all bonds are satisfied without introducing roughness scattering. This allows a wider choice of gate insulators other than SiO_2, such as high dielectric constant and crystalline insulators for improved gate control. (3) All-nanotube-based electronic devices can be produced with metallic tube acting as interconnects due to the high conductivity and exceptional stability, and semiconducting tubes acting as active devices. (4) Semiconducting carbon nanotubes are direct-gap semiconductors that absorb and emit light, offering the possibility of developing optoelectronic devices. For example, optical emitters and photodetectors can be achieved based on CNT FETs. Carbon nanotubes are a promising class of materials with outstanding properties for electronics and

optoelectronics, but many challenges remain. One of the biggest challenges is that the successful and reliable reproduction of a specific type of a CNT is still lacking [5].

A carbon nanotube may be viewed as a hollow cylinder and can be described as a graphene sheet (a layer of graphite) rolled into a cylindrical shape [3]. The electronic structure of a CNT can be obtained from that of a two-dimensional graphene layer together with zone folding [2, 3, 6]. The one-dimensional energy dispersion relation of a CNT can be calculated by a tight-binding model [3]. The unique electronic structure of an individual CNT can be either metallic or semiconducting, depending on the arrangement of carbon atoms. Armchair CNTs (n,n) are always metallic, and zigzag CNTs (n,0) are only metallic when n is a multiple of 3 [3]. Semiconducting CNTs are direct-gap nanostructures, and the energy gaps depend inversely on the CNT diameter [2, 3].

Electron mobility in CNTs, in general, depends on the CNT diameter, electric field, and temperature [6-11]. The mobility of a specific type of semiconducting CNT can be calculated theoretically by using electron-phonon scattering [8, 9, 11], and there are different values for various types of CNTs. Carbon nanotubes exhibit high mobility at low electric fields, exceeding the best semiconductors at room temperature [9, 12, 13]. At low fields the mobility depends strongly on nanotube diameter, and the mobility increases as the CNT diameter increases [9]. For example, at room temperature the values of low-field mobility are calculated as 15,000 cm^2/Vs for (13,0) nanotube with a diameter 1 nm, 35,500 cm^2/Vs for (19,0) nanotube with diameter 1.5 nm, and 65,000 cm^2/Vs for (25,0) nanotube with a diameter 1.98 nm. At high fields the drift velocity saturates [9, 11, 13], and the mobility is dramatically reduced by optical-phonon

scattering [9, 14-16]. For long-channel CNT FETs the electric field is low, and the constant low-field mobility can be applied to this model.

In bulk direct-gap materials, optical spectra at room temperature usually involve inter-band transitions [1, 4]. In one-dimensional systems such as CNTs, the density of states diverges as the inverse of the square root of the energy, leading to van Hove singularities. An inter-band transition means a transition between pairs of van Hove singularities. Most experimental papers discuss the excitation of CNTs in terms of band-to-band transitions; however, a single-particle description of the excited CNT states omits electron-hole interactions, which should be particularly strong in one-dimensional systems. The electron-hole interaction is expected to bind the photoexcited electron and hole to form excitons. Theoretical studies [17-19] and later experimental studies [20-22] showed that electron confinement in the quasi-one-dimensional structure of CNTs leads to high electron-hole binding energies and the formation of strongly bound exciton states. The exciton binding energy depends on the diameter and chirality of the CNT, increasing with decreasing diameter, and on the dielectric constant of the surrounding environment [18]. Typically the binding energy is about 0.2~0.5 eV. For strong binding, most of the optical absorption is associated with photogeneration of excitons. Likewise, photoluminescence may be dominated by excitons.

In carbon nanotubes the energy levels of both conduction and valence bands nearest the band edge are doubly orbitally degenerate [3]. For free electron-hole pairs, the Coulomb interaction creates four distinct lowest-energy singlet excitons. Only the second-lowest-energy singlet exciton is optically active, which is called a “bright exciton” [23, 24]. The other three lowest-energy singlet excitons are optically forbidden,

and are called “dark excitons.” Moreover, all four lowest-energy excitons for the triplet-spin states are dark as well. Therefore, only the singlet bright exciton is considered when evaluating the effective radiative lifetime of excitons in the carbon nanotubes.

There are various gate structures for CNT FETs. The early and common configuration is a back gate [9, 14-16, 25-28]. A top gate [29-32], a partial top gate [33, 34], and a gate with a trench [35] are the gate structures in order to improve the performance of switching devices. All gates as mentioned above are practical planar gates. However, coaxial gates [36-41] are not practical and are only used to simulate the characteristics of CNT FETs. Because a planar back gate is a recent structure for optoelectronic applications [28, 42-44], it is used in this present research.

Ballistic-transport models applied to semiconducting CNT channels have been used to treat switching devices based on CNT FETs; however, these models cannot be directly applied to optical-emitting devices. The mode of transport −whether ballistic or diffusive− is determined by the mean-free-path (MFP) in the channel composed of a CNT. For CNTs at room temperature the mean-free-path is a few μm for defect scattering, a few hundred nm for acoustic-phonon scattering, and 15 nm for optical-phonon scattering [14, 45-48]. At low bias acoustic-phonon scattering is the dominant mechanism, and the transport is ballistic for channel lengths shorter than a few hundred nm. At high bias optical-phonon scattering is the dominant mechanism, and the transport is ballistic for channel lengths shorter than 10 nm. In switching devices based on CNT FETs the channel length is very short; thus, ballistic-transport models applied to CNT channels have been applied. In optical-emitting devices of CNT FETs the channel length ranges from 400 nm to 800 nm in [28], 60 μm in [49], 50 μm in [42], and 10 μm in [50].

In this study the channel length of both optical emitters and photodetectors is 60 μm, and therefore a diffusive-transport model is applied to the CNT channels for both optical emitters and photodetectors [51, 52].

In general, Schottky barriers (SB) at the contacts between a metal and a semiconducting CNT were reported by most experiments [4, 31, 32, 53, 54]. For ambipolar CNT FETs there is a voltage drop associated with each contact that forms the Schottky barriers [49]. In this model their effect is simplified to a constant voltage drop independent of the current, and the values of voltage drop are assumed to be the same at both S and D contacts [49, 51]. This assumption is applied to the boundary conditions of the CNT potential.

The concept of "quantum capacitance" was used by Luryi in order to develop an equivalent-circuit model for devices that incorporate a conducting two-dimensional electron gas [55]. This term has also been used in the modeling of one-dimensional systems, such as CNT devices [39, 41, 56, 57]. The total capacitance of the CNT FETs is considered as an insulator capacitance in series with the quantum capacitance of the CNT. In this study the insulator capacitance of the CNT FET is given by about 0.38 pF/cm for 100 μm of the insulator thickness. The value of the quantum capacitance can be estimated as 4 pF/cm [41, 57]. Since the quantum capacitance is much larger than the insulator capacitance, the total capacitance can be approximated as the insulator capacitance of CNT FETs.

For long-channel CNT FETs the longitudinal electric field is a much more gradual function of position than the transverse electric field, *i.e.*, the gradual-channel approximation (GCA) holds [49, 51, 56]. The observed hysteresis of the current-voltage

characteristics in the fabricated devices [42, 43, 49] indicates that there may be charges in the insulator or in the CNT-insulator interface. The flat-band voltage is treated to include the effect of those charges and the work-function difference between the gate and the channel.

For the drift-diffusion currents with large carrier densities, a Fermi-Dirac distribution rather than the Boltzmann distribution has to be used. In degenerate semiconductors, the Einstein relation can be approximated by the formula of Kroemer [58]. By using the procedure of Joyce and Dixon [59] applied to the Fermi-Dirac integral of order -½ for the one-dimensional case such as CNTs, the parameters in the formula of Kroemer are calculated in this study [51].

In order to fabricate any electroluminescent device, one must have radiative recombination of significant populations of electrons and holes. Typically, this is achieved at an interface between a hole-doped and an electron-doped material, i.e., a *p*-*n* junction. In ambipolar CNT FETs electrons are injected from the source S and accumulate in the CNT nearby for a positive gate-to-source voltage $V_{GS} > 0$, while holes are injected from the drain D and accumulate nearby for a negative gate-to-drain voltage $V_{GD} < 0$. Electrons and holes are simultaneously injected from opposite ends of the CNT and radiatively recombine in the one-dimensional CNT. This enables electroluminescence (EL). Therefore, CNT light-emitting devices are solid-state, electrically driven devices [4, 6, 7]. CNT FETs under ambipolar operation can produce a gate-controlled light source of infrared radiation with undoped CNTs, as distinguished from semiconductor-nanowire optical sources [28, 42]. In optical emitters based on long-channel ambipolar CNT FETs, the area of strong electron–hole recombination, and hence

the region of light emission, can be controlled by varying the gate and drain voltages [42, 49]. Therefore, light emitters based on CNT FETs are spatially tunable light sources. Optical emission from CNT FETs exhibits a variety of interesting properties. The emitted light is strongly polarized along the tube axis [6, 28]. The radiation has a characteristic energy depending on the diameter and chirality of the CNT. The emission spectra are in accord with the expected bandgaps in the experiment [44]. The emitted light-spot size with the long-channel CNT FETs is small (~2-4 μm) [42].

Other theoretical work in optical emitters based on CNT FETs is presented below. An analytic model based on diffusive transport and assuming infinite recombination rate for electrons and holes at the same location has been presented and applied to a very long-channel (60 μm) CNT [49]. Due to the neglect of the finite recombination length, the transport characteristics and optical emission within the recombination region were not of immediate concern. Numerical models with diffusive transport and carrier recombination were developed for long-channel devices in order to calculate the emitted light-spot movement [50, 60]. A quantum treatment is used to compute the injected currents through the Schottky barriers [50], and a drift-diffusion treatment including the radiative-recombination rates is used in the long channel. The calculation is fully numerical and is computationally expensive. Radiative recombination was assumed to be dominant [50, 60]. However, the importance of nonradiative recombination is indicated by the low measured quantum efficiency between 10^{-6} and 10^{-7} photons per injected *e*-*h* pair [44].

In order to understand the recombination-mechanism dependence of the transport characteristics and the optical emission of ambipolar CNT FETs more completely, a

diffusive-transport model accounting for the radiative and several nonradiative recombination mechanisms is presented in this study. When defects and impurities exist, *e.g.* at the CNT-insulator interface, Shockley-Read-Hall (SRH) recombination is important. Band-to-band nonradiative recombination (BBN), in which phonons are emitted, and Auger recombination are considered also [51].

Light emission has also been observed under unipolar transport conditions in suspended tubes [61]. The light intensity is stronger by a factor of ~1000 compared to ambipolar devices. The mechanism of this electroluminescence involves an efficient impact excitation process involving the hot carriers in CNTs generated by high local fields [62]. By this impact-excitation process, high exciton densities can be achieved to generate the bright light. In our study on light emitters based on ambipolar long-channel CNT FETs, the electrical field is small and is not sufficiently strong to generate excitons through impact excitation [51, 61]. Moreover, recently thermal light emission from metallic CNTs was also reported in suspended FET structures [63, 64].

CNT light detectors are solid-state, electrically driven devices as well [4, 6, 7]. Photoconductivity in CNT FETs has been explored experimentally with uniform photoexcitation [21, 43] and with near-field photoexcitation [65-69]. In other theoretical work, theoretical simulations neglecting the effects of excitons for the very short channel (15nm) were carried out in Ref. [70]. Electron-hole interactions, however, should be strong in quasi-one-dimensional system. The electron-hole interaction is thus expected to bind the photoexcited electron and hole to form excitons. For strong binding, most of the optical absorption is associated with photogeneration of excitons. Since the formation of

excitons through photoexcitation is important in CNTs, the model accounting for exciton photogeneration is presented in this study.

Photoconductivity in CNT FETs is the reverse of electroluminescence. In photodetectors based on CNT FETs, photoexcitation can both generate *e-h* pairs through interband transitions and also generate excitons. For strong excitonic binding, the optical absorption is dominated by the large excitonic oscillator strength. Therefore, photogeneration of excitons is taken to be the dominant mechanism. Excitons in CNTs generated by optical radiation are ionized to free electron-hole pairs. With an applied drain-to-source voltage V_{DS}, electrons and holes are collected at the respective contacts, and thus produce a photocurrent. The effect of field ionization of excitons [71] is neglected here since the electric field in long-channel CNT FETs is low [51, 52]. The ratio of the exciton-ionization coefficient to the capture parameter for exciton formation is assumed to follow an Arrhenius relation [72-74], which is the Saha's equation in the case of chemical equilibrium. The three-dimensional Arrhenius equilibrium constant was derived for Si [72, 73], while the two-dimensional Arrhenius equilibrium constant was derived for GaAs quantum wells [74]. Since excitons in CNTs are quasi-one-dimensional, the one-dimensional Arrhenius equilibrium constant is derived in this study.

Since the diameter of a CNT is so small (~1 nm), incident radiation is absorbed very slightly. An experimental measurement determined optical-absorption cross sections of CNTs for visible light copolarized and cross polarized with respect to the CNT axis [75]. Incident light uniformly exciting the entire device including the CNT channel and contacts applies to the experiments in [21, 43], while the relatively small focus of the laser spot exciting part of the CNT channel and the contacts was reported in

[66-69]. In our study on photodetectors based on CNT FETs incident light exciting the CNT channel but not the contacts is considered, and both uniform and Gaussian spatial profiles of the incident light are included.

For the photoconductors the photocurrent is maximized for photons polarized along the direction of the CNT [43]. In addition to the strong exciton transition, a weaker side band about 200 meV above the exciton transition is observed [21]. The side band reflects the effect of exciton-phonon coupling and thus involves phonon-assisted processes [76]. Internal fields, such as those formed at Schottky contacts and those in defect sites, can be used to image such sites and determine band bending in the open-circuit configuration [65-69]. Since the photocurrent is proportional to the absorbed power, photoconductivity can be used as a spectroscopic tool [1].

For optical emitters and photodetectors based on CNT FETs, the system of differential equations with boundary conditions, in general, cannot be solved explicitly. The solution has to be obtained by numerical approaches. The finite-difference method using Scharfetter-Gummel discretization is adopted for the differential continuity equations of electrons and holes and for the exciton continuity equations, and then the discretized equations are solved numerically [51].

1.3 Overview of Research

This research is to study theoretically the properties of carrier transport, optical emission, and photoconductivity in optoelectronic devices based on ambipolar long-channel CNT FETs. First, the CNT and optoelectronic devices based on CNT FETs are

introduced. Next, the modeling and both the analytic and numerical approaches are presented. Finally, the interesting results for optical emitters and photodetectors are presented.

CNT FETs and the related optoelectronic devices are studied in Chapter 2. In Chapter 2.1, the structure and classification of CNTs are introduced. Next, the electronic properties of CNTs including the energy dispersion relation, mobility, and mean-free-path (MFP) are presented. Finally, the optical properties of CNTs such as the inter-band transitions, exciton binding energy, and bright and dark excitons are discussed as well. In Chapter 2.2, the Schottky barriers (SB) and quantum capacitance of CNT FETs are introduced. Next, optical emitters based on CNT FETs including radiative and various nonradiative recombination mechanisms are discussed. In addition, photodetectors based on CNT FETs are discussed as well.

The modeling of both optical emitters and photodetectors based on CNT FETs is studied in Chapter 3. First, modeling of the gradual-channel approximation (GCA), drift-diffusion currents, and electron and hole continuity equations applied to CNT FETs is introduced. Next, modeling of various recombination mechanisms of electron and holes in the optical emitters is presented. Modeling of the photoexication and exciton continuity equations in the photodetectors is studied as well.

In Chapter 4, an analytic diffusive-transport model for various recombination mechanisms is presented, thereby enabling a clearer understanding of the dependence of the transport and optical properties on the various nonradiative recombination mechanisms. In particular, the current, radiative recombination rate, emitted light-spot size, and optical power are all calculated analytically.

For optical emitters and photodetectors based on CNT FETs, the system of differential equations with boundary conditions, in general, cannot be solved explicitly. In Chapter 5, the numerical approach for the optical emitters without exciton formation is studied, and the numerical approach for the photodetectors including the photogeneration of excitons is presented as well.

Both analytic and numerical results for optical emitters based on CNT FETs are calculated in Chapter 6. The interesting results including the device currents, CNT potentials, carrier densities, radiative recombination rates, emitted light-spot sizes, and optical powers are obtained for various recombination mechanisms.

The results for photoconductors based on CNT FETs are calculated in Chapter 7. The interesting results including the photocurrents, current gains, and exciton densities are obtained with both uniform and near-field photoexcitation.

Finally, the conclusion and future work are presented in Chapter 8.

CHAPTER 2

OPTOELECTERONIC DEVICES BASED ON CARBON-NANOTUBE FIELD-EFFECT TRANSISTORS

Carbon nanotubes (CNTs) are novel materials with unique physical and chemical properties [1-3]. Their quasi-one-dimensional character and strong bonding lead to weak carrier scattering. Excellent thermal conductivity, chemical inertness, and high mechanical strength make them excellent candidates for a future nanoelectronic technology. Moreover, semiconducting carbon nanotubes are direct-gap semiconductors that direct absorb and emit light, offering the possibility of developing optoelectronic devices. For example, optical emitters and photodetectors can be achieved based on carbon-nanotube field-effect transistors (CNT FETs). In this chapter CNT FETs and the related optoelectronic devices are studied. Firstly, the structure, electronic, and optical properties of CNTs are introduced in Chapter 2.1. Next, the electronic properties of CNT FETs as well as the optical emitters and photodetectors based on CNT FETs are discussed in Chapter 2.2. Finally, the summary for optoelectronic devices based on CNT FETs is presented in Chapter 2.3.

2.1 Carbon Nanotubes

A carbon nanotube (CNT) may be viewed as a hollow cylinder and can be described as a graphene sheet (a layer of graphite) rolled into a cylindrical shape [3]. A

CNT has a diameter of a few nanometers and a length ranging from nanometers to microns. The aspect ratio of length to diameter is as large as 10^3~10^5, so a CNT can be considered as a one-dimensional nanostructure. A CNT can be either a single-wall (SWCNT) or a multi-wall (MWCNT). Many nested, coaxial nanotubes share the same axis in a MWCNT, while only one nanotube exists in a SWCNT. Here we focus on SWCNTs, and the terminology of CNT and SWCNT is exchangeable. The unique electronic structure of an individual CNT can be either metallic or semiconducting, depending on the arrangement of carbon atoms. In Chapter 2.1.1, the structure and classification of CNTs are introduced. In Chapter 2.1.2, the electronic properties of CNTs including the energy dispersion relation, mobility, and mean-free-path (MFP) are discussed. In Chapter 2.1.3, the optical properties of CNTs such as the inter-band transitions, exciton binding energy, and bright and dark excitons are discussed as well.

2.1.1 Structure of Carbon Nanotubes

SWCNTs are extremely strongly bonded, hollow carbon atomic structures with diameters typically in the range 1-3 nm. Figure 2.1 shows the unrolled honeycomb lattice of a CNT [3], and describes various parameters related to a graphene sheet. The honeycomb sheet rolls into itself to construct a CNT by connecting O and A coincided and B and B' coincided. OA and OB define the chiral unit vector $\boldsymbol{C}_\mathbf{h}$ and the translational unit vector $\boldsymbol{T}$ of a CNT, respectively. The rectangle OAB'B defines the unit cell for the CNT. The chiral vector $\boldsymbol{C}_\mathbf{h}$ is perpendicular to the nanotube axis and corresponds to the equator, while the translational vector $\boldsymbol{T}$ is parallel to the nanotube axis and is normal to

the chiral vector. $\boldsymbol{C}_{\mathbf{h}}$ is expressed by the real space unit vectors $\boldsymbol{a}_{\mathbf{1}}$ and $\boldsymbol{a}_{\mathbf{2}}$ of the hexagonal lattice,

$$\mathbf{C}_{\mathbf{h}} = n\mathbf{a}_{\mathbf{1}} + m\mathbf{a}_{\mathbf{2}} \equiv (n, m), \qquad (n, m \text{ are integers, } m \le n).$$

The magnitude of $\boldsymbol{C}_{\mathbf{h}}$ is equal to the circumference of the CNT, and the CNT diameter d_{cnt} is calculated by

$$d_{\text{cnt}} = \frac{C_h}{\pi} = \frac{a(n^2 + m^2 + nm)^{1/2}}{\pi}. \tag{2.1.1}$$

The constant a is the length of $\mathbf{a}_{\mathbf{1}}$ and $\mathbf{a}_{\mathbf{2}}$ in the honeycomb lattice. The carbon-carbon bond length is expressed as a_{CC}, in which case $a = \sqrt{3}a_{CC}$. The chiral angle θ is defined as the angle between the vectors $\boldsymbol{C}_{\mathbf{h}}$ and $\boldsymbol{a}_{\mathbf{1}}$, and denotes the tilt angle of the hexagons with respect to the direction of the nanotube axis. The symmetry vector $\boldsymbol{R}$ is defined as the site vector OR and is used to generate the coordinates of carbon atoms in the CNT.

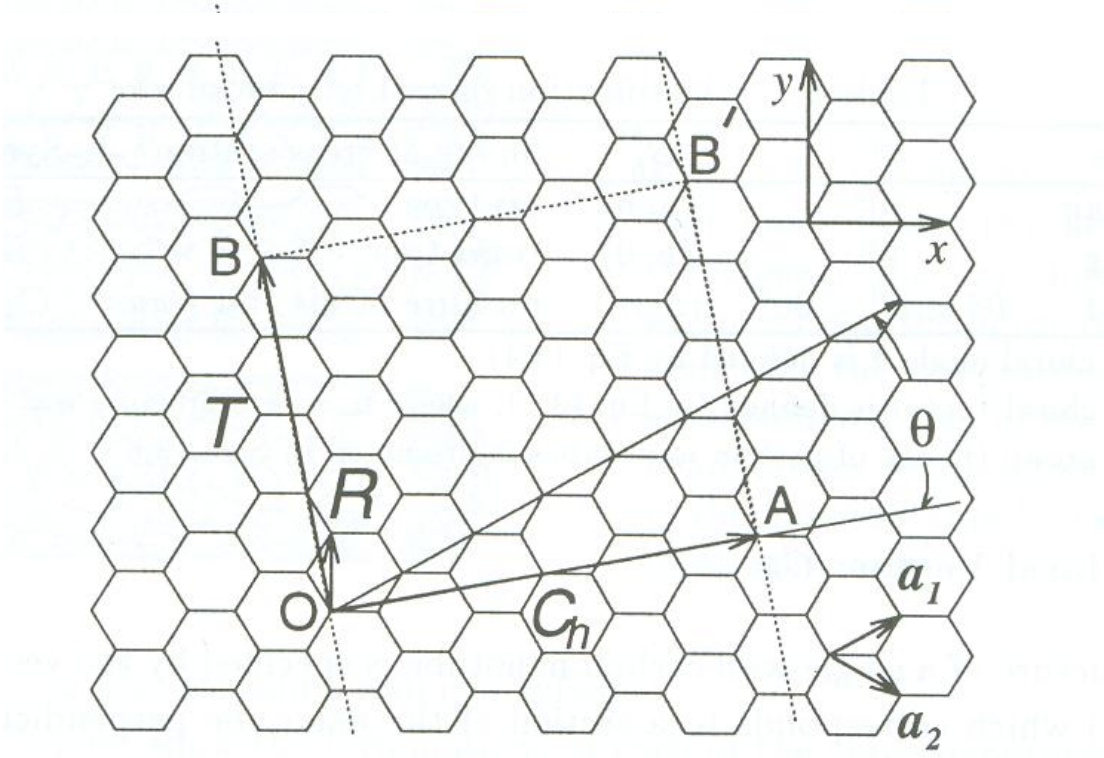

Figure 2.1. The unrolled honeycomb lattice of a nanotube [3].

The symmetry classification of a CNT is as either achiral or chiral. The mirror image of an achiral CNT has an identical structure to the original one. There are only two types of achiral CNTs: armchair and zigzag CNTs as shown in Figure 2.2 [3]. The names of armchair and zigzag CNTs arise from the shapes of the cross sectional rings shown in Figure 2.3. However, the mirror image of a chiral CNT shown in Figure 2.2 cannot be superposed on the original one. An armchair CNT corresponds to the case of $\boldsymbol{C}_\mathbf{h} = (n,n)$, and a zigzag CNT corresponds to the case of $\boldsymbol{C}_\mathbf{h} = (n,0)$. All other (n,m) chiral vectors correspond to chiral CNTs. The orientation of the honeycomb lattice relative to

the axis of a CNT can be taken arbitrary. Moreover, zigzag and armchair CNTs correspond to the chiral angle $\theta = 0^0$ and 30^0, respectively, while a chiral CNT correspond to $0^0 < |\theta| < 30^0$.

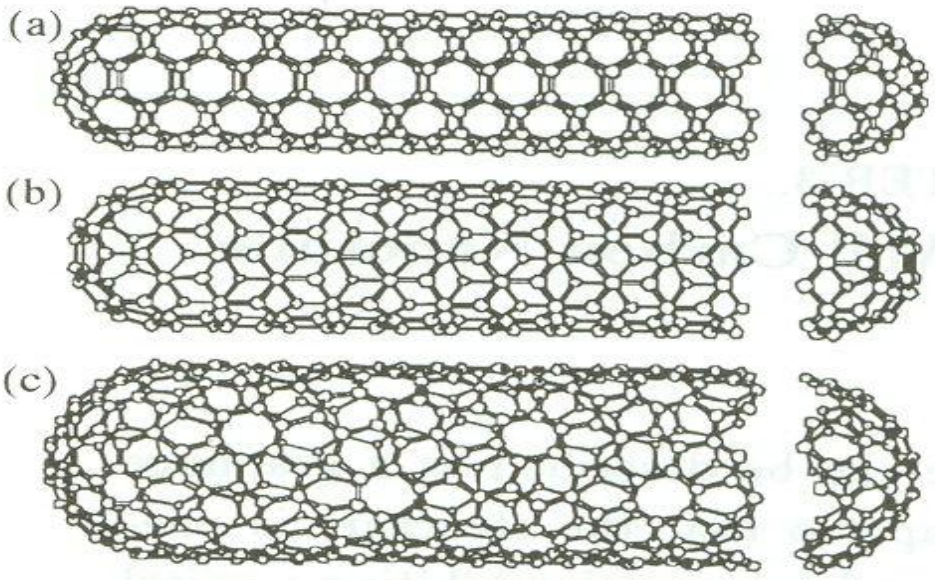

Figure 2.2. Classification of carbon nanotubes: (a) armchair, (b) zigzag, and (c) chiral nanotubes [3].

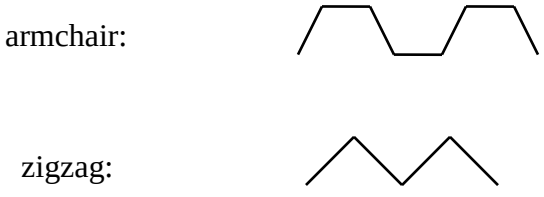

Figure 2.3. The shapes of cross section ring of an armchair and zigzag CNTs.

2.1.2 Electronic Properties of Carbon Nanotubes

The electronic structure of a CNT can be obtained from that of a two-dimensional graphite or graphene layer together with zone folding [2, 3, 6]. By using periodic boundary conditions in the circumferential direction $\boldsymbol{C}_\mathbf{h}$ in Figure 2.1, the wave vector associated with the $\boldsymbol{C}_\mathbf{h}$ direction becomes quantized, while the wave vector associated with the $\boldsymbol{T}$ direction remains continuous. As a result, each graphene band splits into a number of one-dimensional subbands. The Brillouin zone of a CNT is represented by many parallel line segments, and therefore the energy bands consist of a set of one-dimensional energy dispersion relations in which the allowed energy states are cuts of the graphene band structure. When these cuts pass through a *K* point of the graphene Brillouin zone, the tube is metallic [6]. Otherwise the tube is semiconducting. If (*n*-*m*) is a multiple of 3, the one-dimensional energy bands have a zero energy gap, and an individual CNT is metallic [3]. If (*n*-*m*) is not a multiple of 3, the one-dimensional energy bands have an energy gap, and a CNT is semiconducting. Thus armchair CNTs (*n*,*n*) are always metallic, and zigzag CNTs (*n*,0) are only metallic when *n* is a multiple of 3. Semiconducting CNTs are direct-gap nanostructures, and the energy gaps (E_g) depend inversely on the CNT diameter [2, 3]. For example, Figure 2.4 shows the one-dimensional energy dispersion relation of a semiconducting zigzag CNT (17,0) calculated by a tight-binding model with a hopping energy 3 eV [3]. Backward momentum (negative *k*) is symmetric to forward momentum (positive *k*), and the valence subbands are symmetric with respect to the conduction subbands. Thus the hole mobility is equal

to the electron mobility, i.e., $\mu = \mu_n = \mu_p$. Moreover, the first, second, third, and fourth conduction and valence subbands are doubly orbitally degenerate.

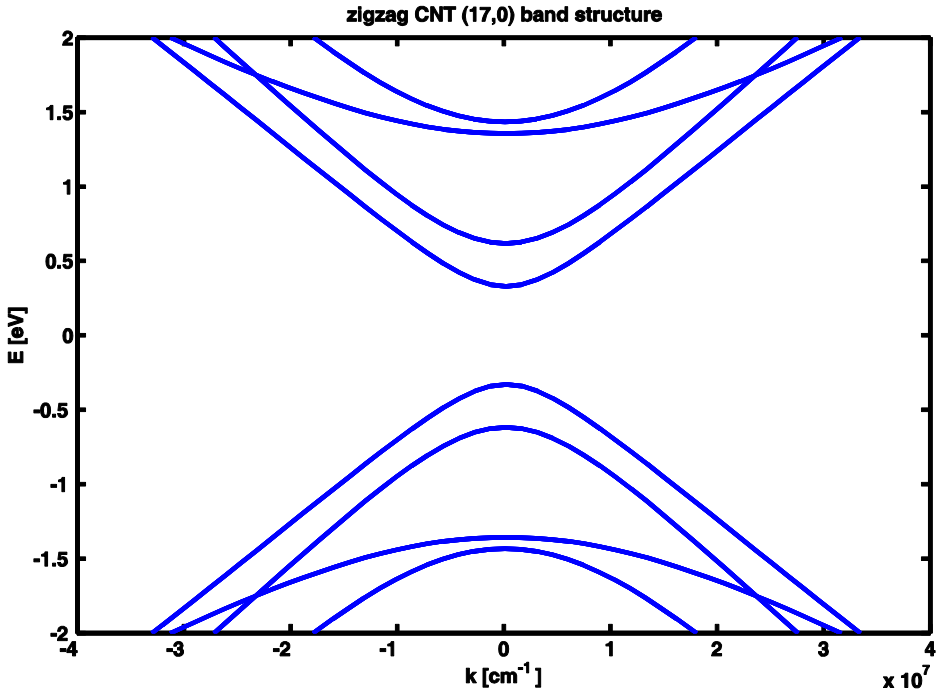

Figure 2.4. The one-dimensional band structure of a semiconducting zigzag CNT (17,0).

Carbon nanotubes exhibit high mobility at low electric fields, exceeding the best semiconductors at room temperature [9, 12, 13]. The criterion of ballistic and diffusive transport is determined by the mean-free-path (MFP) in the channel. References [14, 45-48] show that for CNTs at room temperature the mean-free-path is a few μm for defect scattering, a few hundreds nm for acoustic-phonon scattering, and 15nm for optical-phonon scattering. At low bias the acoustic-phonon scattering is the dominant

mechanism, and the transport is ballistic for the channel length shorter than a few hundred nm. At high bias the optical-phonon scattering is the dominant mechanism, and the transport is ballistic for the channel length shorter than 10nm. At low fields the mobility depends strongly on nanotube diameter, and the mobility increases with CNT diameter [9]. At high fields in excess of 27 kV/cm the drift velocity saturates [9, 11, 13], and the mobility is dramatically reduced by optical-phonon scattering [9, 14-16].

2.1.3 Optical Properties of Carbon Nanotubes

In bulk direct-gap materials, optical spectra at room temperature usually involve inter-band transition [1, 4]. In one-dimensional systems such as CNTs, the density of states diverges as the inverse of the square root of the energy, leading to van Hove singularities. The inter-band transitions mean the transitions between pairs of van Hove singularities. Most experimental papers discuss the excitation of CNTs in terms of band-to-band transitions and use tight-bind theory to predict their properties. However, a single-particle description of the excited CNT states omits electron-hole interactions, which should be particularly strong in the one-dimensional system. The electron-hole interaction is expected to bind the photoexcited electron and hole to form excitons. Theoretical studies [17-19] and later experimental studies [20-22] showed that electron confinement in the quasi-one-dimensional structure of CNTs leads to high electron-hole binding energies and the formation of strongly bound exciton states. The exciton binding energy depends on the diameter and chirality of the CNT, increasing with decreasing diameter, and on the dielectric constant of the surrounding environment. Perebeinos et al.

[18] derived general scaling rules for the properties of CNT excitons. They found that the exciton binding energy E_b scales with the CNT diameter d_{cnt}, effective mass m^*, and the dielectric constant ε_{ox} as

$$E_b = A_{con} d_{cnt}^{\alpha-2} \left(m^*\right)^{\alpha-1} \varepsilon_{ox}^{-\alpha}, \tag{2.1.2}$$

where $\alpha = 1.4$ and A_{con} is a constant value. Typically the binding energy is about 0.2~0.5 eV. For strong binding, most of the optical absorption is associated with photogeneration of excitons. Likewise, photoluminescence may be dominated by excitons.

The conduction and valence bands in CNTs are doubly orbitally degenerate. For free electron-hole pairs, this gives four distinct but degenerate pair excitations. In excitons, the Coulomb interaction partially lifts the fourfold degeneracy. For the excitonic spin-singlet states, the lowest-energy exciton is optically forbidden [23, 24], which is called a "dark exciton." The dark exciton is not directly accessed by photoexcitation due to the selection rule. The second-lowest-energy singlet exciton is optically active, which is called a "bright exciton." This bright exciton gives rise to the so-called E_{11} optical transition. The third-lowest-energy singlet excitons are degenerate, and both are dark. Moreover, all four lowest-energy excitons for the triplet-spin states are dark as well. Therefore, only the singlet bright exciton is considered when evaluating the effective radiative lifetime of excitons in the carbon nanotubes.

2.2 Optoelectronic Devices based on Carbon-Nanotube Field-Effect Transistors

Carbon nanotubes are considered as building blocks of a future nanoelectronic technology and optoelectronic applications, focusing on CNT FETs. The list below shows the advantages of CNT FETs [4, 5].

(1) The one-dimensional character of CNTs reduces the phase space for scattering and leads to large "on" currents in semiconductor CNT FETs.

(2) Unlike a conventional semiconductor channel, in CNTs all bonds are satisfied without introducing roughness scattering. This allows a wider choice of gate insulators other than SiO_2, such as high dielectric constant and crystalline insulators for improved gate control.

(3) All-nanotube-based electronic devices can be produced with metallic tubes acting as interconnects due to the high conductivity and exceptional stability, and semiconducting tubes acting as active devices.

(4) Semiconducting CNTs are direct-gap nanostructures and are the candidates for optoelectronic applications.

Carbon nanotubes are a promising class of materials with outstanding properties for electronics and optoelectronics, but many challenges remain. One of the biggest challenges is that the successful and reliable reproduction of a specific type of a CNT is still lacking [5].

Chapter 2.2.1 describes the electronic properties of CNT FETs, while Chapter 2.2.2 and 2.2.3 present the optical emitters and photodetectors based on CNT FETs.

2.2.1 Electronic Properties of Carbon-Nanotube Field-Effect Transistors

First, basic geometries for CNT FETs are briefly reviewed. There are various gate structures for CNT FETs. A back gate is an early configuration studied for electronic applications [25, 26]. Figure 2.5 shows a structure of a CNT FET with a planar back gate [9, 14-16, 27, 28]. A heavily doped p-type silicon substrate acts as a back gate, an oxide layer is an insulator, an intrinsic semiconducting CNT operates as a channel, and source and drain contacts are composed of a metal. A top gate [29-32], a partial top gate [33, 34], and a gate with a trench [35] are the gate structures in order to improve the performance of switching devices. All gates as mentioned above are practical planar gates. However, coaxial gates [36-41] are not practical and are only used to simulate the characteristics of CNT FETs. The comparison with silicon-on-insulator-based MOSFETs shows that key characteristics of switching CNT FETs, such as the ON current and transconductance, were better than those of Si MOSFETs [4]. Because a planar back gate is a recent structure for the optoelectronic applications [28, 42-44], it is used in this study.

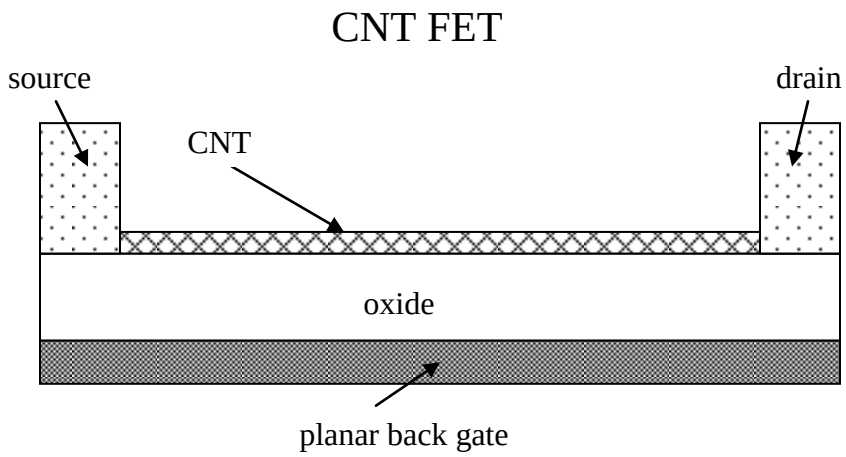

Figure 2.5. The geometry of a CNT FET with a planar back gate.

Next, the electronic properties of carbon-nanotube field-effect transistors are discussed. Ballistic-transport models applied to semiconducting CNT channels and Schottky-barrier models applied to contacts are treated in switching devices based on CNT FETs. However, these models cannot be directly applied to optical-emitting devices and the necessary modifications will be explained below. The mode of transport −whether ballistic or diffusive− is determined by the mean-free-path (MFP) in the channel composed of a CNT. For CNTs at room temperature the mean-free-path is a few μm for defect scattering, a few hundreds nm for acoustic-phonon scattering, and 15nm for optical-phonon scattering, as mentioned above. In switching devices base on CNT FETs the channel length is very short; thus, ballistic-transport models applied to CNT channels have been applied. In optical-emitting devices of CNT FETs the channel length ranges from 400nm to 800nm in [28], 50 μm in [42], and 10 μm in [50], and therefore a

diffusive-transport model applied to CNT channels for optical emitters has been utilized [50].

The contact properties of CNT FETs are determined by the processing. In general, Schottky barriers (SB) at the contacts between a metal and a semiconducting CNT were reported by most experiments [4, 31, 32, 53, 54]. For the ambipolar case there is a voltage drop associated with each contact which forms the Schottky barriers [49]. However, nearly ohmic contacts between a metal and a semiconducting CNT under some conditions are indicated by some experiments. In one case with ohmic contacts, the Schottky barrier to the valence bands of a semiconducting CNT is equal to zero, and the Schottky barrier to the conduction bands is equal to the energy gap [33, 45]. In another case, the contact conductance is much higher than the channel conductance [12].

The concept of "quantum capacitance" was used by Luryi in order to develop an equivalent-circuit model for devices that incorporate a conducting two-dimensional gas [55]. This term has also been used in the modeling of one-dimensional systems, such as CNT devices [39, 41, 56, 57]. The quantum capacitance C_Q of the CNT is defined as $e^2 D_{DOS}$, where D_{DOS} is the average density of states of the carbon nanotube. The total capacitance of the CNT FETs is considered as an insulator capacitance in series with the quantum capacitance of the CNT. The insulator capacitance of the CNT FET is given as Equation (3.1.2), and the value is about 0.38 pF/cm for 100 nm of the insulator thickness. The value of the quantum capacitance can be estimated as 4 pF/cm [41, 57]. Since the quantum capacitance is much larger than the insulator capacitance, the total capacitance can be approximated as the insulator capacitance of CNT FETs.

2.2.2 Optical Emitters Based on Carbon-Nanotube Field-Effect Transistors

In order to fabricate any electroluminescent device, one must radiatively recombine significant populations of electrons and holes. Typically, this is achieved at an interface between a hole-doped and an electron-doped material, i.e., a *p*-*n* junction. However, in ambipolar CNT FETs electrons and holes can be simultaneously injected at the opposite ends of the CNT channel. This enables electroluminescence (EL). Therefore, CNT light-emitting devices are solid-state, electrically driven devices [4, 6, 7]. CNT FETs with a back gate under ambipolar operation can produce a gate-controlled light source of infrared radiation with undoped CNTs, as distinguished from semiconductor-nanowire optical sources [28, 42]. Suspended CNT FETs under unipolar operation can produce unusually bright infrared emission [61]. Thermal light emission from metallic CNTs was reported in suspended FET structures [63, 64]. In the present study optical emitters based on ambipolar CNT FETs with a back gate are focused upon.

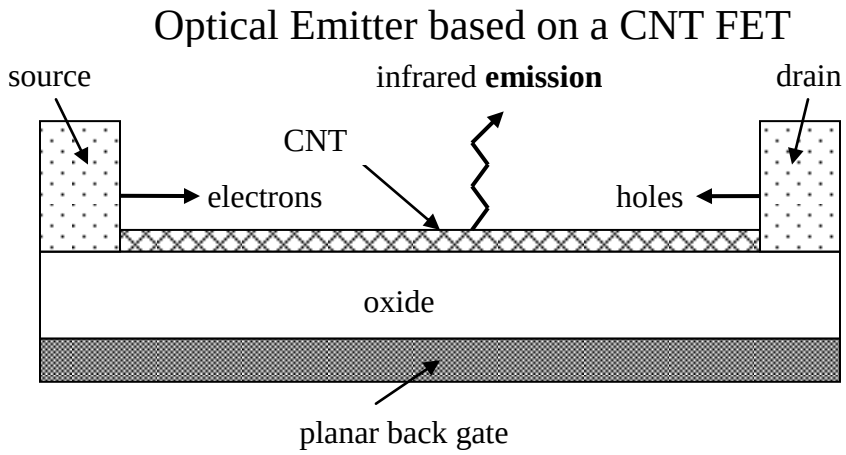

Figure 2.6. An optical emitter based on a long-channel ambipolar CNT FET with a back gate.

Figure 2.6 shows an optical emitter based on a long-channel ambipolar CNT FET with a back gate. Electrons are injected from the source and accumulate in the CNT nearby for a positive gate-to-source voltage, while holes are injected from the drain and accumulate nearby for a negative gate-to-drain voltage. This defines the ambipolar operating regime. Electrons and holes are injected from opposite ends of the CNT and radiatively recombine in the one-dimensional CNT. Spatially resolved studies of the light emission from CNT FETs involving very long channels (50μm), as a function of the applied gate and drain biases, provide unique insights to monitor the location of the electron- and hole-current fronts inside the CNT, to determine the electron-hole recombination length, and to identify local sources of electron-hole pair creation [42]. Electrons and holes in the CNTs can recombine by a variety of different mechanisms. In most cases, the energy will be released as heat (phonons), i.e., a nonradiative mechanism,

but a fraction of the recombination events may involve the emission of a photon, i.e., a radiative mechanism. This later process is termed as electroluminescence (EL) [6]. The infrared emission due to the radiative mechanism is depicted in Figure 2.6. In the publications [50, 51, 60] the radiative mechanism is assumed to be band-to-band recombination of injected electrons and holes. Optical emission from CNT FETs exhibits a variety of interesting properties. The emitted light is strongly polarized along the tube axis [6, 28]. The radiation has a characteristic energy depending on the diameter and chirality of the CNT. In optical emitters, the spatial region along the CNT of strong electron–hole recombination and hence the region of light emission, can be controlled by varying the gate and drain voltages [28, 42, 49]. Therefore, light emitters based on CNT FETs are moveable light sources. The emission spectra are in accord with the expected bandgaps in the experiment, while the emission intensity is highest when $V_{GS} = ½V_{DS}$ [44]. The emitted light-spot size compared with the long-channel CNT FETs is small (~2-~4 μm) [42].

It is worth noting that recently light emission has also been observed under unipolar transport condition in the suspended tubes [61]. The light intensity is stronger by a factor of ~1000 compared to ambipolar devices. The mechanism of this electroluminescence involves an efficient impact excitation process involving the hot carriers in CNTs, generated by the high local field [62]. By this impact excitation process, high exciton densities can be achieved to generate the bright light. In our study on light emitters based on ambipolar long-channel CNT FETs, the electrical field is small and is not sufficiently strong to generate excitons through impact excitation [51, 61].

2.2.3 Photodetectors Based on Carbon-Nanotube Field-Effect Transistors

Photoconductivity is the reverse of electroluminescence, with optical radiation producing electrons and holes that are separated by the applied field. CNT light detectors are also solid-state, electrically driven devices [4, 6, 7]. A photodetector based on a CNT FET with a back gate is shown in Figure 2.7. The photoexcitation of a CNT generates the electron-hole pairs. With an applied drain-to-source voltage both electrons and holes are collected at two contacts, and thus produce a photocurrent [21, 43]. The photocurrent is maximized for photons polarized along the direction of the CNT. Thus, the CNT FET acts as a polarized photodetector with a diameter 1000 times smaller than the wavelength of the light it detects and has an estimated quantum efficiency of > 10% [43]. Alternatively, in the open-circuit configuration, the device generates a photovoltage. Internal fields, such as those formed a Schottky contacts and those in defect sites, can be used to image such sites and determine the band bending in the open-circuit configuration [65-69]. A CNT measures only ~1 nm in at least two dimensions, and as such absorbs very little of the incident radiation [75]. Since the photocurrent is proportional to the absorbed power, photoconductivity can be used for spectroscopy [1]. In Reference [21], in addition to the strong exciton transition, a weaker side-band about 200 meV above the exciton transition is observed. The side-band reflects the effect of exciton-phonon coupling [76].

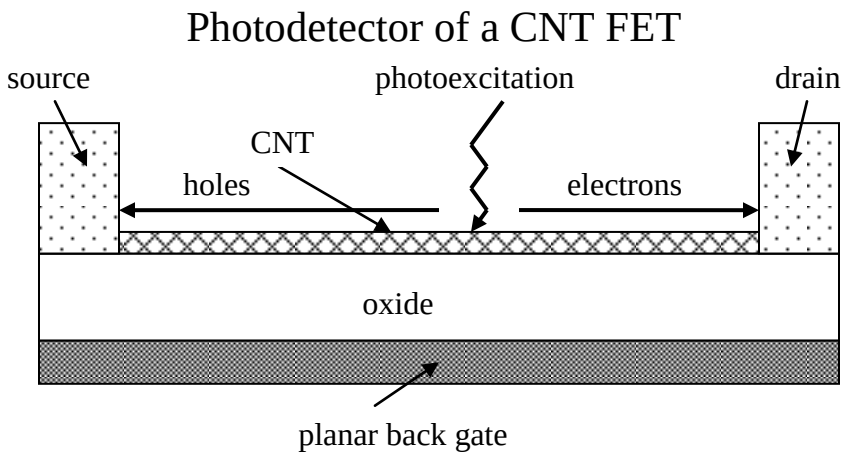

Figure 2.7. A photodetector based on a long-channel CNT FET with a back gate.

2.3 Summary for Optoelectronic Devices Based on Carbon-Nanotube Field-Effect Transistors

In conclusion, we present the electronic and optical properties of CNTs and optical emitters and photodetectors based on CNT FETs. The symmetry classification of a CNT is as either achiral or chiral. There are only two types of achiral CNTs: armchair and zigzag CNTs Armchair CNTs (*n*,*n*) are always metallic, and zigzag CNTs (*n*,0) are only metallic when *n* is a multiple of 3. Carbon nanotubes exhibit high mobility at low electric fields, exceeding the best semiconductors at room temperature. Electron confinement in the quasi-one-dimensional structure of CNTs leads to high exciton binding energies. The exciton binding energy depends on the diameter and chirality of the CNT, increasing with decreasing diameter. In CNTs, only the second-lowest-energy

singlet exciton is a bright exciton. Other three lowest-energy singlet excitons and all four lowest-energy excitons for the triplet-spin states are dark excitons.

For the ambipolar CNT FETs there is a voltage drop associated with each contact which forms the Schottky barriers. The concept of "quantum capacitance" was used to develop an equivalent-circuit model for devices. Since the quantum capacitance is much larger than the insulator capacitance, the total capacitance can be approximated as the insulator capacitance of CNT FETs. In ambipolar CNT FETs electrons and holes can be simultaneously injected at the opposite ends of the CNT channel. The recombination of electrons and holes may involve the emission of a photon, i.e., a radiative mechanism. This enables electroluminescence (EL). Optical emitters based on CNT FETs including radiative and various nonradiative recombination mechanisms are discussed. Photoconductivity is the reverse of electroluminescence, with optical radiation producing electrons and holes that are separated by the applied field. Photodetectors based on CNT FETs are discussed as well.

CHAPTER 3

MODELING OF OPTOELECTRONIC DEVICES BASED ON CARBON-NANOTUBE FIELD-EFFECT TRANSISTORS

The criteria giving rise to ballistic or diffusive transport are determined by the mean-free-path (MFP) in the channel composed of a carbon nanotube. For CNTs at room temperature the mean-free-path is a few μm for defect scattering, a few hundreds nm for acoustic-phonon scattering, and 15nm for optical-phonon scattering, as mentioned above. In optical-emitting devices based on CNT FETs the channel length is 60 μm in [49], 50 μm in [42], and 10 μm in [50]. In our study the channel length of both optical emitters and photodetectors is 60 μm, and therefore a diffusive-transport model is applied to the CNT channels for both optical emitters and photodetectors.

Optical emission and photoconductivity from CNT FETs can be explained in terms of radiative recombination involving both the band-to-band recombination and the generation and decay of excitons, and different nonradiative recombination mechanisms along the channel. A simulated structure of an ambipolar CNT FET with a planar back gate is shown in Figure 3.1. The ambipolar CNT FET modeled consists of an intrinsic semiconducting single-wall CNT providing a long channel with a length L (cm), source and drain contacts composed of Pd or Ti [21, 28, 42, 43], and a SiO_2 gate insulator with a thickness d_{ox} (nm). A drift-diffusion model and a simplified model for Poisson's equation as well as the exciton continuity equation are proposed to the channel, while the boundary conditions (BCs) are used in the region near the contacts. Ambipolar FETs operate with one electron injecting (*e*-source) and one hole injecting (*h*-source) contact.

The *e*-source contact also acts as the drain for holes (*h*-drain) and the *h*-source contact also acts as the drain for electrons (*e*-drain). By using conventional *n*-channel FET terminology, define the *e*-source as the "source" (S) and *h*-source as the "drain" (D). The applied gate (G) and drain (D) voltages, V_G and V_D, are measured with respect to the source (S) $V_S = 0$. Electrons are injected from *e*-source "S" and accumulate in the CNT near *e*-source "S" for positive V_G, while holes are injected from *h*-source "D" and accumulate near there for negative V_G-V_D. This defines the ambipolar operating regime.

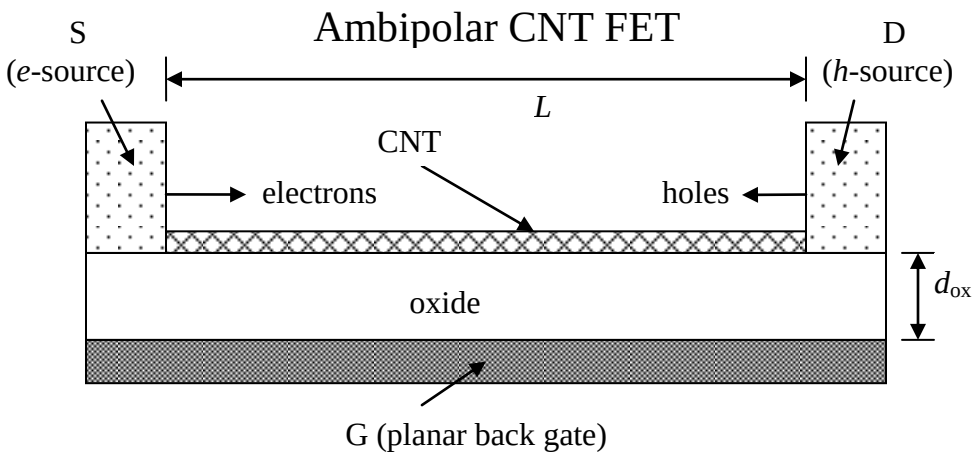

Figure 3.1. A simulated structure of an ambipolar CNT FET with a planar back gate.

The modeling provided through this chapter is applied to both optical emitters and photodetectors based on CNT FETs, while the modeling of the photoexcitation in Chapter 3.6 is only applied to the photodetectors. All the models include a system of

nonlinear differential equations. The interesting electronic properties of both optical emitters and photodetectors, such as the one-dimensional electron and hole densities, CNT potentials, and device currents, can be calculated by solving the system of nonlinear differential equations. However, the calculation will be shown in the following chapters. The interesting optical properties, such as the emitted optical power for the light emitters and the photocurrent and exciton densities for the photodetectors through the photoexcitation will be calculated.

The modeling of both optical emitters and photodetectors based on CNT FETs is studied in this chapter. First, modeling of the gradual-channel approximation (GCA), drift-diffusion currents, and electron and hole continuity equations applied to CNT FETs is introduced. Next, modeling of various recombination mechanisms of electron and holes in the optical emitters is presented. Modeling of the photoexication and exciton continuity equations in the photodetectors is studied as well.

3.1 Poisson Equation

In order to determine the CNT potential, a simplified model for Poisson's equation is chosen. For long-channel CNT FETs the longitudinal electric field F_x is a much more gradual function of position than the transverse electric field, *i.e.*, the gradual-channel approximation (GCA) holds. Thus, the local carrier density is simply related to the gate-capacitance and the voltage drop across the gate insulator [49, 51, 56],

$$\rho(x) = e[p(x) - n(x)] = C[\psi(x) - (V_G - V_{fb})], \tag{3.1.1}$$

where p and n are the linear hole and electron densities in the CNT, e is the fundamental charge, ρ is the linear charge density, C is the linear gate-to-channel capacitance, ψ is the CNT potential, and V_{fb} is the flat-band voltage. The longitudinal position x is along the CNT with source S at $x = 0$ and drain D at $x = L$. The total capacitance of a CNT FET can be approximated as the insulator capacitance, as mentioned above. The capacitance C is given by [77]

$$C = \frac{2\pi\varepsilon_{\mathrm{ox}}\varepsilon_0}{\cosh^{-1}(1+2d_{ox}/d_{cnt})} \approx \frac{2\pi\varepsilon_{\mathrm{ox}}\varepsilon_0}{\ln(4d_{ox}/d_{cnt})}, \tag{3.1.2}$$

where $\varepsilon_{\mathrm{ox}}$ and d_{ox} are the relative dielectric constant and thickness, respectively, of the gate insulator SiO_2. The observed hysteresis of the current-voltage characteristics in the fabricated devices [42, 43, 49] indicates that there are the charges in the insulator or in the CNT-insulator interface. The flat-band voltage V_{fb} includes the effect of those charges and the work-function difference between the gate G and the channel.

The terminal voltages are related to the CNT potential ψ at S and D via

$$\psi_S = V_S + \Delta V_s \tag{3.1.3}$$

and

$$V_D = \psi_D + \Delta V_d. \tag{3.1.4}$$

Here ΔV_{s} and ΔV_{d} are the voltage drops across the contact/channel interfaces, while ψ_{S} is the CNT potential at S and ψ_{D} is the CNT potential at D. The metal-CNT interfaces form the Schottky barriers as mentioned above. For the ambipolar case, the voltage drop cannot be less than the Schottky barrier height [49]. In our model their effect is simplified to a constant voltage drop independent of the current, and the values of ΔV_s

and ΔV_d are assumed to be the same at both S and D contacts [49, 51]. This assumption is applied to the boundary conditions of CNT potential ψ.

3.2 Drift-Diffusion Currents

For the applied voltage with $V_S < V_G < V_D$ in the ambipolar regime, the electrons inject from the *e*-source (S) and the holes inject from the *h*-source, i.e. *e*-drain (D)**.** By assuming the positive carrier currents I_n and I_p defined from D at $x = L$ to S at $x = 0$, the drift-diffusion electron I_n and hole I_p currents are given by

$$I_n(x) = -en(x)\mu F_x(x) - eD_n \frac{dn(x)}{dx}, \tag{3.2.1}$$

$$I_p(x) = -ep(x)\mu F_x(x) + eD_p \frac{dp(x)}{dx}. \tag{3.2.2}$$

The longitudinal electrical field $F_x(x)$ along the CNT is given by $-\partial\psi(x)/\partial x$. The device current I from D to S is equal to I_n+I_p. The values of the mobility μ ($cm^2s^{-1}V^{-1}$) are the same for both electrons and holes due to the symmetry of the band structure about the band-gap center [3]. The electron and hole diffusion coefficients are D_n (cm^2s^{-1}) and D_p (cm^2s^{-1}), respectively. For large carrier densities, a Fermi-Dirac distribution rather than the Boltzmann distribution has to be used. Using the formula of Kroemer [58] in degenerate semiconductors, the Einstein relation can be approximated by

$$\frac{D_n}{\mu} = V_t(1 + A_1\zeta + 2A_2\zeta^2 + 3A_3\zeta^3 + 4A_4\zeta^4 + \ldots), \tag{3.2.3}$$

where $\zeta = n/N_c$, $V_t = k_B T/e$ is the thermal voltage, and N_c is the effective density of states of electrons and holes. By using the procedure of Joyce and Dixon [59] applied to the Fermi-Dirac integral of order -½ for the one-dimensional case, the parameters of A_i, i = 1,2,3,4, can be calculated below. Reference [59] shows that retention of terms through $A_4\zeta^4$ yields the correct result for $\zeta < 6$. The parameter g_i for the Laplace transform of $x^{-1/2}$ for the one-dimensional case is computed as $g_i = \Gamma(½) i^{-1/2} = \left(\sqrt{\pi}/2\right) i^{-1/2}$, and then substituted into the formula for A_i to obtain [49, 51]

$$\begin{cases} A_1 = \dfrac{g_2}{g_1} = \dfrac{1}{\sqrt{2}} = 0.7071, \\ A_2 = \dfrac{3}{2}\left(\dfrac{g_2}{g_1}\right)^2 - \dfrac{g_3}{g_1} = 0.1726, \\ A_3 = \dfrac{g_4}{g_1} + \dfrac{10}{3}\left(\dfrac{g_2}{g_1}\right)^3 - 4\dfrac{g_2}{g_1}\dfrac{g_3}{g_1} = 0.04552, \\ A_4 = \dfrac{5}{2}\left(\dfrac{g_3}{g_1}\right)^2 + \dfrac{35}{4}\left(\dfrac{g_2}{g_1}\right)^4 + 5\dfrac{g_2}{g_1}\dfrac{g_4}{g_1} - 15\left(\dfrac{g_2}{g_1}\right)^2\dfrac{g_3}{g_1} - \dfrac{g_5}{g_1} = 0.01126. \end{cases} \tag{3.2.4}$$

The one-dimensional density of states of electrons is equal to $\dfrac{2}{\pi\hbar}\sqrt{\dfrac{2m_e^*}{E_k}}$ [78], where the first 2 indicates the double-degenerate conduction subbands, m_e^* is the electron effective mass, E_k is the kinetic energy of electrons, and $\hbar$ is the reduced Planck's constant. For the one-dimensional case, the effective density of states N_c of electrons is calculated as $N_c = \dfrac{2}{\hbar}\sqrt{\dfrac{2m_e^* k_B T}{\pi}}$.

3.3 Constant Low-Field Mobility for the Long-Channel CNT FETs

Electron mobility in CNTs, in general, depends on the CNT diameter, electric field, and temperature [6-11]. Low-field mobility at room temperature can be obtained by two different methods. One method is theoretical. The mobility of a specific type of semiconducting CNT can be calculated theoretically by using electron-phonon scattering [8, 9, 11], and there are different values for various types of CNTs. Another method is experimental. A simple channel-conductance model of CNT FETs is used to estimate the low-field mobility from the experimental data [12, 34, 45, 48, 79, 80]. However, the specific type of CNT is frequently unknown, and the values of mobility vary from 1000 to 10,000 $cm^2s^{-1}V^{-1}$. Because the specific type of CNTs is needed for computing purposes, the mobility in the present study is computed theoretically.

Elastic scattering in CNTs is weak, which has long mean free path on the order of a micrometer [6], and thus inelastic scattering processes determine the transport properties [7]. At low bias, only low-energy acoustic phonons can scatter the electrons, which results in a reverse temperature dependence for the carrier mobility in semiconducting CNTs [9]. Acoustic-phonon scattering is predominantly a backscattering event, and only a small fraction of phonons in the vicinity of the zone center and zone boundary can effectively participate in the scattering. The low-field mobility is very high (10^5 cm^2/Vs) even at room temperature [12]. The reason is very weak electron-acoustic-phonon coupling and the very large optical-phonon energy of about 200 meV. The inverse diameter dependence of the effective mass and of the electron-phonon coupling strength leads to a quadratic diameter dependence of the mobility [9], which is confirmed

experimentally [81]. That is, the larger the CNT diameter is, the higher the mobility is. The zero-field mobility μ_0 is given by an empirical relation [9],

$$\mu_0\left(T, d_{\text{cnt}}\right) = \mu_1 \frac{300}{T}\left(\frac{d_{\text{cnt}}}{1\text{ nm}}\right)^{2.26}, \tag{3.3.1}$$

in which μ_1 = 12,000 $cm^2s^{-1}V^{-1}$, and T is the temperature. For example, at room temperature the values of zero-field mobility μ_0 are calculated as 65,000 cm^2/Vs for (25,0) nanotube with a diameter 1.98 nm, 35,500 cm^2/Vs for (19,0) nanotube with diameter 1.5 nm, and 15,000 cm^2/Vs for (13,0) nanotube with a diameter 1 nm.

Optical-phonon scattering is very strong in CNTs. Optical phonons contract and elongate the C-C bond length and leads to a modulation of the electronic structure [7]. However, for electrons to emit an optical phonon, their energy must be larger than the optical-phonon energy. This can be achieved under high bias conditions. At low electrical field, the drift velocity initially increases as the field increases, and then saturates for high field [8, 9, 82]. Therefore, at the low field, the mobility is constant, and then decreases for the high field.

The one-dimensional electronic states of CNTs lead to van-Hove singularities in the density of states, which in return are responsible for the non-monotonic dependence of the mobility on band filling [12, 13, 81]. As the band is filled, by an applied gate potential, the mobility initially increases owing the loss of available final states for the scattered particles. Once the Fermi-level reaches a higher energy subband, in which the carrier density is large enough, an additional scattering channel opens and again lowers the mobility.

For long-channel CNT FETs the electric field is low, and the carrier density is assumed low enough so that the carrier mobility does not depend on carrier density.

Therefore, the constant low-field mobility can be applied to this model. However, this assumption will be justified as the electric field and carrier density are calculated.

3.4 Electron and Hole Continuity Equations in the Steady state

Remember that the positive carrier currents I_n and I_p are defined from D at $x = L$ to S at $x = 0$. The electron and hole continuity equations in steady state are given by

$$\frac{\partial n(x)}{\partial t} = -\frac{1}{e}\frac{dI_n(x)}{dx} + G(x) - R(x) = 0, \tag{3.4.1}$$

$$\frac{\partial p(x)}{\partial t} = \frac{1}{e}\frac{dI_p(x)}{dx} + G(x) - R(x) = 0. \tag{3.4.2}$$

G [$cm^{-1}s^{-1}$] is the generation rate of electrons and holes, and R [$cm^{-1}s^{-1}$] is the recombination rate of electrons and holes. By substituting the drift-diffusion currents of Equations (3.2.1) and (3.2.2) into the continuity equations of Equations (3.4.1) and (3.4.2), two differential equations are obtained, and two boundary conditions are necessary at each contact. For the optical emitters based on ambipolar long-channel CNT FETs, because the channel length exceeds the recombination length, essentially all injected carriers recombine within the channel. Hence, electrons injected from S fully recombine with the holes in the channel and the electron density is negligible at D. Similarly, holes injected from D do not reach S. This assumption is applied to the boundary conditions of the minority carrier density at both S and D in the optical emitters. In general, the contacts between a metal and a semiconducting CNT form Schottky barriers (SB), as mentioned above. A quantum treatment is used to compute the injected

currents through the Schottky barriers [83], but the calculation is numerically intensive. In our model their effect is simplified to a constant voltage drop independent of current, and the values of the voltage drops across the contact/channel interfaces are assumed to be the same value at both (S and D) contacts [49, 51]. For photodetectors based on the long-channel CNT FETs, the incident light shines on the channel but not on the contacts in our model. The excitons generated by photoexcitation are ionized or dissociated to free electron-hole pairs that are separated by the applied field. With an applied drain-to-source voltage, both electrons and holes are collected at two contacts, and thus produce a photocurrent. The photocurrents can be considered as the difference between the device currents with and without photoexcitation. Therefore, the assumption applied to the boundary conditions of the minority carrier density at both S and D, and the assumption of a constant voltage drop across the contact/channel interfaces are used in the photodetectors as well.

3.5 Recombination and Generation of Electrons and Holes

In optical emitters based on ambipolar CNT FETs the carrier recombination can be radiative or nonradiative. Nonradiative recombination is much stronger than radiative, as evidenced by the low measured quantum efficiency between 10^{-6} and 10^{-7} photons per injected *e-h* pair [44]; therefore, the transport properties and carrier densities are determined by assuming only nonradiative recombination. In the publications [50, 60] the radiative mechanism is assumed as the band-to-band recombination of injected electrons and holes. When defects and impurities exist, e.g., at the CNT-insulator

interface, Shockley-Read-Hall (SRH) recombination is important. Band-to-band nonradiative recombination (BBN), in which phonons are emitted, and Auger recombination are considered also [51]. Expressions for the nonradiative recombination rates R_{nr} and the coefficients chosen are listed in Table 3.1. For light emission generated by band-to-band radiative recombination (BBR) of electrons and holes, the radiative recombination rate R_r is assumed as $B_{BBR}(np\text{-}n_i^2)$, where B_{BBR} [cm/s] is the band-to-band radiative recombination coefficient [50, 51, 60]. Then the emitted optical power P_{opt} is calculated as $E_g \int_0^L R_r(x)dx$, in which E_g is the band-gap of the CNT.

Table 3.1. Nonradiative recombination rates R_{nr} and coefficients.

SRH	$R_{nr} = \dfrac{np - n_i^2}{\tau_{SRH}(n + p + 2n_i)}$	τ_{SRH} unit = s
BBN	$R_{nr} = B_{BBN}(np\text{-}n_i^2)$	B_{BBN} unit = cm/s
Auger	$R_{nr} = B_{Auger}(n+p)(np\text{-}n_i^2)$	B_{Auger} unit = cm^2/s

In photodetectors based on CNT FETs, the photoexcitation can both generate the *e-h* pairs through interband transitions and can also generate excitons. Electron confinement in the quasi-one-dimensional structure of CNTs leads to the formation of strongly bound exciton states. For strong binding, most of the optical absorption is associated with photogeneration of excitons. Therefore, photogeneration of excitons is the dominant mechanism, as mentioned above. The generation rate of *e-h* pairs through

the interband transition is depicted as G_{bb}. The exciton-ionization rate $r_d n_{xs}$ is the generation rate of *e-h* pairs, and thus the total generation rate G of electrons and holes is equal to $r_d n_{xs}+G_{bb}$. The bimolecular recombination rate of electrons and holes involved in the exciton-formation is described as $B_x np$, where B_x [cm s^{-1}] is the capture parameter for exciton formation.

3.6 Photoexcitation in the Photodetectors

In the CNT the electron confinement in the quasi-one-dimensional structure leads to electron-hole binding energies and formation of strongly-bound exciton states [1, 17-22], as mentioned above. The exciton binding energy depends on the diameter and chirality of the CNT, increasing with decreasing diameter, and on the dielectric constant of the surrounding environment, shown in Equation (2.1.2). In CNTs most of the oscillator strength is transferred from inter-band to excitonic transitions, which dominate their optical absorption spectra [18, 19]. Only in CNTs embedded in high dielectric constant media, in which the exciton binding energy is small, the inter-band transitions become strong. The fractional value of the number of excitons generated by the electron-hole interaction per one incident photon is given as α_{ex}, while the fractional value of the number of free *e-h* pairs generated by the interband transitions per one incident photon is given as α_{bb}. The spectra of both α_{ex} and α_{bb} depend on the incident photon energies. Since the diameter of a CNT is so small (~1 nm), the incident radiation is absorbed very slightly. An experimental measurement determined optical absorption cross sections of carbon nanotubes for visible light copolarized and cross polarized with respect to the

CNT axis [75]. The measured optical absorption cross section is given as A_{cm} with the unit [cm^2/mole C]. The calculation of the generation rate of excitons through the photoexcitation is shown below. Assume that the incident optical power density is P_{incd} [W/cm^2] and the photon energy is E_{ph} [Joul], and then the number of incident photons per area per second is depicted as P_{incn} [number of incident photons/cm^2 s], which is given as

$$P_{incn} = \frac{P_{incd}}{E_{ph}}. \tag{3.6.1}$$

For a zigzag CNT (n_{zz}, 0) the length of a unit cell is $\sqrt{3}a = 3a_{CC}$, the number of the hexagons in the unit cell is $2n_{zz}$, and the number of the carbons is $4n_{zz}$. In the CNTs the one-dimensional absorbed rate of photons per length per second is depicted as A_{abs} [number of absorbed photons/cm s], which is given as

$$\begin{aligned} A_{abs} &= P_{incn}\left[\frac{\text{number of incident photons}}{\text{cm}^2\ \text{s}}\right] \times A_{cm}\left[\frac{\text{cm}^2}{\text{mole C}}\right] \times \frac{1[\text{mole}]}{6\times 10^{23}} \times \frac{4n_{zz}[\text{C}]}{3a_{CC}[\text{cm}]} \\ &= \frac{P_{incd}A_{cm}\times 4n_{zz}}{E_{ph}\times 6\times 10^{23}\times 3a_{CC}}\left[\frac{\text{number of absorbed photons}}{\text{cm s}}\right]. \end{aligned} \tag{3.6.2}$$

The incident lights uniformly exciting the whole devices including the CNT channel and the contacts were reported in the experiments [21, 43], while the relatively small focus of the laser spot exciting the part of the CNT channel and the contacts was reported [66-69]. In our study in the photodetector based on the CNT FETs the incident light exciting the CNT channel but not the contacts is considered, and both uniform and Gaussian profiles of the incident light are included. The incident light profile is assumed as $f_{inc}(x)$. Therefore, the generation rate of the exciton-*i* through the phtoexcitation is given as

$$G_{xi}\left(x, E_{ph}\right) = A_{abs}\left(E_{ph}\right) \times f_{inc}\left(x\right) \times \alpha_{exi}\left(E_{ph}\right), \tag{3.6.3}$$

where G_{xi} has the unit [number of excitons/cm s]. Since both A_{abs} and α_{exi} depend on the photon energy E_{ph} and f_{inc} depends on x, and then G_{xi} depends on both E_{ph} and x. Similarly, the generation rate of the free *e-h* pairs by the interband transition through the photoexcitation is given as

$$G_{bb}\left(x, E_{ph}\right) = A_{abs}\left(E_{ph}\right) \times f_{inc}\left(x\right) \times \alpha_{bb}\left(E_{ph}\right). \tag{3.6.4}$$

3.7 Exciton Continuity Equations in Carbon Nanotubes

In carbon nanotubes the energy levels of both conduction and valence bands nearest the band edge are doubly orbitally degenerate [3]. For free electron-hole pairs, the Coulomb interaction creates four distinct but degenerate lowest-energy singlet excitons. The lowest-energy exciton is a dipole-forbidden exciton (dark exciton), the second lowest-energy exciton is an optically active exciton (bright exciton), and the third lowest-energy excitons are double-degenerate dark excitons [23, 24]. There are four distinct lowest-energy triplet excitons, but all triplet excitons are dark excitons. Therefore, only the continuity equations of singlet excions are focused here.

The continuity equations for these singlet excitons are given as

$$
\begin{cases}
\dfrac{dn_{x1}}{dt} = G_{x1} + B_{x1}np - r_{d1}n_{x1} - r_{1nr}n_{x1} + \left(-r_{12}n_{x1} + r_{21}n_{x2} - r_{13}n_{x1} + r_{31}n_{x3}\right) \\
\qquad + \dfrac{d}{dx}\left(D_{x1}\dfrac{dn_{x1}}{dx}\right), \\
\dfrac{dn_{x2}}{dt} = G_{x2} + B_{x2}np - r_{d2}n_{x2} - (r_{2r} + r_{2nr})n_{x2} + (r_{12}n_{x1} - r_{21}n_{x2} - r_{23}n_{x2} + r_{32}n_{x3}) \\
\qquad + \dfrac{d}{dx}\left(D_{x2}\dfrac{dn_{x2}}{dx}\right), \\
\dfrac{dn_{x3}}{dt} = G_{x3} + B_{x3}np - r_{d3}n_{x3} - r_{3nr}n_{x3} + (r_{13}n_{x1} - r_{31}n_{x3} + r_{23}n_{x2} - r_{32}n_{x3}) \\
\qquad + \dfrac{d}{dx}\left(D_{x3}\dfrac{dn_{x3}}{dx}\right).
\end{cases}
\tag{3.7.1}
$$

n_{x1}, n_{x2}, and n_{x3} [cm^{-1}] are the singlet-exciton densities for the dark exciton-1, bright exciton-2, and dark exciton-3, respectively. G_{x2} [$cm^{-1}s^{-1}$] is the bright exciton-2 generation rate from photoexcitation, G_{x3} is the dark exciton-3 generation rate due to the exciton-phonon coupling [76], and G_{x1} is the dark exciton-1 generation rate which is assumed as zero. The rate of exciton formation involving the bimolecular recombination of electrons and holes is described as $B_{xi}np$, where B_{xi} [$cm\ s^{-1}$] is the capture parameter for exciton formation. The rate of exciton ionization (i.e., exciton dissociation) to free *e-h* pairs is depicted as $r_{di}n_{xi}$, where r_{di} [s^{-1}] is the coefficient. The radiative-decay and nonradiative-decay coefficients of excitons are given as r_{ir} and r_{inr} [s^{-1}], respectively. The transition rate from exciton-*i* to exciton-*j* is described as $r_{ij}n_{xi}$, where r_{ij} [s^{-1}] is the coefficient. The exciton-diffusion coefficient is given as D_{xi} [$cm^2\ s^{-1}$].

The effect of the field-dependent ionization of excitons [71] is neglected since the electric field in the long channel of CNT FETs is low [51, 52]. The ratio of the exciton-ionization (exciton-dissociation) coefficient r_{di} to the capture parameter B_{xi} of exciton formation, i.e., r_{di}/B_{xi}, is assumed as the Arrhenius equilibrium constant [72-74], which is the Saha's equation in the case of the chemical equilibrium. There were many

approaches published to derive the Arrhenius equilibrium constant and Saha's equation. The three-dimensional Saha's equation for the dissociation equilibrium was derived by using the method of quantum-mechanical canonical grand ensembles [84], or by using the approach of phase-space maximization of statistical mechanics [85]. The three-dimensional Arrhenius equilibrium constant for the silicon in the chemical equilibrium was derived by using the approach of the partition function [72, 73], while the two-dimensional Arrhenius equilibrium constant was derived for the GaAs quantum well [74]. In addition, the three-dimension Saha's equation in exciton condensates was derived by using the property of chemical potentials [86]. Since the excitons in the CNTs are quasi-one-dimensional, the derivation of one-dimensional Arrhenius equilibrium constant, which is equal to the ratio of the exciton-ionization coefficient r_{di} to the capture parameter B_{xi} of exciton formation, i.e., $r_{di}/B_{xi,}$ is shown in Chapter 3.8. Two approaches are used: one is using partition function, and another is using the property of chemical potentials.

The energy levels of the exciton-1, exciton-2, and exciton-3 are depicted as E_{x1}, E_{x2}, and E_{x3}, respectively. The exciton splitting energy δ_1 (=E_{x2}-E_{x1}) is assumed to be energy difference between the energy levels of exciton-1 and exciton-2, and the splitting energy δ_2 (=E_{x3}-E_{x1}) is assumed as the energy difference between the energy levels of exciton-1 and exciton-3. The exciton splitting energies are very small (~4-~23 meV); therefore, thermal equilibrium is a good assumption due to the fast transition between those exciton states. The total singlet-exciton density n_{xs} is assumed as n_{x1}+n_{x2}+n_{x3}. Expressing the *i*th-exciton density in terms of the total singlet-exciton density n_{xs} gives $n_{x1} = \zeta_1 n_{xs}$, $n_{x2} = \zeta_2 n_{xs}$, and $n_{x3} = \zeta_3 n_{xs}$. The parameters $\zeta_{1,2,3}$ in the thermal equilibrium is

derived by two methods, shown in Chapter 3.9. The first method is to calculate the ratio of probability of exciton-*i* to probability of total excitons by using the partition function. The second method is to calculate the ratio of density of exciton-*i* to density of total excitons by using the property of the equal chemical potentials (Fermi levels) of excitons in the thermal equilibrium.

By summing all individual lines of Equation (3.7.1), the continuity equation of the total singlet-exciton density n_{xs} is given as [52]

$$\frac{dn_{xs}}{dt} = G_x + B_x np - r_d n_{xs} - (r_r + r_{nr}) n_{xs} + \frac{d}{dx}\left(D_x \frac{dn_{xs}}{dx} \right). \tag{3.7.2}$$

The relationships of coefficients are shown below.

The generation rate of excitons: $G_x = G_{x1}+G_{x2}+G_{x3}$.

The capture parameter for exciton formation: $B_x = B_{x1}+B_{x2}+B_{x3}$.

The exciton-ionization (exciton-dissociation) coefficient: $r_d = \zeta_1 r_{d1}+\zeta_2 r_{d2}+\zeta_3 r_{d3}$.

The radiative-decay coefficient of excitons: $r_r = \zeta_2 r_{2r}$.

The nonradiative-decay coefficient of excitons: $r_{nr} = \zeta_1 r_{1nr}+\zeta_2 r_{2nr}+\zeta_3 r_{3nr}$.

The diffusion coefficient of excitons: $D_x = \zeta_1 D_{x1}+\zeta_2 D_{x2}+\zeta_3 D_{x3}$.

3.8 The Derivation of One-Dimensional Arrhenius Equilibrium Constant

Two approaches are used to derive the one-dimensional Arrhenius equilibrium constant, which is the Saha's equation in the case of the chemical equilibrium. The first approach is using partition function [72-74]. Although the excitons are approximately Bosons, for the low exciton densities the Boltzmann factors can be assumed. The one-

dimensional single-particle partition function $f_{\text{part,i}}$ of exciton-*i* with parabolic energies in all phase space is given by [72]

$$f_{\text{part,i}} = \frac{g_{xi}}{2\pi}\int_{-\infty}^{\infty}\exp\left(-\frac{E_k + E_{xi}}{k_B T}\right)dk\int dr = \frac{g_{xi}V_{1Dim}}{\lambda_{xi}}\exp\left(\frac{-E_{xi}}{k_B T}\right). \qquad (3.8.1)$$

The kinetic energy E_{k} is equal to $\hbar^2 k^2/2m_{xi}$, m_{xi} is the effective mass of exciton-*i*, g_{xi} is the degeneracy factor of the lowest energy levels of exciton-*i*, k_{B} is the Boltzmann constant, and T is the temperature. By using $\int_0^{\infty}\exp(-x^2)dx = \sqrt{\pi}/2$, the result of the right-hand side of the equation can be obtained, where the one-dimensional thermal de Broglie wavelength λ_{xi} of exciton-*i* is assumed as $h/\sqrt{2\pi m_{xi}k_B T}$, and V_{1Dim} is the one-dimensional volume. Similarly, the one-dimensional single-particle partition function $f_{\text{part,e}}$ of electrons with parabolic energies in all phase space is given by

$$f_{\text{part,e}} = \frac{g_e}{2\pi}\int_{-\infty}^{\infty}\exp\left(-\frac{E_k + E_e}{k_B T}\right)dk\int dr = \frac{g_e V_{1Dim}}{\lambda_e}\exp\left(\frac{-E_e}{k_B T}\right). \qquad (3.8.2)$$

E_{e} is the ground-state energy of electrons, and g_{e} is the degeneracy factor of the lowest energy levels of electrons, and the one-dimensional thermal de Broglie wavelength λ_{e} of electrons is equal to $h/\sqrt{2\pi m_e^* k_B T}$, where m_{e}^* is the effective mass of electrons. In chemical equilibrium, the rate of exciton formation involving bimolecular recombination of electrons and holes is described as $B_{\text{xi}}n^0p^0$ for the system of "$e^- + h^+ \rightarrow$ exciton-*i*" where e^- and h^+ are the electrons and holes, respectively, while the rate of exciton ionization (i.e., exciton dissociation) to free *e*-*h* pairs is depicted as $r_{\text{di}}n_{\text{xi}}{}^0$ for the system of exciton-$i \rightarrow e^- + h^+$. The notations n^0, p^0, and $n_{\text{xi}}{}^0$ indicate the equilibrium densities. Since the density of exciton-*i* is proportional to the probability of the partition function

divided by the one-dimensional volume, i.e., $f_{par,i}/V_{1Dim}$, for the one-dimensional case the Arrhenius equilibrium constant, which is equal to the ratio of the exciton-ionization coefficient r_{di} to the capture parameter B_{xi} of exciton formation, i.e., r_{di}/B_{xi} [72-74], can be calculated as

$$\frac{r_{di}}{B_{xi}} = \frac{n^0 p^0}{n_{xi}{}^0} = \frac{g_e g_h}{g_{xi}} \frac{1}{\lambda_{ri}} \exp\left(\frac{-W_i}{k_B T}\right). \tag{3.8.3}$$

The ionization (dissociation) energy of exciton-*i* is described as $W_i = E_e + E_h - E_{xi}$, and W_2 is equal to the exciton binding energy E_b for the bright exciton-2. The associated thermal de Broglie wavelength λ_{ri} is equal to $\lambda_e \lambda_h / \lambda_{xi} = h/\sqrt{2\pi m_{ri} k_B T}$, and the reduced mass m_{ri} is equal to $m_e^* m_h^* / m_{xi}$. In the original Saha's equation the values of degeneracy in Equation (3.8.3) are replaced by the sum of the partition functions of any possible internal states [84, 85]; however, only the lowest energy levels are considered here. Since in the CNT the lowest energy levels of both conduction and valence subbands are doubly degenerate [3], the values of both g_e and g_h are two. Since the Coulomb interaction creates four lowest-energy singlet excitons, the lowest-energy exciton, i.e., exciton-1, is a dark exciton, the second lowest-energy exciton, i.e., exciton-2, is a bright exciton, and the third lowest-energy excitons, i.e., exciton-3, are double-degenerate dark excitons [23, 24]. Therefore, the values of both g_{x1} and g_{x2} are one, and the value of g_{x3} is two.

The second approach is using the property of chemical potentials in the chemical equilibrium [86]. The one-dimensional density of states $D_{xi}(E_k)$ of exciton-*i* is equal to $\frac{g_{xi}}{h}\sqrt{\frac{2m_{xi}}{E_k}}$ [78], where the kinetic energy E_k is equal to E-E_{xi}, and h is the Planck constant. Although the excitons are approximately Bosons, for the low exciton density

the exciton distribution function f_b can be assumed as Boltzmann distribution, i.e., $f_b(E) = \exp\left(\frac{-(E-\mu_{xi})}{k_B T}\right)$, where μ_{xi} is the chemical potential (Fermi level) of exciton-*i*. The one-dimensional exciton density n_{xi} is calculated as

$$n_{xi} = \int_0^\infty f_b(E) D_{xi}(E_k) dE_k = \frac{g_{xi}}{\lambda_{xi}} \exp\left(\frac{\mu_{xi} - E_{xi}}{k_B T}\right). \quad (3.8.4)$$

The Gamma function $\int_0^\infty x^{-1/2} e^{-x} dx = \Gamma(½) = \sqrt{\pi}$ is used to compute the formula. Again λ_{xi} is the one-dimensional thermal de Broglie wavelength of exciton-*i*. In chemical equilibrium of the system $e^- + h^+ \leftrightarrow$ exciton-*i*, the chemical potentials have the property of $\mu_e + \mu_h = \mu_{xi}$. For the one-dimensional case the Arrhenius equilibrium constant is equal to the ratio r_{di}/B_{xi}, and can be calculated as

$$\frac{r_{di}}{B_{xi}} = \frac{n^0 p^0}{n_{xi}^{\ 0}} = \frac{g_e g_h}{g_{xi}} \frac{1}{\lambda_{ri}} \exp\left(\frac{-W_i}{k_B T}\right).$$

This formula has the same form as that in Equation (3.8.3).

3.9 The Derivation of Parameters $\zeta_{1,2,3}$ in the Thermal Equilibrium

The parameters $\zeta_{1,2,3}$ in the thermal equilibrium can be derived by two methods. The first method is to calculate the ratio of probability of exciton-*i* to probability of total excitons by using the partition function to obtain the parameters ζ_i. Although the excitons are Bosons, for the low exciton densities the Boltzmann factors can be assumed. The one-dimensional single-particle partition function $f_{part,i}$ of exciton-*i* with parabolic energies in all phase space is given by Equation (3.8.1) in Chapter 3.8 [72]. Since the

density of the exciton-*i* is proportional to the probability of the partition function divided by the one-dimensional volume, i.e., $f_{\mathrm{par,i}}/V_{\mathrm{1Dim}}$, the parameters ζ_{i} is obtained by the ratio of the density of individual exciton-*i* to total excitons.

$$
\begin{cases}
\zeta_1 = \dfrac{n_{x1}}{n_{xs}} = \dfrac{n_{x1}}{n_{x1}+n_{x2}+n_{x3}} \\
\quad = \dfrac{f_{part,1}/V_{1Dim}}{f_{part,1}/V_{1Dim} + f_{part,2}/V_{1Dim} + f_{part,3}/V_{1Dim}} \\
\quad = \dfrac{\dfrac{g_{x1}}{\lambda_{x1}}\exp\left(\dfrac{-E_{x1}}{k_BT}\right)}{\dfrac{g_{x1}}{\lambda_{x1}}\exp\left(\dfrac{-E_{x1}}{k_BT}\right)+\dfrac{g_{x2}}{\lambda_{x2}}\exp\left(\dfrac{-E_{x2}}{k_BT}\right)+\dfrac{g_{x3}}{\lambda_{x3}}\exp\left(\dfrac{-E_{x3}}{k_BT}\right)} \\
\quad = \dfrac{g_{x1}\sqrt{m_{x1}}}{g_{x1}\sqrt{m_{x1}}+g_{x2}\sqrt{m_{x2}}\exp\left(\dfrac{-\delta_1}{k_BT}\right)+g_{x3}\sqrt{m_{x3}}\exp\left(\dfrac{-\delta_2}{k_BT}\right)} \\
\zeta_2 = \dfrac{n_{x2}}{n_{xs}} = \dfrac{g_{x2}\sqrt{m_{x2}}\exp\left(\dfrac{-\delta_1}{k_BT}\right)}{g_{x1}\sqrt{m_{x1}}+g_{x2}\sqrt{m_{x2}}\exp\left(\dfrac{-\delta_1}{k_BT}\right)+g_{x3}\sqrt{m_{x3}}\exp\left(\dfrac{-\delta_2}{k_BT}\right)} \\
\zeta_3 = \dfrac{n_{x3}}{n_{xs}} = \dfrac{g_{x3}\sqrt{m_{x3}}\exp\left(\dfrac{-\delta_2}{k_BT}\right)}{g_{x1}\sqrt{m_{x1}}+g_{x2}\sqrt{m_{x2}}\exp\left(\dfrac{-\delta_1}{k_BT}\right)+g_{x3}\sqrt{m_{x3}}\exp\left(\dfrac{-\delta_2}{k_BT}\right)}.
\end{cases}
\tag{3.9.1}
$$

The second method is to directly calculate the exciton density n_{xi} through the density of states, and then to compute $\zeta_{\mathrm{i}} = n_{\mathrm{xi}}/n_{\mathrm{xs}}$ by using the property of the equal chemical potentials (Fermi levels) of excitons in the thermal equilibrium. The one-dimensional exciton density n_{xi} is given by Equation (3.8.4) in Chapter 3.8. In the thermal equilibrium the chemical potentials among three states of excitons are equal, i.e., $\mu_{\mathrm{x1}} = \mu_{\mathrm{x2}} = \mu_{\mathrm{x3}}$, and thus the parameters $\zeta_{1,2,3}$ are computed as

$$\zeta_1 = \frac{n_{x1}}{n_{xs}} = \frac{n_{x1}}{n_{x1}+n_{x2}+n_{x3}}$$
$$= \frac{\frac{g_{x1}}{\lambda_{x1}}\exp\left(\frac{-E_{x1}}{k_BT}\right)}{\frac{g_{x1}}{\lambda_{x1}}\exp\left(\frac{-E_{x1}}{k_BT}\right)+\frac{g_{x2}}{\lambda_{x2}}\exp\left(\frac{-E_{x2}}{k_BT}\right)+\frac{g_{x3}}{\lambda_{x3}}\exp\left(\frac{-E_{x3}}{k_BT}\right)}$$
$$= \frac{g_{x1}\sqrt{m_{x1}}}{g_{x1}\sqrt{m_{x1}}+g_{x2}\sqrt{m_{x2}}\exp\left(\frac{-\delta_1}{k_BT}\right)+g_{x3}\sqrt{m_{x3}}\exp\left(\frac{-\delta_2}{k_BT}\right)}$$

The ζ_1 has the same form as that in Equation (3.9.1). Similarly, ζ_2 and ζ_3 have the same formula, too.

3.10 Summary for the Modeling of Optical Emitters and Photodetectors Based on CNT FETs

For long-channel CNT FETs the gradual-channel approximation (GCA) is used. In general, the metal-CNT interfaces form the Schottky barriers. In our model their effect is simplified to a constant voltage drop independent of the current, and the values are assumed to be the same at both S and D contacts. The channel length is long, and thus a diffusive-transport model is applied to both optical emitters and photodetectors. That is, the electron and hole continuity equations coupled with the drift-diffusion currents are used. For large carrier densities, a Fermi-Dirac distribution rather than the Boltzmann distribution has to be used. In degenerate semiconductors, the Einstein relation can be approximated by the formula of Kroemer [58]. By using the procedure of Joyce and Dixon [59] applied to the Fermi-Dirac integral of order -½ for the one-dimensional case,

the parameters in the formula can be calculated. Electron mobility in CNTs, in general, depends on the CNT diameter, electric field, and temperature. The low-field mobility is very high (10^5 cm^2/Vs) even at room temperature. The inverse diameter dependence of the effective mass and of the electron-phonon coupling strength leads to a quadratic diameter dependence of the mobility. That is, the larger the CNT diameter is, the higher the mobility is. For long-channel CNT FETs the electric field is low, and thus the constant low-field mobility can be applied to this model.

In optical emitters based on ambipolar CNT FETs, nonradiative recombination of electrons and holes is much stronger than radiative, as evidenced by the low measured quantum efficiency between 10^{-6} and 10^{-7} photons per injected *e*-*h* pair [44]. Light emission is assumed as the band-to-band radiative recombination (BBR) of electrons and holes. Various nonradiative recombination mechanisms, such as Shockley-Read-Hall (SRH) recombination, band-to-band nonradiative recombination (BBN), and Auger recombination, are considered.

Electron confinement in the quasi-one-dimensional structure of CNTs leads to the formation of strongly bound exciton states. For strong binding, most of the optical absorption is associated with photogeneration of excitons. Therefore, photogeneration of excitons is the dominant mechanism in photodetectors based on CNT FETs. Since the diameter of a CNT is so small (~1 nm), the incident radiation is absorbed very slightly. The calculation of the generation rate of excitons through the photoexcitation is expressed. In CNTs the exciton splitting energies are very small (~4-~23 meV); therefore, thermal equilibrium is a good assumption due to the fast transition between those exciton states. The *i*th-exciton density in terms of the total singlet-exciton density

can be obtained, and thus the continuity equation of the total singlet-exciton density is derived.

CHAPTER 4

ANALYTIC CALCULATION FOR OPTICAL EMITTERS BASED ON CARBON-NANOTUBE FIELD-EFFECT TRANSISTORS

In optical emitters based on long-channel ambipolar CNT FETs, the region of light emission can be controlled by varying the gate and drain voltages [42, 49]. An analytic model based on diffusive transport and assuming infinite recombination rate for electrons and holes has been presented and applied to very long-channel (60 μm) CNT FETs, but the spatial size of the optical emission region was not considered [49]. In addition, two numerical models with carrier recombination were developed for long-channel devices [50, 60]. Radiative recombination was assumed to be dominant; however, the dominant role of nonradiative recombination is evident in the extremely low measured quantum efficiency of the light output, which ranges from 10^{-6} to 10^{-7} [44]. The new model accounting for both radiative and nonradiative recombination, allowing for several mechanisms, was described in Chapter 3.5. In the next chapter, the numerical approach will be presented; however, the physical origin of important effects may be difficult to trace from a purely numerical approach. An analytic diffusive-transport model for various recombination mechanisms [51] is therefore presented in this chapter, thereby enabling a clearer understanding of the dependence of the transport and optical properties on the various nonradiative recombination mechanisms. In particular, the current, radiative recombination rate, emitted light-spot size, and optical power are all calculated analytically. The focus is on the effects of radiative and nonradiative recombination in the channel, with the movement of the spatial recombination profile in

response to the gate and drain voltages being explored analytically, which provides physical insight not afforded by purely numerical approaches. All formula in this chapter are implemented by using the MATLAB in order to calculate the analytic solutions.

The analytic modeling for optical emitters based on carbon-nanotube field-effect transistors is given in Chapter 4.1, and the approach of analytic calculation is described in Chapter 4.2. The analytic calculation of electronic and optical properties of optical emitters is given in Chapter 4.3. The analytic calculation of parameters for the rectangular function is shown in Chapter 4.4. The conclusion of the analytic calculation is given in Chapter 4.5.

4.1 Analytic Modeling for Optical Emitters Based on Carbon-Nanotube Field-Effect Transistors

For optical emitters based on ambipolar long-channel CNT FETs, electrons are injected from *e*-source S and accumulate in the CNT near *e*-source S for positive V_G, while holes are injected from *h*-source D and accumulate near there for negative V_G-V_D. For the optical emitters both the electron- and hole-generation rates are neglected. Notice that $\partial\psi/\partial x$ is replaced by $d\psi/dx$ since the only longitudinal dependent variable x of the CNT potential ψ is of interest. By substituting both $F_x = -d\psi/dx$ and Equation (3.1.1) of the GCA into Equation (3.2.1) and (3.2.2) of the drift-diffusion currents, one finds that the drift currents are much larger than the diffusion currents if the carrier densities are

much larger than the value of $CD/e\mu$. Therefore, only the drift currents are considered for the analytic calculation:

$$I_{\mathrm{n}}(x) = en\mu\frac{d\psi}{dx}, \tag{4.1.1}$$

$$I_{\mathrm{p}}(x) = ep\mu\frac{d\psi}{dx}. \tag{4.1.2}$$

Moreover, current conservation at any channel position *x* implies that the device current satisfies

$$I = I_{\mathrm{n}}(x) + I_{\mathrm{p}}(x). \tag{4.1.3}$$

Substitute Equations (4.1.1) and (4.1.2) into Equation (4.1.3) to obtain

$$I = e(n+p)\mu\frac{d\psi}{dx}. \tag{4.1.4}$$

Using Equations (3.1.1) and (4.1.4) to express the carrier densities *n* and *p* in terms of the CNT potential ψ and the device current *I* gives [87]

$$n(x) = \frac{C}{2e}\left(\frac{I}{\mu C(\psi - V_G + V_{fb})d\psi/dx} - 1\right)(\psi - V_{\mathrm{G}} + V_{\mathrm{fb}}), \tag{4.1.5}$$

$$p(x) = \frac{C}{2e}\left(\frac{I}{\mu C(\psi - V_G + V_{fb})d\psi/dx} + 1\right)(\psi - V_{\mathrm{G}} + V_{\mathrm{fb}}). \tag{4.1.6}$$

Subtracting Equation (4.1.2) from Equation (4.1.1) and then substituting it into Equation (3.1.1) of the gradual-channel approximation, I_{p}-I_{n} is given as

$$I_{\mathrm{p}} - I_{\mathrm{n}} = \mu C(\psi - V_{\mathrm{G}} + V_{\mathrm{fb}})\frac{d\psi}{dx}. \tag{4.1.7}$$

For optical emitters based on CNT FETs, both the electron and hole generation rates are effectively zero. In steady-state, the carrier continuity equations of Equations (3.4.1) and (3.4.2) can be expressed as

$$\frac{1}{e}\frac{d(I_p - I_n)}{dx} = 2R(n, p), \tag{4.1.8}$$

where $R(n,p)$ describes the recombination mechanism of electrons and holes in terms of carrier densities n and p. Substituting Equation (4.1.7) into Equation (4.1.8) gives [88]

$$\frac{1}{e}\frac{d}{dx}\left(\mu C(\psi - V_G + V_{fb})\frac{d\psi}{dx}\right) = 2R(n, p). \tag{4.1.9}$$

Thus the carrier continuity equation of Equation (4.1.9) can be described as the differential equation for the CNT potential $\psi(x)$ through the recombination mechanism $R(n,p)$ of electrons and holes,

$$\frac{1}{2e}\frac{d}{dx}\left(\mu C\frac{d}{dx}\left[(\psi - V_G + V_{fb})^2\right]\right) = 2R[n(x), p(x)]. \tag{4.1.10}$$

It is convenient to adopt dimensionless quantities. The position w is defined as x/L, and the position x_m is defined as the position with $p(x_m) = n(x_m)$, and $w_m \equiv x_m/L$. Thus $\psi(x_m) = V_G\text{-}V_{fb}$ and $I_p(x_m) = I_n(x_m) = I/2$ due to the relation $I_n/I_p = n/p$. The normalized electron and hole recombination rate is defined as a function $f_0(w) \equiv \frac{eL}{I}R(x)$. Referring to Equation (4.1.8), I_p-I_n is related to the integration of R, therefore a function $f_1(w)$ is defined in terms of the function f_0: $f_1(w) \equiv \int_{w_m}^{w} f_0(u)du$. The function $f_1(w)$ is equal to the normalized hole-to-electron current difference $\frac{I_p(x) - I_n(x)}{2I}$, which can be proved by using Equation (4.1.8). Since $I_p(x_m) = I_n(x_m)$ at the position $x =$

x_m , it means $f_1(w_m) = 0$. Thus w_m is used as the initial value of the integration. Referring to Equation (4.1.7), $(\psi - V_G + V_{fb})^2$ is related to the integration of I_p-I_n, therefore a function $f_2(w)$ is defined in terms of the function f_1: $f_2(w) \equiv \int_{w_m}^{w} f_1(u)du$. The normalized function $f_2(w)$ is equal to $\frac{\mu C}{4LI}\left[\psi(x) - V_G + V_{fb}\right]^2$, which can be proved by using Equation (4.1.7). Moreover, a function f_ψ is defined in terms of the function f_2: $f_\psi(w) \equiv \sqrt{f_2(w)}$ for $w \geq w_m$ and $-\sqrt{f_2(w)}$ for $w < w_m$. Thus the function $f_\psi(w)$ is equal to the normalized CNT potential $\frac{1}{2}\sqrt{\frac{\mu C}{LI}}\left[\psi(x) - V_G + V_{fb}\right]$. Similarly, since $\psi(x_m) = V_G$-V_{fb} at the position $x = x_m$, it gives $f_\psi(w_m) = 0$ and $f_2(w_m) = 0$. Thus w_m is used as the initial value of the integration, too. In summary, the normalized functions f_1, f_2, f_ψ are defined in terms of the normalized function f_0:

$$\begin{cases} f_1(w) \equiv \int_{w_m}^{w} f_0(u)du, \\ f_2(w) \equiv \int_{w_m}^{w} f_1(u)du, \\ f_\psi(w) \equiv \begin{cases} \sqrt{f_2(w)} & \text{for } w \geq w_m \\ -\sqrt{f_2(w)} & \text{for } w < w_m. \end{cases} \end{cases} \tag{4.1.11}$$

In addition, the normalized functions f_0, f_1, f_2, f_ψ have the formulae:

$$\begin{cases} f_0(w) \equiv \frac{eL}{I} R(x), \\ f_1(w) = \frac{I_p(x) - I_n(x)}{2I}, \\ f_2(w) = \frac{\mu C}{4LI}\left[\psi(x) - V_G + V_{fb}\right]^2, \\ f_\psi(w) = \frac{1}{2}\sqrt{\frac{\mu C}{LI}}\left[\psi(x) - V_G + V_{fb}\right]. \end{cases} \tag{4.1.12}$$

The CNT potential ψ and the carrier densities n and p referring to Equations (4.1.5) and (4.1.6) can be written in terms of the normalized functions f_ψ and f_1,

$$\psi(x) = V_G - V_{\text{fb}} + 2\sqrt{\frac{LI}{\mu C}} f_\psi(w), \tag{4.1.13}$$

$$n(x) = \frac{1}{e}\sqrt{\frac{CLI}{\mu}}\left(\frac{1}{2f_1(w)} - 1\right) f_\psi(w), \tag{4.1.14}$$

$$p(x) = \frac{1}{e}\sqrt{\frac{CLI}{\mu}}\left(\frac{1}{2f_1(w)} + 1\right) f_\psi(w). \tag{4.1.15}$$

Similarly, the linear charge density ρ, longitudinal electric field F_x , and electron and hole carrier currents I_{n} and I_{p} can be written in terms of the normalized functions f_ψ and f_1 as well,

$$\rho(x) = 2\sqrt{\frac{CLI}{\mu}} f_\psi(w), \tag{4.1.16}$$

$$F_x(x) = -\sqrt{\frac{I}{\mu CL}} \frac{f_1(w)}{f_\psi(w)}, \tag{4.1.17}$$

$$I_{\text{n}}(x) = \left(\frac{1}{2} - f_1(w)\right) I, \tag{4.1.18}$$

$$I_p(x) = \left(\frac{1}{2} + f_1(w)\right) I. \tag{4.1.19}$$

Therefore, the carrier continuity equation of Equation (4.1.10) can be normalized as [88]

$$\frac{d^2 f_2(w)}{dw^2} = \frac{eL}{I} R(n, p) \equiv f_0(w). \tag{4.1.20}$$

4.2 Approach of Analytic Calculation for Optical Emitters

For the optical emitters based on CNT FETs, nonradiative recombination is much stronger than radiative recombination, as evidenced by the low measured quantum efficiency ranging from 10^{-6} to 10^{-7} photons per injected e-h pair [44]. Therefore, the transport properties, such as the CNT potential and carrier densities, are determined here assuming only nonradiative recombination. In this chapter, Shockley-Read-Hall (SRH) recombination, band-to-band nonradiative recombination (BBN), and Auger recombination are considered. Expressions for the nonradiative recombination rates R_{nr} and the coefficients are listed in Table 3.1.

The optical properties, in turn, are calculated based on the transport properties thus obtained. Optical emission is generated by band-to-band radiative recombination (BBR) of electrons and holes, the radiative recombination rate R_{r} is equal to $B_{\mathrm{BBR}}(np\text{-}n_{\mathrm{i}}^2)$, where B_{BBR} is the band-to-band radiative recombination coefficient [50, 51, 60]. Then the emitted optical power P_{opt} is calculated as $E_g \int_0^L R_r(x)dx$, in which E_{g} is the CNT band-gap. The quantum efficiency of R_{r}/R is computed as $B_{\mathrm{BBR}}/(B_{\mathrm{BBR}}+B_{\mathrm{BBN}})$, i.e., the ratio of the radiative to the total coefficients (radiative and nonradiative) of band-to-band recombination.

The carrier continuity equation of Equation (4.1.20) is a differential equation. This differential equation is solved analytically as follows. (a) An initial guess assuming a simple form for the nonradiative recombination-rate profile, i.e. $f_0(w)$, is made. (b) Both the function $f_2(w)$ and device current I_1 of the first iteration are computed simultaneously by integrating Equation (4.1.20) with suitable boundary conditions, and

then the functions $f_\psi(w)$ and $f_1(w)$ can be obtained. (c) Thus $n(x)$ and $p(x)$ of the first iteration are obtained by using Equations (4.1.14) and (4.1.15). (d) The nonradiative recombination rate $R(n,p)$ of the first iteration is then calculated. One then iterates (a) to (d) to obtain the device current for the ith iteration until I_i is converged. If I_2 is close to I_1, then only a single iteration is sufficient. Assuming the first iteration is good enough, the analytic forms of $\psi(x)$, $n(x)$, and $p(x)$ are obtained in terms of $f_\psi(w)$ and $f_1(w)$ in Equations (4.1.13) to (4.1.15). Moreover, the analytic forms of $\rho(x)$, $F_x(x)$, $I_n(x)$, and $I_p(x)$ are computed in terms of $f_\psi(w)$ and $f_1(w)$ in Equations (4.1.16) to (4.1.19).

4.3 Analytic Calculation of Electronic and Optical Properties of Optical Emitters

Since R_{nr} have approximate first-, second-, or third-order dependences on the carrier densities, we define the order η as 1, 2, or 3 for SRH, BBN, or Auger recombination, respectively. The normalized recombination rates are defined as

$$h_\eta(w) \equiv \frac{\left(\frac{1}{4} - f_1(w)^2\right) f_\psi(w)^\eta}{f_1(w)^\eta}. \tag{4.3.1}$$

The recombination parameter B_η is defined as τ_{SRH}^{-1}, B_{BBN}, or B_{Auger} for SRH, BBN, or Auger, respectively. Therefore, the nonradiative recombination rate is approximately as

$$R_{nr}(x) = B_\eta \left(\frac{CLI}{e^2 \mu}\right)^{\frac{\eta}{2}} h_\eta(w). \tag{4.3.2}$$

The radiative decay rate is approximately

$$R_{\mathrm{r}}(x) = B_{\mathrm{BBR}}\left(\frac{CLI}{e^{2}\mu}\right)h_{2}(w). \tag{4.3.3}$$

Because we have

$$\frac{dh_2}{dw} = \frac{(-2f_0 f_2 + f_1^{\,2} - 4f_1^{\,4})}{4f_1^{\,3}},$$

where $f_1 = f_2 = 0$ but $f_0 \neq 0$ at w_{m}, we may take derivatives in both the numerator and denominator to obtain $-\frac{4f_1}{3} = 0$. Then $\frac{dR_r}{dx} = 0$ at x_{m}, and x_{m} is thus shown to be the position R_{r} of the maximum in which $p = n$, $\rho = 0$ and $\psi = V_{\mathrm{G}}$-V_{fb}. Therefore, the emitted-light position is assumed as x_{m}. This phenomenon was observed in our published numerical results [51]. The maximum value of R_{r} is given as

$$R_{r,\max} = \frac{B_{BBR}CLI}{8e^{2}\mu f_{\,0}(w_m)}$$

due to the relationship $\frac{f_\psi}{f_1} = \sqrt{\frac{1}{2f_0}}$ at w_{m}, while the maximum value of $|F_{\mathrm{x}}|$ is given as

$$\left|F_{\mathrm{x}}\right|_{\max} = \sqrt{\frac{2f_0(w_m)I}{\mu CL}}$$

due to $\frac{d}{dw}\left(\frac{f_1}{f_\psi}\right) = 0$ at w_{m}.

When the channel length exceeds the recombination length, essentially all injected carriers recombine within the channel. Outside the recombination region the minority carrier densities are negligible, and thus recombination is negligible there. The minority carrier currents are also negligible, and the majority carrier currents are equal to the device current due to the current conservation. According to Equations(4.1.12) this means that outside the recombination region $f_0 \approx 0$, and $f_1 \approx$ ½ for $w > w_m$ and -½ for $w <$

w_m. Moreover, outside the recombination region f_2 is approximated as ½|w-w_m|-β, where the integration parameter β depends on the recombination profile. Substituting these values into Equations (4.1.13), (4.1.16), and (4.1.17) gives

$$\begin{aligned} \rho(x) &\approx \pm\sqrt{\frac{2CI}{\mu}}a(x), \\ \psi(x) &\approx V_G - V_{fb} \pm \sqrt{\frac{2I}{\mu C}}a(x), \\ F_x(x) &\approx -\sqrt{\frac{I}{2\mu C}}\frac{1}{a(x)}, \end{aligned} \tag{4.3.4}$$

where

$$a(x) = \sqrt{|x - x_m| - 2\beta L}. \tag{4.3.5}$$

The majority carrier density is $\frac{|\rho|}{e}$. If an infinite recombination rate for electrons and holes is assumed, then the width of the recombination zone is ignored. Thus β is zero, and the results in Equation (4.3.4) reduce to those of Reference [49]. The effect of the metal-CNT interfaces is simplified to a constant voltage drop V_c, which is the same at both (S and D) contacts, i.e., $\Delta V_s = \Delta V_d = V_c$. The resulting boundary conditions (BCs) are $\psi_S = V_c$ and V_D-$\psi_D = V_c$, where ψ_S is the CNT potential at S and ψ_D is the CNT potential at D [49, 51]. The BCs are expressed as

$$V_G - V_{fb} - V_c = \sqrt{\frac{2I}{\mu C}}\sqrt{x_m - 2\beta L}, \tag{4.3.6}$$

$$V_D - V_G + V_{fb} - V_c = \sqrt{\frac{2I}{\mu C}}\sqrt{L - x_m - 2\beta L}. \tag{4.3.7}$$

The current I is obtained by summing the squares of Equations (4.3.6) and (4.3.7) to eliminate the dependence on x_m, and the emitted-light position x_m is obtained by taking

the quotient of the square of Equation (4.3.6) and the sum of the squares of Equations (4.3.6) and (4.3.7) to eliminate I,

$$I = \frac{\mu C}{2L(1-4\beta)}\left[(V_{\mathrm{G}} - V_{\mathrm{fb}} - V_{\mathrm{c}})^2 + (V_{\mathrm{D}} - V_{\mathrm{G}} + V_{\mathrm{fb}} - V_{\mathrm{c}})^2\right], \tag{4.3.8}$$

$$x_{\mathrm{m}} = 2\beta L + \frac{L(1-4\beta)(V_G - V_{fb} - V_c)^2}{(V_G - V_{fb} - V_c)^2 + (V_D - V_G + V_{fb} - V_c)^2}. \tag{4.3.9}$$

If $\beta = 0$, the foregoing equations reduce to those of Reference [49]. For constant V_{D}, the I-V_{G} curve is parabolic, and the minimum I occurs at the center of symmetry, i.e. V_{G}-V_{fb} = ½V_{D}; then x_{m} = ½L.

The emitted light-spot size S_{spot} is defined as the spot's full-width at half maximum (FWHM) with respect to R_{r}, while Σ is the FWHM with respect to initial guess R_{ini} and S_{w} (= Σ/L) is the FWHM with respect to f_0. In the first iteration the current $I_1 = e\int_0^L R_{ini}(x)dx$ is assumed to be I. Substituting the initial guess R_{ini} into the integral, f_0 must satisfy the condition

$$\int_0^1 f_0(w)dw = 1. \tag{4.3.10}$$

Since f_0 scales as w^{-1}, it follows that f_1, f_ψ, h_η scale as w^0, $w^{1/2}$, $w^{\eta/2}$, respectively. In the second iteration the current $I_2 = e\int_0^L R_{nr}(x)dx$ is assumed as I_1 (= I). Substituting R_{nr} into the integral, the relation is obtained as

$$eB_\eta \left(\frac{CI}{e^2\mu}\right)^{\eta/2} L^{1+\eta/2}\int_0^1 h_\eta(w)dw = I. \tag{4.3.11}$$

Since $\int_0^1 h_\eta dw$ scales as $w^{1+\eta/2}$, and S_{w} scales as w^1, we define g_η to satisfy

$$\int_0^1 h_\eta(w)dw = g_\eta S_{\mathrm{w}}{}^{1+\eta/2}. \tag{4.3.12}$$

Thus S_w and Σ can be calculated. The emitted light-spot size S_{spot} is FWHM with respect to R_r, which is related to h_2 due to Equation (4.3.3). The FWHM of h_2 scales as w^1, therefore we define g_{fwhm} such that the FWHM of h_2 is equal to $g_{fwhm}S_w$; hence, $S_{spot} = g_{fwhm}\Sigma$. By integrating $R_r(x)$ from 0 to L over x, the emitted optical power P_{opt} is computed as $E_g B_{BBR}\left(\frac{CI}{e^2\mu}\right)g_2\Sigma^2$. Thus, the emitted light-spot size S_{spot} and the emitted optical power P_{opt} are calculated as

$$S_{spot} = g_{fwhm}\left(\frac{e^{2\eta-2}\mu^{\eta}I^{2-\eta}}{g_{\eta}{}^2 B_{\eta}{}^2 C^{\eta}}\right)^{1/(2+\eta)}, \tag{4.3.13}$$

$$P_{opt} = E_g B_{BBR} g_2\left(\frac{e^{2\eta-8}\mu^{\eta-2}I^{6-\eta}}{g_{\eta}{}^4 B_{\eta}{}^4 C^{\eta-2}}\right)^{1/(2+\eta)}. \tag{4.3.14}$$

In particular, for $\eta = 1$ with respect to SRH recombination, we have

$$S_{spot} = g_{fwhm}\left(\frac{\tau_{SRH}{}^2\mu I}{g_1{}^2 C}\right)^{1/3}, \quad \text{for } \eta = 1, \tag{4.3.15}$$

$$P_{opt} = E_g B_{BBR} g_2\left(\frac{\tau_{SRH}{}^4 C I^5}{g_1{}^4 e^6 \mu}\right)^{1/3}, \quad \text{for } \eta = 1. \tag{4.3.16}$$

For $\eta = 2$ with respect to BBN recombination, we have

$$S_{spot} = g_{fwhm}\sqrt{\frac{e\mu}{g_2 B_{BBN} C}}, \quad \text{for } \eta = 2, \tag{4.3.17}$$

$$P_{opt} = \frac{E_g I}{e}\frac{B_{BBR}}{B_{BBN}}, \quad \text{for } \eta = 2. \tag{4.3.18}$$

The emitted optical power of Equation(4.3.18) shows the conventional form including the quantum efficiency of B_{BBR}/B_{BBN}. This quantum efficiency is computed as B_{BBR}/B_{BBN}, i.e.,

the ratio of radiative to nonradiative coefficients of band-to-band recombination of electrons and holes. In the organic ambipolar light-emitting FETs, bimolecular recombination of injected electrons and holes involves the formation and recombination of excitons and exciton formation has the same form as that for $\eta = 2$. Moreover, the width of the recombination zone shows the same scaling formula as Equation (4.3.17) [88, 89].

Similarly, for $\eta = 3$ with respect to Auger recombination, we have

$$S_{\text{spot}} = g_{\text{fwhm}} \left(\frac{e^4 \mu^3}{g_3^{\,2} B_{Auger}^{\,2} C^3 I} \right)^{1/5}, \qquad \text{for } \eta = 3, \tag{4.3.19}$$

$$P_{\text{opt}} = E_g B_{\text{BBR}} g_2 \left(\frac{\mu I^3}{g_3^{\,4} B_{Auger}^{\,4} e^2 C} \right)^{1/5}, \quad \text{for } \eta = 3. \tag{4.3.20}$$

From Equation (4.3.8) it is seen that I is proportional to μC, and thus S_{spot} is proportional to $B_\eta^{-2/(2+\eta)}$, $\mu^{2/(2+\eta)}$, $C^{6/(2+\eta)-2}$, $I^{4/(2+\eta)-1}$, and P_{opt} is proportional to $B_\eta^{-4/(2+\eta)}$, $\mu^{4/(2+\eta)}$, $C^{12/(2+\eta)-2}$, $I^{8/(2+\eta)-1}$. For the analytic powers of the parameters in both S_{spot} and P_{opt} are summarized in Table 4.1. When the mobility μ is increased, the carrier velocity also increases, and the recombination region increases, and thus both S_{spot} and P_{opt} become larger. Increases in B_{BBN} or B_{Auger} or decreases in τ_{SRH} all lead to increases in the recombination rates, and the carrier densities decrease rapidly with x, leading to a decrease in both S_{spot} and P_{opt}. Because of the value of $1/(2+\eta)$, the powers of μ, C, and I in both S_{spot} and P_{opt} are largest for SRH recombination ($\eta = 1$) and smallest for Auger recombination ($\eta = 3$).

Table 4.1. Analytic powers of the parameters in S_{spot} and P_{opt}.

S_{spot}	SRH	BBN	Auger	P_{opt}	SRH	BBN	Auger
B_η [i]	$-\frac{2}{3}$	$-\frac{1}{2}$	$-\frac{2}{5}$		$-\frac{4}{3}$	-1	$-\frac{4}{5}$
μ	$\frac{2}{3}$	$\frac{1}{2}$	$\frac{2}{5}$		$\frac{4}{3}$	1	$\frac{4}{5}$
C	0	$-\frac{1}{2}$	$-\frac{4}{5}$		2	1	$\frac{2}{5}$
I	$\frac{1}{3}$	0	$-\frac{1}{5}$		$\frac{5}{3}$	1	$\frac{3}{5}$

[i] B_η is defined as τ_{SRH}^{-1}, B_{BBN}, B_{Auger} for SRH, BBN, or Auger, respectively.

Similarly, since β scales as w^1, we define g_b to satisfy $\beta = g_b S_w$, hence $\beta = \frac{g_b}{g_{fwhm}} \frac{S_{spot}}{L}$. In order to calculate S_{spot} and P_{opt} by using Equations (4.3.13) and (4.3.14), the values of the parameters g_1, g_2, etc., have to be computed. We find that the values of g_η depend on the initial guess f_0. For example, if $f_0(w)$ is assumed to be a rectangular function with a FWHM of S_w, i.e.,

$$f_0(w) = \begin{cases} \frac{1}{S_w}, & \text{for } w_m - \frac{S_w}{2} \le w \le w_m + \frac{S_w}{2}, \\ 0, & \text{elsewhere,} \end{cases} \tag{4.3.21}$$

in which f_0 satisfies $\int_0^1 f_0(w)dw = 1$. We analytically calculate $g_1 = 0.118$, $g_2 = 0.0833$, $g_3 = 0.0589$, $g_{\text{fwhm}} = 0.707$, $g_b = 0.125$, shown in Chapter 4.4. If f_0 is a Gaussian with a FWHM of S_w, i.e.,

$$f_0(w) = \frac{2}{S_w}\sqrt{\frac{\ln 2}{\pi}}\exp\left[-\ln 2\left(\frac{2(w-w_m)}{S_w}\right)^2\right], \tag{4.3.22}$$

in which f_0 also satisfies $\int_0^1 f_0(w)dw = 1$, we numerically calculate $g_1 = 0.192$, $g_2 = 0.156$, $g_3 = 0.13$, $g_{\text{fwhm}} = 1.12$, $g_b = 0.17$. In the following analytic calculation in the later chapter, the normalized recombination rate f_0 is chosen to be a Gaussian.

When the emitted light-spot size is much smaller than the channel length, the value of $\frac{1}{1-4\beta}$ is obtained as $\frac{1}{1-0.6S_{spot}/L} \approx 1$; therefore, the current equation (4.3.8) can reduce to that of Reference [49], which means that the current is not sensitive to the recombination rate and various recombination mechanism. Because of the relationship $f_0(w_m) = \frac{2}{S_w}\sqrt{\frac{\ln 2}{\pi}}$, the maximum value of electric field $|F_x|$ can be obtained.

The advantage of the analytical approach is that the relationship and the scaling are clearly depicted. In particular, the electronic and optical properties, such as the device current, emitted light-spot size and emitted optical power, are clearly shown in terms of the some parameters in the foregoing equations. We find that the emitted light-spot size and the optical power are indeed sensitive to the operative nonradiative recombination mechanisms.

4.4 Analytic Calculation of Parameters g_1, g_2, g_3, g_{fwhm}, and g_b for the Rectangular Function f_0

The rectangular function $f_0(w)$ with a FWHM of S_w, is described by Equation (4.3.21). Since f_0 is the normalized recombination rate of electrons and holes, the initial guess of the nonradiative recombination rate is rectangular inside the recombination zone, and is zero outside the recombination zone. Referring to Equation (4.1.11), $f_1(w) = \int_{w_m}^{w} f_0(u)du$, which is obtained as

$$f_1(w) = \begin{cases} \dfrac{1}{S_w}(w - w_m), & \text{for } w_m - \dfrac{S_w}{2} \le w \le w_m + \dfrac{S_w}{2}, \\ -\dfrac{1}{2}, & \text{for } w < w_m - \dfrac{S_w}{2}, \\ \dfrac{1}{2}, & \text{for } w > w_m + \dfrac{S_w}{2}. \end{cases} \tag{4.4.1}$$

$f_1(w)$ is linear inside the recombination zone, and is constant outside the recombination zone. Similarly, referring to Equation (4.1.11), $f_2(w)$ and $f_\psi(w)$ are obtained as

$$f_2(w) = \begin{cases} \dfrac{1}{2S_w}(w - w_m)^2, & \text{for } w_m - \dfrac{S_w}{2} \le w \le w_m + \dfrac{S_w}{2}, \\ \dfrac{1}{2}(w_m - w) - \dfrac{S_w}{8}, & \text{for } w < w_m - \dfrac{S_w}{2}, \\ \dfrac{1}{2}(w - w_m) - \dfrac{S_w}{8}, & \text{for } w > w_m + \dfrac{S_w}{2}. \end{cases} \tag{4.4.2}$$

and

$$f_{\psi}(w)=\begin{cases}\dfrac{1}{\sqrt{2S_w}}(w-w_{\mathrm{m}}), & \text{for } w_{\mathrm{m}}-\dfrac{S_w}{2}\le w\le w_{\mathrm{m}}+\dfrac{S_w}{2},\\ -\sqrt{\dfrac{w_m-w}{2}-\dfrac{S_w}{8}}, & \text{for } w<w_{\mathrm{m}}-\dfrac{S_w}{2},\\ \sqrt{\dfrac{w-w_m}{2}-\dfrac{S_w}{8}}, & \text{for } w>w_{\mathrm{m}}+\dfrac{S_w}{2}.\end{cases} \tag{4.4.3}$$

Since f_{ψ} is the normalized function of the CNT potential, $\psi(x)$ is a linear function inside the recombination zone, and is a square-root function outside the recombination zone. For $w = w_{\mathrm{m}}$, we find $f_1(w_{\mathrm{m}}) = f_2(w_{\mathrm{m}}) = f_{\psi}(w_{\mathrm{m}}) = 0$. Due to Equation (4.3.1) $h_{\eta}(w)$ is computed as

$$h_{\eta}(w)=\begin{cases}\left(\dfrac{S_w}{2}\right)^{\eta/2}\left(\dfrac{1}{4}-\dfrac{1}{S_w{}^2}(w-w_m)^2\right), & \text{for } w_{\mathrm{m}}-\dfrac{S_w}{2}\le w\le w_{\mathrm{m}}+\dfrac{S_w}{2},\\ 0, & \text{elsewhere.}\end{cases} \tag{4.4.4}$$

Since the nonradiative and radiative recombination are in terms of h_{η} and h_2, respectively, the recombination rates of the first iteration are parabolic inside the recombination zone, and are zero outside the recombination zone. Since

$$\int_0^1 h_{\eta}(w)dw=\left(\frac{S_w}{2}\right)^{\eta/2}\int_{w_m-S_w/2}^{w_m+S_w/2}\left(\frac{1}{4}-\frac{1}{S_w{}^2}(w-w_m)^2\right)dw=\left(\frac{S_w}{2}\right)^{\eta/2}\frac{S_w}{6},$$

by using Equation (3.22) the value of g_{η} is given as $\dfrac{1}{6\times 2^{\eta/2}}$. Hence the values of parameters are givens as

$$\begin{cases} g_1=\dfrac{1}{6\sqrt{2}}=\ 0.118,\\ g_2=\dfrac{1}{12}=\ 0.0833,\\ g_3=\dfrac{1}{12\sqrt{2}}=0.0589.\end{cases} \tag{4.4.5}$$

The function h_2 is given as

$$h_2(w) = \begin{cases} \left(\frac{S_w}{2}\right)\left(\frac{1}{4} - \frac{1}{S_w^{\,2}}(w - w_m)^2\right), & \text{for } w_{\mathrm{m}} - \frac{S_w}{2} \le w \le w_{\mathrm{m}} + \frac{S_w}{2}, \\ 0, & \text{elsewhere.} \end{cases} \tag{4.4.6}$$

At $w = w_{\mathrm{m}}$ the maximum value of $h_2(w)$ is equal to $\frac{S_w}{8}$, while at $w = w_{\mathrm{m}} \pm \frac{S_w}{2\sqrt{2}}$ the value of $h_2(w)$ is equal to $\frac{S_w}{16}$. Thus the FWHM of h_2 is equal to $\frac{S_w}{\sqrt{2}}$, which is assumed as $g_{\mathrm{fwhm}} S_{\mathrm{w}}$ according to the definition of g_{fwhm}. Thus the value of g_{fwhm} is given as

$$g_{\mathrm{fwhm}} = \frac{1}{\sqrt{2}} = 0.707. \tag{4.4.7}$$

Since outside the recombination region f_2 is equal to $\frac{1}{2}|w - w_{\mathrm{m}}| - \frac{S_w}{8}$, which is equal to $\frac{1}{2}|w - w_{\mathrm{m}}| - \beta$. Thus $\beta = \frac{S_w}{8}$. According to the definition of g_{b} to satisfy $\beta = g_{\mathrm{b}} S_{\mathrm{w}}$, we find

$$g_{\mathrm{b}} = \frac{1}{8} = 0.125. \tag{4.4.8}$$

4.5 Conclusion of the Analytic Calculation for Optical Emitters Based on Carbon-Nanotube Field-Effect Transistors

In conclusion, a new analytic diffusive-transport model for various recombination mechanisms is provided for the first time. The focus is on the effects of radiative and nonradiative recombination in the channel, with the movement of the spatial recombination profile in response to the gate and drain voltages calculated analytically,

which provides physical insight not afforded by purely numerical approaches. The relationship and the scaling are clearly depicted for the first time. In particular, the electronic and optical properties, such as the device current, emitted light-spot size and emitted optical power, are clearly shown in terms of the some parameters in the foregoing equations. Nonradiative recombination is shown to play a decisive role in the transport characteristics. For the first time, we find that the emitted light-spot size and the optical power are indeed sensitive to the operative nonradiative recombination mechanisms.

CHAPTER 5

NUMERICAL CALCULATION FOR OPTOELECTRONIC DEVICES BASED ON CARBON-NANOTUBE FIELD-EFFECT TRANSISTORS

For optical emitters and photodetectors based on CNT FETs, the system of differential equations with boundary conditions, in general, cannot be solved explicitly. The solution has to be calculated by numerical approaches. In this chapter the numerical approach for the system of differential equations consists of three tasks [90]. First, the domain of the simulation is partitioned into a finite number of subdomains, and the solution can be approximated with a desired accuracy. Secondly, the differential equation in each of the subdomains is approximated by algebraic equations involving only values of the continuous dependent variables at discrete point and involving the chosen functions, which approximate the dependent variables within each of the subdomains. In that way one obtains a system of nonlinear algebraic equations with unknowns comprised of dependent variables at discrete point. Thirdly, the solution of this system of nonlinear algebraic equations is calculated numerically. There are many classical methods for the partitioning of the domain (discretization) and the choice of functions to approximate the dependent variables within the subdomains. Both the finite difference method and finite element method can approximate the differential equations into the discretized equations. There are two approaches for the finite differences; the first is the finite difference method, in which the differential operators are directly replaced by difference operators, and the second is the box integration method, in which

the differential equation is integrated over each of the subdomains [90, 91]. The same discretized equations are obtained by both methods [90]. In Chapter 5.1 the approach of the box integration method is adopted to derive difference approximations for the electron and hole differential continuity equations, while in Chapter 5.3 the approach of finite difference method is applied to the exciton differential continuity equation. In the following subchapters the numerical approach for the optical emitters without exciton formation is studies in Chapter 5.1 and 5.2, while the numerical approach for the photodetectors including exciton formation is presented in Chapter 5.3. The calculation in this chapter is implemented by using the object-oriented C++ programming language in order to compute the numerical solutions.

The discretized equations for optical emitters based on CNT FETs without exciton formation are given in Chapter 5.1, and the solution of a system of discrete equations for optical emitters without exciton formation is given in Chapter 5.2. The numerical approach for photodetectors including exciton generation is given in Chapter 5.3. The conclusion of the numerical calculation for optoelectronic devices based on CNT FETs is shown in Chapter 5.4.

5.1 Discretized Equations for Optical Emitters Based on Carbon-Nanotube Field-Effect Transistors without Exciton Formation

In optical emitters based on long-channel ambipolar CNT FETs, the area of strong electron–hole recombination, and hence the region of light emission, can be controlled by varying the gate and drain voltages [42, 49]. Two numerical models with diffusive

transport and carrier recombination were developed for long-channel devices in order to calculate the emitted light-spot movement [50, 60]. The radiative mechanism is assumed as the band-to-band recombination of injected electrons and holes. Radiative recombination was assumed to be dominant; however, the importance of nonradiative recombination is indicated by the low measured quantum efficiency of the light output, which ranges from 10^{-6} to 10^{-7} [44]. The new model accounting for both radiative and nonradiative recombination, allowing for several mechanisms [51], was presented in Chapter 3. An analytic diffusive-transport model is already described in Chapter 4. In this Chapter 5.1 the numerical diffusive-transport approach for the light emission based on band-to-band radiative recombination with various nonradiative recombination mechanisms but neglecting exciton formation is presented here.

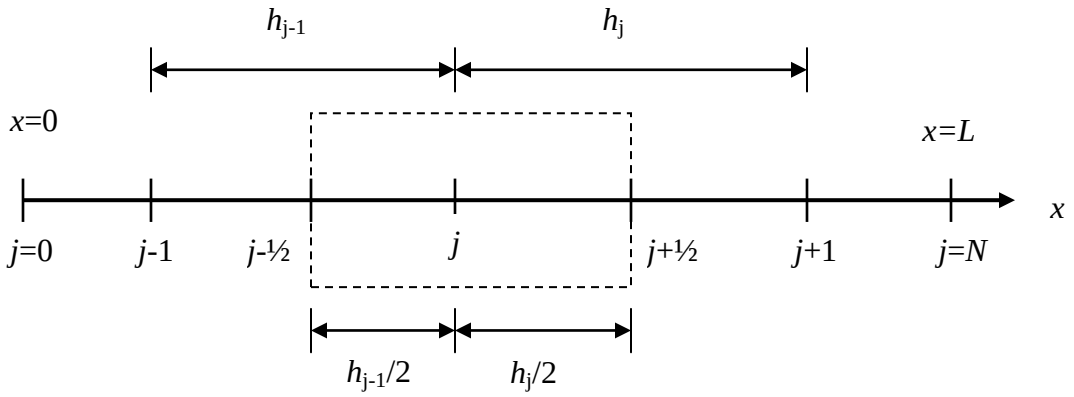

Figure 5.1. The adopted nomenclature for finite differences.

In the classical method of finite differences, the two-dimensional domain is partitioned into rectangular subdomains by a mesh that is a set of meshlines parallel to the coordinate axes. In the optical emitters and photodetectors the dependent variables, such as the CNT potential, electron and hole densities, exciton density, and recombination rates, are in the one-dimensional domain along the CNT axis. In this one-dimensional case, the meshlines intersect the CNT axis at the node points. The adopted nomenclature for finite differences is shown in Figure 5.1. Each discrete node point is depicted by the symbol *j*, and the values of unknown dependent variables at each node point *j* need to be solved. The x_j is assumed to be the distance from the source S along the carbon-nanotube axis. The first ($j = 0$) and the last ($j = N$) node points coincide with the boundaries close to the source S and drain D, respectively. Thus the total number of node points is N+1. The following abbreviation is used:

$$h_j = x_{j+1} - x_j, \quad j = 0,1,...,N-1. \tag{5.1.1}$$

For flexibility in the numerical calculations, non-uniform meshes are used, that is h_j is not necessarily constant. The areas encircled by the dashed lines around the node point *j* depict the subdomains. The box integration method is used to render the differential equations into discretized equations. The differential equation is integrated over each of the subdomains respected to the node points inside the boundaries

$$\mathrm{DOM}_j = \left\{ x_j - \frac{h_{j-1}}{2} \le x \le x_j + \frac{h_j}{2},\ j = 1,2,...,N-1 \right\}. \tag{5.1.2}$$

The symbols of $j = 0$ and $j = N$ indicate the boundary node points, while the symbols of $j = 1, 2,..., N$-1 depicts the node points inside the boundary. The differential continuity equation of electrons of Equation (3.4.1) in steady state recall is

$$-\frac{1}{e}\frac{dI_n(x)}{dx}+\big(G(x)-R(x)\big)=0.$$

Remember that the positive carrier currents I_n and I_p are defined from D at $x = L$ to S at $x = 0$. The electron continuity equation is integrated over each of the subdomains DOM_j respected to the node point j except the node points at the boundaries

$$\int_{x_{j-1/2}}^{x_{j+1/2}}\left\{-\frac{1}{e}\frac{dI_n(x)}{dx}+\big(G(x)-R(x)\big)\right\}dx=0. \tag{5.1.3}$$

The symbols j-½ and j+½ indicate the boundary points of the integration box upon the node point j, which locate at $x = x_j–h_{j-1}/2$ and $x = x_j+h_j/2$, respectively. Assuming that the electron and hole generation and recombination rates are constant within the integration subdomain DOM_j, we obtain

$$\frac{1}{e}\big(-I_{n,j+1/2}+I_{n,j-1/2}\big)+\big(G_j-R_j\big)\frac{h_j+h_{j-1}}{2}=0,\ \ j=1,2,...,N-1. \tag{5.1.4}$$

Similarly, the hole continuity equation of Equation (3.4.2) is integrated over each of the subdomains DOM_j with respect to the node point j except the node points at the boundaries

$$\frac{1}{e}\big(I_{p,j+1/2}-I_{p,j-1/2}\big)+\big(G_j-R_j\big)\frac{h_j+h_{j-1}}{2}=0,\quad j=1,2,...,N-1. \tag{5.1.5}$$

Using the longitudinal electrical field $F_x(x) = -\partial\psi(x)/\partial x$, the electron and hole drift-diffusion currents of Equations (3.2.1) and (3.2.2) can be rewritten as

$$I_n(x)=en(x)\mu\frac{d\psi(x)}{dx}-eD_n\frac{dn(x)}{dx}, \tag{5.1.6}$$

$$I_p(x)=ep(x)\mu\frac{d\psi(x)}{dx}+eD_p\frac{dp(x)}{dx}, \tag{5.1.7}$$

in which $\partial\psi/\partial x$ is replaced by $d\psi/dx$ since the only longitudinal dependent variable x of the CNT potential ψ is interested. The electron current I_n at the point $j+½$ is given as

$$I_{n,j+1/2} = e\mu n_{j+1/2} \frac{d\psi}{dx}\Big|_{j+1/2} - eD_{n,j+1/2} \frac{dn}{dx}\Big|_{j+1/2}. \tag{5.1.8}$$

Since the values, such as $n_{j+1/2}$, $(dn/dx)_{j+1/2}$, and $(d\psi/dx)_{j+1/2}$, do not locate in the node point j, the profile of the interpolation scheme for the unknown dependent variables n and ψ within each interval between the node point j and node point $j+1$ have to be chosen. Assuming that the profile of CNT potential ψ is a linear function of x within each interval of $x \in [x_j, x_{j+1}]$, that is $d\psi/dx$ is constant, we obtain

$$\frac{d\psi}{dx}\Big|_{j+1/2} = \frac{\psi_{j+1} - \psi_j}{h_j}. \tag{5.1.9}$$

The Scharfetter-Gummel approach [90, 92] is adopted for the profile of the interpolation scheme for the unknown dependent variable n. The electron density within each interval is interpolated as

$$n(x) = \left(1 - g_j(x,\psi)\right) \cdot n_j + g_j(x,\psi) \cdot n_{j+1}, \qquad \forall x \in \left[x_j, x_{j+1}\right], \tag{5.1.10}$$

The growth function $g_j(x,\psi)$ in term of the exponential dependence on the CNT potential is given as

$$g_j(x,\psi) = \frac{1 - \exp\left(\dfrac{\psi_{j+1} - \psi_j}{V_t} \cdot \dfrac{x - x_j}{h_j}\right)}{1 - \exp\left(\dfrac{\psi_{j+1} - \psi_j}{V_t}\right)}, \tag{5.1.11}$$

in which $g_j(x,\psi)$ satisfies two conditions

$$g_j\left(x_j,\psi\right) = 0, \;\; g_j\left(x_{j+1},\psi\right) = 1,$$

and V_t ($= k_B T/e$) is the thermal voltage. Thus n matches two boundary conditions

$$n(x_j) = n_j, \qquad n(x_{j+1}) = n_{j+1}.$$

Therefore, $n_{j+1/2}$ can be obtained as

$$n_{j+1/2} = n(x_{j+1/2}) = \frac{n_j}{1+\exp\left(\frac{\psi_j - \psi_{j+1}}{2V_t}\right)} + \frac{n_{j+1}}{1+\exp\left(\frac{\psi_{j+1} - \psi_j}{2V_t}\right)}. \tag{5.1.12}$$

Be(x) is the Bernoulli function

$$\mathrm{Be}(x) = \frac{x}{e^x - 1}. \tag{5.1.13}$$

Using the Bernoulli function, $dn(x)/dx$ is computed as

$$\begin{aligned} \frac{dn(x)}{dx} &= \left(n_{j+1} - n_j\right)\frac{\partial g_j(x,\psi)}{\partial x} \\ &= \frac{(n_{j+1} - n_j)}{h_j}\mathrm{Be}\left(\frac{\psi_{j+1} - \psi_j}{V_t}\right)\exp\left(\frac{\psi_{j+1} - \psi_j}{V_t}\cdot\frac{x - x_j}{h_j}\right), \end{aligned} \tag{5.1.14}$$

and then

$$\left.\frac{dn}{dx}\right|_{j+1/2} = \frac{(n_{j+1} - n_j)}{h_j}\mathrm{Be}\left(\frac{\psi_{j+1} - \psi_j}{V_t}\right)\exp\left(\frac{\psi_{j+1} - \psi_j}{2V_t}\right). \tag{5.1.15}$$

Referring to Equation (3.2.3) based on the formula of Kroemer [58], for large carrier densities the Einstein relation in the degenerate semiconductors can be approximated as

$$D_n = \mu V_t(1 + \delta_n), \tag{5.1.16}$$

with

$$\delta_n = A_1\zeta + 2A_2\zeta^2 + 3A_3\zeta^3 + 4A_4\zeta^4, \quad \text{in degenerate semiconductors,} \tag{5.1.17}$$

and $\zeta = n/N_c$. The values of A_i are obtained in Equation (3.2.4) where the Fermi-Dirac integral of order -½ is applied to one-dimensional case by using the similar procedure of Joyce and Dixon [51, 59]. Notice that in the nondegenerate semiconductors for

$n / N_c < e^{-3}$, we obtain $\delta_{\mathrm{n}} << 1$, and then the Einstein relation in nondegenerate semiconductors is hold. Hence $D_{\mathrm{n,j+1/2}}$ is obtained as

$$\begin{cases} D_{n,j+1/2} = \mu V_t (1+\delta_{n,j+1/2}), \\ \delta_{n,j+1/2} = A_1 \zeta_{n,j+1/2} + 2A_2 \zeta_{n,j+1/2}{}^2 + 3A_3 \zeta_{n,j+1/2}{}^3 + 4A_4 \zeta_{n,j+1/2}{}^4, \\ \zeta_{n,j+1/2} = \dfrac{n_{j+1/2}}{N_c}. \end{cases} \tag{5.1.18}$$

Substituting Equations (5.1.9), (5.1.12), (5.1.15), and (5.1.18) into Equation (5.1.8), the value of $I_{\mathrm{n,j+1/2}}$ is given as the nonlinear algebraic form in terms of the values of the unknown dependent variables n and ψ at the node points j and j+1:

$$\begin{aligned} I_{n,j+1/2} = {} & n_j \frac{e\mu V_t}{h_j}\left[\mathrm{Be}\left(\frac{\psi_j - \psi_{j+1}}{V_t} \right) + \delta_{n,j+1/2}\, \mathrm{Be}\left(\frac{\psi_{j+1} - \psi_j}{V_t} \right) \exp\left(\frac{\psi_{j+1} - \psi_j}{2V_t} \right) \right] \\ & - n_{j+1} \frac{e\mu V_t}{h_j}\left[\mathrm{Be}\left(\frac{\psi_{j+1} - \psi_j}{V_t} \right) + \delta_{n,j+1/2}\, \mathrm{Be}\left(\frac{\psi_{j+1} - \psi_j}{V_t} \right) \exp\left(\frac{\psi_{j+1} - \psi_j}{2V_t} \right) \right]. \end{aligned} \tag{5.1.19}$$

Similarly, the value of $I_{\mathrm{n,j-1/2}}$ is given as the nonlinear algebraic form in terms of the values of the unknown dependent variables n and ψ at the node points j and j-1. Replacing j by j-1, we obtain

$$I_{n,j-1/2} = e\mu n_{j-1/2} \left. \frac{d\psi}{dx} \right|_{j-1/2} - eD_{n,j-1/2} \left. \frac{dn}{dx} \right|_{j-1/2}, \tag{5.1.20}$$

$$\left. \frac{d\psi}{dx} \right|_{j-1/2} = \frac{\psi_j - \psi_{j-1}}{h_{j-1}}, \tag{5.1.21}$$

$$n_{j-1/2} = n(x_{j-1/2}) = \frac{n_{j-1}}{1+\exp\left(\dfrac{\psi_{j-1} - \psi_j}{2V_t} \right)} + \frac{n_j}{1+\exp\left(\dfrac{\psi_j - \psi_{j-1}}{2V_t} \right)}, \tag{5.1.22}$$

$$\left. \frac{dn}{dx} \right|_{j-1/2} = \frac{(n_j - n_{j-1})}{h_{j-1}} \mathrm{Be}\left(\frac{\psi_j - \psi_{j-1}}{V_t} \right) \exp\left(\frac{\psi_j - \psi_{j-1}}{2V_t} \right), \tag{5.1.23}$$

$$\begin{cases} D_{n,j-1/2} = \mu V_t (1+\delta_{n,j-1/2}), \\ \delta_{n,j-1/2} = A_1\zeta_{n,j-1/2} + 2A_2{\zeta_{n,j-1/2}}^2 + 3A_3{\zeta_{n,j-1/2}}^3 + 4A_4{\zeta_{n,j-1/2}}^4, \\ \zeta_{n,j-1/2} = \dfrac{n_{j-1/2}}{N_c}, \end{cases} \tag{5.1.24}$$

and thus

$$\begin{aligned} I_{n,j-1/2} = {} & n_{j-1}\frac{e\mu V_t}{h_{j-1}}\left[\mathrm{Be}\left(\frac{\psi_{j-1}-\psi_j}{V_t}\right)+\delta_{n,j-1/2}\,\mathrm{Be}\left(\frac{\psi_j-\psi_{j-1}}{V_t}\right)\exp\left(\frac{\psi_j-\psi_{j-1}}{2V_t}\right)\right] \\ & -n_j\frac{e\mu V_t}{h_{j-1}}\left[\mathrm{Be}\left(\frac{\psi_j-\psi_{j-1}}{V_t}\right)+\delta_{n,j-1/2}\,\mathrm{Be}\left(\frac{\psi_j-\psi_{j-1}}{V_t}\right)\exp\left(\frac{\psi_j-\psi_{j-1}}{2V_t}\right)\right]. \end{aligned} \tag{5.1.25}$$

Similarly, the hole currents $I_{p,j+1/2}$ and $I_{p,j-1/2}$ are given as

$$I_{p,j+1/2} = e\mu p_{j+1/2}\left.\frac{d\psi}{dx}\right|_{j+1/2} + eD_{p,j+1/2}\left.\frac{dp}{dx}\right|_{j+1/2}, \tag{5.1.26}$$

$$I_{p,j-1/2} = e\mu p_{j-1/2}\left.\frac{d\psi}{dx}\right|_{j-1/2} + eD_{p,j-1/2}\left.\frac{dp}{dx}\right|_{j-1/2}. \tag{5.1.27}$$

The hole density within each interval in terms of the growth function $g_j(x,-\psi)$ is interpolated as

$$p(x) = \left(1-g_j(x,-\psi)\right)\cdot p_j + g_j(x,-\psi)\cdot p_{j+1}, \quad \forall x \in \left[x_j, x_{j+1}\right], \tag{5.1.28}$$

and

$$p_{j+1/2} = p(x_{j+1/2}) = \frac{p_j}{1+\exp\left(\dfrac{\psi_{j+1}-\psi_j}{2V_t}\right)} + \frac{p_{j+1}}{1+\exp\left(\dfrac{\psi_j-\psi_{j+1}}{2V_t}\right)}, \tag{5.1.29}$$

$$p_{j-1/2} = p(x_{j-1/2}) = \frac{p_{j-1}}{1+\exp\left(\dfrac{\psi_j-\psi_{j-1}}{2V_t}\right)} + \frac{p_j}{1+\exp\left(\dfrac{\psi_{j-1}-\psi_j}{2V_t}\right)}. \tag{5.1.30}$$

$$\left.\frac{dp}{dx}\right|_{j+1/2} = \frac{(p_{j+1}-p_j)}{h_j}\mathrm{Be}\left(\frac{\psi_j-\psi_{j+1}}{V_t}\right)\exp\left(\frac{\psi_j-\psi_{j+1}}{2V_t}\right), \tag{5.1.31}$$

$$\left.\frac{dp}{dx}\right|_{j-1/2}=\frac{(p_j-p_{j-1})}{h_{j-1}}\mathrm{Be}\left(\frac{\psi_{j-1}-\psi_j}{V_t}\right)\exp\left(\frac{\psi_{j-1}-\psi_j}{2V_t}\right), \tag{5.1.32}$$

$$\begin{cases} D_{p,j\pm1/2}=\mu V_t(1+\delta_{p,j\pm1/2}), \\ \delta_{p,j\pm1/2}=A_1\zeta_{p,j\pm1/2}+2A_2{\zeta_{p,j\pm1/2}}^2+3A_3{\zeta_{p,j\pm1/2}}^3+4A_4{\zeta_{p,j\pm1/2}}^4, \\ \zeta_{p,j\pm1/2}=\dfrac{p_{j\pm1/2}}{N_c}. \end{cases} \tag{5.1.33}$$

The values of $I_{p,j+1/2}$ and $I_{p,j-1/2}$ are given as the nonlinear algebraic form,

$$\begin{aligned} I_{p,j+1/2}=&-p_j\frac{e\mu V_t}{h_j}\left[\mathrm{Be}\left(\frac{\psi_{j+1}-\psi_j}{V_t}\right)+\delta_{p,j+1/2}\,\mathrm{Be}\left(\frac{\psi_j-\psi_{j+1}}{V_t}\right)\exp\left(\frac{\psi_j-\psi_{j+1}}{2V_t}\right)\right] \\ &+p_{j+1}\frac{e\mu V_t}{h_j}\left[\mathrm{Be}\left(\frac{\psi_j-\psi_{j+1}}{V_t}\right)+\delta_{p,j+1/2}\,\mathrm{Be}\left(\frac{\psi_j-\psi_{j+1}}{V_t}\right)\exp\left(\frac{\psi_j-\psi_{j+1}}{2V_t}\right)\right], \end{aligned} \tag{5.1.34}$$

$$\begin{aligned} I_{p,j-1/2}=&-p_{j-1}\frac{e\mu V_t}{h_{j-1}}\left[\mathrm{Be}\left(\frac{\psi_j-\psi_{j-1}}{V_t}\right)+\delta_{p,j-1/2}\,\mathrm{Be}\left(\frac{\psi_{j-1}-\psi_j}{V_t}\right)\exp\left(\frac{\psi_{j-1}-\psi_j}{2V_t}\right)\right] \\ &+p_j\frac{e\mu V_t}{h_{j-1}}\left[\mathrm{Be}\left(\frac{\psi_{j-1}-\psi_j}{V_t}\right)+\delta_{p,j-1/2}\,\mathrm{Be}\left(\frac{\psi_{j-1}-\psi_j}{V_t}\right)\exp\left(\frac{\psi_{j-1}-\psi_j}{2V_t}\right)\right]. \end{aligned} \tag{5.1.35}$$

Substituting Equations (5.1.19) and (5.1.25) into Equation (5.1.4), the discrete equation for the differential continuity equation of electrons is obtained as

$$
\begin{aligned}
&n_{j-1}\frac{\mu V_t}{h_{j-1}}\left[\mathrm{Be}\left(\frac{\psi_{j-1}-\psi_j}{V_t}\right)+\delta_{n,j-1/2}\,\mathrm{Be}\left(\frac{\psi_j-\psi_{j-1}}{V_t}\right)\exp\left(\frac{\psi_j-\psi_{j-1}}{2V_t}\right)\right]\\
&-n_j\frac{\mu V_t}{h_{j-1}}\left[\mathrm{Be}\left(\frac{\psi_j-\psi_{j-1}}{V_t}\right)+\delta_{n,j-1/2}\,\mathrm{Be}\left(\frac{\psi_j-\psi_{j-1}}{V_t}\right)\exp\left(\frac{\psi_j-\psi_{j-1}}{2V_t}\right)\right]\\
&-n_j\frac{\mu V_t}{h_j}\left[\mathrm{Be}\left(\frac{\psi_j-\psi_{j+1}}{V_t}\right)+\delta_{n,j+1/2}\,\mathrm{Be}\left(\frac{\psi_{j+1}-\psi_j}{V_t}\right)\exp\left(\frac{\psi_{j+1}-\psi_j}{2V_t}\right)\right]\\
&+n_{j+1}\frac{\mu V_t}{h_j}\left[\mathrm{Be}\left(\frac{\psi_{j+1}-\psi_j}{V_t}\right)+\delta_{n,j+1/2}\,\mathrm{Be}\left(\frac{\psi_{j+1}-\psi_j}{V_t}\right)\exp\left(\frac{\psi_{j+1}-\psi_j}{2V_t}\right)\right]\\
&+\left(G_j-R_j\right)\frac{h_j+h_{j-1}}{2}\\
&=0, \qquad\qquad j=1,2,...,N-1.
\end{aligned}
\tag{5.1.36}
$$

Similarly, substituting Equations (5.1.34) and (5.1.35) into Equation (5.1.5), the discrete equation for the differential continuity equation of holes is obtained as

$$
\begin{aligned}
&p_{j-1}\frac{\mu V_t}{h_{j-1}}\left[\mathrm{Be}\left(\frac{\psi_j-\psi_{j-1}}{V_t}\right)+\delta_{p,j-1/2}\,\mathrm{Be}\left(\frac{\psi_{j-1}-\psi_j}{V_t}\right)\exp\left(\frac{\psi_{j-1}-\psi_j}{2V_t}\right)\right]\\
&-p_j\frac{\mu V_t}{h_{j-1}}\left[\mathrm{Be}\left(\frac{\psi_{j-1}-\psi_j}{V_t}\right)+\delta_{p,j-1/2}\,\mathrm{Be}\left(\frac{\psi_{j-1}-\psi_j}{V_t}\right)\exp\left(\frac{\psi_{j-1}-\psi_j}{2V_t}\right)\right].\\
&-p_j\frac{\mu V_t}{h_j}\left[\mathrm{Be}\left(\frac{\psi_{j+1}-\psi_j}{V_t}\right)+\delta_{p,j+1/2}\,\mathrm{Be}\left(\frac{\psi_j-\psi_{j+1}}{V_t}\right)\exp\left(\frac{\psi_j-\psi_{j+1}}{2V_t}\right)\right]\\
&+p_{j+1}\frac{\mu V_t}{h_j}\left[\mathrm{Be}\left(\frac{\psi_j-\psi_{j+1}}{V_t}\right)+\delta_{p,j+1/2}\,\mathrm{Be}\left(\frac{\psi_j-\psi_{j+1}}{V_t}\right)\exp\left(\frac{\psi_j-\psi_{j+1}}{2V_t}\right)\right],\\
&+\left(G_j-R_j\right)\frac{h_j+h_{j-1}}{2}\\
&=0, \qquad\qquad j=1,2,...,N-1.
\end{aligned}
\tag{5.1.37}
$$

Notice that in nondegenerate semiconductors, both δ_{n} and δ_{p} are neglected, Equations (5.1.36) and (5.1.37) are reduced to the formula in Reference [90].

For numerical calculation it is convenient to take the normalized forms. By choosing the values of C_{nor} [cm^{-1}] for the carrier densities and V_{nor} [V] for the CNT potential, the normalized forms are introduced as

$$\bar{n}=\frac{n}{C_{nor}},\qquad \bar{p}=\frac{p}{C_{nor}},\qquad \bar{\psi}=\frac{\psi}{V_{nor}},\qquad \bar{h}=\frac{h}{L},\qquad \bar{V}_t=\frac{V_t}{V_{nor}},\quad (5.1.38)$$

Equation (5.1.36) is multiplied by $L/C_{nor}\mu V_t$ to obtain the normalized nonlinear algebraic equations $f_{n,j}$ of electrons, which is expressed as

$$\begin{aligned} f_{n,j} &= \bar{n}_{j-1}\frac{1}{\bar{h}_{j-1}}\left[\mathrm{Be}\left(\frac{\bar{\psi}_{j-1}-\bar{\psi}_j}{\bar{V}_t}\right)+\delta_{n,j-1/2}\,\mathrm{Be}\left(\frac{\bar{\psi}_j-\bar{\psi}_{j-1}}{\bar{V}_t}\right)\exp\left(\frac{\bar{\psi}_j-\bar{\psi}_{j-1}}{2\bar{V}_t}\right)\right] \\ &-\bar{n}_j\frac{1}{\bar{h}_{j-1}}\left[\mathrm{Be}\left(\frac{\bar{\psi}_j-\bar{\psi}_{j-1}}{\bar{V}_t}\right)+\delta_{n,j-1/2}\,\mathrm{Be}\left(\frac{\bar{\psi}_j-\bar{\psi}_{j-1}}{\bar{V}_t}\right)\exp\left(\frac{\bar{\psi}_j-\bar{\psi}_{j-1}}{2\bar{V}_t}\right)\right] \\ &-\bar{n}_j\frac{1}{\bar{h}_j}\left[\mathrm{Be}\left(\frac{\bar{\psi}_j-\bar{\psi}_{j+1}}{\bar{V}_t}\right)+\delta_{n,j+1/2}\,\mathrm{Be}\left(\frac{\bar{\psi}_{j+1}-\bar{\psi}_j}{\bar{V}_t}\right)\exp\left(\frac{\bar{\psi}_{j+1}-\bar{\psi}_j}{2\bar{V}_t}\right)\right] \\ &+\bar{n}_{j+1}\frac{1}{\bar{h}_j}\left[\mathrm{Be}\left(\frac{\bar{\psi}_{j+1}-\bar{\psi}_j}{\bar{V}_t}\right)+\delta_{n,j+1/2}\,\mathrm{Be}\left(\frac{\bar{\psi}_{j+1}-\bar{\psi}_j}{\bar{V}_t}\right)\exp\left(\frac{\bar{\psi}_{j+1}-\bar{\psi}_j}{2\bar{V}_t}\right)\right] \\ &+\frac{\bar{h}_j+\bar{h}_{j-1}}{2}\left(\bar{G}_j-\bar{R}_j\right) \\ &=0, \qquad\qquad j=1,2,...,N-1. \end{aligned} \quad (5.1.39)$$

The normalized generation-recombination of carrier densities is given as

$$\bar{G}_j-\bar{R}_j=\frac{L^2}{C_{nor}\mu V_t}\left(G_j-R_j\right). \quad (5.1.40)$$

Similarly, Equation (5.1.37) is multiplied by $L/C_{nor}\mu V_t$ to obtain the normalized nonlinear algebraic equations $f_{p,j}$ of holes, which is expressed as

$$
\begin{aligned}
f_{p,j} = {} & \bar{p}_{j-1}\frac{1}{\bar{h}_{j-1}}\left[\mathrm{Be}\left(\frac{\bar{\psi}_j-\bar{\psi}_{j-1}}{\bar{V}_t}\right)+\delta_{p,j-1/2}\,\mathrm{Be}\left(\frac{\bar{\psi}_{j-1}-\bar{\psi}_j}{\bar{V}_t}\right)\exp\left(\frac{\bar{\psi}_{j-1}-\bar{\psi}_j}{2\bar{V}_t}\right)\right] \\
& -\bar{p}_j\frac{1}{\bar{h}_{j-1}}\left[\mathrm{Be}\left(\frac{\bar{\psi}_{j-1}-\bar{\psi}_j}{\bar{V}_t}\right)+\delta_{p,j-1/2}\,\mathrm{Be}\left(\frac{\bar{\psi}_{j-1}-\bar{\psi}_j}{\bar{V}_t}\right)\exp\left(\frac{\bar{\psi}_{j-1}-\bar{\psi}_j}{2\bar{V}_t}\right)\right] \\
& -\bar{p}_j\frac{1}{\bar{h}_j}\left[\mathrm{Be}\left(\frac{\bar{\psi}_{j+1}-\bar{\psi}_j}{\bar{V}_t}\right)+\delta_{p,j+1/2}\,\mathrm{Be}\left(\frac{\bar{\psi}_j-\bar{\psi}_{j+1}}{\bar{V}_t}\right)\exp\left(\frac{\bar{\psi}_j-\bar{\psi}_{j+1}}{2\bar{V}_t}\right)\right] \\
& +\bar{p}_{j+1}\frac{1}{\bar{h}_j}\left[\mathrm{Be}\left(\frac{\bar{\psi}_j-\bar{\psi}_{j+1}}{\bar{V}_t}\right)+\delta_{p,j+1/2}\,\mathrm{Be}\left(\frac{\bar{\psi}_j-\bar{\psi}_{j+1}}{\bar{V}_t}\right)\exp\left(\frac{\bar{\psi}_j-\bar{\psi}_{j+1}}{2\bar{V}_t}\right)\right] \\
& +\frac{\bar{h}_j+\bar{h}_{j-1}}{2}\left(\bar{G}_j-\bar{R}_j\right) \\
= {} & 0, \qquad\qquad j=1,2,\ldots,N-1.
\end{aligned}
\tag{5.1.41}
$$

Since exciton formation is neglected, the generation rate of electron-hole pairs is assumed to be zero. In optical emitters based on the ambipolar CNT FETs the recombination mechanism of electrons and holes can be radiative or nonradiative, and nonradiative recombination is much stronger than radiative, as evidenced by the low measured quantum efficiency, as mentioned above. Assuming light emission generated by band-to-band radiative recombination (BBR) of electrons and holes, the radiative recombination rate R_r is expressed as $B_{BBR}(np\text{-}n_i^2)$, where B_{BBR} [cm/s] is the band-to-band radiative recombination coefficient [50, 51, 60]. When defects and impurities exist, e.g. at the CNT-insulator interface, Shockley-Read-Hall (SRH) recombination is important. Band-to-band nonradiative recombination (BBN), and Auger recombination are considered as well. Expressions for the nonradiative recombination rates R_{nr} and the coefficients chosen are listed in Table 2.1 [51], in which the coefficient values of τ_{SRH}, B_{BBN}, and B_{Auger} were chosen to yield light-spot sizes in agreement with the experimental data of Reference [42]. The total recombination rate of electrons and holes is given as R

= R_r+R_{nr}. Therefore, at node point j the value of G_j is zero, and the value of the recombination rate of electrons and holes is given as

$$R_j = R_{r,j} + R_{nr,j}. \tag{5.1.42}$$

In the Equations (5.1.39) and (5.1.41) the normalized recombination rate is given as

$$\overline{R}_j = \overline{R}_{r,j} + \overline{R}_{nr,j}, \tag{5.1.43}$$

and

$$\overline{R}_{r,j} = \frac{L^2 C_{nor} B_{BBR}}{\mu V_t}\left(\overline{n}_j \overline{p}_j - \left(\frac{n_i}{C_{nor}}\right)^2\right), \tag{5.1.44}$$

$$\overline{R}_{nr,j} = \begin{cases} \dfrac{L^2}{\tau_{SRH}\mu V_t\left(\overline{n}_j + \overline{p}_j + 2\left(\dfrac{n_i}{C_{nor}}\right)\right)}\left(\overline{n}_j \overline{p}_j - \left(\dfrac{n_i}{C_{nor}}\right)^2\right), & \text{for SRH,} \\ \dfrac{L^2 C_{nor} B_{BBN}}{\mu V_t}\left(\overline{n}_j \overline{p}_j - \left(\dfrac{n_i}{C_{nor}}\right)^2\right), & \text{for BBN,} \\ \dfrac{L^2 C_{nor}{}^2 B_{Auger}}{\mu V_t}\left(\overline{n}_j + \overline{p}_j\right)\left(\overline{n}_j \overline{p}_j - \left(\dfrac{n_i}{C_{nor}}\right)^2\right), & \text{for Auger.} \end{cases} \tag{5.1.45}$$

In order to calculate the CNT potential ψ, in general, Poisson's equation has to be solved. For long-channel CNT FETs the longitudinal electric field F_x is a much more gradual function of position than the transverse electric field, and thus the GCA can be invoked as a simplified model for Poisson's equation, as mentioned in Chapter 3. The local carrier density is simply related to the gate-capacitance and the voltage drop across the gate insulator. The relationship is shown in Equation (3.1.1) and is rewritten here for convenience

$$C[\psi(x) - (V_G - V_{fb})] = e[p(x) - n(x)], \tag{5.1.46}$$

where C is the linear gate-to-channel capacitance, and V_{fb} is the flat-band voltage. The normalized discrete equation $f_{\psi,\mathrm{j}}$ for the CNT potential ψ at the node point j is expressed as

$$f_{\psi,j} = \bar{\psi}_j - \frac{V_{\mathrm{G}} - V_{\mathrm{fb}}}{V_{nor}} - \frac{eC_{nor}}{CV_{nor}}\left(\bar{p}_j - \bar{n}_j\right) = 0, \qquad j = 1, 2, ..., N-1. \tag{5.1.47}$$

Three discrete equations, Equations (5.1.39), (5.1.41), and (5.1.47) are obtained in terms of three unknown dependent variables, the CNT potential ψ, electron density n, and hole density p. For the differential continuity equation of electrons, one boundary condition is necessary for each contact. Similarly, for the differential continuity equation of holes, another boundary condition is necessary for each contact. Therefore, two boundary conditions for the source and two boundary conditions for the drain are required. In CNT FETs the metal-CNT interfaces form the Schottky barriers. In our model their effect is simplified to a constant voltage drop independent of the current, and the values of the voltage drops across the contact/channel interfaces are assumed to be the same value V_{c} at both (S and D) contacts [49, 51],

$$\Delta V_s = \Delta V_d = V_c. \tag{5.1.48}$$

Referring to Equations (3.1.3) and (3.1.4), the relationship between the terminal voltages and the CNT potential ψ shows the boundary conditions at S and D:

$$\psi_S = V_S + V_c, \qquad \text{at the source,} \tag{5.1.49}$$

$$V_D = \psi_D + V_c, \qquad \text{at the drain,} \tag{5.1.50}$$

where ψ_{S} is the CNT potential at S and ψ_{D} is the CNT potential at D. In the discrete equations, ψ_{S} and ψ_{D} are described as ψ_0 and ψ_{N}, respectively. The discrete boundary conditions are given as

$$\psi_0 = V_S + V_c, \quad \text{and} \quad \psi_N = V_D - V_c, \tag{5.1.51}$$

and the normalized forms $f_{\psi,0}$ and $f_{\psi,N}$ of the discrete boundary conditions are given as

$$f_{\psi,0} = \bar{\psi}_0 - \frac{V_S + V_c}{V_{nor}} = 0, \qquad \text{at the source,} \tag{5.1.52}$$

$$f_{\psi,N} = \bar{\psi}_N - \frac{V_D - V_c}{V_{nor}} = 0, \qquad \text{at the drain.} \tag{5.1.53}$$

When the channel length exceeds the recombination length, essentially all injected carriers recombine within the channel. Hence, electrons injected from S fully recombine with the holes in the channel and the electron density is negligible at D. Similarly, holes injected from D do not reach S. The boundary conditions are given as

$$n_D = 0 \ \text{ and } \quad p_S = 0, \tag{5.1.54}$$

and the normalized forms $f_{n,N}$ and $f_{p,0}$ of the discrete boundary conditions are given as

$$f_{n,N} = \bar{n}_N = 0, \qquad \text{at the drain,} \tag{5.1.55}$$

$$f_{p,0} = \bar{p}_0 = 0, \qquad \text{at the source.} \tag{5.1.56}$$

Notice that $f_{\psi,0}$, $f_{\psi,N}$, $f_{n,N}$, and $f_{p,0}$, all show Dirichlet type of boundary conditions. Since Equation (5.1.46) of the GCA can be applied to the boundary node points $j = 0$ and $j = N$, the normalized forms $f_{n,0}$ at the source and $f_{p,N}$ at the drain are given as

$$f_{n,0} = \bar{n}_0 + \frac{C}{eC_{nor}}\left(V_S + V_c - V_G + V_{fb}\right) = 0, \qquad \text{at the source,} \tag{5.1.57}$$

$$f_{p,N} = \bar{p}_N - \frac{C}{eC_{nor}}\left(V_D - V_c - V_G + V_{fb}\right) = 0, \qquad \text{at the drain,} \tag{5.1.58}$$

where Equations (5.1.51), (5.1.55), and (5.1.56) are used.

The Bernoulli function Be(x) of Equation (5.1.13) has to be implemented very carefully for numerical computation. The approximation of the Bernoulli function is given as [90, 91]

$$\mathrm{Be}(x)=\begin{cases}-x, & x\le x_1\\ \dfrac{x}{\exp(x)-1}, & x_1\le x<x_2\\ 1-\dfrac{x}{2}, & x_2\le x<x_3\\ \dfrac{x\cdot\exp(-x)}{1-\exp(-x)}, & x_3\le x<x_4\\ x\cdot\exp(-x), & x_4\le x<x_5\\ 0, & x\ge x_5,\end{cases} \tag{5.1.59}$$

and the values of parameters are chosen as [91]

$$x_1=-36,\qquad x_2=-8\times10^{-7},\ x_3=2\times10^{-7},\quad x_4=36,\qquad x_5=-746. \tag{5.1.60}$$

The value of Be(-x) can be used as

$$\mathrm{Be}(-x)=x+\mathrm{Be}(x). \tag{5.1.61}$$

5.2 The Solution of a System of Discrete Equations for Optical Emitters without Exciton Formation

In last subchapter the discretization of the differential equations yields a system of nonlinear algebraic equations with the values of dependent variables at the discrete node points j = 0, 1,…, N-1, N. The total number of the discrete unknown variables ψ, n, and p are 3(N+1). Inside the boundary the number of the discrete equations of $f_{n,j}$, $f_{p,j}$, and $f_{\psi,j}$, are 3(N-1), while at the boundary node points the number of the equations, including $f_{n,0}$,

$f_{p,0}$, $f_{\psi,0}$, $f_{n,N}$, $f_{p,N}$, and $f_{\psi,N}$, are 6. Therefore, with the 3(N+1) unknowns and 3(N+1) equations the system of nonlinear algebraic equations can be computed self-consistently. The solution of the unknown dependent variables n_j, p_j, and ψ_j is arranged together as a column matrix **x**, while the discrete functions $f_{n,j}$, $f_{p,j}$, and $f_{\psi,j}$ is also arranged as a column matrix **F**:

$$\mathbf{x} = \begin{bmatrix} \bar{n}_0 \\ \bar{p}_0 \\ \bar{\psi}_0 \\ \vdots \\ \bar{n}_j \\ \bar{p}_j \\ \bar{\psi}_j \\ \vdots \\ \bar{n}_N \\ \bar{p}_N \\ \bar{\psi}_N \end{bmatrix}, \qquad \mathbf{F} = \begin{bmatrix} f_{n,0} \\ f_{p,0} \\ f_{\psi,0} \\ \vdots \\ f_{n,j} \\ f_{p,j} \\ f_{\psi,j} \\ \vdots \\ f_{n,N} \\ f_{p,N} \\ f_{\psi,N} \end{bmatrix}. \tag{5.2.1}$$

The system of the discrete nonlinear algebraic equations is expressed as

$$\mathbf{F}(\mathbf{x}) = 0. \tag{5.2.2}$$

In general, only iterative methods are applicable for the solution of Equation (5.2.2). The multi-variable Newton's method is adopted to implement the calculation [90, 91]. The solution for the iterative method is given as

$$\mathbf{x}^{k+1} = \mathbf{x}^k - \mathbf{J}\left(\mathbf{x}^k\right)^{-1} \cdot \mathbf{F}\left(\mathbf{x}^k\right), \tag{5.2.3}$$

in which **J** is the Jacobian matrix, and k (= 0, 1, 2,…) is the iterative step. In order to avoid the expensive inversion of **J** we use instead:

$$\mathbf{J}\left(\mathbf{x}^k\right) \cdot \Delta\mathbf{x}^k = -\mathbf{F}(\mathbf{x}^k), \tag{5.2.4}$$

$$\mathbf{x}^{k+1} = \mathbf{x}^{k} + \mathbf{\Delta x}^{k}. \tag{5.2.5}$$

First, for $k = 0$ the initial guess $\mathbf{x}^0$ is given, and then $\mathbf{F}(\mathbf{x}^0)$ and $\mathbf{J}(\mathbf{x}^0)$ are computed. Second, solve Equation (5.2.4) to obtain $\mathbf{\Delta x}^0$, and then update the solution $\mathbf{x}^1$ by using Equation (5.2.5). For $k = 1$, compute $\mathbf{F}(\mathbf{x}^1)$ and $\mathbf{J}(\mathbf{x}^1)$, solve Equation (5.2.4) again, and update the solution $\mathbf{x}^2$. Repeat the iteration until the termination criterion is reached, and thus the numerical solution of Equation (5.2.2) is obtained as $\mathbf{x}^{k+1}$. Assume that the termination criterion is in terms of the norm value of $\mathbf{F}$,

$$\left\| \mathbf{F}\left(\mathbf{x}^{k+1}\right) \right\| < \delta_{ter}, \tag{5.2.6}$$

where the small value of δ_{ter} is the proper chosen absolute accuracy. The Jacobian matrix $\mathbf{J}$ is given as

$$
\begin{bmatrix}
\ddots & & & & & & & & \\
\frac{\partial f_{n,j-1}}{\partial \bar{n}_{j-1}} & \frac{\partial f_{n,j-1}}{\partial \bar{p}_{j-1}} & \frac{\partial f_{n,j-1}}{\partial \bar{\psi}_{j-1}} & \frac{\partial f_{n,j-1}}{\partial \bar{n}_{j}} & \frac{\partial f_{n,j-1}}{\partial \bar{p}_{j}} & \frac{\partial f_{n,j-1}}{\partial \bar{\psi}_{j}} & 0 & 0 & 0 \\
\frac{\partial f_{p,j-1}}{\partial \bar{n}_{j-1}} & \frac{\partial f_{p,j-1}}{\partial \bar{p}_{j-1}} & \frac{\partial f_{p,j-1}}{\partial \bar{\psi}_{j-1}} & \frac{\partial f_{p,j-1}}{\partial \bar{n}_{j}} & \frac{\partial f_{p,j-1}}{\partial \bar{p}_{j}} & \frac{\partial f_{p,j-1}}{\partial \bar{\psi}_{j}} & 0 & 0 & 0 \\
\frac{\partial f_{\psi,j-1}}{\partial \bar{n}_{j-1}} & \frac{\partial f_{\psi,j-1}}{\partial \bar{p}_{j-1}} & \frac{\partial f_{\psi,j-1}}{\partial \bar{\psi}_{j-1}} & \frac{\partial f_{\psi,j-1}}{\partial \bar{n}_{j}} & \frac{\partial f_{\psi,j-1}}{\partial \bar{p}_{j}} & \frac{\partial f_{\psi,j-1}}{\partial \bar{\psi}_{j}} & 0 & 0 & 0 \\
\frac{\partial f_{n,j}}{\partial \bar{n}_{j-1}} & \frac{\partial f_{n,j}}{\partial \bar{p}_{j-1}} & \frac{\partial f_{n,j}}{\partial \bar{\psi}_{j-1}} & \frac{\partial f_{n,j}}{\partial \bar{n}_{j}} & \frac{\partial f_{n,j}}{\partial \bar{p}_{j}} & \frac{\partial f_{n,j}}{\partial \bar{\psi}_{j}} & \frac{\partial f_{n,j}}{\partial \bar{n}_{j+1}} & \frac{\partial f_{n,j}}{\partial \bar{p}_{j+1}} & \frac{\partial f_{n,j}}{\partial \bar{\psi}_{j+1}} \\
\frac{\partial f_{p,j}}{\partial \bar{n}_{j-1}} & \frac{\partial f_{p,j}}{\partial \bar{p}_{j-1}} & \frac{\partial f_{p,j}}{\partial \bar{\psi}_{j-1}} & \frac{\partial f_{p,j}}{\partial \bar{n}_{j}} & \frac{\partial f_{p,j}}{\partial \bar{p}_{j}} & \frac{\partial f_{p,j}}{\partial \bar{\psi}_{j}} & \frac{\partial f_{p,j}}{\partial \bar{n}_{j+1}} & \frac{\partial f_{p,j}}{\partial \bar{p}_{j+1}} & \frac{\partial f_{p,j}}{\partial \bar{\psi}_{j+1}} \\
\frac{\partial f_{\psi,j}}{\partial \bar{n}_{j-1}} & \frac{\partial f_{\psi,j}}{\partial \bar{p}_{j-1}} & \frac{\partial f_{\psi,j}}{\partial \bar{\psi}_{j-1}} & \frac{\partial f_{\psi,j}}{\partial \bar{n}_{j}} & \frac{\partial f_{\psi,j}}{\partial \bar{p}_{j}} & \frac{\partial f_{\psi,j}}{\partial \bar{\psi}_{j}} & \frac{\partial f_{\psi,j}}{\partial \bar{n}_{j+1}} & \frac{\partial f_{\psi,j}}{\partial \bar{p}_{j+1}} & \frac{\partial f_{\psi,j}}{\partial \bar{\psi}_{j+1}} \\
0 & 0 & 0 & \frac{\partial f_{n,j+1}}{\partial \bar{n}_{j}} & \frac{\partial f_{n,j+1}}{\partial \bar{p}_{j}} & \frac{\partial f_{n,j+1}}{\partial \bar{\psi}_{j}} & \frac{\partial f_{n,j+1}}{\partial \bar{n}_{j+1}} & \frac{\partial f_{n,j+1}}{\partial \bar{p}_{j+1}} & \frac{\partial f_{n,j+1}}{\partial \bar{\psi}_{j+1}} \\
0 & 0 & 0 & \frac{\partial f_{p,j+1}}{\partial \bar{n}_{j}} & \frac{\partial f_{p,j+1}}{\partial \bar{p}_{j}} & \frac{\partial f_{p,j+1}}{\partial \bar{\psi}_{j}} & \frac{\partial f_{p,j+1}}{\partial \bar{n}_{j+1}} & \frac{\partial f_{p,j+1}}{\partial \bar{p}_{j+1}} & \frac{\partial f_{p,j+1}}{\partial \bar{\psi}_{j+1}} \\
0 & 0 & 0 & \frac{\partial f_{\psi,j+1}}{\partial \bar{n}_{j}} & \frac{\partial f_{\psi,j+1}}{\partial \bar{p}_{j}} & \frac{\partial f_{\psi,j+1}}{\partial \bar{\psi}_{j}} & \frac{\partial f_{\psi,j+1}}{\partial \bar{n}_{j+1}} & \frac{\partial f_{\psi,j+1}}{\partial \bar{p}_{j+1}} & \frac{\partial f_{\psi,j+1}}{\partial \bar{\psi}_{j+1}} \\
 & & & & & & & & \ddots
\end{bmatrix} \tag{5.2.7}
$$

Since the function values at the node point j are only related to the values of the dependent variables at the node point j and the nearest neighbor node points j-1 and j+1, the Jacobian matrix **J** is a band-diagonal matrix. For convenience, the parameters are defined as

$$\varphi_1 = \frac{\bar{\psi}_{j+1} - \bar{\psi}_j}{\bar{V}_t}, \qquad \varphi_2 = \frac{\bar{\psi}_j - \bar{\psi}_{j-1}}{\bar{V}_t}, \tag{5.2.8}$$

and the derivative of Be(x) is defined as

$$\mathrm{DB}(x) = \frac{d\,\mathrm{Be}(x)}{dx}. \tag{5.2.9}$$

For to the node points inside the boundary, i.e., $j = 1, 2, \ldots, N\text{-}1$, the elements of **J** are given as

$$\frac{\partial f_{n,j}}{\partial \bar{n}_j} = -\frac{1}{\bar{h}_{j-1}}\left[\mathrm{Be}(\varphi_2) + \left(\delta_{n,j-1/2} + \left(\bar{n}_j - \bar{n}_{j-1}\right)\frac{\partial \delta_{n,j-1/2}}{\partial \bar{n}_j}\right)\mathrm{Be}(\varphi_2)\exp\left(\frac{\varphi_2}{2}\right)\right]$$
$$-\frac{1}{\bar{h}_j}\left[\mathrm{Be}(-\varphi_1) + \left(\delta_{n,j+1/2} + \left(\bar{n}_j - \bar{n}_{j+1}\right)\right)\frac{\partial \delta_{n,j+1/2}}{\partial \bar{n}_j}\mathrm{Be}(\varphi_1)\exp\left(\frac{\varphi_1}{2}\right)\right] \quad (5.2.10)$$
$$+\frac{\bar{h}_j + \bar{h}_{j-1}}{2}\frac{\partial\left(\bar{G}_j - \bar{R}_j\right)}{\partial \bar{n}_j},$$

$$\frac{\partial f_{n,j}}{\partial \bar{n}_{j-1}} = \frac{1}{\bar{h}_{j-1}}\left[\mathrm{Be}(-\varphi_2) + \left(\delta_{n,j-1/2} + \left(\bar{n}_{j-1} - \bar{n}_j\right)\frac{\partial \delta_{n,j-1/2}}{\partial \bar{n}_{j-1}}\right)\mathrm{Be}(\varphi_2)\exp\left(\frac{\varphi_2}{2}\right)\right], \quad (5.2.11)$$

$$\frac{\partial f_{n,j}}{\partial \bar{n}_{j+1}} = \frac{1}{\bar{h}_j}\left[\mathrm{Be}(\varphi_1) + \left(\delta_{n,j+1/2} + \left(\bar{n}_{j+1} - \bar{n}_j\right)\frac{\partial \delta_{n,j+1/2}}{\partial \bar{n}_{j+1}}\right)\mathrm{Be}(\varphi_1)\exp\left(\frac{\varphi_1}{2}\right)\right], \quad (5.2.12)$$

$$\frac{\partial f_{p,j}}{\partial \bar{p}_j} = -\frac{1}{\bar{h}_{j-1}}\left[\mathrm{Be}(-\varphi_2) + \left(\delta_{p,j-1/2} + \left(\bar{p}_j - \bar{p}_{j-1}\right)\frac{\partial \delta_{p,j-1/2}}{\partial \bar{p}_j}\right)\mathrm{Be}(-\varphi_2)\exp\left(\frac{-\varphi_2}{2}\right)\right]$$
$$-\frac{1}{\bar{h}_j}\left[\mathrm{Be}(\varphi_1) + \left(\delta_{p,j+1/2} + \left(\bar{p}_j - \bar{p}_{j+1}\right)\right)\frac{\partial \delta_{p,j+1/2}}{\partial \bar{p}_j}\mathrm{Be}(-\varphi_1)\exp\left(\frac{-\varphi_1}{2}\right)\right] \quad (5.2.13)$$
$$+\frac{\bar{h}_j + \bar{h}_{j-1}}{2}\frac{\partial\left(\bar{G}_j - \bar{R}_j\right)}{\partial \bar{p}_j},$$

$$\frac{\partial f_{p,j}}{\partial \bar{p}_{j-1}} = \frac{1}{\bar{h}_{j-1}}\left[\mathrm{Be}(\varphi_2) + \left(\delta_{p,j-1/2} + \left(\bar{p}_{j-1} - \bar{p}_j\right)\frac{\partial \delta_{p,j-1/2}}{\partial \bar{p}_{j-1}}\right)\mathrm{Be}(-\varphi_2)\exp\left(\frac{-\varphi_2}{2}\right)\right], \quad (5.2.14)$$

$$\frac{\partial f_{p,j}}{\partial \bar{p}_{j+1}} = \frac{1}{\bar{h}_j}\left[\mathrm{Be}(-\varphi_1) + \left(\delta_{p,j+1/2} + \left(\bar{p}_{j+1} - \bar{p}_j\right)\frac{\partial \delta_{p,j+1/2}}{\partial \bar{p}_{j+1}}\right)\mathrm{Be}(-\varphi_1)\exp\left(\frac{-\varphi_1}{2}\right)\right], \quad (5.2.15)$$

$$\frac{\partial f_{n,j}}{\partial \bar{p}_j} = \frac{\bar{h}_j + \bar{h}_{j-1}}{2}\frac{\partial\left(\bar{G}_j - \bar{R}_j\right)}{\partial \bar{p}_j}, \quad (5.2.16)$$

$$\frac{\partial f_{p,j}}{\partial \bar{n}_j} = \frac{\bar{h}_j + \bar{h}_{j-1}}{2} \frac{\partial \left(\bar{G}_j - \bar{R}_j \right)}{\partial \bar{n}_j}, \tag{5.2.17}$$

$$\frac{\partial f_{\psi,j}}{\partial \bar{\psi}_j} = 1, \tag{5.2.18}$$

$$\frac{\partial f_{\psi,j}}{\partial \bar{n}_j} = \frac{eC_{nor}}{CV_{nor}}, \tag{5.2.19}$$

$$\frac{\partial f_{\psi,j}}{\partial \bar{p}_j} = -\frac{eC_{nor}}{CV_{nor}}, \tag{5.2.20}$$

$$\begin{aligned}
\frac{\partial f_{n,j}}{\partial \bar{\psi}_j} = & \frac{\bar{n}_{j-1}}{\bar{V}_t \bar{h}_{j-1}} \left[-\mathrm{DB}\left(-\varphi_2\right) + \delta_{n,j-1/2} \left(\mathrm{DB}\left(\varphi_2\right) + \frac{1}{2}\mathrm{Be}\left(\varphi_2\right) \right) \exp\left(\frac{\varphi_2}{2} \right) \right] \\
& - \frac{\bar{n}_j}{\bar{V}_t \bar{h}_{j-1}} \left[\mathrm{DB}\left(\varphi_2\right) + \delta_{n,j-1/2} \left(\mathrm{DB}\left(\varphi_2\right) + \frac{1}{2}\mathrm{Be}\left(\varphi_2\right) \right) \exp\left(\frac{\varphi_2}{2} \right) \right] \\
& - \frac{\bar{n}_j}{\bar{V}_t \bar{h}_j} \left[\mathrm{DB}\left(-\varphi_1\right) + \delta_{n,j+1/2} \left(-\mathrm{DB}\left(\varphi_1\right) - \frac{1}{2}\mathrm{Be}\left(\varphi_1\right) \right) \exp\left(\frac{\varphi_1}{2} \right) \right] \\
& + \frac{\bar{n}_{j+1}}{\bar{V}_t \bar{h}_j} \left[-\mathrm{DB}\left(\varphi_1\right) + \delta_{n,j+1/2} \left(-\mathrm{DB}\left(\varphi_1\right) - \frac{1}{2}\mathrm{Be}\left(\varphi_1\right) \right) \exp\left(\frac{\varphi_1}{2} \right) \right],
\end{aligned} \tag{5.2.21}$$

$$\begin{aligned}
\frac{\partial f_{n,j}}{\partial \bar{\psi}_{j-1}} = & \frac{\bar{n}_{j-1}}{\bar{V}_t \bar{h}_{j-1}} \left[\mathrm{DB}\left(-\varphi_2\right) + \delta_{n,j-1/2} \left(-\mathrm{DB}\left(\varphi_2\right) - \frac{1}{2}\mathrm{Be}\left(\varphi_2\right) \right) \exp\left(\frac{\varphi_2}{2} \right) \right] \\
& - \frac{\bar{n}_j}{\bar{V}_t \bar{h}_{j-1}} \left[-\mathrm{DB}\left(\varphi_2\right) + \delta_{n,j-1/2} \left(-\mathrm{DB}\left(\varphi_2\right) - \frac{1}{2}\mathrm{Be}\left(\varphi_2\right) \right) \exp\left(\frac{\varphi_2}{2} \right) \right],
\end{aligned} \tag{5.2.22}$$

$$\begin{aligned}
\frac{\partial f_{n,j}}{\partial \bar{\psi}_{j+1}} = & -\frac{\bar{n}_j}{\bar{V}_t \bar{h}_j} \left[-\mathrm{DB}\left(-\varphi_1\right) + \delta_{n,j+1/2} \left(\mathrm{DB}\left(\varphi_1\right) + \frac{1}{2}\mathrm{Be}\left(\varphi_1\right) \right) \exp\left(\frac{\varphi_1}{2} \right) \right] \\
& + \frac{\bar{n}_{j+1}}{\bar{V}_t \bar{h}_j} \left[\mathrm{DB}\left(\varphi_1\right) + \delta_{n,j+1/2} \left(\mathrm{DB}\left(\varphi_1\right) + \frac{1}{2}\mathrm{Be}\left(\varphi_1\right) \right) \exp\left(\frac{\varphi_1}{2} \right) \right],
\end{aligned} \tag{5.2.23}$$

$$\begin{aligned}\frac{\partial f_{p,j}}{\partial \bar{\psi}_j} &= \frac{\bar{p}_{j-1}}{\bar{V}_t \bar{h}_{j-1}}\left[\mathrm{DB}(\varphi_2)+\delta_{p,j-1/2}\left(-\mathrm{DB}(-\varphi_2)-\frac{1}{2}\mathrm{Be}(-\varphi_2)\right)\exp\left(\frac{-\varphi_2}{2}\right)\right] \\ &\quad -\frac{\bar{p}_j}{\bar{V}_t \bar{h}_{j-1}}\left[-\mathrm{DB}(-\varphi_2)+\delta_{p,j-1/2}\left(-\mathrm{DB}(-\varphi_2)-\frac{1}{2}\mathrm{Be}(-\varphi_2)\right)\exp\left(\frac{-\varphi_2}{2}\right)\right] \\ &\quad -\frac{\bar{p}_j}{\bar{V}_t \bar{h}_j}\left[-\mathrm{DB}(\varphi_1)+\delta_{p,j+1/2}\left(\mathrm{DB}(-\varphi_1)+\frac{1}{2}\mathrm{Be}(-\varphi_1)\right)\exp\left(\frac{-\varphi_1}{2}\right)\right] \\ &\quad +\frac{\bar{p}_{j+1}}{\bar{V}_t \bar{h}_j}\left[\mathrm{DB}(-\varphi_1)+\delta_{p,j+1/2}\left(\mathrm{DB}(-\varphi_1)+\frac{1}{2}\mathrm{Be}(-\varphi_1)\right)\exp\left(\frac{-\varphi_1}{2}\right)\right],\end{aligned} \tag{5.2.24}$$

$$\begin{aligned}\frac{\partial f_{p,j}}{\partial \bar{\psi}_{j-1}} &= \frac{\bar{p}_{j-1}}{\bar{V}_t \bar{h}_{j-1}}\left[-\mathrm{DB}(\varphi_2)+\delta_{p,j-1/2}\left(\mathrm{DB}(-\varphi_2)+\frac{1}{2}\mathrm{Be}(-\varphi_2)\right)\exp\left(\frac{-\varphi_2}{2}\right)\right] \\ &\quad -\frac{\bar{p}_j}{\bar{V}_t \bar{h}_{j-1}}\left[\mathrm{DB}(-\varphi_2)+\delta_{p,j-1/2}\left(\mathrm{DB}(-\varphi_2)+\frac{1}{2}\mathrm{Be}(-\varphi_2)\right)\exp\left(\frac{-\varphi_2}{2}\right)\right],\end{aligned} \tag{5.2.25}$$

$$\begin{aligned}\frac{\partial f_{p,j}}{\partial \bar{\psi}_{j+1}} &= -\frac{\bar{p}_j}{\bar{V}_t \bar{h}_j}\left[\mathrm{DB}(\varphi_1)+\delta_{p,j+1/2}\left(-\mathrm{DB}(-\varphi_1)-\frac{1}{2}\mathrm{Be}(-\varphi_1)\right)\exp\left(\frac{-\varphi_1}{2}\right)\right] \\ &\quad +\frac{\bar{p}_{j+1}}{\bar{V}_t \bar{h}_j}\left[-\mathrm{DB}(-\varphi_1)+\delta_{p,j+1/2}\left(-\mathrm{DB}(-\varphi_1)-\frac{1}{2}\mathrm{Be}(-\varphi_1)\right)\exp\left(\frac{-\varphi_1}{2}\right)\right],\end{aligned} \tag{5.2.26}$$

and the other elements are zero,

$$\begin{aligned}&\frac{\partial f_{n,j}}{\partial \bar{p}_{j-1}} = \frac{\partial f_{n,j}}{\partial \bar{p}_{j+1}} = \frac{\partial f_{p,j}}{\partial \bar{n}_{j-1}} = \frac{\partial f_{p,j}}{\partial \bar{n}_{j+1}} = 0, \\ &\frac{\partial f_{\psi,j}}{\partial \bar{\psi}_{j-1}} = \frac{\partial f_{\psi,j}}{\partial \bar{\psi}_{j+1}} = \frac{\partial f_{\psi,j}}{\partial \bar{n}_{j-1}} = \frac{\partial f_{\psi,j}}{\partial \bar{n}_{j+1}} = \frac{\partial f_{\psi,j}}{\partial \bar{p}_{j-1}} = \frac{\partial f_{\psi,j}}{\partial \bar{p}_{j+1}} = 0.\end{aligned} \tag{5.2.27}$$

The terms in the foregoing equations are given as

$$\begin{aligned}\frac{\partial \delta_{n,j+1/2}}{\partial \bar{n}_j} &= \frac{\partial \bar{n}_{j+1/2}}{\partial \bar{n}_j}\frac{\partial \delta_{n,j+1/2}}{\partial \bar{n}_{j+1/2}} \\ &= \frac{1}{1+\exp\left(\frac{-\varphi_1}{2}\right)}\left(\frac{C_{nor}}{N_c}\right)\left(A_1+4A_2\zeta_{n,j+1/2}+9A_3{\zeta_{n,j+1/2}}^2+16A_4{\zeta_{n,j+1/2}}^3\right),\end{aligned} \tag{5.2.28}$$

$$\frac{\partial \delta_{n,j+1/2}}{\partial \bar{n}_{j+1}} = \frac{\partial \bar{n}_{j+1/2}}{\partial \bar{n}_{j+1}} \frac{\partial \delta_{n,j+1/2}}{\partial \bar{n}_{j+1/2}}$$
$$= \frac{1}{1+\exp\left(\frac{\varphi_1}{2}\right)} \left(\frac{C_{nor}}{N_c}\right) \left(A_1 + 4A_2\zeta_{n,j+1/2} + 9A_3{\zeta_{n,j+1/2}}^2 + 16A_4{\zeta_{n,j+1/2}}^3\right), \quad (5.2.29)$$

in which

$$\zeta_{n,j+1/2} = \bar{n}_{j+1/2}\left(\frac{C_{nor}}{N_c}\right). \quad (5.2.30)$$

By replacing j by j-1, the terms of $\frac{\partial \delta_{n,j-1/2}}{\partial \bar{n}_{j-1}}$ and $\frac{\partial \delta_{n,j-1/2}}{\partial \bar{n}_j}$ can be obtained, too. Similarly,

$$\frac{\partial \delta_{p,j+1/2}}{\partial \bar{p}_j} = \frac{\partial \bar{p}_{j+1/2}}{\partial \bar{p}_j} \frac{\partial \delta_{p,j+1/2}}{\partial \bar{p}_{j+1/2}}$$
$$= \frac{1}{1+\exp\left(\frac{\varphi_1}{2}\right)} \left(\frac{C_{nor}}{N_c}\right) \left(A_1 + 4A_2\zeta_{p,j+1/2} + 9A_3{\zeta_{p,j+1/2}}^2 + 16A_4{\zeta_{p,j+1/2}}^3\right), \quad (5.2.31)$$

$$\frac{\partial \delta_{p,j+1/2}}{\partial \bar{p}_{j+1}} = \frac{\partial \bar{p}_{j+1/2}}{\partial \bar{p}_{j+1}} \frac{\partial \delta_{p,j+1/2}}{\partial \bar{p}_{j+1/2}}$$
$$= \frac{1}{1+\exp\left(\frac{-\varphi_1}{2}\right)} \left(\frac{C_{nor}}{N_c}\right) \left(A_1 + 4A_2\zeta_{p,j+1/2} + 9A_3{\zeta_{p,j+1/2}}^2 + 16A_4{\zeta_{p,j+1/2}}^3\right), \quad (5.2.32)$$

in which

$$\zeta_{p,j+1/2} = \bar{p}_{j+1/2}\left(\frac{C_{nor}}{N_c}\right). \quad (5.2.33)$$

By replacing j by j-1, the terms of $\frac{\partial \delta_{p,j-1/2}}{\partial \bar{p}_{j-1}}$ and $\frac{\partial \delta_{p,j-1/2}}{\partial \bar{p}_j}$ can be obtained, too.

The exciton formation is neglected, and thus $G_j = 0$. The derivative terms related to the carrier recombination rates are given as

$$\begin{cases} \dfrac{\partial \bar{R}_j}{\partial \bar{n}_j} = \dfrac{\partial \bar{R}_{r,j}}{\partial \bar{n}_j} + \dfrac{\partial \bar{R}_{nr,j}}{\partial \bar{n}_j}, \\ \dfrac{\partial \bar{R}_j}{\partial \bar{p}_j} = \dfrac{\partial \bar{R}_{r,j}}{\partial \bar{p}_j} + \dfrac{\partial \bar{R}_{nr,j}}{\partial \bar{p}_j}, \end{cases} \tag{5.2.34}$$

$$\frac{\partial \bar{R}_{r,j}}{\partial \bar{n}_j} = \frac{L^2 C_{nor} B_{BBR}}{\mu V_t} \bar{p}_j, \tag{5.2.35}$$

$$\frac{\partial \bar{R}_{r,j}}{\partial \bar{p}_j} = \frac{L^2 C_{nor} B_{BBR}}{\mu V_t} \bar{n}_j, \tag{5.2.36}$$

$$\frac{\partial \bar{R}_{nr,j}}{\partial \bar{n}_j} = \begin{cases} \dfrac{L^2}{\tau_{SRH} \mu V_t} \left(\dfrac{\bar{p}_j + \left(\dfrac{n_i}{C_{nor}} \right)}{\bar{n}_j + \bar{p}_j + 2\left(\dfrac{n_i}{C_{nor}} \right)} \right)^2, & \text{for SRH,} \\ \dfrac{L^2 C_{nor} B_{BBN}}{\mu V_t} \bar{p}_j, & \text{for BBN,} \\ \dfrac{L^2 C_{nor}{}^2 B_{Auger}}{\mu V_t} \left(2\bar{n}_j \bar{p}_j + \bar{p}_j{}^2 - \left(\dfrac{n_i}{C_{nor}} \right)^2 \right), & \text{for Auger.} \end{cases} \tag{5.2.37}$$

$$\frac{\partial \bar{R}_{nr,j}}{\partial \bar{p}_j} = \begin{cases} \dfrac{L^2}{\tau_{SRH} \mu V_t} \left(\dfrac{\bar{n}_j + \left(\dfrac{n_i}{C_{nor}} \right)}{\bar{n}_j + \bar{p}_j + 2\left(\dfrac{n_i}{C_{nor}} \right)} \right)^2, & \text{for SRH,} \\ \dfrac{L^2 C_{nor} B_{BBN}}{\mu V_t} \bar{n}_j, & \text{for BBN,} \\ \dfrac{L^2 C_{nor}{}^2 B_{Auger}}{\mu V_t} \left(2\bar{n}_j \bar{p}_j + \bar{n}_j{}^2 - \left(\dfrac{n_i}{C_{nor}} \right)^2 \right), & \text{for Auger.} \end{cases} \tag{5.2.38}$$

For to the node points at the boundary, i.e., $j = 0$ and $j = N$, the elements of **J** are given as

$$\begin{cases} \dfrac{\partial f_{n,0}}{\partial \bar{n}_0} = 1, & \dfrac{\partial f_{n,N}}{\partial \bar{n}_N} = 1, \\ \dfrac{\partial f_{p,0}}{\partial \bar{p}_0} = 1, & \dfrac{\partial f_{p,N}}{\partial \bar{p}_N} = 1, \\ \dfrac{\partial f_{\psi,0}}{\partial \bar{\psi}_0} = 1, & \dfrac{\partial f_{\psi,N}}{\partial \bar{\psi}_N} = 1, \end{cases} \tag{5.2.39}$$

and the other elements are zero.

The derivative of the Bernoulli function has to be implemented carefully for numerical computation. The derivative of Be(x) is given as [91]

$$\mathrm{DB}(x) = \frac{d\,\mathrm{Be}(x)}{dx} = \mathrm{Be}(x) \cdot \frac{1 - \mathrm{Be}(-x)}{x}. \tag{5.2.40}$$

In order to solve Equation (5.2.4) efficiently, the elements of the band-diagonal matrix **J** is stored by a compact form to save the memory, and the library of the band-diagonal solver is used to calculate the results of $\mathbf{\Delta x}^{\mathrm{k}}$ [93].

After the numerical solution **x** of the system of the discrete nonlinear algebraic equations of Equation (5.2.2) is obtained, the discrete values at the node point j of the dependent variables including the electron density n_{j}, hole density p_{j}, and CNT potential ψ_{j} are immediately obtained. Therefore, the profiles of $n(x)$, $p(x)$, and $\psi(x)$ can be illustrated. The discrete electron and hole currents $I_{\mathrm{n,j}}$ and $I_{\mathrm{p,j}}$ at the node point j can be obtained by Equations (5.1.19) and (5.1.34), and then the carrier current profiles of $I_{\mathrm{n}}(x)$ and $I_{\mathrm{p}}(x)$ can be depicted. Thus the total device current I is obtained as $I_{\mathrm{n}}+I_{\mathrm{p}}$. Moreover, the discrete nonradiative recombination rate $R_{\mathrm{nr,j}}$ is calculated by using Equation (5.1.45) for various recombination mechanism, such as SRH, BBN, and Auger recombination. For light emission generated by band-to-band radiative recombination (BBR) of electrons and holes, the discrete radiative recombination rate $R_{\mathrm{r,j}}$ is calculated as $B_{BBR}(n_{\mathrm{j}}p_{\mathrm{j}}-n_i^2)$, and

then the emitted optical power P_{opt} is calculated as $E_g \int_0^L R_r(x)dx$, in which E_g is the band-gap of the carbon nanotube. Therefore, the profiles of $R_r(x)$ and $R_{nr}(x)$ can be obtained. Furthermore, the profile of the longitudinal electric field, the position of light emission, and emitted light-spot size can be obtained, too.

5.3 Numerical Approach for Photodetectors Based on CNT FETs Including Exciton Generation

In photodetectors based on CNTs, excitonic transitions dominate their optical absorption spectra, as mentioned above. After the excitons are generated from photoexcitation, the excitons would ionize to free e-h pairs that are separated by the applied field. With an applied drain-to-source voltage both electrons and holes are collected at two contacts, and thus produce a photocurrent. The excitons also decay radiatively and nonradiatively. The radiative decay will emitted the infrared light. The forgoing mechanisms involve the continuity differential equation of the singlet excitons in carbon nanotubes, shown in Equation (3.7.2). The numerical approach to solve the exciton continuity differential equation coupled with the electron and hole continuity differential equations will study in the following. The finite difference method is used to derive the discrete algebraic equations for the continuity differential equation of the singlet excitons in Equation (3.7.2) [90]. In the steady state the finite difference is applied to the differential operator for the node points inside the boundary, i.e., j = 1, 2,…, N-1,

$$G_{\mathrm{x,j}} + B_{\mathrm{x}} n_j p_j - r_{\mathrm{d}} n_{\mathrm{xs,j}} - \left(r_{\mathrm{r}} + r_{\mathrm{nr}}\right) n_{\mathrm{xs,j}} + D_x \left(\frac{\frac{n_{\mathrm{xs,j+1}} - n_{\mathrm{xs,j}}}{h_j} - \frac{n_{\mathrm{xs,j}} - n_{\mathrm{xs,j-1}}}{h_{j-1}}}{\frac{1}{2}\left(h_j + h_{j-1}\right)} \right) = 0. \quad (5.3.1)$$

By choosing the values of C_{xnor} [cm^{-1}], the normalized form of exciton density is introduced as

$$\bar{n}_{xs,j} = \frac{n_{xs,j}}{C_{xnor}}. \quad (5.3.2)$$

Moreover, D_{xm} [$\mathrm{cm}^2\ \mathrm{s}^{-1}$] is assumed as a nonzero value. Equation (5.3.1) is multiplied by $\frac{\left(h_j + h_{j-1}\right)L}{2C_{xnor}D_{xm}}$ to obtain the normalized algebraic equations $f_{\mathrm{s,j}}$ of singlet excitons, which is expressed as

$$\begin{aligned} f_{s,j} = {} & \bar{n}_{xs,j+1}\left(\frac{D_x}{\bar{h}_j D_{xm}}\right) - \bar{n}_{xs,j}\left(\frac{1}{\bar{h}_j} + \frac{1}{\bar{h}_{j-1}}\right)\left(\frac{D_x}{D_{xm}}\right) + \bar{n}_{xs,j-1}\left(\frac{D_x}{\bar{h}_{j-1} D_{xm}}\right) \\ & - \bar{n}_{xs,j}\left(\frac{\left(\bar{h}_j + \bar{h}_{j-1}\right)L^2\left(r_d + r_r + r_{nr}\right)}{2D_{xm}}\right) + \bar{n}_j \bar{p}_j \left(\frac{\left(\bar{h}_j + \bar{h}_{j-1}\right)L^2 C_{nor}{}^2 B_x}{2C_{xnor}D_{xm}}\right) \\ & + \frac{\left(\bar{h}_j + \bar{h}_{j-1}\right)L^2 G_{x,j}}{2C_{xnor}D_{xm}} \\ = {} & 0. \qquad\qquad j = 1, 2, ..., N-1. \end{aligned} \quad (5.3.3)$$

If the exciton diffusion is neglected, i.e., $D_{\mathrm{x}} = 0$, the first three terms in the right-hand side are vanished. The term D_{xm} is introduced in order to avoid the singularity, which can be divided by zero if D_{x} appears in the denominator. In our study the incident light shines the part of the CNT channel but does not shine the contacts. Thus the normalized discrete equations of the boundary conditions for the excitons at the node points $j = 0$ and N are given as

$$f_{s,0} = \bar{n}_{xs,0} = 0,$$
$$f_{s,N} = \bar{n}_{xs,N} = 0. \tag{5.3.4}$$

In the photodetectors the excitons ionize to free *e*-*h* pairs, the exciton ionization rate is the generation rate of electrons and holes, which is given as $r_d n_{xs}$. Another generation rate of the free *e*-*h* pairs by the interband transition through the phtoexcitation is given as G_{bb}, as mentioned above. Therefore, the total generation rate G of electrons and holes is given as

$$G = r_d n_{xs} + G_{bb}. \tag{5.3.5}$$

The discrete value at the node point j is given as

$$G_j = r_d n_{xs,j} + G_{bb,j}. \tag{5.3.6}$$

The normalized form is given as

$$\bar{G}_j = \frac{L^2 G_j}{C_{nor}\mu V_t} = \frac{L^2}{C_{nor}\mu V_t}\left(r_d C_{xnor}\bar{n}_{xs,j} + G_{bb,j}\right). \tag{5.3.7}$$

The recombination of electrons and holes involves the exciton formation, and the recombination rate R of electrons and holes is given as

$$R = B_x np. \tag{5.3.8}$$

The discrete value at the node point j is given as

$$R_j = B_x n_j p_j. \tag{5.3.9}$$

The normalized form is given as

$$\bar{R}_j = \frac{L^2 R_j}{C_{nor}\mu V_t} = \frac{L^2 C_{nor} B_x}{\mu V_t}\bar{n}_j \bar{p}_j. \tag{5.3.10}$$

The discretization of the differential equations yields a system of nonlinear algebraic equations with the values of dependent variables at the discrete node points j =

0, 1,…, N-1, N. The total number of the discrete unknown variables ψ, n, p, and n_{xs} are 4(N+1). Inside the boundary the number of the discrete equations of $f_{n,j}$, $f_{p,j}$, $f_{\psi,j}$, and $f_{s,j}$ are 4(N-1), while at the boundary node points the number of the equations, including $f_{n,0}$, $f_{p,0}$, $f_{\psi,0}$, $f_{n,N}$, $f_{p,N}$, $f_{\psi,N}$, $f_{s,0}$, and $f_{s,N}$ are 8. Therefore, with the 4(N+1) unknowns and 4(N+1) equations the system of nonlinear algebraic equations can be computed self-consistently. The solution of the unknown dependent variables n_j, p_j, ψ_j, and $n_{xs,j}$ is rearranged together as a column matrix **x**, while the discrete functions $f_{n,j}$, $f_{p,j}$, $f_{\psi,j}$, and $f_{s,j}$ is also rearranged as a column matrix **F**:

$$\mathbf{x} = \begin{bmatrix} \bar{n}_0 \\ \bar{p}_0 \\ \bar{\psi}_0 \\ \bar{n}_{xs,0} \\ \vdots \\ \bar{n}_j \\ \bar{p}_j \\ \bar{\psi}_j \\ \bar{n}_{xs,j} \\ \vdots \\ \bar{n}_N \\ \bar{p}_N \\ \bar{\psi}_N \\ \bar{n}_{xs,N} \end{bmatrix}, \qquad \mathbf{F} = \begin{bmatrix} f_{n,0} \\ f_{p,0} \\ f_{\psi,0} \\ f_{s,0} \\ \vdots \\ f_{n,j} \\ f_{p,j} \\ f_{\psi,j} \\ f_{s,j} \\ \vdots \\ f_{n,N} \\ f_{p,N} \\ f_{\psi,N} \\ f_{s,N} \end{bmatrix}. \tag{5.3.11}$$

The Jacobian matrix is **J** given as

$$\mathbf{J}=\begin{bmatrix} \ddots & & & & \\ & \frac{\partial f_{n,j}}{\partial \bar{n}_j} & \frac{\partial f_{n,j}}{\partial \bar{p}_j} & \frac{\partial f_{n,j}}{\partial \bar{\psi}_j} & \frac{\partial f_{n,j}}{\partial \bar{n}_{xs,j}} \\ & \frac{\partial f_{p,j}}{\partial \bar{n}_j} & \frac{\partial f_{p,j}}{\partial \bar{p}_j} & \frac{\partial f_{p,j}}{\partial \bar{\psi}_j} & \frac{\partial f_{p,j}}{\partial \bar{n}_{xs,j}} \\ & \frac{\partial f_{\psi,j}}{\partial \bar{n}_j} & \frac{\partial f_{\psi,j}}{\partial \bar{p}_j} & \frac{\partial f_{\psi,j}}{\partial \bar{\psi}_j} & \frac{\partial f_{\psi,j}}{\partial \bar{n}_{xs,j}} \\ & \frac{\partial f_{s,j}}{\partial \bar{n}_j} & \frac{\partial f_{s,j}}{\partial \bar{p}_j} & \frac{\partial f_{s,j}}{\partial \bar{\psi}_j} & \frac{\partial f_{s,j}}{\partial \bar{n}_{xs,j}} \\ & & & & \ddots \end{bmatrix}. \tag{5.3.12}$$

The Jacobian matrix **J** is a band diagonal matrix, too. The elements of the Jacobian matrix for the exciton density are given as

$$\frac{\partial f_{s,j}}{\partial \bar{n}_{xs,j-1}}=\frac{D_x}{\bar{h}_{j-1}D_{xm}}, \tag{5.3.13}$$

$$\frac{\partial f_{s,j}}{\partial \bar{n}_{xs,j}}=-\left(\frac{1}{\bar{h}_j}+\frac{1}{\bar{h}_{j-1}}\right)\left(\frac{D_x}{D_{xm}}\right)-\left(\frac{\left(\bar{h}_j+\bar{h}_{j-1}\right)L^2\left(r_d+r_r+r_{nr}\right)}{2D_{xm}}\right), \tag{5.3.14}$$

$$\frac{\partial f_{s,j}}{\partial \bar{n}_{xs,j+1}}=\frac{D_x}{\bar{h}_j D_{xm}}, \tag{5.3.15}$$

$$\frac{\partial f_{s,j}}{\partial \bar{n}_j}=\bar{p}_j\left(\frac{\left(\bar{h}_j+\bar{h}_{j-1}\right)L^2 {C_{nor}}^2 B_x}{2C_{xnor}D_{xm}}\right), \tag{5.3.16}$$

$$\frac{\partial f_{s,j}}{\partial \bar{p}_j}=\bar{n}_j\left(\frac{\left(\bar{h}_j+\bar{h}_{j-1}\right)L^2 {C_{nor}}^2 B_x}{2C_{xnor}D_{xm}}\right), \tag{5.3.17}$$

$$\frac{\partial f_{s,0}}{\partial \bar{n}_{xs,0}}=1, \qquad \frac{\partial f_{s,N}}{\partial \bar{n}_{xs,N}}=1, \tag{5.3.18}$$

Moreover, the derivative terms related to the generation and recombination rates of electrons and holes are given as

$$\frac{\partial\left(\overline{G}_j - \overline{R}_j\right)}{\partial \overline{n}_j} = -\frac{L^2 C_{nor} B_x}{\mu V_t} \overline{p}_j, \tag{5.3.19}$$

$$\frac{\partial\left(\overline{G}_j - \overline{R}_j\right)}{\partial \overline{p}_j} = -\frac{L^2 C_{nor} B_x}{\mu V_t} \overline{n}_j, \tag{5.3.20}$$

$$\frac{\partial\left(\overline{G}_j - \overline{R}_j\right)}{\partial \overline{n}_{xs,j}} = \frac{L^2 r_d C_{xnor}}{C_{nor} \mu V_t}. \tag{5.3.21}$$

The other elements in the Jacobian matrix **J** are zeros.

Following the same procedure expressed in Chapter 5.2, the numerical solution **x** of the system of the discrete nonlinear algebraic equations of Equation (5.2.2) can be calculated. The discrete values at the node point *j* of the dependent variables including the electron density n_j, hole density p_j, CNT potential ψ_j, and exciton density n_{xs} are immediately obtained. Therefore, the profiles of $n(x)$, $p(x)$, $\psi(x)$, and $n_{xs}(x)$ can be depicted. The electron and hole current profiles of $I_n(x)$ and $I_p(x)$ and the total device current I can be obtained, too. The recombination and generation rates R and G of electrons and holes can be obtained as well.

For photodetectors, the dark current I_{dark} is defined as the device current without illumination, while the device current with illumination is expressed as I_{light}. The photocurrent I_{ph} is defined as the difference between I_{light} and I_{dark}, i.e., $I_{ph} = I_{light} - I_{dark}$ [43, 94, 95]. Since the absorption spectra of CNTs depend on the incident photon energies, and thus the photocurrent spectra in the photodetectors based on CNT FETs depend on the photo-excitation energies [21].

5.4 Conclusion of the Numerical Calculation for Optoelectronic Devices Based on Carbon-Nanotube Field-Effect Transistors

In conclusion, we provide a numerical diffusive-transport approach for the light emission based on band-to-band radiative recombination with various nonradiative recombination mechanisms but neglecting exciton formation. In photodetectors based on CNT FETs, excitonic transitions dominate their optical absorption spectra since electron confinement in the quasi-one-dimensional structure of CNTs leads to the formation of strongly bound exciton states. We provide a numerical diffusive-transport approach for photodetectors in order to solve the exciton continuity equation coupled with the electron and hole continuity equations. Therefore, in numerical approaches the systems of differential equations with boundary conditions are presented for both optical emitters and photodetectors. There are two approaches for the finite differences to obtain the discretized equations; the first is the finite difference method, in which the differential operators are directly replaced by difference operators, and the second is the box integration method, in which the differential equation is integrated over each of the subdomains [90, 91]. The same discretized equations are obtained by both methods. In this study the approach of the box integration method is adopted to derive difference approximations for the electron and hole differential continuity equations, while the approach of finite difference method is applied to the exciton differential continuity equation. The Scharfetter-Gummel approach [90, 92] is adopted for the profile of the interpolation scheme for the electron and hole densities. In the drift-diffusion currents, for large carrier densities the Einstein relation in the degenerate semiconductors can be

approximated as the formula of Kroemer [58], while the Fermi-Dirac integral of order -½ is applied to one-dimensional case by using the similar procedure of Joyce and Dixon [51, 59]. The discretization of the differential equations yields a system of nonlinear algebraic equations, which can be computed self-consistently. The multi-variable Newton's method is adopted to implement the calculation [90, 91]. The explicit forms of the Jacobian matrix related to the electron and hole continuity equations for the degenerate semiconducting CNTs are derived. In order to solve efficiently, the elements of the band-diagonal matrix **J** is stored by a compact form to save the memory, and the library of the band-diagonal solver is used to calculate the results [93]. The interesting electronic and optical properties such as the electron and hole densities, CNT potential, and exciton density can be solved immediately. The other properties such as the device current, recombination rate and emitted optical power for the light emitters and the photocurrent for the photodetectors through the photoexcitation, in turn, can be obtained as well.

CHAPTER 6

RESULTS FOR OPTICAL EMITTERS BASED ON CARBON-NANOTUBE FIELD-EFFECT TRANSISTORS

In optical emitters based on long-channel ambipolar CNT FETs, the area of strong electron–hole recombination, and hence the region of light emission, can be controlled by varying the gate and drain voltages [42, 49]. An analytical model based on diffusive transport and assuming infinite recombination rate for electrons and holes at the same location has been presented and applied to a very long-channel (60 μm) CNT [49]. Due to the neglect of the finite recombination length, the transport characteristics and optical emission within the recombination region were not of immediate concern. Numerical models with diffusive transport and carrier recombination were developed for long-channel devices in order to calculate the emitted light-spot movement [50, 60]. Radiative recombination was assumed to be dominant; however, this assumption is ill justified. The importance of nonradiative recombination is indicated by the low measured quantum efficiency [44]. In order to understand the recombination-mechanism dependence of the transport characteristics and the optical emission of ambipolar CNT FETs more completely, a diffusive-transport model accounting for a radiative and several nonradiative recombination mechanisms was presented above in earlier chapters. Inside the recombination region the carrier densities, radiative recombination rate, and emitted light spot size are here calculated for various recombination mechanisms. The input data for optical emitters based on CNT FETs are given in Chapter 6.1. Chapter 6.2 presents

the analytic results for optical emitters based on CNT FETs, while Chapter 6.3 gives the numerical results [51].

6.1 Calculation for Optical Emitters Based on Carbon-Nanotube Field-Effect Transistors

The ambipolar CNT FET modeled consists of an intrinsic semiconducting single-wall CNT providing a 60 μm long channel, source and drain Schottky contacts composed of Pd [42, 49], and a 100 nm thick SiO_2 gate insulator. Ambipolar FETs operate with one electron injecting (*e*-source) and one hole injecting (*h*-source) contact. The *e*-source contact also acts as the drain for holes (*h*-drain) and the *h*-source contact acts as the drain for electrons (*e*-drain). By using conventional *n*-channel FET terminology, we define the *e*-source as the *source* (S) and *h*-source as the *drain* (D), as mentioned above. The applied gate (G) and drain (D) voltages, V_G and V_D, are measured with respect to the source (S) $V_S = 0$. Electrons are injected from S and accumulate in the CNT near S for positive V_G, while holes are injected from D and accumulate near there for negative V_G-V_D. This defines the ambipolar operating regime. A zigzag (17,0) CNT is chosen in order to compare the calculated results with published experimental data [49]. The CNT diameter d_{cnt} is computed as 1.35 nm by using Equation (2.1.1) with the carbon-carbon bond length $a_{CC} = 0.144$ nm [3]. The constant low-field mobility μ is calculated as 27,600 cm^2/Vs by using Equation (3.3.1) [9]. The insulator capacitance C is computed as 0.381 pF/cm by using Equation (3.1.2) with the relative dielectric constant of SiO_2, ε_{ox} =

3.9. The value of the quantum capacitance can be estimated as 4 pF/cm [41, 57]. Since the quantum capacitance is much larger than the insulator capacitance, the total capacitance can be approximated as the insulator capacitance of CNT FETs, as mentioned above. The averaged electron effective mass m_e^* is $0.0568m_0$ obtained from $e\tau/\mu$, in which the average momentum relaxation time τ is 0.89 ps [13], and therefore N_c = 0.222 nm^{-1}. Although τ varies with the carrier density [13], we have verified that the device current does not depend significantly on m_e^* within the relevant density range. In CNT FETs the metal-CNT interfaces form the Schottky barriers. In our model their effect is simplified to a constant voltage drop independent of the current, and the values of the voltage drops across the contact/channel interfaces are assumed to be the same value V_c at both (S and D) contacts [49, 51], i.e., $\Delta V_s = \Delta V_d = V_c$. For V_D = 15 V a constant voltage drop V_c of 5.5 V and the flat-band voltage V_{fb} of 5.5 V were extracted from the experimental data in earlier work [49]. Nonradiative recombination is much stronger than radiative, as evidenced by the low measured quantum efficiency of 10^{-7} photons per injected e-h pair [44]. Shockley-Read-Hall (SRH) recombination, band-to-band nonradiative recombination (BBN), in which phonons are emitted, and Auger recombination are considered here. Expressions for the nonradiative recombination rates R_{nr} and the values of coefficients chosen are listed in Table 6.1. The coefficient values were chosen to yield light-spot sizes in agreement with the experimental data of Ref. [42].

Table 6.1. Nonradiative recombination rates R_{nr} and values of coefficients.

SRH	$R_{nr} = \dfrac{np - n_i^2}{\tau_{SRH}(n + p + 2n_i)}$	τ_{SRH} = 0.89 ps
BBN	$R_{nr} = B_{BBN}(np\text{-}n_i^2)$	B_{BBN} = 10 km/s
Auger	$R_{nr} = B_{Auger}(n+p)(np\text{-}n_i^2)$	B_{Auger} = 1 cm^2/s

Optical emission is generated by band-to-band radiative recombination (BBR) of injected electrons and holes. The radiative recombination rate R_r is obtained as $B_{BBR}(np\text{-}n_i^2)$, where B_{BBR} is the radiative coefficient. Moreover, the emitted optical power P_{opt} is calculated as $E_g\int_0^L R_r(x)dx$, in which E_g is the CNT band-gap, as mentioned above.

6.2 Analytic Results for Optical Emitters Based on Carbon-Nanotube Field-Effect Transistors

For optical emitters based on long-channel ambipolar CNT FETs, an analytic model based on diffusive transport and neglecting the recombination length has been presented and applied to very long-channel (60 μm) CNT FETs, but the spatial size of the optical emission region and emitted optical power were not considered in Ref. [49]. The physical origin of important effects may be difficult to trace from a purely numerical approach. A new analytic model accounting for both radiative and nonradiative recombination, allowing for several recombination mechanisms, has been presented in

Chapter 4, thereby enabling a clearer understanding of the dependence of the transport and optical properties on the various nonradiative recombination mechanisms. Nonradiative recombination is much stronger than radiative; therefore, the transport properties and carrier densities are determined by assuming only nonradiative recombination. The optical properties, in turn, are calculated based on the transport properties thus obtained, as presented in Chapter 4. In particular, the current, radiative recombination rate, emitted light-spot size, and emitted optical power are all calculated analytically.

The analytic formula calculated for transport and optical properties in optical emitters are presented in Chapter 4. In the following analytic calculation, the normalized recombination rate f_0 is chosen to be a Gaussian. Figure 6.1 shows the current I as a function of V_G for V_D = 15 V in a CNT FET with a semiconducting zigzag CNT (17,0) with L = 60 μm by using Equation (4.3.8). The solid line is for SRH recombination, the dashed line is for BBN recombination, and the dash-dot line is the result of the analytic model of Ref. [49]. The two analytic results for I coincide, and are close to the dash-dot line. These analytic results are in agreement with the experimental data in Ref. [49] if the experimentally observed hysteresis is neglected. When V_G = 13 V, V_G and V_D satisfy the symmetric condition V_G-V_{fb} = 7.5 V and V_G-V_{fb}-V_D = -7.5 V, with V_G-V_{fb} = ½V_D, a current minimum occurs.

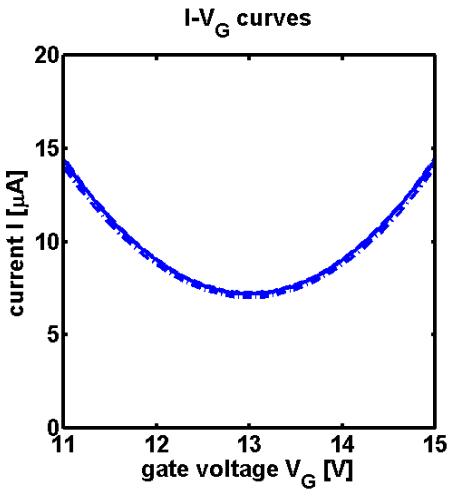

Figure 6.1. Current I as a function of V_G for V_D = 15 V in a CNT FET with a semiconducting zigzag CNT (17,0) with L = 60 μm by using analytic formula. The solid line is for SRH recombination, the dashed line is for BBN recombination, and the dash-dot line is the result of the analytic model of Ref. [49].

Figure 6.2 shows the electron and hole densities n and p as functions of position x for various values of V_G (V_D = 15 V) by using Equations (4.1.14) and (4.1.15). Figure 6.3 shows the radiative recombination rate R_r as a function of position x for various values of V_G (V_D = 15 V). Figure 6.4 shows the CNT potential ψ as a function of position x for various values of V_G (V_D = 15 V) by using Equation (4.1.13). In Figure 6.2 to 6.4, the solid lines are for SRH recombination, and the dashed lines are for BBN recombination. When the channel length exceeds the recombination length, essentially all injected carriers recombine within the channel. Hence, electrons injected from S fully recombine with the holes in the channel and the electron density is negligible outside the recombination region, as shown in Figure 6.2. Similarly, holes injected from D fully recombine with the electrons in the channel and the hole density is negligible outside the recombination region as well. In Figure 6.3, radiative recombination is negligible outside

the recombination region since the minority carrier densities are negligible. Evidently, the position of the maximum R_r occurs where the electron density is equal to the hole density, i.e., where the linear charge density is zero. When V_G = 13 V, i.e., in the symmetric condition, n is equal to p at the channel center, and R_r is large there. When V_G < 13 V, the injected electron density is smaller and the injected hole density is larger. Therefore, the position, where n equals p, moves toward S, and the emitted light spot shifts accordingly. In Figure 6.3, the values of R_r are smaller for the SRH recombination and larger for the BBN recombination, because the light spot is smaller for SRH and bigger for BBN recombination. Since the maximum value of R_r is proportional to the current, the relationship R_r vs. V_G exhibits similar trends as the I- V_G curves. In Figure 6.4, the slope of the CNT potential ψ is greater inside the recombination region than outside, that is, the longitudinal electric field is enhanced inside the recombination region. When the V_G < 13 V, the position, where n equals p, moves toward S, and the position of higher slope of CNT potential ψ moves accordingly due to the movement of the recombination region.

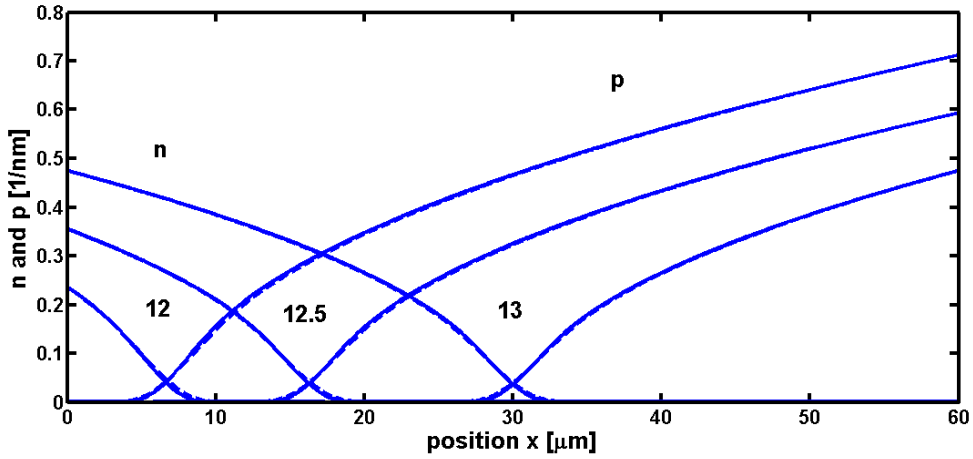

Figure 6.2. Electron and hole densities n and p as functions of position x for various values of V_G (V_D = 15 V) by using analytic formula. The solid lines are for SRH recombination, and the dashed lines are for BBN recombination.

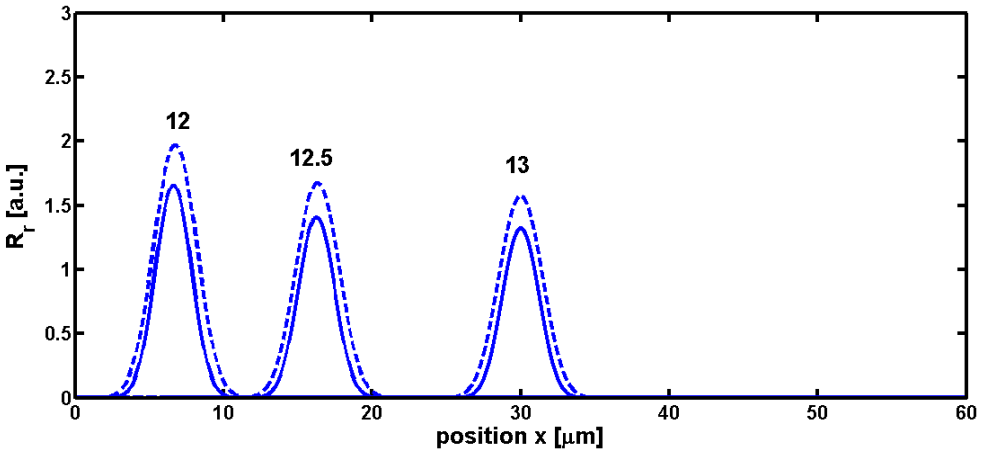

Figure 6.3. Radiative recombination rate R_r as a function of position x for various values of V_G (V_D = 15 V) by using analytic formula. The solid lines are for SRH recombination, and the dashed lines are for BBN recombination.

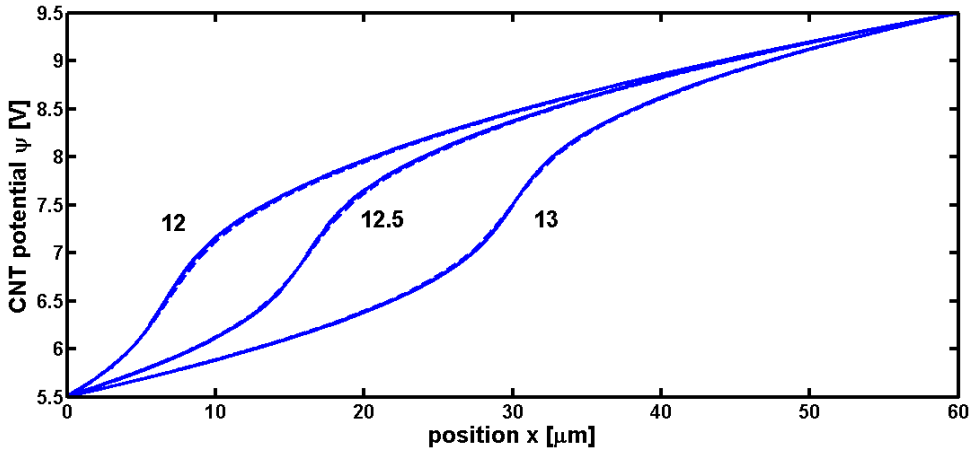

Figure 6.4. CNT potential ψ as a function of position x for various values of V_G (V_D = 15 V) by using analytic formula. The solid lines are for SRH recombination, and the dashed lines are for BBN recombination.

Figure 6.5 shows the position x_m as a function of V_G for V_D = 15 V using Equation (4.3.9). The solid line is for SRH recombination, the dashed line is for BBN recombination, and the dotted line is from the analytic model of Ref. [49]. The two analytic results for x_m coincide, and are close to the dotted line. The analytic results are in agreement with the experimental data in Ref. [49], if the experimentally observed hysteresis is neglected. When V_G = 13 V, i.e., the symmetric condition, x_m locates in the channel center. When V_G < 13 V, the position x_m of the emitted light spot shifts toward S, as mentioned above.

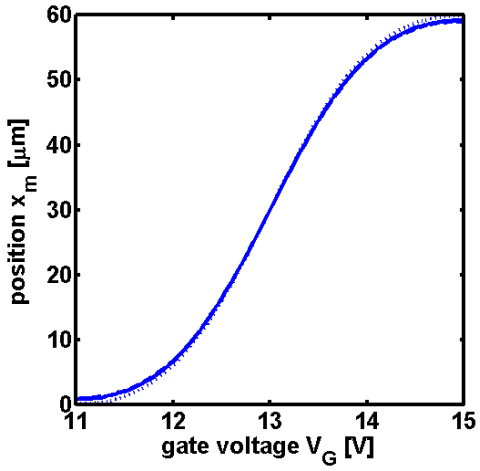

Figure 6.5. Position x_m as a function of V_G for V_D = 15 V by using analytic formula. The solid line is for SRH recombination, the dashed line is for BBN recombination, and the dotted line is from the analytic model of Ref. [49].

Figure 6.6 shows (a) the light-spot size S_{spot} and (b) the emitted optical power P_{opt} as functions of the current I for the symmetric condition V_G-V_{fb} = ½V_D for various nonradiative recombination mechanisms for V_G = 13 V and V_D = 15 V. The calculated light spot size is consistent with the measured size 2~4 μm [42]. The light-spot size S_{spot} is calculated by Equation (4.3.13), and the emitted optical power P_{opt} is calculated by Equation (4.3.14). The solid lines are for SRH recombination, the dashed lines for BBN recombination, and the dotted lines for Auger recombination. For the analytic powers of the current I in both S_{spot} and P_{opt} are summarized in Table 4.1. The powers of I in both S_{spot} and P_{opt} are largest for SRH recombination and smallest for Auger recombination. For BBN recombination (dashed lines), S_{spot} is not sensitive to the current I, while P_{opt} depicts a linear relationship with current I since more emitted optical power is generated with increasing radiative recombination corresponding to the larger carrier densities for

the higher currents. SRH recombination (solid line) depends approximately linearly on the carrier densities, but radiative recombination has a second-order relationship. Therefore, S_{spot} is larger for higher carrier densities, i.e. larger currents. Similarly, Auger recombination (dotted line) is of third order in the carrier densities, thus S_{spot} is smaller for higher currents. SRH recombination (solid line) has a larger slope in P_{opt}-I curves than for BBN recombination (dashed line) due to the positive slope in S_{spot}-I curves, while Auger recombination (dotted line) shows the smaller slope in P_{opt}-I curves, due to the negative slope in S_{spot}-I curves.

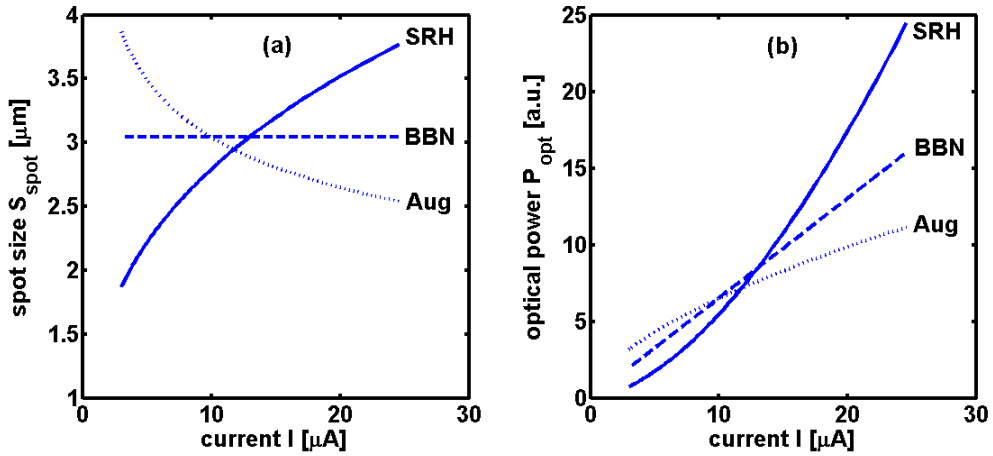

Figure 6.6. (a) Light-spot size S_{spot} and (b) emitted optical power P_{opt} as functions of the current I for V_G-V_{fb} = ½V_D for various nonradiative recombination mechanisms for V_G = 13 V and V_D = 15 V. The solid lines are the analytic results for SRH recombination, the dashed lines for BBN recombination, and the dotted lines for Auger recombination.

In conclusion, we implement an analytical transport model for optical emitters based on CNT FETs that accounts for a radiative and several nonradiative recombination

mechanisms in the conduction channel. The focus is on the effects of radiative and nonradiative recombination in the channel, with the movement of the recombination profile in response to the gate and drain voltages being explored analytically. We show that transport characteristics are essentially determined by nonradiative recombination. The emitted light-spot size and optical power are predicted to exhibit sensitive dependences on the operative nonradiative recombination mechanisms. Analytic calculations for the transport and optical properties are in good agreement in all regions of the conduction channel.

6.3 Numerical Results for Optical Emitters Based on Carbon-Nanotube Field-Effect Transistors

For optical emitters based on ambipolar CNT FETs, numerical models with diffusive transport and carrier recombination were developed for long-channel devices in order to calculate the emitted light-spot movement [50, 60]. Radiative recombination was assumed to be dominant; however, the central importance of nonradiative recombination is indicated by the low measured quantum efficiency [44]. In order to understand the transport characteristics and the optical emission of ambipolar CNT FETs, a diffusive-transport model accounting for a radiative and several nonradiative recombination mechanisms was presented in earlier chapters. The analytic results have been computed in Chapter 6.2. The detail of the numerical calculation has been provided in Chapter 5; therefore, the numerical results for optical emitters based on CNT FETs will be presented in this Chapter 6.3 [51]. The effects associated with radiative and

nonradiative recombination of injected electrons and holes in the channel are considered, and the spatial dependence of the recombination profile on the gate and drain voltages is explored. In particular, the current, radiative recombination rate, emitted light-spot size, and emitted optical power are all calculated numerically.

Figure 6.7 shows the current I as a function of V_G for V_D = 15 V in a CNT FET with a semiconducting zigzag CNT (17,0) with L = 60 μm. The numerical results for SRH recombination, for BBN recombination, and for Auger recombination coincide and are shown in the solid lines, while the analytic results for SRH and for BBN coincide and are shown in the dashed lines. The dotted line is the result of the analytical model of Ref. [49]. These numerical results (solid lines) are in excellent agreement with the experimental data in Ref. [49] if the experimentally observed hysteresis is neglected, but neglecting the non-zero length of the recombination region results in a current (dotted line) that is about 10 % lower. When V_G = 13 V, i.e., in the symmetric condition, a current minimum occurs.

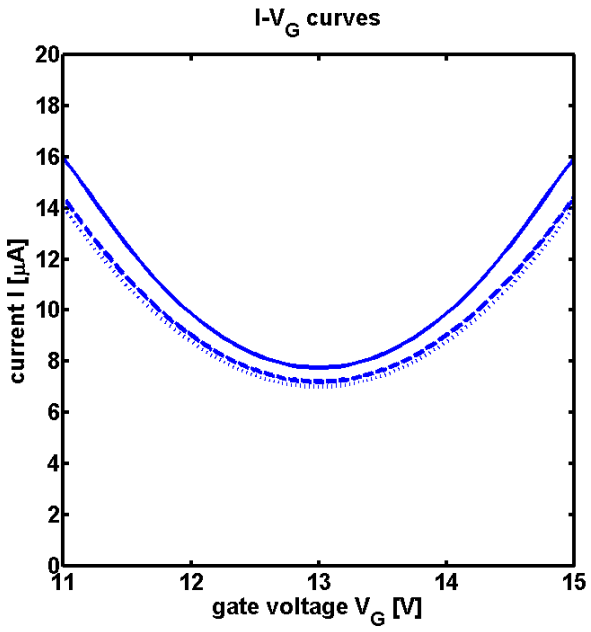

Figure 6.7. Current I as a function of V_G for V_D = 15 V in a CNT FET with a semiconducting zigzag CNT (17,0) with L = 60 μm. The numerical results for SRH recombination, for BBN recombination, and for Auger recombination coincide and are shown in the solid lines, while the analytic results for SRH and for BBN coincide and are shown in the dashed lines. The dotted line is the result of the analytical model of Ref. [49].

Figure 6.8 shows the electron and hole densities n and p as functions of position x for various values of V_G (V_D = 15 V). The solid lines are for SRH recombination, the dashed lines are for BBN recombination, and the dotted lines are for Auger recombination. All three lines are close to each other. Moreover, the analytic results in Figure 6.2 are close to the numerical results in Figure 6.8. When the channel length exceeds the recombination length, essentially all injected carriers recombine within the channel. Hence, electrons injected from S fully recombine with the holes in the channel and the electron density is negligible outside the recombination region. Similarly, holes

injected from D fully recombine with the electrons in the channel and the hole density is negligible outside the recombination region, as mentioned above. When V_G = 13 V, i.e., the symmetric condition, *n* is equal to *p* at the channel center. When the V_G < 13 V, the position, where *n* equals *p*, moves toward S, as mentioned above.

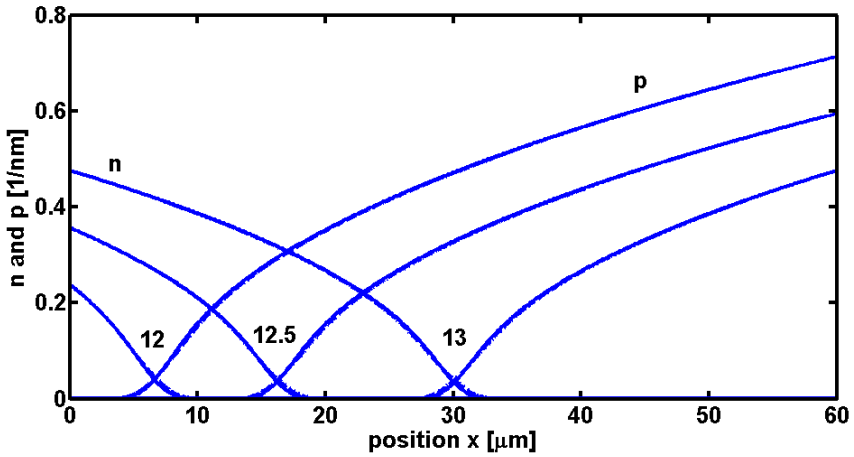

Figure 6.8. Electron and hole densities *n* and *p* as functions of position *x* for various values of V_G (V_D = 15 V) by using numerical calculation. The solid lines are for SRH recombination, the dashed lines are for BBN recombination, and the dotted lines are for Auger recombination.

Figure 6.9 shows the electron and hole currents I_n (solid line) and I_p (dashed line) as functions of position *x* for BBN recombination for various values of V_G (V_D = 15 V). The minority carrier currents are negligible outside the recombination region since the minority carrier densities are negligible outside the recombination region. The total currents are constant with respect to the position *x* due to the current conservation. When V_G = 13 V, i.e., the symmetric condition, I_n is equal to I_p at the channel center. When the

V_G < 13 V, the position, where I_n equals I_p, moves toward S due to the movement of the recombination region. The total currents with respect to V_G in Figure 6.9 have the same trend as the I-V_G curves in Figure 6.7. Figure 6.10 shows the electron drift and diffusion currents $I_{n,dri}$ (solid line) and $I_{n,diff}$ (dashed line), hole drift and diffusion currents $I_{p,dri}$ (solid line) and $I_{p,diff}$ (dashed line) as functions of position x for BBN recombination for V_G = 13 V and V_D = 15V, i.e., in the symmetric condition. This provides evidence of the dominant role played by the drift currents. Therefore, the assumption that only the drift currents are considered for the analytic calculation is reasonable in Chapter 4.

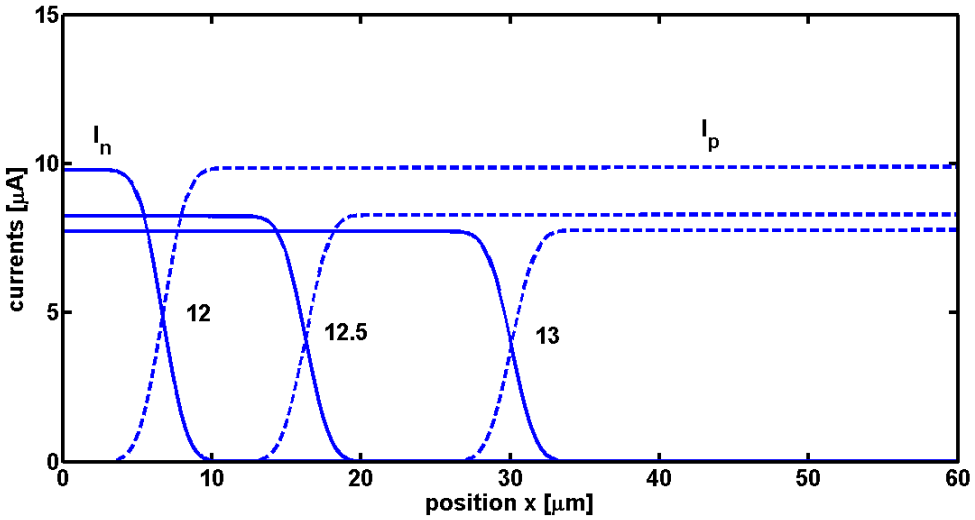

Figure 6.9. Electron and hole currents I_n (solid line) and I_p (dashed line) as functions of position x for BBN recombination for various values of V_G (V_D = 15 V) by using numerical calculation.

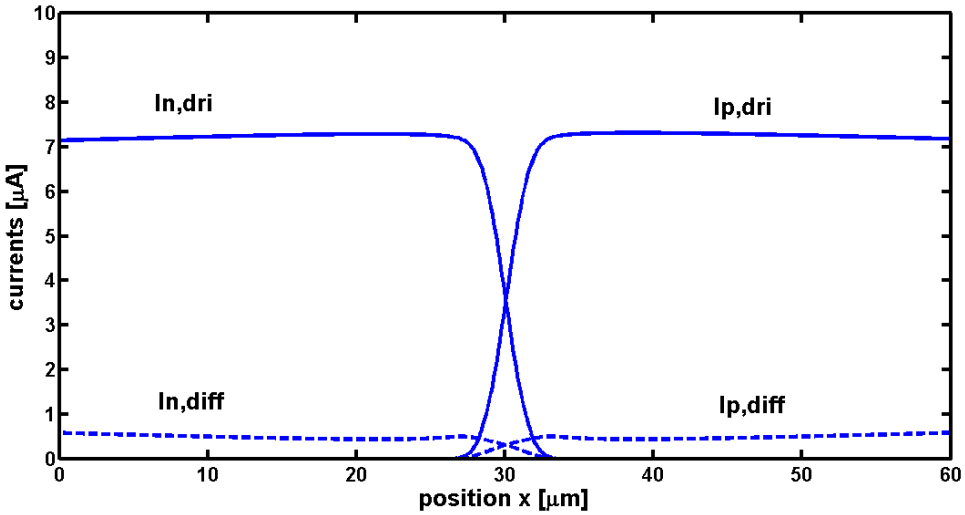

Figure 6.10. Electron drift and diffusion currents $I_{n,dri}$ (solid line) and $I_{n,diff}$ (dashed line), hole drift and diffusion currents $I_{p,dri}$ (solid line) and $I_{p,diff}$ (dashed line) as functions of position x for BBN recombination for V_G = 13 V and V_D = 15V by using numerical calculation.

Figure 6.11 shows the radiative recombination rate R_r as a function of position x for various values of V_G (V_D = 15 V). The solid lines are for SRH recombination, the dashed lines are for BBN recombination, and the dotted lines for Auger recombination. The analytic curves of R_r in Figure 6.3 are close to the numerical ones in Figure 6.11. The position of the maximum R_r occurs where the electron density is equal to the hole density. When V_G = 13 V, i.e., in the symmetric condition, n is equal to p at the channel center, and R_r is large there. When the V_G < 13 V, the position, where n equals p, moves toward S, and the emitted light spot shifts accordingly, as mentioned above. The values

of R_r are smallest for the SRH recombination and largest for the Auger recombination, because the light spot is smallest for SRH and biggest for Auger recombination. Since the maximum value of R_r is proportional to the current, the relationship R_r vs. V_G exhibits similar trends as the I- V_G curves.

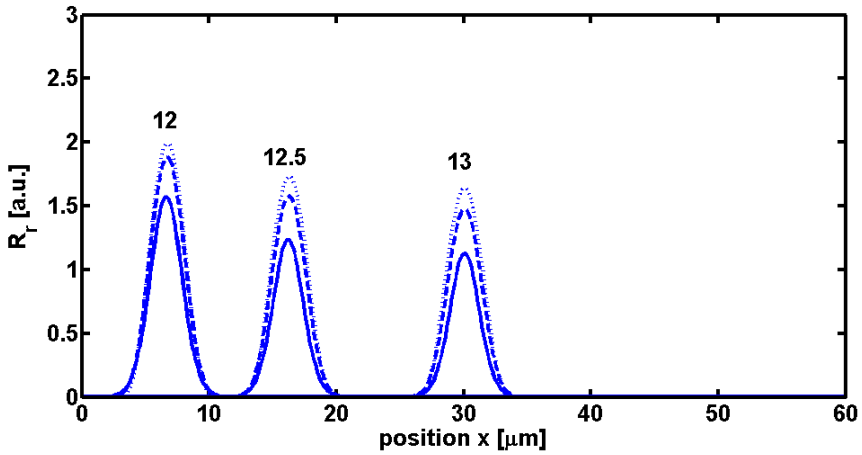

Figure 6.11. Radiative recombination rate R_r as a function of position x for various values of V_G (V_D = 15 V) by using numerical calculation. The solid lines are for SRH recombination, the dashed lines are for BBN recombination, and the dotted lines for Auger recombination.

Figure 6.12 shows (a) the CNT potential ψ and (b) the longitudinal electric field $|F_x|$ as functions of position x for various values of V_G (V_D = 15 V). The solid lines are for SRH recombination, the dashed lines are for BBN recombination, and the dotted lines are for Auger recombination. The analytic curves of ψ in Figure 6.4 are close to the numerical ones in Figure 6.12(a). In Figure 6.12(b), the electric field $|F_x|$ is greater inside

the recombination region than outside, and the maximum $|F_x|$ is about 2~2.6 kV/cm. When V_G = 13 V, i.e., in the symmetric condition, n is equal to p at the channel center, and $|F_x|$ is large there. When the V_G < 13 V, the position of higher values of electric field $|F_x|$ moves toward S due to the movement of the recombination region. When the carrier density is larger than 1.1 nm^{-1}, the quasi-Fermi-level moves to the second subband, which opens another scattering channel, and thus the mobility decreases significantly [13]. The carrier densities are smaller than 1.1 nm^{-1}, as shown in Fig. 6.12(b), and the value of maximum $|F_x|$ is much smaller than the electric field of 27 kV/cm corresponding to the maximum drift velocity in CNT (17,0) [13], hence the model of constant low-field mobility can be applied for this long-channel device.

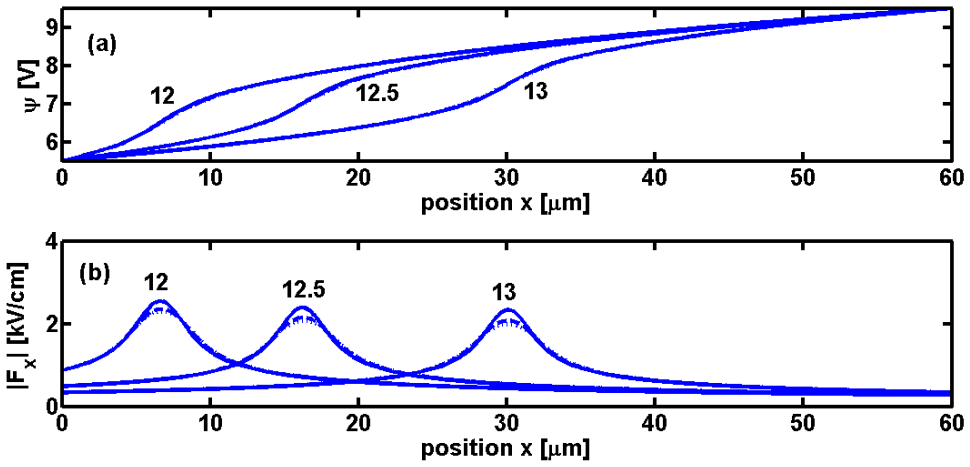

Figure 6.12. (a) CNT potential ψ and (b) longitudinal electric field $|F_x|$ as functions of position x for various values of V_G (V_D = 15 V) by using numerical calculation. The solid lines are for SRH recombination, the dashed lines are for BBN recombination, and the dotted lines are for Auger recombination.

Figure 6.13 shows the position x_m as a function of V_G for V_D = 15 V. The solid line is for SRH recombination, the dashed line is for BBN recombination, and the dotted line is for Auger recombination. The three numerical curves for x_m coincide, and are close to the analytic results in Figure 6.5. The numerical results are in agreement with the experimental data in Ref. [49], if the experimentally observed hysteresis is neglected. When V_G = 13 V, i.e., the symmetric condition, x_m locates in the channel center. When the V_G < 13 V, the position x_m of the emitted light spot shifts toward S, as mentioned above.

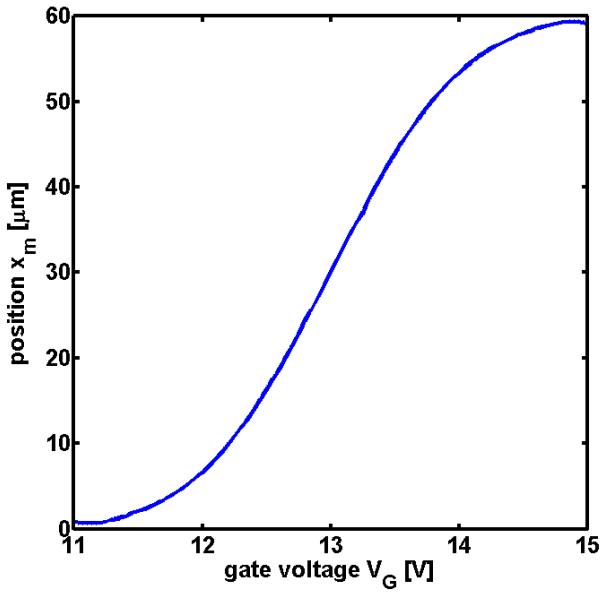

Figure 6.13. Position x_m as a function of V_G for V_D = 15 V by using numerical calculation The solid line is for SRH recombination, the dashed line is for BBN recombination, and the dotted line is for Auger recombination.

Figure 6.14 shows (a) the light-spot size S_{spot} and (b) the emitted optical power P_{opt} as functions of the current I for V_G-V_{fb} = ½V_D for various nonradiative recombination mechanisms for V_G = 13 V and V_D = 15 V. The calculated light spot size is consistent with the measured size 2~4 μm [42]. The numerical results for both S_{spot} and P_{opt} in Figure 6.14 are close to the analytic results in Figure 6.6. For BBN recombination only (dashed lines), S_{spot} is not sensitive to the current I, while P_{opt} depicts a linear relationship with current I, as mentioned above. SRH recombination depends approximately linearly on the carrier densities, and Auger recombination is of third order in the carrier densities, but radiative recombination has a second order relationship. Therefore, for SRH recombination only (upper solid line) S_{spot} is larger for higher carrier densities, i.e. larger currents, while for Auger recombination only (upper dotted line) S_{spot} is smaller for higher currents. In addition, SRH recombination only (upper solid line) has a larger slope in P_{opt}-I curves than for BBN recombination (dashed line), while Auger recombination only (upper dotted line) shows the smaller slope in P_{opt}-I curves, as mentioned above. Numerically fitted powers of I in S_{spot} and P_{opt} are summarized in Table 6.2. All are close to the analytic values in Table 4.1. The difference between the analytic and numerical curves is to be attributed to the single iteration and the Gaussian initial guess in the analytic model. The powers of I in both S_{spot} and P_{opt} are largest for SRH recombination and smallest for Auger recombination. In Figure 6.14(a), for both SRH and BBN combined (lower solid line), S_{spot} is smaller than for either for SRH or for BBN individually. Similarly, for both Auger and BBN considered simultaneously (lower dashed line), S_{spot} is smaller than that for either one individually. In Figure 6.14(b), for both SRH and BBN considered together the values of P_{opt} in the lower solid line are

smaller than those either for SRH or for BBN because of the lower radiative efficiency. Similarly, for Auger and BBN combined the lower dotted line has lower values of P_{opt} than for either one individually.

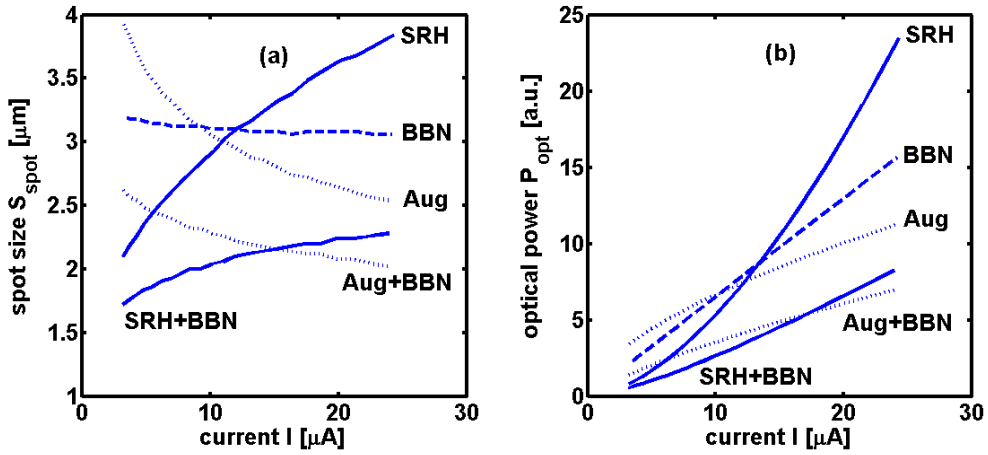

Figure 6.14. (a) Light-spot size S_{spot} and (b) emitted optical power P_{opt} as functions of the current I for V_G-V_{fb} = ½V_D for various nonradiative recombination mechanisms for V_G = 13 V and V_D = 15 V. The upper solid lines are the numerical results for SRH recombination only, the dashed lines for BBN recombination only, the upper dotted lines for Auger recombination only, the lower solid lines for both SRH and BBN combined together, and the lower dotted lines for both Auger and BBN combined together.

Table 6.2. Numerically fitted powers of C and I in S_{spot} and P_{opt}.

S_{spot}	SRH	BBN	Auger	P_{opt}	SRH	BBN	Auger
C	0.02	-0.49	-0.79		2.12	1.06	0.43
I	0.30	-0.02	-0.22		1.68	1.0	0.59

Since the gate capacitance can be changed by fabricating various insulator thicknesses and by choosing different insulator materials, the optical emission for various C can be tested experimentally. Figure 6.15 shows (a) the light-spot size S_{spot} and (b) the emitted optical power P_{opt} as functions of the gate capacitance C for V_G-V_{fb} = ½V_D for various nonradiative recombination mechanisms for V_G = 13 V and V_D = 15 V. In Figure 6.15(a), if SRH recombination (upper solid line) dominates, S_{spot} is not sensitive to the gate capacitance C, while S_{spot} decreases strongly as C increases if Auger recombination (upper dotted line) dominates. When C is larger, the current is larger and thus P_{opt} is larger. This gives rise to the positive slope in the P_{opt}-C curves, shown in Figure 6.15(b). For both SRH and BBN combined (lower solid lines), S_{spot} and P_{opt} are smaller than those either for SRH (upper solid line) or for BBN (dashed line) individually due to the lower radiative efficiency. Similarly, for both Auger and BBN combined (lower dotted lines), S_{spot} and P_{opt} are smaller than those either for Auger (upper dotted line) or for BBN (dashed line) individually. Numerically fitted powers of C in S_{spot} and P_{opt} are summarized in Table 6.2. All are close to the analytic values in Table 4.1.

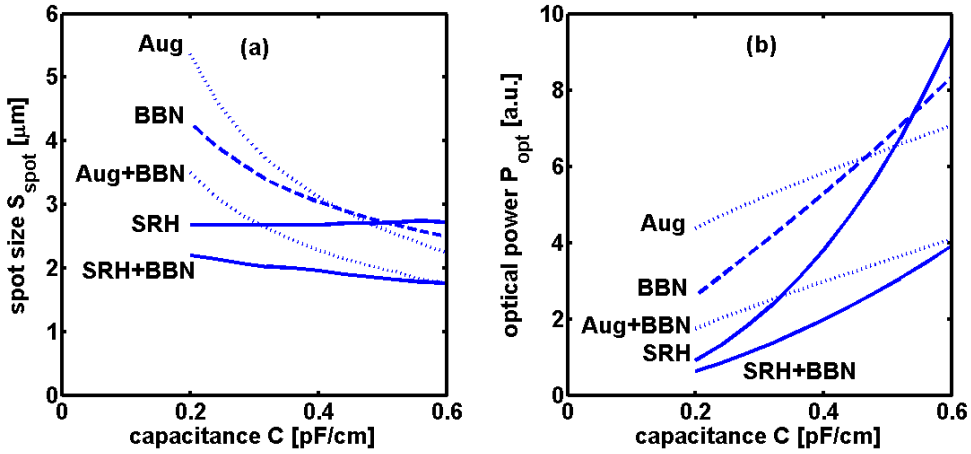

Figure 6.15. (a) Light-spot size S_{spot} and (b) emitted optical power P_{opt} as functions of the gate capacitance C for V_G-V_{fb} = ½V_D for various nonradiative recombination mechanisms for V_G = 13 V and V_D = 15 V. The upper solid lines are the numerical results for SRH recombination only, the dashed lines for BBN recombination only, the upper dotted lines for Auger recombination only, the lower solid lines for both SRH and BBN combined together, and the lower dotted lines for both Auger and BBN combined together.

In conclusion, we implement a numerical transport model for optical emitters based on CNT FETs that accounts for finite radiative and nonradiative recombination probability in the conduction channel. Based on our model, we show that inside the recombination region the transport properties are essentially determined by nonradiative recombination, and we predict that the dependence of the light spot size on the current is sensitive to the nonradiative recombination mechanisms. The decisive role of nonradiative recombination here is consistent with the observed low quantum efficiency in the optical emission from CNT FETs [44]. The electric field inside the recombination region is enhanced but it remains sufficiently small so that a model based on constant low-field mobility can be applied to long-channel ambipolar CNT FETs. Furthermore,

the electric field is not high enough for exciton-formation through impact excitation in long-channel devices [61].

CHAPTER 7

RESULTS FOR PHOTODETECTORS BASED ON CARBON-NANOTUBE FIELD-EFFECT TRANSISTORS

A photodetector absorbs optical energy and converts it to electrical energy. There are generally three steps involving in the photodetection process [94]: (1) absorption of optical energy and generation of carriers, (2) transport of photogenerated carriers across the absorption and transit regions, and (3) carrier collection and generation of a photocurrent, which flows through the external circuitry. There are three main types of photodetectors: photoconductors, PIN diodes, and avalanche photodiodes [94]. The photodetectors based on CNT FETs in our study operate as photoconductors. Photoconductivity of CNT FETs is the reverse of electroluminescence for optical emitters based on CNT FETs, with optical radiation producing electrons and holes that are separated by the applied field. With an applied drain-to-source voltage, both electrons and holes are collected at the two contacts, and thus produce a photocurrent. In this chapter we present calculated results for the photoconductors based on CNT FETs.

Photoconductivity in CNT FETs has been explored experimentally with uniform photoexcitation [21, 43] and with near-field photoexcitation [65-69]. Theoretical simulations neglecting the effects of excitons for the very short channel (15nm) were carried out in Ref. [70]. Electron-hole interactions, however, should be strong in quasi-one-dimensional system. The electron-hole interaction is thus expected to bind the photoexcited electron and hole to form excitons. Theoretical [17-19] and experimental studies [20-22] have shown that electron confinement in the quasi-one-dimensional

structure of CNTs leads to high electron-hole binding energies and the formation of strongly bound exciton states. For strong binding, most of the optical absorption is associated with photogeneration of excitons. Since the formation of excitons through photoexcitation is important in CNTs, we have developed the model accounting for excitons already presented in earlier chapters. The input data and the properties of photoconductors based on CNT FETs are given in Chapter 7.1. Results for photoconductors based on long-channel CNT FETs with uniform photoexcitation are given in Chapter 7.2, and those for near-field photoexcitation are given in Chapter 7.3. Based on these, we obtain the photocurrents and resulting exciton densities as a function of photoexcitation conditions. The summary for photoconductors based on carbon-nanotube field-effect transistors is presented in Chapter 7.4.

7.1 Calculation for Photoconductors Based on Carbon-Nanotube Field-Effect Transistors

The ambipolar CNT FET modeled consists of an intrinsic semiconducting single-wall CNT providing a 60-μm long channel, source and drain Schottky contacts composed of titanium and cobalt [21, 43], and a 100-nm thick SiO_2 gate insulator. A photoconductor based on a CNT FET with a back gate is shown in Figure 2.7. Since the photoconductivity is the reverse of electroluminescence, the same values of the channel length and insulator thickness are used in the photoconductors in this chapter as in the optical emitters in Chapter 6. In our study of CNT-FET-based photoconductors the effects considered are those resulting from excitation of the CNT channel while

neglecting any possible effects arising from light incident on the contacts. Ambipolar FETs operate with one electron injecting (*e*-source) and one hole injecting (*h*-source) contact. We define the *e*-source as the *source* (S) and *h*-source as the *drain* (D), as mentioned above. The applied gate (G) and drain (D) voltages, V_G and V_D, are measured with respect to the source (S) $V_S = 0$. Electrons are injected from S and accumulate in the CNT near S for positive V_G, while holes are injected from D and accumulate near there for negative V_G-V_D. This defines the ambipolar operating regime, as mentioned above. A zigzag (19,0) CNT is chosen in order to use existing calculated data for the properties of excitons [23]. The CNT diameter d_{cnt} is computed as 1.5 nm by using Equation (2.1.1) with the carbon-carbon bond length $a_{CC} = 0.144$ nm [3]. The constant low-field mobility μ is calculated as 35,500 cm^2/Vs using Equation (3.3.1) [9]. The insulator capacitance C is computed as 0.388 pF/cm from Equation (3.1.2) with the relative dielectric constant of SiO_2, $\varepsilon_{ox} = 3.9$. The averaged electron effective mass m_e^* is $0.053m_0$ [13], and therefore $N_c = 0.214$ nm^{-1}. In CNT FETs the metal-CNT interfaces form Schottky barriers. In our model their effect is simplified to a constant voltage drop independent of current. Assuming the intrinsic $V_s = 0$, the extrinsic terminal voltages V_G and V_D in terms of the intrinsic ones V_g and V_d are given as $V_G = V_g+\Delta V_s$ and $V_D = V_d+\Delta V_s+\Delta V_d$, where ΔV_s and ΔV_d are the voltage drops across the contact-channel interfaces. Since the voltage drops and flat-band voltage V_{fb} are not known in CNT-FET-based photoconductors, the results are solved in terms of the intrinsic voltages V_g-V_{fb} and V_d. Typical applied drain voltages in the range of 0.5 V to 1 V were reported in photoconductors based on CNT FETs [21, 43]. Therefore, the value of the intrinsic drain voltage $V_d = 0.2$ V is chosen to be calculated due to the unknown voltage drops at both S and D contacts.

Electron confinement in the quasi-one-dimensional structure of the CNTs leads to the formation of strongly bound excitons. The exciton binding energy E_b for a zigzag (19,0) CNT is computed as 0.16 eV based on Equation (2.1.2) with the relative dielectric constant (ε_{ox} = 3.9) of SiO_2 [1, 18]. For strong binding, most of the optical absorption is associated with photogeneration of excitons, as mentioned above. The conduction and valence bands in CNTs are doubly orbitally degenerate. For free electron-hole pairs, this gives four distinct but degenerate pair excitations. In excitons, the Coulomb interaction partially lifts the fourfold degeneracy, as mentioned above. In CNTs, the Coulomb interaction creates the four lowest-energy singlet excitons, but only the second lowest-energy exciton is optically active, which is called a *bright exciton* [23, 24]. The other excitons are optically (dipole) forbidden, which are called *dark excitons*. Moreover, all four lowest-energy excitons for the triplet-spin states are dark as well [23, 24]. Therefore, only the singlet bright exciton is considered when evaluating the radiative lifetime of excitons in CNTs. For a CNT (19,0), the effective mass of excitons is given as $m_{x1} = m_{x3} = 3m_e^* = 0.159\, m_0$ [23], where m_e^* is the electron effective mass, and m_{x2} is calculated to be $0.0234\, m_0$ [18]. The energy levels of the exciton-1, exciton-2, and exciton-3 are depicted as E_{x1}, E_{x2}, and E_{x3}, respectively. The exciton splitting energy δ_1 ($=E_{x2}-E_{x1}$) is defined to be the energy difference between the energy levels of exciton-1 and exciton-2, and the splitting energy δ_2 ($=E_{x3}-E_{x1}$) is assumed to be the energy difference between the energy levels of exciton-1 and exciton-3. For a (19,0) CNT, δ_1 and δ_2 are given as 4 meV and 27 meV, respectively [23]. Since the exciton splitting energies are very small, thermal equilibrium is a good assumption due to the likely fast transition between those exciton states. The total singlet-exciton density n_{xs} is

$n_{x1}+n_{x2}+n_{x3}$. By summing all individual exciton continuity equations given in Equation (3.7.1), the continuity equation of the *total* singlet-exciton density n_{xs} is given as Equation (3.7.2) [52]. Expressing the *i*th-exciton density in terms of the total singlet-exciton density n_{xs} gives $n_{x1} = \zeta_1 n_{xs}$, $n_{x2} = \zeta_2 n_{xs}$, and $n_{x3} = \zeta_3 n_{xs}$. By using Equation (3.9.1) in Chapter 3.9 and assuming $g_{x1} = g_{x2} = 1$ and $g_{x3} = 2$, we obtain $\zeta_1 = 0.492$, $\zeta_2 = 0.162$, and $\zeta_3 = 0.346$. We find that the density of bright excitons is smaller than those of dark excitons due to the smaller density-of-states through the smaller effective mass. The radiative-decay coefficient r_{2r} of bright excitons is assumed to be 0.4 ns^{-1} (i.e., 2.5 ns lifetime) [23], and thus r_r is obtained as 0.065 ns^{-1} (i.e., 15.4 ns lifetime). The CNT *radiative* lifetime has been calculated [23, 24] to be of the order of magnitude ~ 10 ns. However, the *measured* lifetime is much shorter, in the range of 10 to100 ps [96], indicating the presence of nonradiative decay channels. The theoretical calculation of the nonradiative decay rates of excited semiconducting nanotubes by a variety of decay mechanisms including multiphonon decay (MPD) was published recently [1, 96]. For a CNT (19,0) with the relative dielectric constant ($\varepsilon_{ox} = 3.9$) of SiO_2, the nonradiative decay coefficient is 20 ns^{-1} (i.e., 50 ps lifetime). Therefore, all values of the excitonic nonradiative-decay coefficients r_{1nr}, r_{2nr}, and r_{3nr} are assumed to be 20 ns^{-1}, and r_{nr} is obtained as 20 ns^{-1} as well. The rate of exciton formation involving bimolecular recombination of electrons and holes is $B_{xi}np$, where B_{xi} is the capture parameter for exciton formation [72, 73]. The rate of exciton ionization to free *e-h* pairs is depicted as $r_{di}n_{xi}$, where r_{di} is the exciton-ionization coefficient. The effect of the field ionization of excitons [71] is neglected since the electric field in the long-channel CNT FETs is low [51, 52]. For CNTs, the ratio of the exciton-ionization coefficient r_{di} to the capture

parameter B_{xi} for exciton formation, i.e., r_{di}/B_{xi}, is assumed to be the one-dimensional Arrhenius equilibrium constant, which is shown in Equation (3.8.3) in Chapter 3.8. The measured exciton-diffusion coefficient is ~100±50 $cm^2\ s^{-1}$ [97-99]. Therefore, all values of the exciton-diffusion coefficients D_{x1}, D_{x2}, and D_{x3} are assumed to be 100 $cm^2\ s^{-1}$, and D_x is obtained as 100 $cm^2\ s^{-1}$ as well.

In CNTs, most of the oscillator strength is transferred from band-to-band to excitonic transitions, which dominate the optical absorption spectra [18, 19], as mentioned above. The fractional value of the number of excitons generated per incident photon is α_{ex}, and the absorption spectrum if α_{ex} as a function of the incident photon energy. The bright singlet exciton-2 gives rise to the E_{11} optical transition, and the value of E_{11} is assumed as 0.56 eV. The absorption spectrum of the bright exciton-2 is expressed as α_{ex2}. The value of α_{ex2} at E_{11} is assumed as 1, and the full-width at half maximum (FWHM) is assumed as 30 meV for a zigzag (19,0) CNT [1, 21]. In addition to the strong exciton transition, a weaker side-band ~ 190 meV above the exciton transition is observed [21]. The dark exciton-3 level is doubly degenerate; while these states are optically forbidden, they can nonetheless be observed as a side-band in the photoconductivity spectrum arising from exciton-phonon coupling [21, 23, 76]. The absorption spectrum of the dark exciton-3 is expressed as α_{ex3}. The peak of α_{ex3} is taken to be 190 meV above E_{11}, and the magnitude of the peak of α_{ex3} is assumed as 0.3 [21]. Since the diameter of a zigzag CNT (19,0) is so small (1.5 nm), the incident radiation is absorbed very slightly. The optical absorption cross section A_{cm} is assumed as $0.5x10^6$ cm^2/mole C [75]. In CNTs, the one-dimensional photon-absorption rate A_{abs} [number of absorbed photons $cm^{-1}\ s^{-1}$] is given in Equation (3.6.2), where P_{incd} [W/cm^2] is the

incident optical power density and E_{ph} [J] is the photon energy. For the incident light profile $f_{inc}(x)$, the exciton-*i* generation rate G_{xi} [number of excitons cm^{-1} s^{-1}] through the phtoexcitation is computed in Equation (3.6.3). G_{x2} [$cm^{-1}s^{-1}$] is the bright exciton-2 generation rate from photoexcitation, G_{x3} is the dark exciton-3 generation rate due to the exciton-phonon coupling, and G_{x1} is the dark exciton-1 generation rate which is assumed as zero. The total exciton generation rate is given as $G_x = G_{x1}+G_{x2}+G_{x3}$.

For the photoconductors, the dark current I_{dark} is defined as the device current without illumination, while the device current with illumination is expressed as I_{light}. The photocurrent I_{ph} is defined as the difference between I_{light} and I_{dark}, i.e., $I_{ph} = I_{light}-I_{dark}$ [43, 94, 95]. Since the absorption spectrum depends on the incident photon energies, the photocurrent spectrum depends on the photo-excitation energies [21]. Current gain in photoconductors is computed below. If all the photogenerated excitons are ionized to e-h pairs and if all the photogenerated carriers are swept out before recombination and are collected at the contacts, this photocurrent is expressed as $I_{ph,swept}$. The value of $I_{ph,swept}$ is calculated as

$$I_{ph,swept} = 2e\int_0^L G_x(x)dx. \tag{7.1.1}$$

The prefactor 2 indicates the contribution of both electrons and holes to the photocurrent. The current gain Γ_G is defined as [94, 95]

$$\Gamma_G = \frac{I_{ph}}{I_{ph,swept}}. \tag{7.1.2}$$

For long-channel CNT FETs, there is no sweep-out of the carriers and the recombination dominates. Since both the average electron and hole transit times $t_{tr,e}$ and $t_{tr,h}$ are larger than the recombination time τ_{recomb}, the gain can be expressed as [94]

$$\Gamma_G = \eta_{ionized} \times \frac{L_e + L_h}{L}, \tag{7.1.3}$$

where η_{ionized} is the exciton-ionization efficiency, and L_e and L_h are the average paths traveled by electrons and holes, respectively. For the average electron and hole velocities V_e and V_h, the values of L_e and L_h are given as

$$L_e = V_e \tau_{recomb}, \quad L_h = V_h \tau_{recomb}, \tag{7.1.4}$$

and the average electron and hole transit times are given as

$$\begin{aligned} t_{tr,e} &= \frac{L}{V_e} = \frac{L}{\mu_e \mid F_x \mid_{ave}}, \\ t_{tr,h} &= \frac{L}{V_h} = \frac{L}{\mu_h \mid F_x \mid_{ave}}, \end{aligned} \tag{7.1.5}$$

where $|F_\text{x}|_\text{ave}$ is the average longitudinal electrical field. For CNT FETs, $t_\text{tr,e} = t_\text{tr,h}$ due to $\mu = \mu_\text{e} = \mu_\text{h}$. Therefore, the gain is obtained as

$$\Gamma_G = \eta_{ionized} \times \frac{2\tau_{recomb}}{t_{tr,e}}. \tag{7.1.6}$$

In Chapter 7.2, the exciton diffusion in CNT-based photoconductors with uniform photoexcitation is not considered. In Chapter 7.3, exciton diffusion with near-field photoexciation is taken into account in order to calculate the spatial profiles of the exciton densities.

7.2 Results for Photoconductors Based on Carbon-Nanotube Field-Effect Transistors with Uniform Photoexcitation

Photoconductivity in CNT FETs has been explored experimentally with uniform photoexcitation [21, 43], and the typical incident optical-power density is in the range of 1-10 kW/cm^2. Thus CNT-FET-based photoconductors employing semiconducting zigzag CNTs (19,0) for an incident-light power density P_{incd} = 10 kW/cm^2 with uniform photoexcitation are chosen to be for our calculation. Since the voltage drops and flat-band voltage are not known in these devices, the results are expressed in terms of the intrinsic voltages V_g-V_{fb} and V_d, and the value of V_d = 0.2 V is chosen to be calculated, as mentioned above. In earlier chapters, the nonradiative recombination of electrons and holes in the optical emitters based on CNT FETs is assumed as SRH, BBN, or Auger recombination. For the simplified calculations presented here, only band-to-band nonradiative (BBN) recombination rate is considered in the photoconductors based on CNT FETs. Thus the nonradiative recombination rate of electrons and holes is expressed as $R_{nr} = B_{BBN}np$. The coefficient B_{BBN} of BBN recombination is assumed as 10 km/s (= 10^6 cm/s), as mentioned above. For CNTs, the rate of exciton formation involving bimolecular recombination of electrons and holes is described as $B_{xi}np$, and the ratio of the exciton-ionization coefficient r_{di} to the capture parameter B_{xi} for exciton formation, i.e., r_{di}/B_{xi}, can be computed by Equation (3.8.3). Since the values of both r_{di} and B_{xi} in CNTs are not known, three cases for the values of r_d and B_x are chosen to be calculated by way of comparison. In the first case, $B_x = 10^6$ cm/s, from which the value of r_d is obtained as 1.07x10^9 s^{-1}. In this case BBN nonradiative recombination is not included.

This means that all of the recombination of electrons and holes generates excitons. For convenience, this case is abbreviated as

$$C_1 = \{B_x = 10^6 \text{ cm/s}, r_d = 1.07\text{x}10^9 \text{ s}^{-1}, B_{BBN} = 0\}. \quad (7.2.1)$$

In the second case, the value of B_x is assumed as 10^4 cm/s, and from which $r_d = 1.07\text{x}10^7$ s^{-1} is obtained. In this case BBN nonradiative recombination ($B_{BBN} = 10^6$ cm/s) *is* included. This means that the exciton-formation rate involving the recombination of electrons and holes is equal to only 1% of the BBN recombination rate; that is, most of the recombination of electrons and holes does not generate excitons. This case is abbreviated by

$$C_2 = \{B_x = 10^4 \text{ cm/s}, r_d = 1.07\text{x}10^7 \text{ s}^{-1}, B_{BBN} = 10^6 \text{ cm/s}\}. \quad (7.2.2)$$

The total recombination rate of electrons and holes has about the same value in case C_2 as in case C_1. In the third case, the value of B_x is taken to be 10^6 cm/s, giving $r_d = 1.07\text{x}10^9$ s^{-1}. In this case BBN recombination ($B_{BBN} = 10^6$ cm/s) is included. Notice that B_x and B_{BBN} have the same values. This case is abbreviated by

$$C_3 = \{B_x = 10^6 \text{ cm/s}, r_d = 1.07\text{x}10^9 \text{ s}^{-1}, B_{BBN} = 10^6 \text{ cm/s}\}. \quad (7.2.3)$$

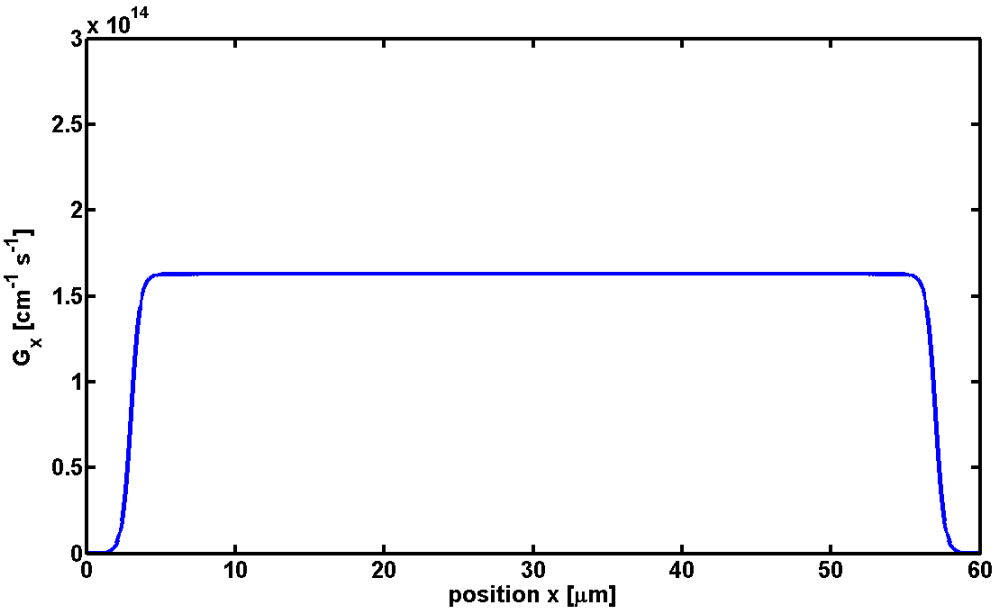

Figure 7.1. Generation rate G_x of excitons as a function of position x with spatially uniform illumination at photon energy $E_{ph} = E_{11}$ (= 0.56 eV) for the incident optical-power density P_{incd} = 10 kW/cm^2.

Figure 7.1 shows the generation rate G_x of excitons as a function of position x with spatially uniform illumination at photon energy $E_{ph} = E_{11}$ (= 0.56 eV) for incident optical-power density P_{incd} = 10 kW/cm^2. In order to calculate the incident light exciting the CNT channel but not the contacts, the incident light is assumed to illuminate the entire channel but not the contacts, as shown in Figure 7.1. The profile of G_x in the channel depicts a flat line due to uniform illumination. By using Equation (3.6.3), the value of G_x is obtained as 1.63x10^{14} cm^{-1} s^{-1}, which agrees with that in Figure 7.1. In order to compute the current gain, the value of $I_{ph,swept}$ is calculated as 276 nA using Equation (7.1.1). Since the diameter of a zigzag CNT (19,0) is so small (1.5 nm), the incident radiation absorbed by CNTs is very slight. The value of $I_{ph,swept}$ is small even for this large incident power density P_{incd}.

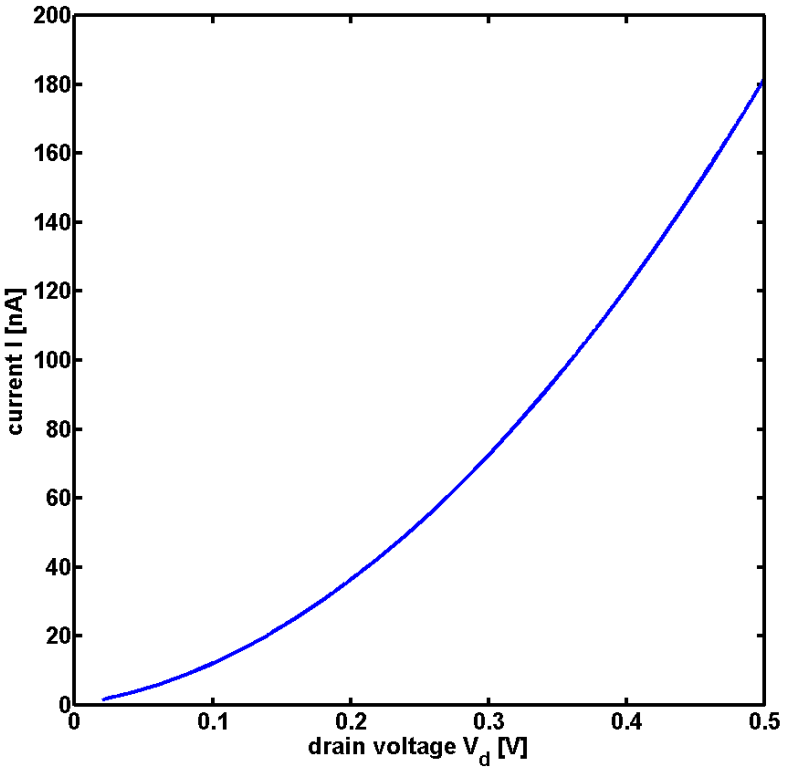

Figure 7.2. Current I as functions of V_d for V_g-V_{fb} = ½V_d with uniform photoexcitation at excitation energy $E_{ph} = E_{11}$ (= 0.56 eV) for incident power density P_{incd} = 10 kW/cm^2 in a CNT FET with a semiconducting zigzag CNT (19,0). The curves of I_{light} for cases C_1 and C_2 and of the dark current I_{dark} without illumination can not be distinguished in the plot.

Figure 7.2 shows the current I as a function of V_d for V_g-V_{fb} = ½V_d, i.e., the symmetric condition, with uniform photoexcitation at excitation energy $E_{ph} = E_{11}$ (= 0.56 eV) for incident power density P_{incd} = 10 kW/cm^2. The curves of I_{light} for cases C_1 and C_2 and of the dark current I_{dark} without illumination can not be distinguished in the plot. This means that the photocurrent I_{ph} (= I_{light}–I_{dark}) is very small compared with the dark current I_{dark}.

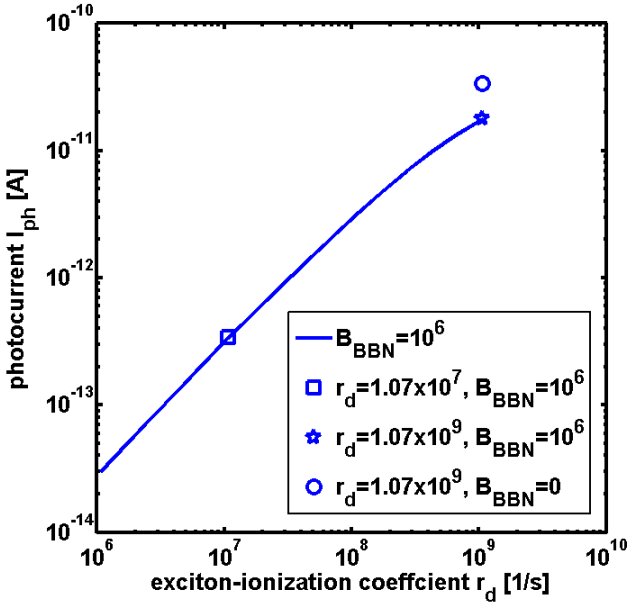

Figure 7.3. Photocurrent I_{ph} as a function of exciton-ionization coefficient r_d with uniform photoexcitation at excitation energy E_{ph} = 0.56 eV for the incident power density P_{incd} = 10 kW/cm^2 for V_d = 0.2 V and V_g-V_{fb} = 0.1 V, i.e., V_g-V_{fb} = ½V_d. The solid line includes BBN recombination (B_{BBN} = 10^6 cm/s). The square symbol is for case C_2, i.e., r_d = 1.07x10^7 s^{-1} and B_x = 10^4 cm/s, and the pentagonal symbol is for case C_3, i.e., r_d = 1.07x10^9 s^{-1} and B_x = 10^6 cm/s, while the circle is for case C_1, i.e., r_d = 1.07x10^9 s^{-1} and B_x = 10^6 cm/s but without BBN recombination.

Figure 7.3 shows the photocurrent I_{ph} as a function of exciton-ionization coefficient r_d with uniform photoexcitation at excitation energy E_{ph} = 0.56 eV for incident power density P_{incd} = 10 kW/cm^2 for V_d = 0.2 V and V_g-V_{fb} = 0.1 V, i.e., V_g-V_{fb} = ½V_d. The solid line includes BBN recombination (B_{BBN} = 10^6 cm/s). The square symol is for case C_2, i.e., r_d = 1.07x10^7 s^{-1} and B_x = 10^4 cm/s, and the pentagonal symbol is for case C_3, i.e., r_d = 1.07x10^9 s^{-1} and B_x = 10^6 cm/s, while the circle is for case C_1, i.e., r_d = 1.07x10^9 s^{-1} and B_x = 10^6 cm/s but without BBN recombination. The values of the photocurrent I_{ph} for cases C_1, C_2, and C_3 are 34 pA, 0.34 pA, and 18 pA, respectively.

Since the dark current I_{dark} is 36 nA, all values of the photocurrent I_{ph} are very small compared with the dark current. Since $I_{ph,swept}$ = 276 nA, the current gains Γ_G for cases C_1, C_2, and C_3 are $1.2\text{x}10^{-4}$, $1.2\text{x}10^{-6}$, and $6.5\text{x}10^{-5}$, respectively. We find that the current gains are very small. For a larger exciton-ionization coefficient r_d, more excitons ionize to e-h pairs, leading to a larger photocurrent I_{ph}. Larger r_d gives larger exciton-ionization efficiency $\eta_{ionized}$, and thus the current gain Γ_G is enhanced. Therefore, I_{ph} and Γ_G are larger in both cases C_1 and C_3 than in case C_2. The total recombination coefficient of electrons and holes is two times larger for case C_3 than for case C_1. The larger recombination coefficient means faster recombination and shorter recombination time τ_{recomb}, and thus using Equation (7.1.6) the gain Γ_G is smaller. Therefore, Γ_G and I_{ph} is smaller in case C_3 than in case C_1. The reasons for the very small photocurrent and current gain are explained below. Radiative and nonradiative decay of excitons compete with exciton ionization. Since the nonradiative decay coefficient r_{nr} of excitons is 20 ns^{-1} (= $2\text{x}10^{10}$ s^{-1}), the exciton-ionization coefficient r_d in Figure 7.3 is much smaller than the nonradiative decay coefficient r_{nr} of excitons. Most of the excitons nonradiatively decay rather than ionize to e-h pairs to contribute to the photocurrent. Therefore, the exciton-ionization efficiency $\eta_{ionized}$, the current gain Γ_G, and photocurrent I_{ph} are all small. Referring to Equation (3.8.3), the ratio of the exciton-ionization coefficient r_{di} to the capture parameter B_{xi} for exciton formation, i.e., r_{di}/B_{xi}, is proportional to $\exp(-E_b / k_b T)$, where E_b is the exciton binding energy. Since the exciton binding energy E_b (= 0.16 eV) is large in CNTs, even for the same value of B_x the value of the exciton-ionization coefficient r_d is small, and thus the exciton-ionization efficiency $\eta_{ionized}$, the current gain Γ_G, and photocurrent I_{ph} are small as well. Since the average longitudinal electrical field

$|F_x|_{ave}$ is proportional to the inverse of the channel length L for the same applied voltage V_d, referring to Equation (7.1.5) the average electron and hole transit times $t_{tr,e}$ and $t_{tr,h}$ are proportional to L^2. Thus the current gain Γ_G is proportional to L^{-2} due to Equation (7.1.6). Therefore, for photoconductors based on the long-channel (L = 60 μm) CNT FETs, the current gain Γ_G and photocurrent I_{ph} are small.

For comparison, results for photoconductors based on CNT FETs are calculated for case C_1, in which all of recombination of electrons and holes generates excitons, and for case C_2, in which most of recombination of electrons and holes does not generate excitons.

For case C_1, $B_x = 10^6$ cm/s, $r_d = 1.07\text{x}10^9$ s^{-1}, and BBN recombination is not included. All of recombination of electrons and holes generates excitons. Figure 7.4 shows photocurrent I_{ph} as a function of incident power density P_{incd} with uniform photoexcitation at photon energy E_{ph} = 0.56 eV with $r_d = 1.07\text{x}10^9$ s^{-1} and $B_x = 10^6$ cm/s for V_d = 0.2 V and V_g-V_{fb} = 0.1 V. For comparison, the results for cases C_1 and C_3 are shown as well. The solid line is for case C_1 without BBN recombination, and the dashed line is for case C_3 including BBN recombination. By referring to Equations (3.6.2) and (3.6.3), the absorption rate A_{abs} of the incident photons is proportional to P_{incd}, and the generation rate G_x of excitons is also proportional to P_{incd}. Thus both the exciton density n_{xs} and the exciton-ionization rate $r_d n_{xs}$ that contribute to the photocurrent are proportional to P_{incd} as well. Therefore, both the solid and dashed curves are linear in incident optical power, i.e., the photocurrent I_{ph} is proportional P_{incd}. This prediction is in excellent agreement with the reported experimental results [43]. The total recombination coefficient of electrons and holes is larger in case C_3 than in case C_1, and thus Γ_G and I_{ph}

are smaller in case C_3 (dashed line) than in case C_1 (solid line) due to the shorter recombination time, as mentioned above.

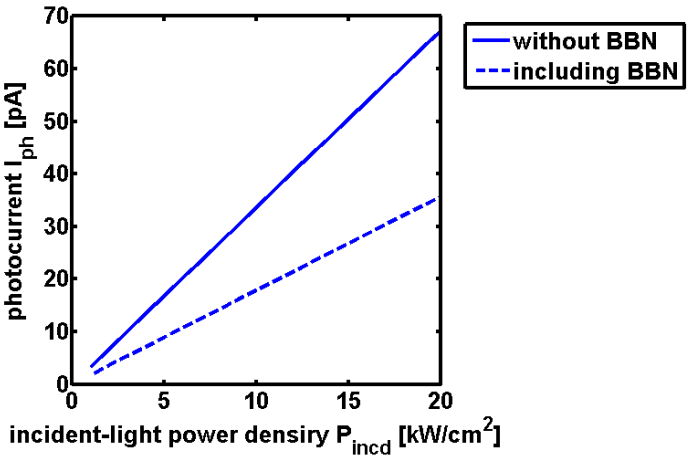

Figure 7.4. Photocurrent I_{ph} as a function of incident power density P_{incd} with uniform photoexcitation at photon energy E_{ph} = 0.56 eV with r_d = 1.07x10^9 s^{-1} and B_x = 10^6 cm/s for V_d = 0.2 V and V_g-V_{fb} = 0.1 V. The solid line is for case C_1 without BBN recombination, and the dashed line is for case C_3 including BBN recombination.

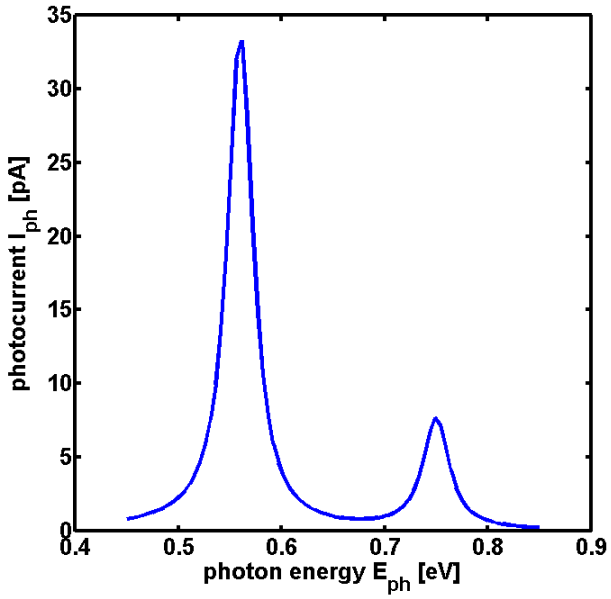

Figure 7.5. Photocurrent spectrum for case C_1. Photocurrent I_{ph} as a function of photon energy E_{ph} with uniform photoexcitation for the incident power density P_{incd} = 10 kW/cm^2 for V_d = 0.2 V and V_g-V_{fb} = 0.1 V.

Figure 7.5 shows the photocurrent spectrum for case C_1. The curve depicts photocurrent I_{ph} as a function of photon energy E_{ph} with uniform photoexcitation for the incident power density P_{incd} = 10 kW/cm^2 for V_d = 0.2 V and V_g-V_{fb} = 0.1 V. The photocurrent I_{ph} has the largest peak at the $E_{ph} = E_{11}$ (= 0.56 eV) corresponding to the excitation of bright excitons, and the full-width at half maximum (FWHM) is 0.03 eV. There is a side-band with a peak at $E_{ph} = E_{11}$+0.19 eV (= 0.75 eV), where the 0.19 eV corresponds to the effect of exciton-phonon coupling (longitudinal optical phonon energy) [21, 76], as mentioned above.

In Figures 7.6-7.8, the results for case C_1 are calculated with uniform photoexcitation at photon energy E_{ph} = 0.56 eV for incident power density P_{incd} = 10

kW/cm^2 for V_d = 0.2 V and V_g-V_{fb} = 0.1 V, i.e., V_g-V_{fb} = ½V_d for the symmetric condition. Figure 7.6 shows the electron and hole densities n and p as functions of position x with uniform photoexcitation for case C_1. The solid lines are for incident power density P_{incd} = 10 kW/cm^2, and the dashed lines are without illumination. The profiles of the electron and hole densities without illumination are similar to those for the optical emitters based on CNT FETs in an earlier chapter. When the channel length exceeds the recombination length, essentially all injected carriers recombine within the channel. Hence, for ambipolar CNT FETs, electrons injected from S fully recombine with holes in the channel and the electron density is negligible outside the recombination region, as mentioned above. Similarly, holes injected from D fully recombine with electrons in the channel and the hole density is negligible outside the recombination region as well. In Figure 7.6, two curves can not be distinguished in the plot. This means that with illumination the electrons and holes from exciton ionization are very few compared to the electrons and holes without illumination. This agrees with the small photocurrent compared with the dark current in Figure 7.2.

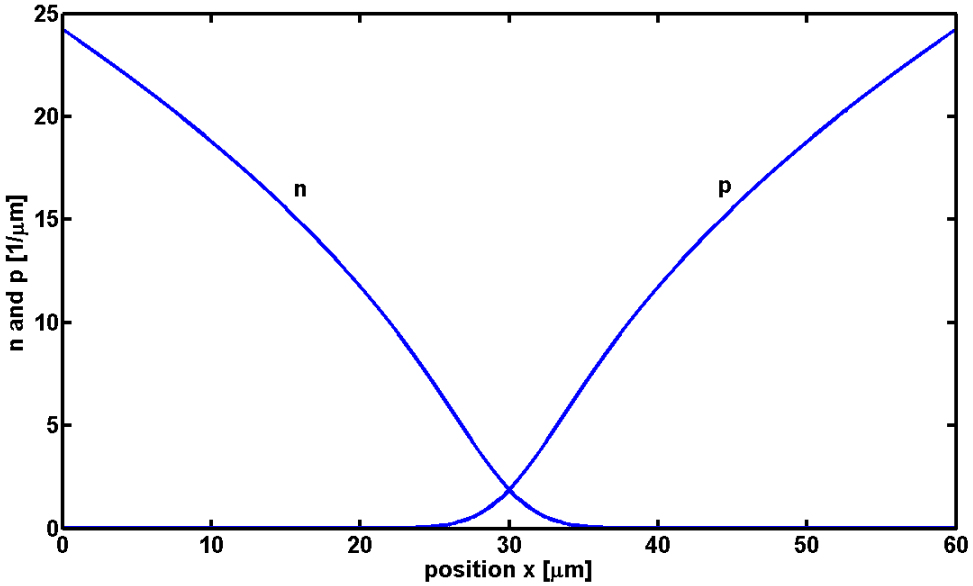

Figure 7.6. Electron and hole densities n and p as functions of position x with uniform photoexcitation at photon energy E_{ph} = 0.56 eV for V_d = 0.2 V and V_g-V_{fb} = 0.1 V for case C_1. The solid lines are for the incident power density P_{incd} = 10 kW/cm^2, and the dashed lines are without illumination. Two curves can not be distinguished in the plot.

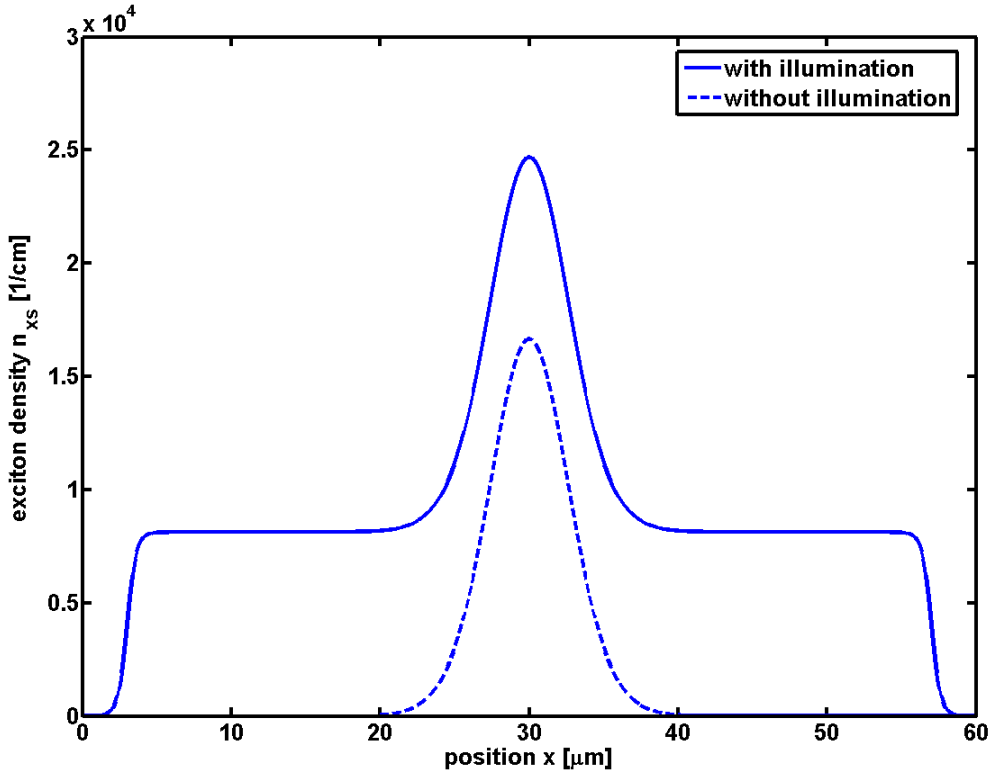

Figure 7.7. Singlet-exciton density n_{xs} (solid curve) as a function of position x with uniform photoexcitation at photon energy E_{ph} = 0.56 eV for the incident power density P_{incd} = 10 kW/cm^2 for V_d = 0.2 V and V_g-V_{fb} = 0.1 V for case C_1. The dashed curve is the exciton density without illumination.

Figure 7.7 shows the singlet-exciton density n_{xs} (solid curve) as a function of position x with uniform photoexcitation for case C_1. For V_d = 0.2 V and V_g-V_{fb} = 0.1 V, i.e., V_g-V_{fb} = ½V_d for the symmetric condition, the peak of the recombination rate of electrons and holes is at the middle of the channel. Without illumination there are the exciton densities (dashed curve) in the recombination region since all of recombination of electrons and holes generate the excitons through $B_x np$. With illumination the profile of exciton density (solid curve) is flat line outside the recombination region due to the flat

profile of the exciton generation rate resulting from uniform photoexcitation, as shown in Figure 7.1. Within the recombination region the exciton generation rates both by the photoexcitation and by the recombination of electrons and holes combine together to obtain higher exciton densities.

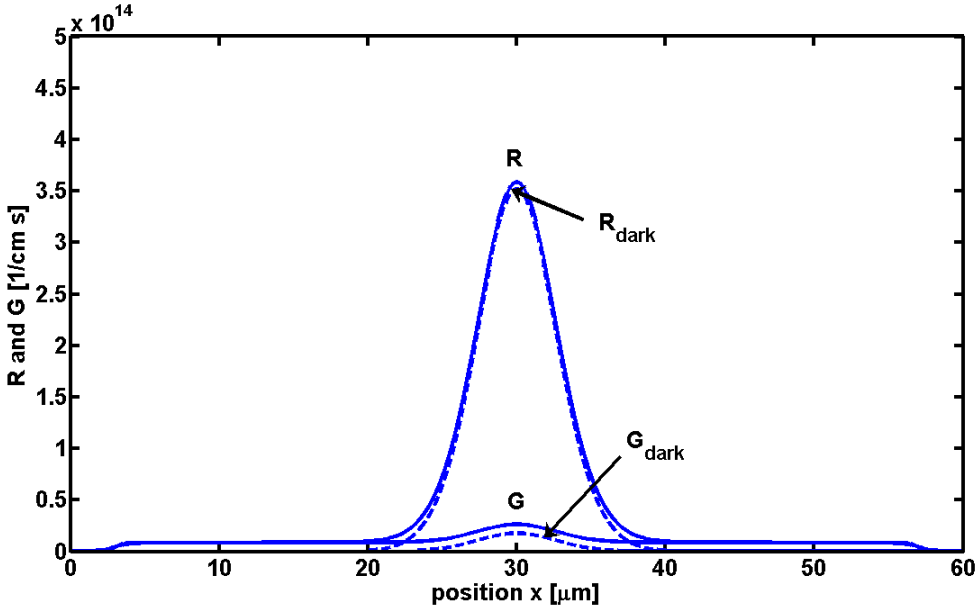

Figure 7.8. Recombination and generation rates R (upper solid curve) and G (lower solid curve) of electrons and holes as functions of position x with uniform photoexcitation at photon energy E_{ph} = 0.56 eV for the incident power density P_{incd} = 10 kW/cm^2 for V_d = 0.2 V and V_g-V_{fb} = 0.1 V for case C_1. The recombination and generation rates without illumination are indicated as R_{dark} (upper dashed curve) and G_{dark} (lower dashed curve), respectively.

Figure 7.8 shows the recombination and generation rates R (upper solid curve) and G (lower solid curve) of electrons and holes as functions of position x with uniform

photoexcitation for case C_1. The exciton-ionization rate $r_d n_{xs}$ is the generation rate of electrons and holes, and thus G (lower solid curve) with illumination and G_{dark} (lower dashed curve) without illumination show the same profiles as the exciton densities in Figure 7.7. For $r_d = 1.07 \times 10^9$ s^{-1}, the flat part of G in Figure 7.8 has the value of 8.7×10^{12} cm^{-1}s^{-1} corresponding to the exciton density $n_{xs} = 8.1 \times 10^3$ cm^{-1} in Figure 7.7. When the channel length exceeds the recombination length for the long channel CNT FETs, essentially all electrons and holes recombine within the channel, and thus the device current is equal to the recombination current. Hence, without illumination, the recombination rate R_{dark} (upper dashed curve) is much larger than the generation rate G_{dark} (lower dashed curve) within the recombination region in the middle of the channel. Similarly, with illumination, the recombination rate R (upper solid curve) is much larger than the generation rate G (lower solid curve) in the middle of the channel. Moreover, R is close to G in the area away from the middle of the channel since all generated electrons and holes recombine there. In addition, the value of the current $I_{light} = e\int_0^L (R-G)dx$ with illumination is close to the value of the current $I_{dark} = e\int_0^L (R_{dark} - G_{dark})dx$ without illumination due to I_{light} is close to I_{dark}, as shown in Figure 7.2.

For case C_2, $B_x = 10^4$ cm/s, $r_d = 1.07 \times 10^7$ s^{-1}, and BBN recombination ($B_{BBN} = 10^6$ cm/s) is included. Most of the recombination of electrons and holes does not generate excitons. Figure 7.9 shows the photocurrent I_{ph} as a function of incident power density P_{incd} with uniform photoexcitation at photon energy $E_{ph} = 0.56$ eV for $V_d = 0.2$ V and V_g-$V_{fb} = 0.1$ V for case C_2. The photocurrent I_{ph} lies on a straight line, i.e., the photocurrent I_{ph} is proportional to the incident power density P_{incd}, as mentioned above. For $P_{incd} = 10$ kW/cm^2, the value of I_{ph} (= 0.34 pA) for case C_2 in Figure 7.9 is about 1% of the value of

I_{ph} (= 34 pA) for case C_1 in Figure 7.4 since the value of the exciton-ionization coefficient r_d for case C_2 is about 1% of the value for case C_1.

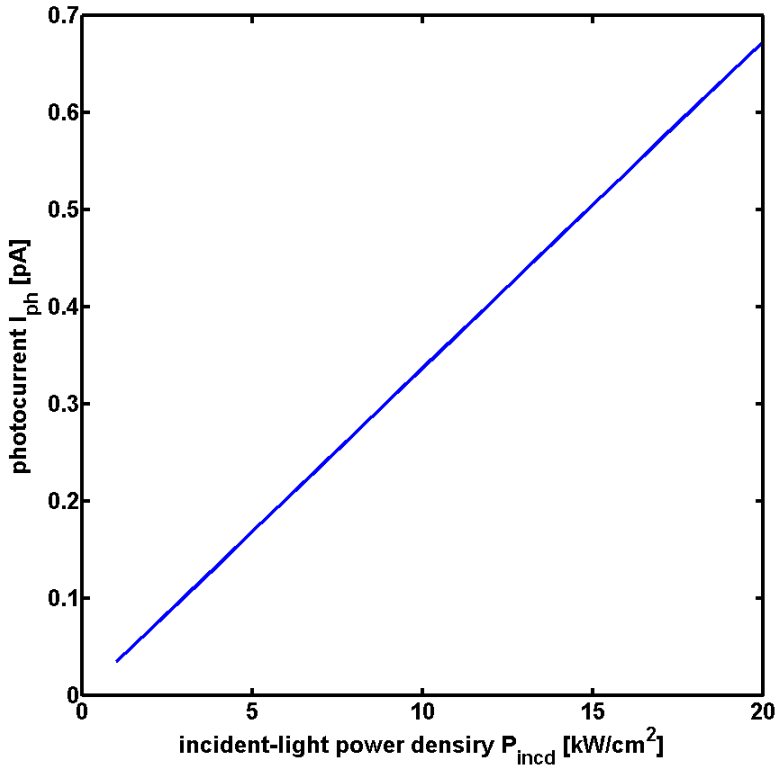

Figure 7.9. Photocurrent I_{ph} as a function of incident power density P_{incd} with uniform photoexcitation at photon energy E_{ph} = 0.56 eV with $r_d = 1.07 \times 10^7$ s^{-1} and $B_x = 10^4$ cm/s including BBN recombination for V_d = 0.2 V and V_g-V_{fb} = 0.1 V for case C_2.

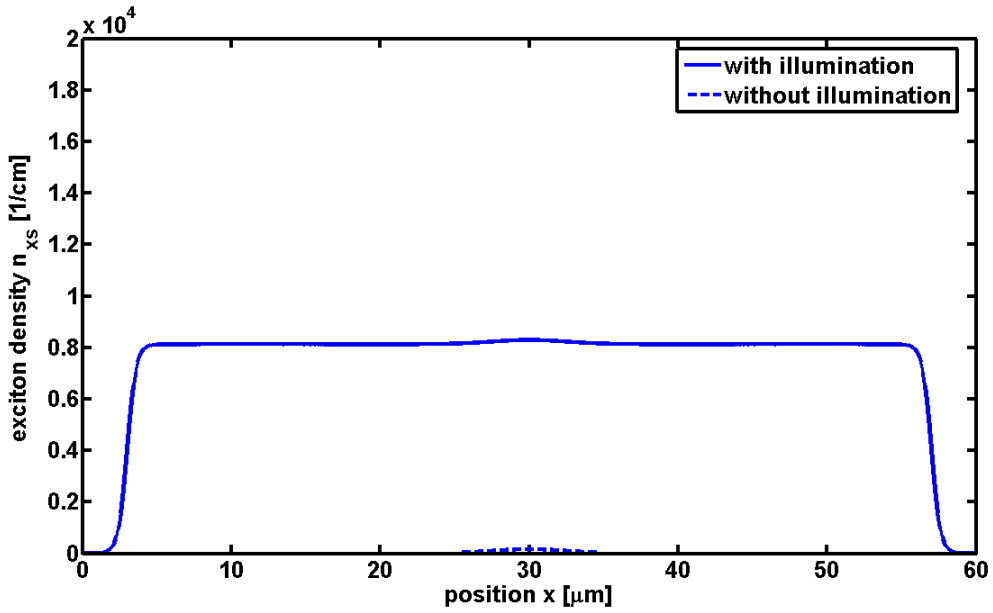

Figure 7.10. Singlet-exciton density n_{xs} (solid curve) as a function of position x along the channel with uniform photoexcitation at photon energy E_{ph} = 0.56 eV for the incident power density P_{incd} = 10 kW/cm^2 for V_d = 0.2 V and V_g-V_{fb} = 0.1 V for case C_2. The dashed curve is without illumination.

In Figures 7.10 and 7.11, results for case C_2 are shown for uniform photoexcitation at photon energy E_{ph} = 0.56 eV for incident-density P_{incd} = 10 kW/cm^2 for V_d = 0.2 V and V_g-V_{fb} = 0.1 V, i.e., V_g-V_{fb} = ½V_d for the symmetric condition. Figure 7.10 shows the singlet-exciton density n_{xs} (solid curve) as a function of position x along the channel with uniform photoexcitation for case C_2. Since the value of B_x is about 1 % B_{BBN}, only ~1% of the recombination of electrons and holes generates the excitons. Without illumination there is an exciton density (dashed curve) within the recombination region, but the value of n_{xs} (dashed curve) in Figure 7.10 is about 1 % of the value of n_{xs} (dashed ccurve) in Figure 7.7. With illumination the profile of n_{xs} (solid curve) is a flat

line due to the flat profile of the exciton generation through the uniform photoexcitation in Figure 7.1, and the value of n_{xs} in Figure 7.10 has the same value 8.1 x10^3 cm^{-1} as in Figure 7.7. Since n_{xs} (dashed curve) due to the recombination of electrons and holes is much lower than n_{xs} (solid curve) through the photoexcitation, the profile of n_{xs} looks like a flat line within the entire channel. Moreover, the profiles of the electron and hole densities n and p as functions of position x with uniform photoexcitation for case C_2 are similar to those in Figure 7.6 since with illumination the electrons and holes from the exciton ionization are very few compared to the electrons and holes without illumination, as mentioned above.

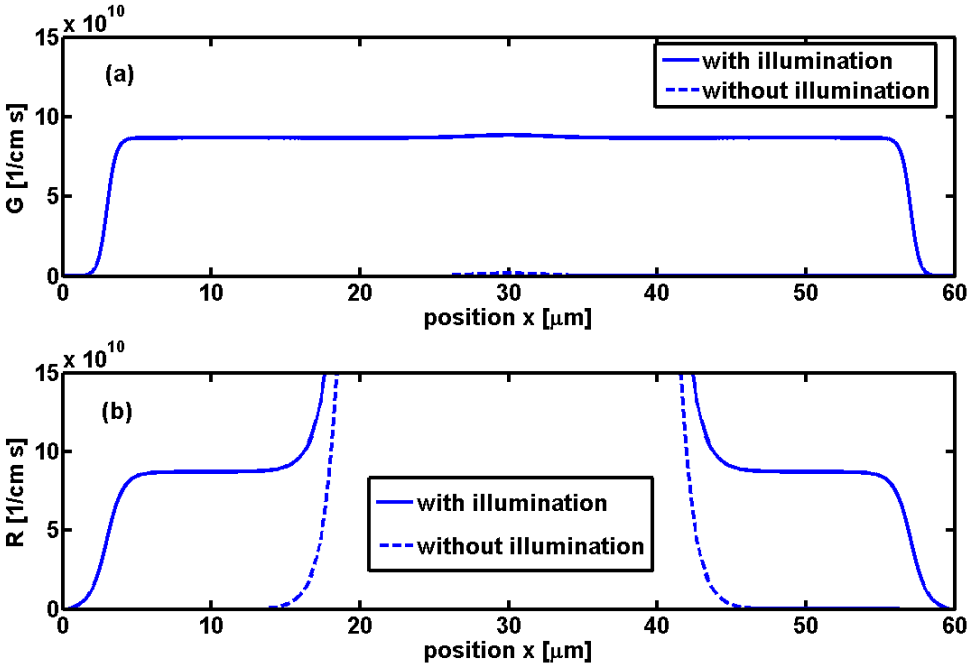

Figure 7.11. (a) Generation rate G (solid curve) and (b) recombination rate R (solid curve of electrons and holes as functions of position x with uniform photoexcitation at photon energy E_{ph} = 0.56 eV for the incident power density P_{incd} = 10 kW/cm^2 for V_d = 0.2 V and V_g-V_{fb} = 0.1 V for case C_2. The dashed curves are for the generation and recombination rates without illumination.

Figure 7.11 shows (a) the generation rate G (solid curve) and (b) recombination rate R (solid curve) of electrons and holes as functions of position x with uniform photoexcitation for case C_2. Since the exciton-ionization rate $r_d n_{xs}$ is the generation rate of electrons and holes, the solid curve with illumination and the dashed curve without illumination in Figure 7.11(a) show the same profiles as the exciton densities in Figure 7.10. For r_d = 1.07x10^7 s^{-1}, the flat line of G in Figure 7.11(a) has the value of 8.7 x10^{10} cm^{-1}s^{-1} corresponding to the exciton density n_{xs} = 8.1 x10^3 cm^{-1} in Figure 7.10. Since essentially all electrons and holes recombine within the channel, the device current is

equal to the recombination current. Hence, with illumination, the recombination rate R (solid curve) in Figure 7.11(b) in the middle of the channel is much larger than the generation rate G, as mentioned above. Moreover, R (solid curve) in Figure 7.11(b) is close to G (solid curve) in Figure 7.11(a) in the area away from the middle of the channel since all generated electrons and holes recombine there.

7.3 Results for Photoconductors Based on Carbon-Nanotube Field-Effect Transistors with Near-Field Photoexcitation

The photoconductivity of CNT FETs has been explored experimentally with near-field photoexcitation [65-69], and the typical incident laser power is in the range of 0.5-1 mW. The laser was focused to a 300-400 nm diameter spot and scanned across the samples of CNT FETs, and the incident power densities are on the order of hundreds kW/cm^2. Hence, the photoconductors based on CNT FETs with a semiconducting zigzag CNT (19,0) for the incident laser power W_{incd} = 1 mW with near-field photoexcitation with the laser focused to a 400 nm diameter spot are chosen to be calculated. The incident power density is assumed as a spatial Gaussian, and thus the maximum value is computed as 552 kW/cm^2. The laser is assumed to be scanned across the channel of CNT FETs but not across the contacts. The results are solved for in terms of the intrinsic voltages V_g-V_{fb} and V_d, and the value of V_d = 0.2 V is chosen to be calculated, as mentioned above.

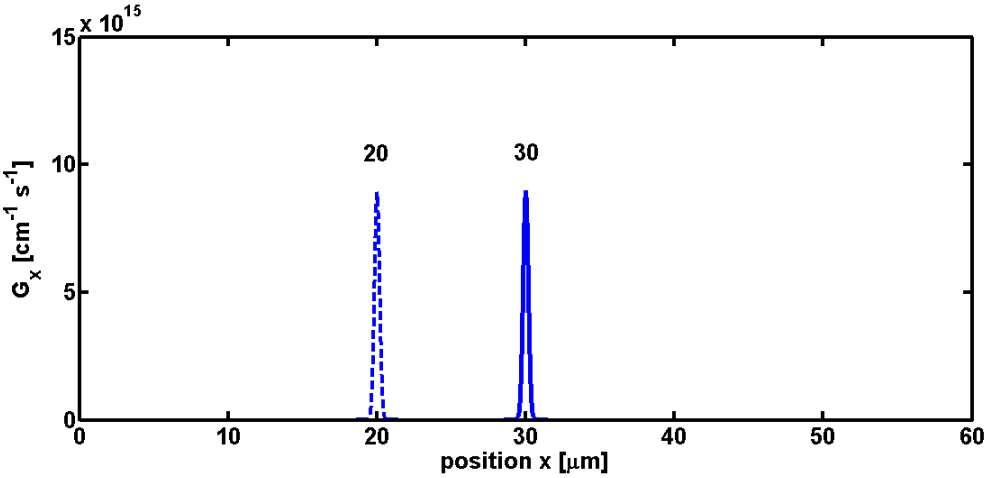

Figure 7.12. Generation rate G_x of excitons as a function of position x with near-field photoexcitation at photon energy E_{ph} = 0.56 eV with the incident laser power W_{incd} = 1 mW. The laser is focused to a 400-nm diameter spot, and illuminates at the photoexcitation position x_{ph} = 30 μm (solid curve) and 20 μm (dashed curve).

Figure 7.12 shows the generation rate G_x of excitons as a function of position x with near-field photoexcitation at photon energy E_{ph} = 0.56 eV with the incident laser power W_{incd} = 1 mW. The laser is focused to a 400-nm diameter spot, and illuminates at the photoexcitation position x_{ph} = 30 μm (solid curve) and 20 μm (dashed curve). The spatial profile of G_x in the channel follows that of the excitation spot, i.e., a Gaussian. By using Equation (3.6.3), the peak value of G_x can be obtained as 8.98×10^{15} cm^{-1} s^{-1}, and this value agrees with that in Figure 7.12. In order to compute the current gain, the value of $I_{ph,swept}$ is calculated as 123 nA by Equation (7.1.1). Since the diameter of a zigzag CNT (19,0) is so small (1.5 nm), the incident radiation absorbed by the CNTs is very small. The value of $I_{ph,swept}$ is small even for this large incident laser power W_{incd}.

For comparison, the results for photoconductors based on CNT FETs are calculated for case C_1, in which all of recombination of electrons and holes generates the excitons, and for case C_2, in which most of recombination of electrons and holes do not generate excitons.

For case C_1, $B_x = 10^6$ cm/s, = $r_d = 1.07\text{x}10^9$ s^{-1}, and BBN recombination is not included. All of recombination of electrons and holes generates excitons. Figure 7.13 shows photocurrent I_{ph} as a function of incident power W_{incd} with near-field photoexcitation at photon energy $E_{ph} = 0.56$ eV for $V_d = 0.2$ V and V_g-$V_{fb} = 0.1$ V for case C_1. The laser is focused to a 400-nm diameter spot, and illuminates at the position x_{ph} = 30 μm (solid curve) and 20 μm (dashed curve). Since the incident laser-power density is proportional to the incident-laser power W_{incd}, by referring to Equations (3.6.2) and (3.6.3) the absorption rate A_{abs} of the incident photons is proportional to W_{incd}, and the generation rate G_x of excitons is also proportional to W_{incd}. Thus both the exciton density n_{xs} and the exciton-ionization rate $r_d n_{xs}$ contributing to the photocurrent are proportional to W_{incd} as well. Therefore, both solid and dashed curves are linear, i.e., photocurrent I_{ph} is proportional to incident power W_{incd}. In the following figures of Figures 7.14-7.21, the results for case C_1 are calculated with near-field photoexcitation at photon energy E_{ph} = 0.56 eV for incident power $W_{incd} = 1$ mW for $V_d = 0.2$ V and V_g-$V_{fb} = 0.1$ V, and the laser is focused to a 400-nm diameter spot. By referring to Equations (7.1.5) and (7.1.6), the average electron and hole transit times $t_{tr,e}$ and $t_{tr,h}$ are proportional to the inverse of the average longitudinal electrical field $|F_x|_{ave}$, and thus both the current gain Γ_G and the photocurrent I_{ph} are proportional to $|F_x|_{ave}$. Figure 7.14 shows the longitudinal electric field $|F_x|$ as a function of position x with near-field photoexcitation with the incident

power W_{incd} = 1 mW for case C_1. In the symmetric condition, i.e., V_g-V_{fb} = ½V_d, the maximum longitudinal electric field $|F_x|$ is at the middle of the channel, i.e., at the position x = 30 μm. Figure 7.15 shows photocurrent I_{ph} as a function of photoexcitation position x_{ph} with near-field excitation with incident power W_{incd} = 1 mW for case C_1. Since the average value $|F_x|$ of at x = 30 μm is larger than at x = 20 μm as shown in Figure 7.14, the photocurrent I_{ph} at photoexcitation position x_{ph} = 30 μm is larger than at x_{ph} = 20 μm, as shown in both Figures 7.13 and 7.15. The values of photocurrent I_{ph} for photoexcitation position x_{ph} = 30 μm and x_{ph} = 20 μm with W_{incd} = 1 mW are 48 pA and 12 pA, respectively. Since the dark current I_{dark} is 36 nA, the values of the photocurrent I_{ph} are very small compared with the dark current. Since $I_{ph,swept}$ = 123 nA, the current gains Γ_G for the photoexcitation position x_{ph} = 30 μm and x_{ph} = 20 μm are 3.9×10^{-4} and 9.6×10^{-5}, respectively. We find that the current gains are very small. The explanations for the small current gain and small photocurrent are presented in Chapter 7.2. Since the photocurrents are small compared to the dark current, in Figure 7.14 the longitudinal electric fields $|F_x|$ for the photoexcitation position x_{ph} = 30 μm (solid curve) and for x_{ph} = 20 μm (dashed curve) are close to the dotted curve (dark) without illumination.

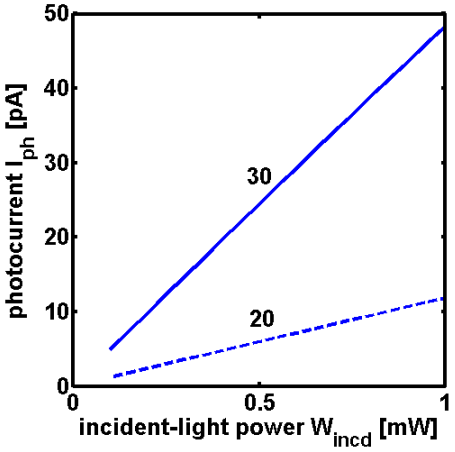

Figure 7.13. Photocurrent I_{ph} as a function of incident power W_{incd} with near-field photoexcitation at photon energy E_{ph} = 0.56 eV for V_d = 0.2 V and V_g-V_{fb} = 0.1 V for case C_1. The laser is focused to a 400-nm diameter spot, and illuminates at the position x_{ph} = 30 μm (solid curve) and 20 μm (dashed curve).

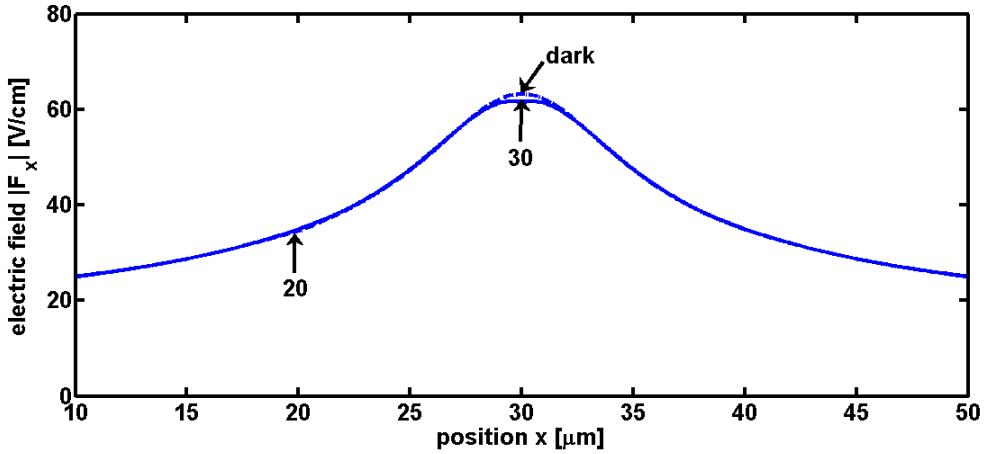

Figure 7.14. Longitudinal electric field $|F_x|$ as a function of position x with near-field photoexcitation at photon energy E_{ph} = 0.56 eV with the incident power W_{incd} = 1 mW for V_d = 0.2 V and V_g-V_{fb} = 0.1 V for case C_1. The laser is focused to a 400-nm diameter spot. The solid and dashed curves are for the photoexcitation position x_{ph} = 30 μm and 20 μm, respectively, while the dotted curve (dark) is without illumination.

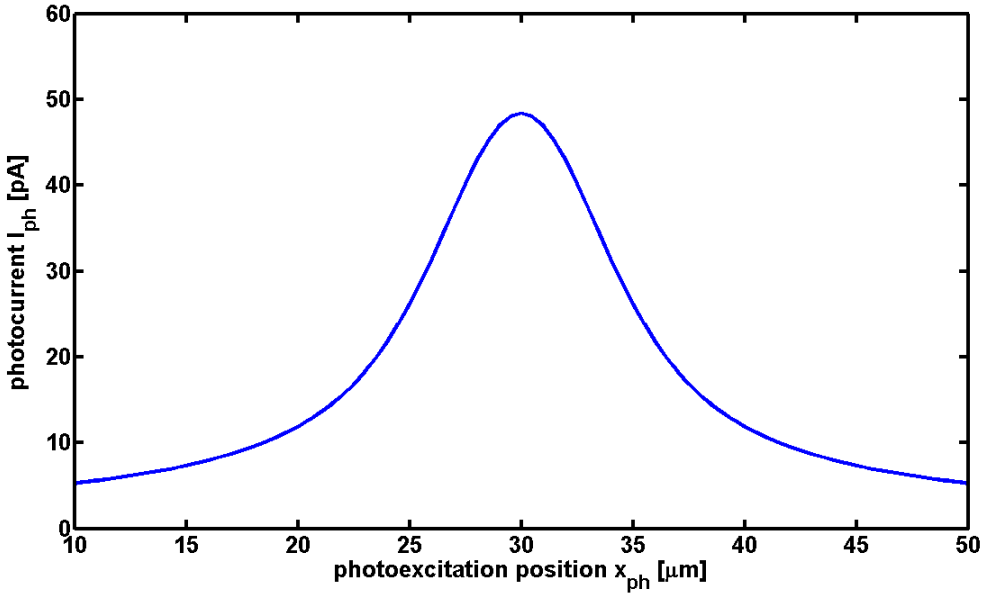

Figure 7.15. Photocurrent I_{ph} as a function of photoexcitation position x_{ph} with near-field photoexcitation at photon energy E_{ph} = 0.56 eV with the incident power W_{incd} = 1 mW for V_d = 0.2 V and V_g-V_{fb} = 0.1 V for case C_1. The laser is focused to a 400-nm diameter spot.

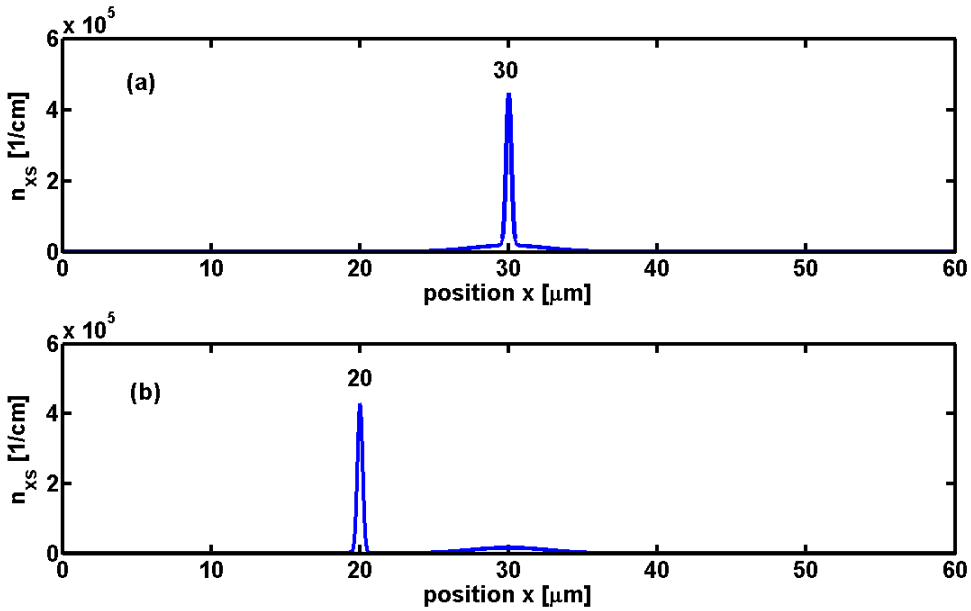

Figure 7.16. Singlet-exciton density n_{xs} as functions of position x with near-field photoexcitation at photon energy E_{ph} = 0.56 eV with the incident power W_{incd} = 1 mW for V_d = 0.2 V and V_g-V_{fb} = 0.1 V for case C_1. The laser is focused to a 400-nm diameter spot. The illumination is at the photoexcitation position x_{ph} = 30 μm in (a) and at x_{ph} = 20 μm in (b).

Figure 7.16 shows the singlet-exciton density n_{xs} as functions of position x with near-field photoexcitation for case C_1. The illumination is at photoexcitation position x_{ph} = 30 μm in Figure 7.16(a) and at x_{ph} = 20 μm in Figure 7.16(b). For V_d = 0.2 V and V_g-V_{fb} = 0.1 V, i.e., V_g-V_{fb} = ½V_d for the symmetric condition, the peak of the recombination rate of electrons and holes is at the middle of the channel. Without illumination there are the exciton densities at the middle of the channel within the recombination region since all the recombination of electrons and holes generates excitons through $B_x np$, as mentioned above. With illumination the profile of exciton density in both Figure 7.16(a) and Figure 7.16(b) depicts a Gaussian profile at the photoexcitation position x_{ph} due to

the Gaussian profile of the exciton generation rate through near-field photoexcitation, as shown in Figure 7.12. The peak values of n_{xs} in Figure 7.16 are much larger than those in Figure 7.7 since the peak value of the incident power density (= 522 kW/cm^2) with near-field photoexcitation is much larger than that (= 10 kW/cm^2) with uniform photoexcitation. The exciton generation rates both by the photoexcitation and by recombination of electrons and holes sum to give the total exciton densities. In Figure 7.16(b), n_{xs} shows two parts: one is from exciton ionization at the photoexcitation position x_{ph} through the photoexcitation, another is from the recombination of electrons and holes in the middle of the channel. However, in Figure 7.16(a), n_{xs} shows only one part since the photoexcitation position x_{ph} is close to the recombination region of electrons and holes. Moreover, the profiles of the electron and hole densities n and p as functions of position x with near-field photoexcitation for case C_1 are similar to those in Figure 7.6 since with illumination the densities of the electrons and holes from the exciton ionization through photoexcitation are very few in comparison with those without illumination, as mentioned above.

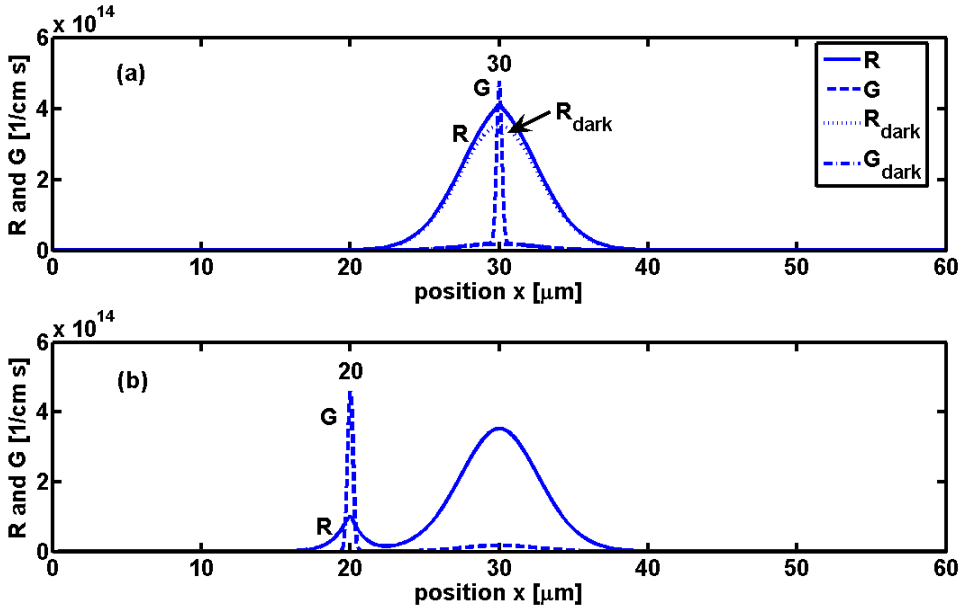

Figure 7.17. Recombination and generation rates R (solid curves) and G (dashed curves) of electrons and holes as functions of position x with near-field photoexcitation at photon energy E_{ph} = 0.56 eV with the incident power W_{incd} = 1 mW for V_d = 0.2 V and V_g-V_{fb} = 0.1 V for case C_1. The laser is focused to a 400-nm diameter spot. The illumination is centered at the photoexcitation position x_{ph} = 30 μm in (a), and at x_{ph} = 20 μm in (b). The dotted curve (R_{dark}) and the dash-dot curve (G_{dark}) are for the recombination and generation rates without illumination.

Figure 7.17 shows the recombination and generation rates R (solid curves) and G (dashed curves) of electrons and holes as functions of position x with near-field photoexcitation for case C_1. The illumination is centered at x_{ph} = 30 μm in Figure 7.17(a), and at x_{ph} = 20 μm in Figure 7.17(b). The exciton-ionization rate $r_d n_{xs}$ is the generation rate of electrons and holes, and thus G (dashed curves) with illumination and G_{dark} (dash-dot curves) without illumination show the same profiles as the exciton densities in Figure 7.16. For $r_d = 1.07 \times 10^9$ s^{-1}, the peak of G in Figure 7.17(b) has the value of 4.5×10^{14} cm^{-1}s^{-1} corresponding to the peak value of the exciton density n_{xs} =

$4.2\text{x}10^5$ cm^{-1} in Figure 7.16(b). In Figure 7.17(b) *R* and *G* show two parts since the photoexcitation position x_{ph} is far from the middle of the channel, which is the major recombination region of electrons and holes. However, in Figure 7.17(a) *R* and *G* show only one part since the photoexcitation position x_{ph} is close to the middle of the channel. In Figure 7.17(b) the profile of the recombination rate *R* broadens in comparison with that of the generation rate *G* at the photoexcitation position x_{ph}. This means that the generated electrons from exciton ionization at x_{ph} move toward D and recombine with the holes nearby. Similarly, the generated holes from exciton ionization at x_{ph} move toward S and recombine with the electrons near there. When the channel length exceeds the recombination length, the device current is equal to the recombination current, as mentioned above. The value of current $I_{light} = e\int_0^L (R-G)dx$ with illumination is close to the value of the current $I_{dark} = e\int_0^L (R_{dark} - G_{dark})dx$ without illumination due to I_{light} is close to I_{dark}, i.e., the photocurrent I_{ph} is small. Hence, in Figure 7.17(b) at photoexcitation position x_{ph} the value of $\int_0^L Rdx$ is close to the value of $\int_0^L Gdx$, and the peak of *R* is lower than that of *G*.

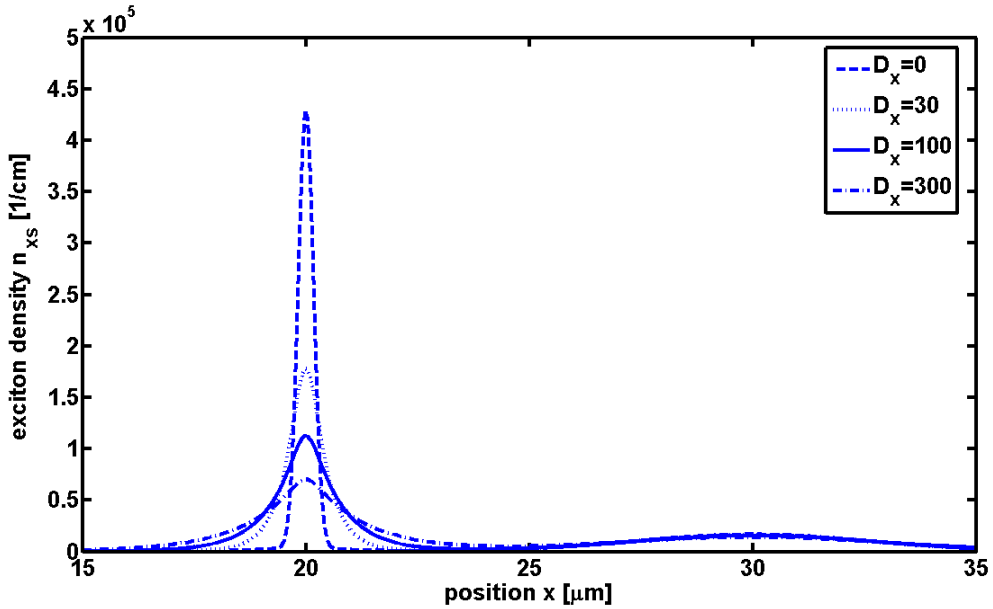

Figure 7.18. Singlet-exciton density n_{xs} as a function of position x with near-field photoexcitation at photon energy E_{ph} = 0.56 eV with the incident power W_{incd} = 1 mW for V_d = 0.2 V and V_g-V_{fb} = 0.1 V for case C_1. The laser illumination is focused at x_{ph} = 20 μm. The dashed, dotted, solid, and dash-dot curves are for the exciton-diffusion coefficients D_x = 0, 30, 100, 300 cm^2/s, respectively.

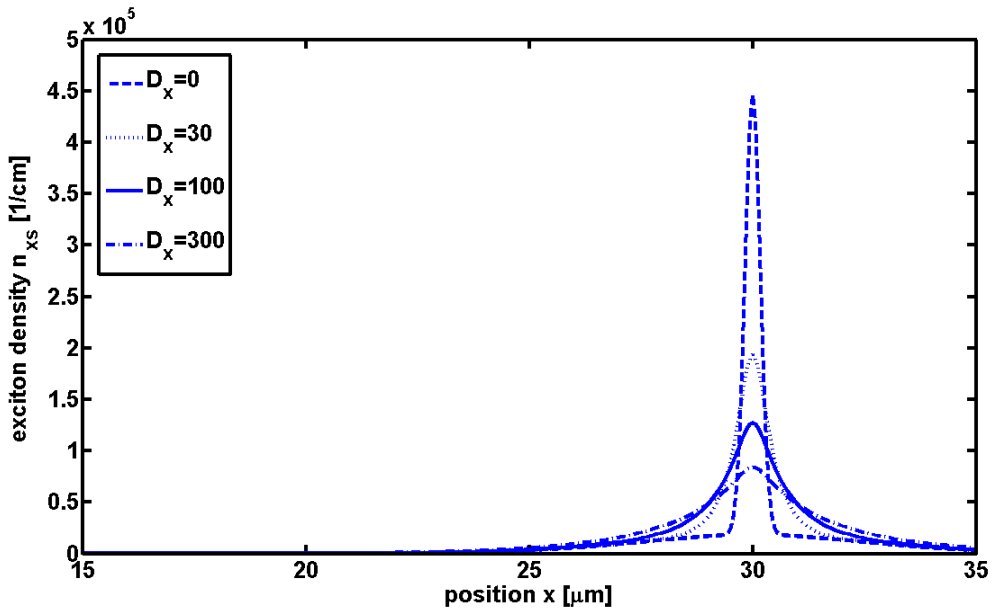

Figure 7.19. Singlet-exciton density n_{xs} as a function of x with near-field photoexcitation at photon energy E_{ph} = 0.56 eV with the incident power W_{incd} = 1 mW for V_d = 0.2 V and V_g-V_{fb} = 0.1 V for case C_1. The laser illumination is focused at x_{ph} = 30 μm. The dashed, dotted, solid, and dash-dot curves are for the exciton-diffusion coefficients D_x = 0, 30, 100, 300 cm^2/s, respectively.

Since the measured exciton-diffusion coefficient is ~100±50 cm^2 s^{-1} [97-99], D_x is assumed as 100 cm^2 s^{-1}. For comparison, the results for D_x = 30 and 300 cm^2 s^{-1} are calculated as well. Figure 7.18 shows the singlet-exciton density n_{xs} as a function of position x with near-field photoexcitation for case C_1. The laser illumination is focused at x_{ph} = 20 μm. The dashed, dotted, solid, and dash-dot curves are for the exciton-diffusion coefficients D_x = 0, 30, 100, 300 cm^2/s, respectively. There are two parts for n_{xs}: one from the photoexcitation at the photoexcitation position x_{ph}, and another from the recombination of electrons and holes in the middle of the channel, as mentioned above. At photoexcitation position x_{ph} = 20 μm, the value of n_{xs} broadens more, and the peak of

n_{xs} is lower for the higher D_x. Figure 7.19 shows n_{xs} as a function of x under near-field photoexcitation at position x_{ph} = 30 μm for case C_1. Since the photoexcitation position x_{ph} is close to the middle of the channel in the recombination region, two contributions to n_{xs} contribute at the same position; one from exciton ionization through the photoexcitation, and another from the recombination of electrons and holes. Similarly, the value of n_{xs} broadens more, and the peak of n_{xs} is lower for higher D_x, as well. The photocurrents I_{ph} at photoexcitation position x_{ph} = 30 μm for D_x = 0, 30, 100, 300 cm^2/s are calculated as 48.4 pA, 47.9 pA, 46.9 pA, 44.3 pA, respectively. For the higher value of D_x the profile of n_{xs} broadens more, and then the average longitudinal electrical field $|F_x|_{ave}$ is lower. Since both the current gain Γ_G and the photocurrent I_{ph} are proportional to $|F_x|_{ave}$ as mentioned above, the photocurrent I_{ph} is lower for the higher value of D_x.

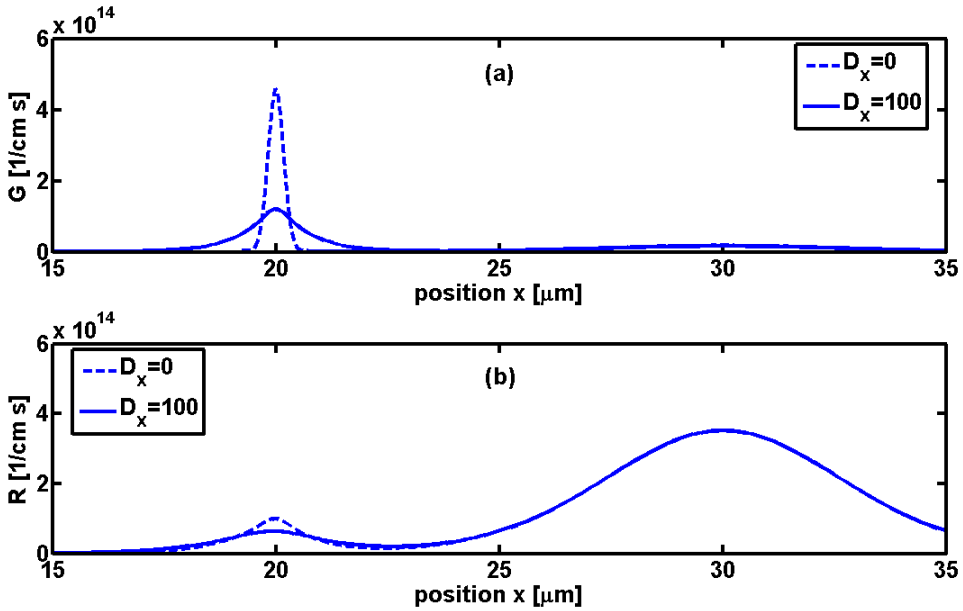

Figure 7.20. (a) Generation rate G and (b) recombination rate R of electrons and holes as functions of position x with near-field photoexcitation centered at x_{ph} = 20 μm for case C_1 The dashed and solid curves are for the exciton-diffusion coefficients D_x = 0 and 100 cm^2/s, respectively.

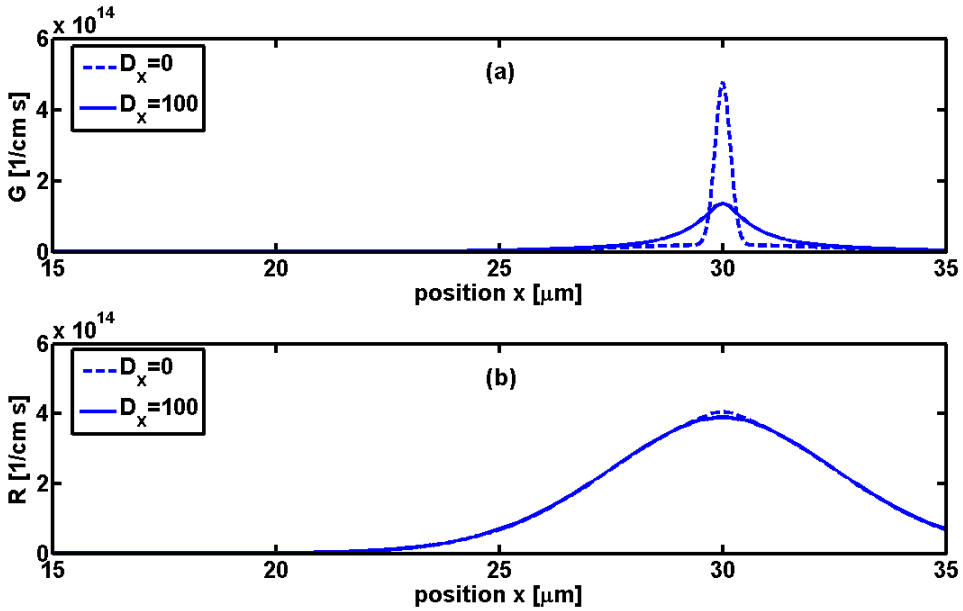

Figure 7.21. (a) Generation rate G and (b) recombination rate R of electrons and holes as functions of position x with near-field photoexcitation centered at x_{ph} = 30 μm for case C_1 The dashed and solid curves are for the exciton-diffusion coefficients D_x = 0 and 100 cm^2/s, respectively.

Figure 7.20 shows (a) the generation rate G and (b) the recombination rate R of electrons and holes as functions of position x with near-field photoexcitation centered at position x_{ph} = 20 μm for case C_1. The dashed and solid curves are for exciton-diffusion coefficients D_x = 0 and 100 cm^2/s, respectively. There are two main contributions from G and R since the photoexcitation position x_{ph} is away from the middle of the channel, which is the recombination region of electrons and holes. The profile of R broadens in comparison with that for G at photoexcitation position x_{ph}, as mentioned above. At photoexcitation position x_{ph} = 20 μm, the values of R and G broaden more and the peak values of R and G are lower for the higher D_x since the exciton density n_{xs} broadens.

Figure 7.21 shows (a) the generation rate G and (b) the recombination rate R of electrons and holes as functions of position x with near-field photoexcitation centered at x_{ph} = 30 μm for case C_1. In Figure 7.21, R and G show only one part since the photoexcitation position x_{ph} is close to the middle of the channel. At photoexcitation position x_{ph} = 30 μm, G broadens and the peak of G is lower for the higher D_x since the exciton density n_{xs} broadens. At x_{ph} = 30 μm the value of R for D_x = 100 cm^2/s is close to that of R for D_x = 0 since the recombination rate is large there.

For case C_2, $B_x = 10^4$ cm/s, $r_d = 1.07 \times 10^7$ s^{-1}, and BBN recombination ($B_{BBN} = 10^6$ cm/s) is included. Most of the recombination of electrons and holes does not generate excitons. Figure 7.22 shows photocurrent I_{ph} as a function of incident power W_{incd} with near-field photoexcitation at photon energy E_{ph} = 0.56 eV for V_d = 0.2 V and V_g-V_{fb} = 0.1 V for case C_2. The laser is focused to a 400-nm diameter spot, and illuminates at the photoexcitation position x_{ph} = 30 μm (solid curve) and 20 μm (dashed curve). Both solid and dashed curves fall on straight lines, i.e., the photocurrent I_{ph} is proportional to the incident power W_{incd}, as mentioned above. In the following figures of Figures 7.23-7.29, the results for case C_2 are calculated with near-field photoexcitation at photon energy E_{ph} = 0.56 eV for the incident power W_{incd} = 1 mW for V_d = 0.2 V and V_g-V_{fb} = 0.1 V, and the laser is focused to a 400-nm diameter spot. Figure 7.23 shows photocurrent I_{ph} as a function of photoexcitation position x_{ph} with near-field photoexcitation for incident power W_{incd} = 1 mW for case C_2. Both the current gain Γ_G and photocurrent I_{ph} are proportional to the average longitudinal electrical field $|F_x|_{ave}$, as mentioned above. Since the average value $|F_x|$ of at x = 30 μm is larger than at x = 20 μm, the photocurrent I_{ph} at the photoexcitation position x_{ph} = 30 μm is larger than at x_{ph} = 20 μm as shown in both

Figures 7.22 and 7.23. The values of photocurrent I_{ph} for photoexcitation position x_{ph} = 30 μm and x_{ph} = 20 μm with W_{incd} = 1 mW are 0.5 pA and 0.12 pA, respectively. Since the dark current I_{dark} is 36 nA, the values of the photocurrent I_{ph} are very small compared with the dark current. Since $I_{ph,swept}$ = 123 nA, the current gains Γ_G for the photoexcitation position x_{ph} = 30 μm and x_{ph} = 20 μm are 4.1×10^{-6} and 9.8×10^{-7}, respectively. We find that the current gains are very small. For x_{ph} = 30 μm with W_{incd} = 1 mW, the value of I_{ph} (= 0.5 pA) for case C_2 in Figure 7.22 is about 1 % of the value of I_{ph} (= 48 pA) for case C_1 in Figure 7.13 since the value of the exciton-ionization coefficient r_d for case C_2 is about 1 % of the value for case C_1.

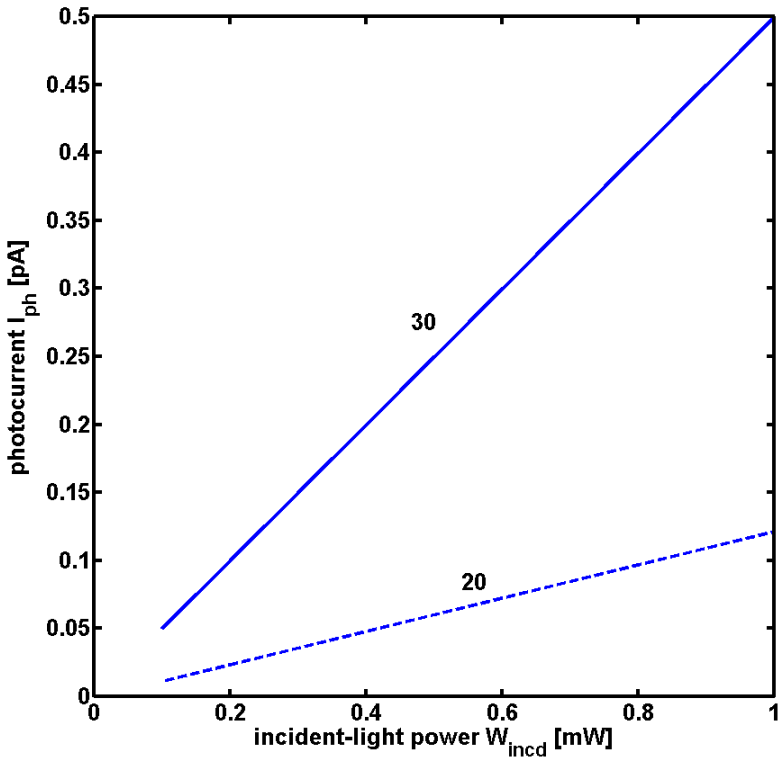

Figure 7.22. Photocurrent I_{ph} as a function of incident power W_{incd} with near-field photoexcitation at photon energy E_{ph} = 0.56 eV for V_d = 0.2 V and V_g-V_{fb} = 0.1 V for case C_2. The laser is focused to a 400-nm diameter spot, and illuminates at the photoexcitation position x_{ph} = 30 μm (solid curve) and 20 μm (dashed curve).

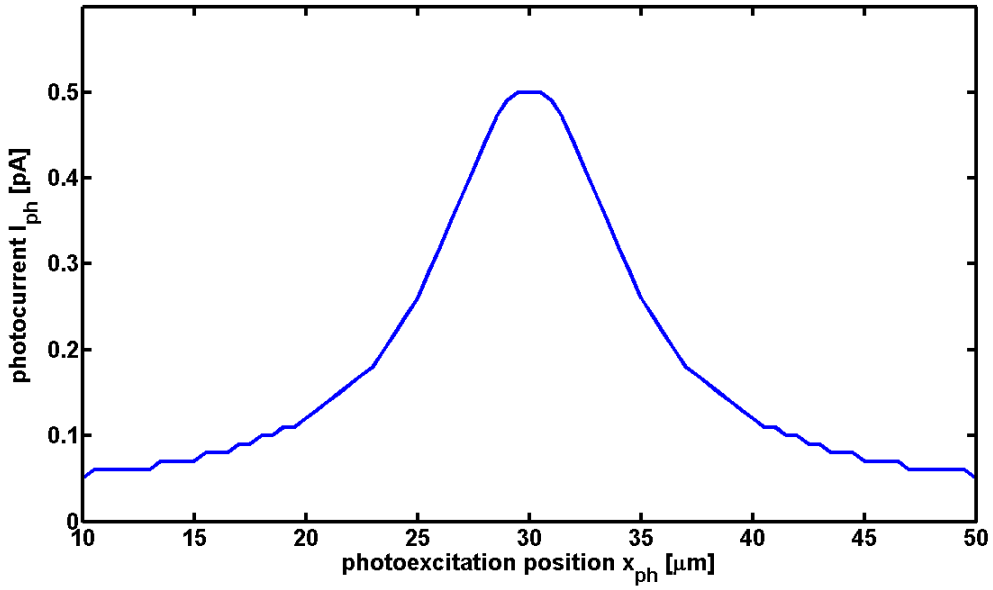

Figure 7.23. Photocurrent I_{ph} as a function of photoexcitation position x_{ph} with near-field photoexcitation at photon energy E_{ph} = 0.56 eV with the incident power W_{incd} = 1 mW for V_d = 0.2 V and V_g-V_{fb} = 0.1 V for case C_2. The laser is focused to a 400-nm diameter spot.

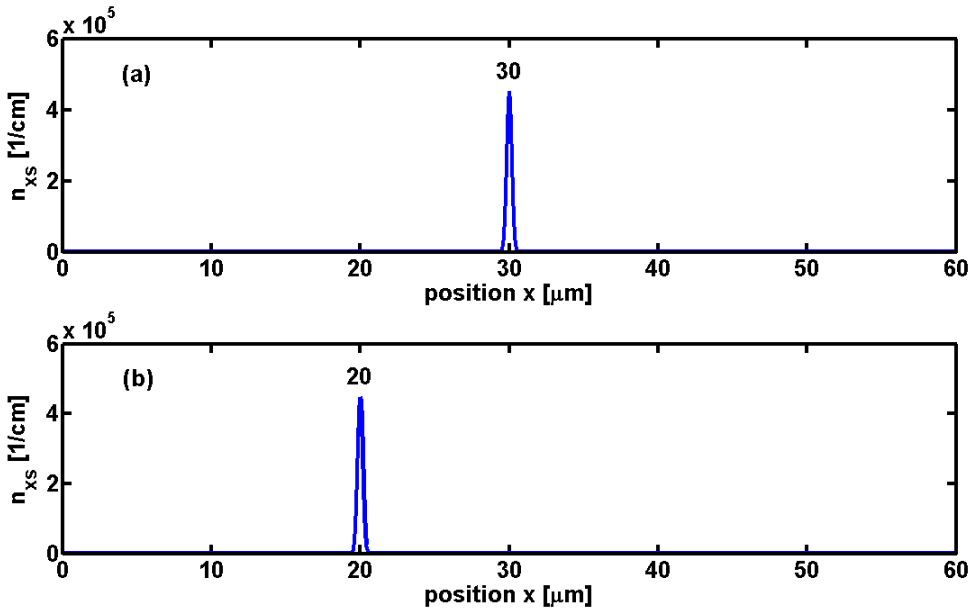

Figure 7.24. Singlet-exciton density n_{xs} as a function of position x with near-field photoexcitation at photon energy E_{ph} = 0.56 eV with the incident power W_{incd} = 1 mW for V_d = 0.2 V and V_g-V_{fb} = 0.1 V for case C_2. The laser is focused to a 400-nm diameter spot. The illumination is at x_{ph} = 30 μm in (a) and at x = 20 μm in (b).

Figure 7.24 shows the singlet-exciton density n_{xs} as a function of x with near-field photoexcitation for case C_2. The illumination is at x_{ph} = 30 μm in Figure 7.24(a) and at x = 20 μm in Figure 7.24(b). Since the value of B_x is about 1 % of the value of B_{BBN}, only 1 % of the recombination of electrons and holes generates the excitons. The exciton density n_{xs} from the recombination of electrons and holes is at the middle of the channel, but the value of n_{xs} is about 1 % of the value of n_{xs} in Figure 7.16. Since this value is too low to be seen in the length scale in Figure 7.24, n_{xs} shows only one part at the photoexcitation position x_{ph}. With illumination the profile of n_{xs} depicts a Gaussian profile at the photoexcitation position x_{ph} due to the Gaussian profile of the exciton

generation rate through the near-field photoexcitation in Figure 7.12, as mentioned above. The magnitude of n_{xs} is the same in Figure 7.24 as in Figure 7.16.

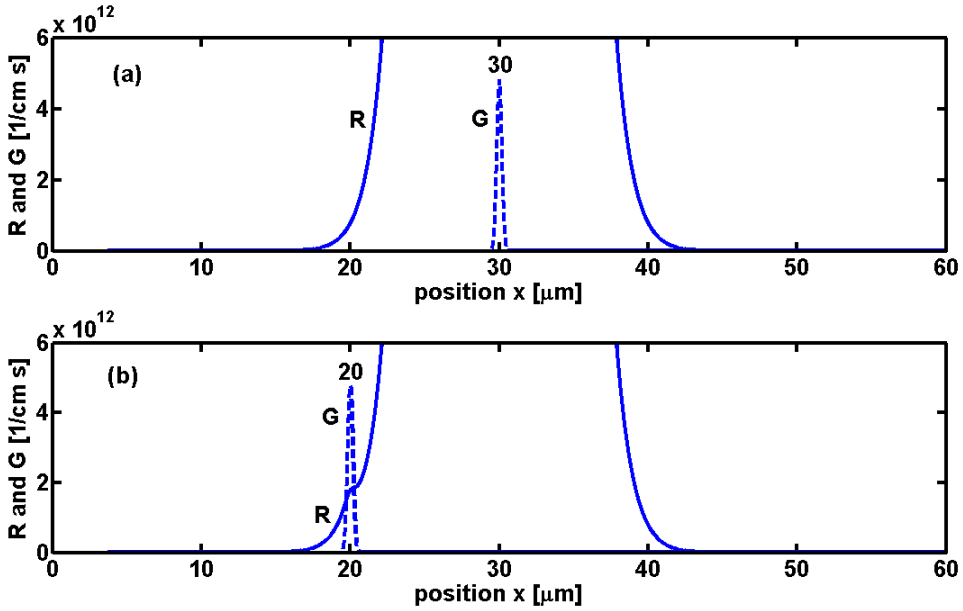

Figure 7.25. Recombination and generation rates R (solid curves) and G (dashed curves) of electrons and holes as functions of x with near-field photoexcitation at photon energy E_{ph} = 0.56 eV with the incident power W_{incd} = 1 mW for V_d = 0.2 V and V_g-V_{fb} = 0.1 V for case C_2. The laser is focused to a 400-nm diameter spot. The illumination shines at x_{ph} = 30 μm in (a), and at x = 20 μm in (b).

Figure 7.25 shows the recombination and generation rates R (solid curves) and G (dashed curves) of electrons and holes as functions of x with near-field photoexcitation for case C_2. The illumination shines at x_{ph} = 30 μm in Figure 7.25(a), and at x = 20 μm in Figure 7.25(b). The exciton-ionization rate $r_d n_{xs}$ is the generation rate of electrons and holes, and thus G (dashed curves) shows the same profiles as the exciton densities in

Figure 7.24. For $r_d = 1.07\text{x}10^7\ s^{-1}$, the peak of G in Figure 7.25(b) has the value of $4.7\text{x}10^{12}\ cm^{-1}s^{-1}$ corresponding to the peak value of the exciton density $n_{xs} = 4.4\text{x}10^5\ cm^{-1}$ in Figure 7.24(b). Since essentially all electrons and holes recombine within the channel, the device current is equal to the recombination current. Hence, the recombination rate R is much larger than the generation rate G, as mentioned above. In Figure 7.25(b) the profile of the recombination rate R broadens in comparison with that of the generation rate G at the photoexcitation position x_{ph}, and the peak of R is lower than that of G, as mentioned above.

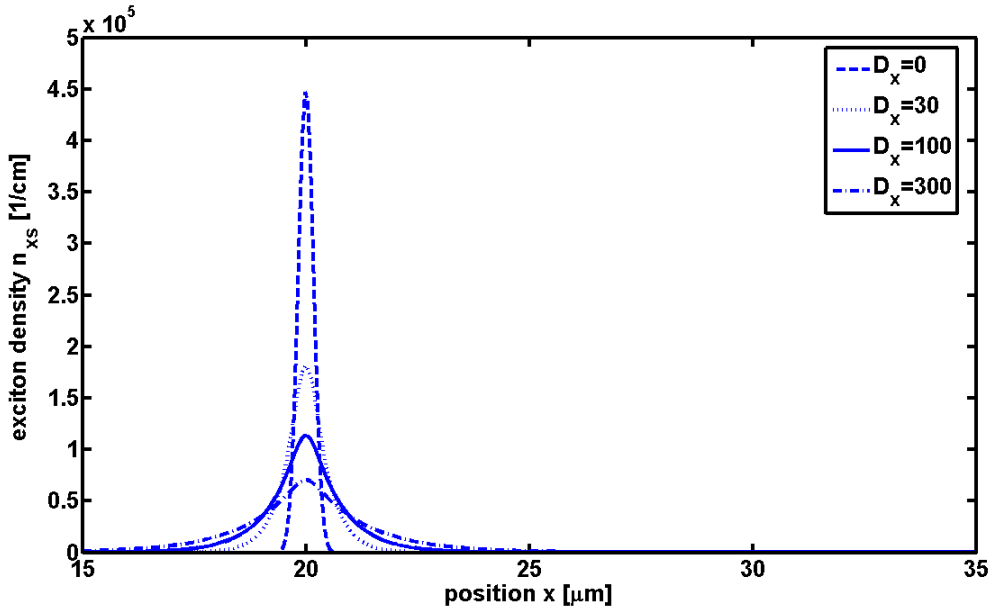

Figure 7.26. Singlet-exciton density n_{xs} as a function of position x with near-field photoexcitation at $x_{ph} = 20$ μm for case C_2. The dashed, dotted, solid, and dash-dot curves are for the exciton-diffusion coefficients $D_x = 0$, 30, 100, 300 cm^2/s, respectively.

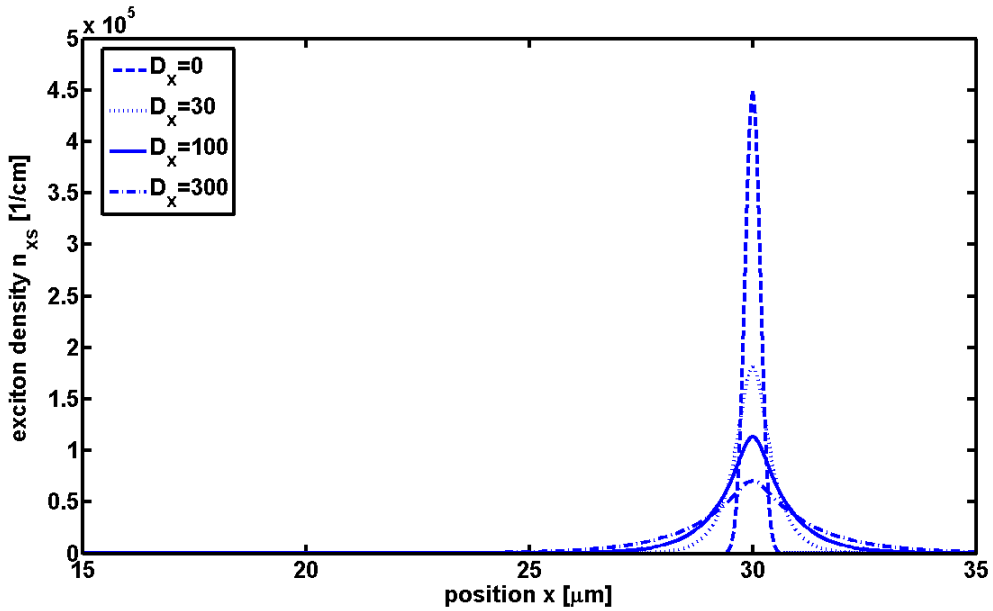

Figure 7.27. Singlet-exciton density n_{xs} as a function of x with near-field photoexcitation at x_{ph} = 30 μm for case C_2. The dashed, dotted, solid, and dash-dot curves are for the exciton-diffusion coefficients D_x = 0, 30, 100, 300 cm^2/s, respectively.

The exciton-diffusion coefficient D_x is assumed to be 100 cm^2 s^{-1}, as mentioned above. For comparison, the results for D_x = 30 and 300 cm^2 s^{-1} are calculated as well. Figure 7.26 shows the singlet-exciton density n_{xs} as a function of x with near-field photoexcitation at x_{ph} = 20 μm for case C_2. The dashed, dotted, solid, and dash-dot curves are for the exciton-diffusion coefficients D_x = 0, 30, 100, 300 cm^2/s, respectively. The profile of n_{xs} shows only one part at the photoexcitation position x_{ph}, as mentioned above. For x_{ph} = 20 μm, the value of n_{xs} broadens more, and the peak of n_{xs} is lower for the higher D_x. Figure 7.27 shows the singlet-exciton density n_{xs} as a function of x with near-field photoexcitation at x_{ph} = 30 μm for case C_2. Similarly, the value of n_{xs} broadens more at x_{ph} = 30 μm, and the peak of n_{xs} is lower for the higher D_x, as well.

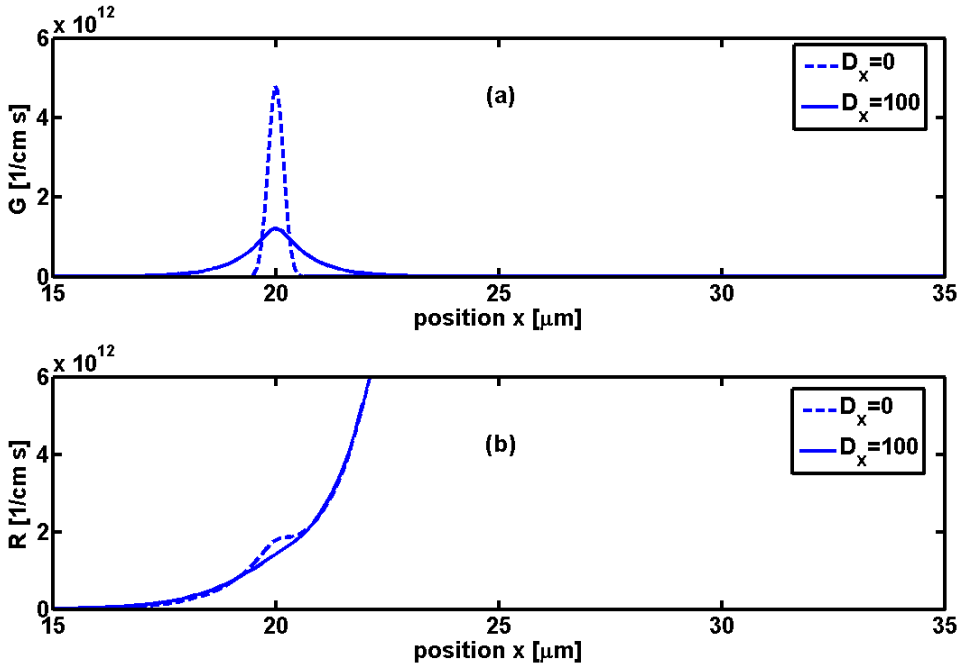

Figure 7.28. (a) G and (b) R of electrons and holes as functions of x with near-field photoexcitation at x_{ph} = 20 μm for case C_2. The dashed and solid curves are for the exciton-diffusion coefficients D_x = 0 and 100 cm^2/s, respectively.

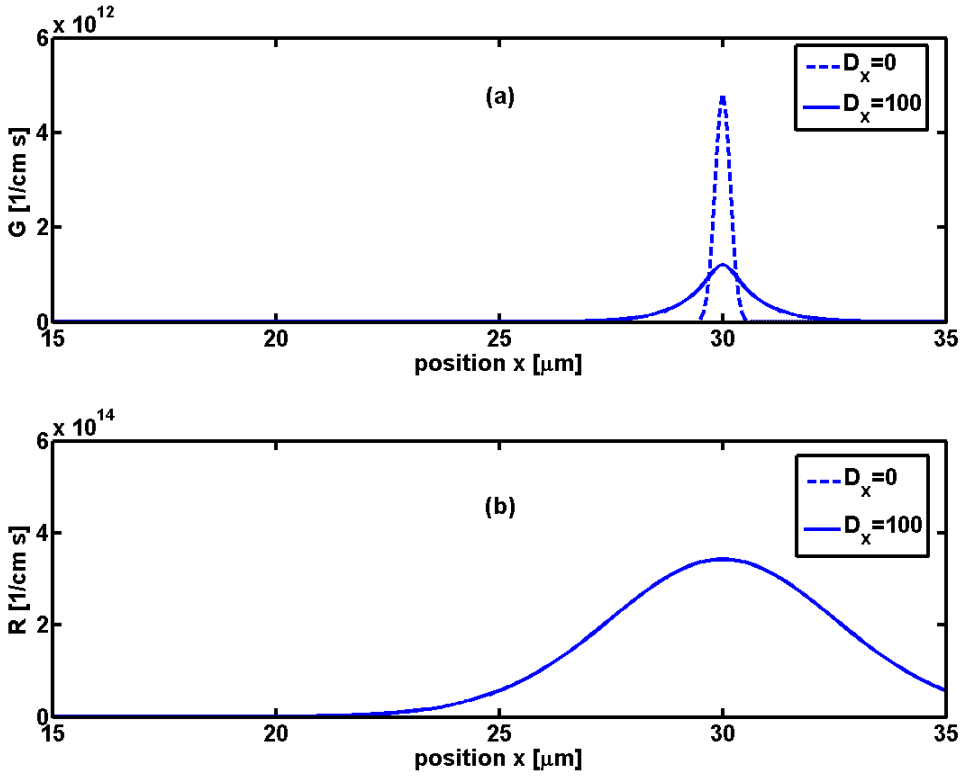

Figure 7.29. (a) G and (b) R of electrons and holes as functions of x with near-field photoexcitation at x_{ph} = 30 μm for case C_2. The dashed and solid curves are for the exciton-diffusion coefficients D_x = 0 and 100 cm^2/s, respectively.

Figure 7.28 shows (a) G and (b) R of electrons and holes as functions of x with near-field photoexcitation at x_{ph} = 20 μm for case C_2. The dashed and solid curves are for the exciton-diffusion coefficients D_x = 0 and 100 cm^2/s, respectively. The exciton-ionization rate $r_d n_{xs}$ is the generation rate of electrons and holes, and thus G shows the same profiles as the exciton densities for D_x = 0 and 100 cm^2/s in Figure 7.26. Hence, the profile of G shows only one part at the photoexcitation position x_{ph}. At the position x_{ph} = 20 μm, the values of R and G broaden more and the peak values of R and G are lower for

the higher D_x since the exciton density n_{xs} broadens. Figure 7.29 shows (a) G and (b) R of electrons and holes as functions of x with near-field photoexcitation at the position x_{ph} = 30 μm for case C_2. At the position x_{ph} = 30 μm, G broadens and its peak is lower for the higher D_x since the exciton density n_{xs} broadens. At x_{ph} = 30 μm the value of R for D_x = 100 cm^2/s is very close to that of R for D_x = 0 since the recombination rate is large there.

7.4 Summary for Photoconductors Based on Carbon-Nanotube Field-Effect Transistors

In conclusion, we implement numerical calculations for photoconductors based on ambipolar long-channel CNT FETs with both uniform and near-field photoexcitation. Photocurrent, current gain, and exciton density with both types of photoexcitation are obtained. Electron confinement in the quasi-one-dimensional structure of CNTs leads to the formation of strongly bound exciton states. For strong binding, most of the optical absorption is associated with photogeneration of excitons; therefore, the calculation of photoconductivity accounts for exciton formation and exciton ionization in CNTs as well.

We find that for the uniform photoexcitation the photocurrent is proportional to the incident power density. This phenomenon is in agreement with the reported experimental results [43]. Similarly, for the near-field photoexcitation, the photocurrent is proportional to the incident power. Based on our model, we show that the photocurrents for photoconductors based on CNT FETs are much smaller than the dark currents, and current gains are very low as well [52]. The reasons for small photocurrent

and current gain are explained below. Firstly, since the diameter of a zigzag CNT (19,0) is so small (1.5 nm), the incident radiation absorbed by CNTs is very slight. The exciton densities through photogeneration are low, and then the densities of e-h pairs through exciton ionization and the photocurrents are small as well. Secondly, radiative and nonradiative decay of excitons compete with the exciton ionization. Since the exciton-ionization coefficient is much smaller than the nonradiative decay coefficient of excitons, most of the excitons nonradiatively decay rather than ionize to e-h pairs to contribute to the photocurrent. Thus the exciton-ionization efficiency, the current gain, and photocurrent are all small. Thirdly, the ratio of the exciton-ionization coefficient r_{di} to the capture parameter B_{xi} for exciton formation, i.e., $r_{\mathrm{di}}/B_{\mathrm{xi}}$, is proportional to $\exp(-E_b / k_b T)$. Since the exciton binding energy E_{b} (= 0.16 eV) in CNTs is large, even for the same value of B_{x} the value of the exciton-ionization coefficient r_{d} is small, and thus the exciton-ionization efficiency, the current gain, and photocurrent are small as well. Fourthly, since the current gain is proportional to the inverse of the square of the channel length, i.e., proportional to L^{-2}, and thus for the photoconductors based on the long-channel (L = 60 μm) CNT FETs, the current gain and photocurrent are small. Although the quantitative values of the photocurrents are very small, the qualitative phenomena of the photoconductivity are reasonable.

If the electric fields applied in the carbon nanotubes are large enough, most of excitons will be ionized to e-h pairs to contribute to the photocurrent. The calculated values of the exciton dissociation (ionization) rates in an external static electric field directed along the tube axis were reported [71]. The exciton ionization rate r_{d} is proportional to $\exp(-cE_b^{3/2} / F_x)$, in which c is a constant. The value of r_{d} decreases

exponentially as the binding energy E_b of the excitons increases, and increases exponentially as the longitudinal electric field F_x increases. For the CNT (19, 0), the exciton-ionization rate is estimated as 1.5×10^8 s^{-1} as the electric field is equal to 60 kV/cm. In our case the value of the electric field is given as 0.07 kV/cm, as shown in the Figure 7.14, and thus the exciton-ionization rate is very small. Therefore, the effect of the field-dependent ionization of excitons for the large binding energy of excitons in CNTs is neglected since the electric field in the long-channel CNT FETs is low. The ratio of the exciton-ionization coefficient r_{di} to the capture parameter B_{xi} for exciton formation, i.e., r_{di}/B_{xi}, is assumed to be the Arrhenius equilibrium constant [72-74], which is the Saha's equation in the case of the chemical equilibrium. Since the excitons in the CNTs are quasi-one-dimensional, the derivation of one-dimensional Arrhenius equilibrium constant, i.e., $r_{di}/B_{xi,}$ is shown in Chapter 3.8. Since the values of both r_{di} and B_{xi} in CNTs are not known, we choose two cases to compare the results. In case C_1, the high value of r_d is chosen by 1.07×10^9 s^{-1}, from which the value of B_x is obtained as 10^6 cm/s. BBN nonradiative recombination is not included so that all of the recombination of electrons and holes generates excitons. In case C_2, the low value of r_d is chosen by 1.07×10^7 s^{-1} and BBN nonradiative recombination ($B_{BBN} = 10^6$ cm/s) *is* included, so that most of the recombination of electrons and holes does not generate excitons due to the smaller value of B_x ($= 10^4$ cm/s) for exciton formation. The photocurrents for case C_1 and C_2 are calculated as 34 pA and 0.34 pA, respectively. For larger exciton-ionization coefficient, more excitons ionize to e-h pairs, and consequently the photocurrent is enhanced, as shown in Figure 7.3. The value of the photocurrent in case C_1 is much bigger than that in case C_2, as expectedly. For case C_1 the profiles of the exciton

densities show two parts; one is the exciton generation through photoexcitation, another is the exciton formation through the recombination of the electrons and holes. However, in case C_2 the majority of the exciton densities are from the exciton generation through photoexcitation, but the exciton formation through the recombination of the electrons and holes is much smaller due to the smaller value of B_x of exciton formation. In case C_2, the profiles of exciton densities show a flat line for the uniform photoexcitation and a Gaussian for the near-field photoexcitation.

In the near-field photoexcitation, we find that the photocurrent is bigger at the photoexcitation position with larger value of the average electric field $|F_x|_{ave}$ since both the current gain and the photocurrent are proportional to $|F_x|_{ave}$. Moreover, for the higher exciton-diffusion coefficient, the profile of the exciton density broadens more and the peak of the exciton density is lower.

CHAPTER 8

CONCLUSIONS AND RECOMMENDATIONS

8.1 Conclusions

The objective of this dissertation is to study theoretically carrier transport, optical emission, and photoconductivity from optoelectronic devices based on ambipolar long-channel CNT FETs. In optical emitters based on CNT FETs, nonradiative recombination is much stronger than radiative, as evidenced by the low measured quantum efficiency between 10^{-6} and 10^{-7} photons per injected *e*-*h* pair [44]; therefore, the transport properties and carrier densities are determined by assuming only nonradiative recombination. A new analytic diffusive-transport model for various recombination mechanisms is provided for the first time. The focus is on the effects of radiative and nonradiative recombination in the channel, with the movement of the spatial recombination profile in response to the gate and drain voltages calculated analytically, which provides physical insight not afforded by purely numerical approaches. The relationship and the scaling are clearly depicted for the first time. In particular, the electronic and optical properties, such as the device current, emitted light-spot size and emitted optical power, are clearly shown in terms of the some parameters in the foregoing equations. Nonradiative recombination is shown to play a decisive role in the transport characteristics. For the first time, we find that the emitted light-spot size and the optical power are indeed sensitive to the operative nonradiative recombination mechanisms.

For long-channel CNT FETs the gradual-channel approximation (GCA) is adopted. We provide a numerical diffusive-transport approach for the light emission based on band-to-band radiative recombination with various nonradiative recombination mechanisms but neglecting exciton formation. In photodetectors based on CNT FETs, excitonic transitions dominate their optical absorption spectra since electron confinement in the quasi-one-dimensional structure of CNTs leads to the formation of strongly bound exciton states. We provide a numerical diffusive-transport approach for photodetectors in order to solve the exciton continuity equation coupled with the electron and hole continuity equations. Therefore, in numerical approaches the systems of differential equations with boundary conditions are presented for both optical emitters and photodetectors. There are two approaches for the finite differences to obtain the discretized equations; the first is the finite difference method, in which the differential operators are directly replaced by difference operators, and the second is the box integration method, in which the differential equation is integrated over each of the subdomains [90, 91]. The same discretized equations are obtained by both methods. In this study the approach of the box integration method is adopted to derive difference approximations for the electron and hole differential continuity equations, while the approach of finite difference method is applied to the exciton differential continuity equation. The Scharfetter-Gummel approach [90, 92] is adopted for the profile of the interpolation scheme for the electron and hole densities. In the drift-diffusion currents, for large carrier densities the Einstein relation in the degenerate semiconductors can be approximated as the formula of Kroemer [58], while the Fermi-Dirac integral of order -½ is applied to one-dimensional case by using the similar procedure of Joyce and Dixon [51,

59]. The discretization of the differential equations yields a system of nonlinear algebraic equations, which can be computed self-consistently. The multi-variable Newton's method is adopted to implement the calculation [90, 91]. The explicit forms of the Jacobian matrix related to the electron and hole continuity equations for the degenerate semiconducting CNTs are derived. In order to solve efficiently, the elements of the band-diagonal matrix **J** is stored by a compact form to save the memory, and the library of the band-diagonal solver is used to calculate the results [93]. The interesting electronic and optical properties such as the electron and hole densities, CNT potential, and exciton density can be solved immediately. The other properties such as the device current, recombination rate and emitted optical power for the light emitters and the photocurrent for the photodetectors through the photoexcitation, in turn, can be obtained as well.

For optical emitters based on ambipolar long-channel CNT FETs, we implement both analytic and numerical transport models that the focus is on the effects of finite radiative and nonradiative recombination probability in the conduction channel, with the movement of the recombination profile in response to the gate and drain voltages. We show that inside the recombination region transport characteristics are essentially determined by nonradiative recombination. The decisive role of nonradiative recombination here is consistent with the observed low quantum efficiency in the optical emission from CNT FETs [44]. Both analytic and numerical results for the currents and the movement of the position of light emission are in agreement with the experimental data in Ref. [49] if the experimentally observed hysteresis is neglected. In the ambipolar operation regime, when the channel length exceeds the recombination length, essentially all electrons and holes injected from opposite contacts recombine within the channel.

When the applied gate and drain voltages satisfy the symmetric condition with V_G-V_{fb} = ½V_D, a current minimum occurs and the position of radiative recombination locates in the channel center. The position of the maximum radiative recombination rate occurs where the electron density is equal to the hole density, *i.e.*, where the linear charge density is zero. The emitted light-spot size and optical power on the current and on the gate capacitance are predicted to exhibit sensitive dependences on the operative nonradiative recombination mechanisms. The electric field inside the recombination region is enhanced but it remains sufficiently small so that a model based on constant low-field mobility can be applied to ambipolar long-channel CNT FETs. Furthermore, the electric field is not high enough for exciton-formation through impact excitation in long-channel devices [61].

For photoconductors based on ambipolar long-channel CNT FETs, we implement the numerical calculation with both uniform and near-field photoexcitation. The photocurrent, current gain, and exciton density with both types of photoexcitation are obtained. For strong bound exciton states in CNTs, most of the optical absorption is associated with photogeneration of excitons; therefore, the calculation of photoconductivity accounting for exciton photogeneration and exciton ionization in CNTs is provided. We find that for the uniform photoexcitation the photocurrent is proportional to the incident power density. This phenomenon is in agreement with the reported experimental results [43]. Similarly, for the near-field photoexcitation, the photocurrent is proportional to the incident power. Based on our model, we show that the photocurrents for photoconductors based on CNT FETs are much smaller than the dark currents, and current gains are very low as well. The reasons for small photocurrents and

current gains are explained below. Firstly, the incident radiation absorbed by CNTs is very slight due to small diameter (1.5 nm) of a CNT. The exciton densities through photogeneration are low, and then the densities of e-h pairs through exciton ionization and the photocurrents are small as well. Secondly, since the exciton-ionization coefficient is much smaller than the nonradiative decay coefficient of excitons, most of the excitons nonradiatively decay rather than ionize to e-h pairs to contribute to the photocurrent. Thirdly, the exciton-ionization coefficient is small due to the large exciton binding energy (0.16 eV) in CNTs, and thus the exciton-ionization efficiency and photocurrent are small. Fourthly, since the current gain is proportional to L^{-2}, and thus the current gain and photocurrent are small due to the long conduction channel (L = 60 μm). Although the quantitative values of the photocurrents are very small, the qualitative phenomena of the photoconductivity are reasonable. Moreover, the effect of the field-dependent ionization of excitons for the large binding energy of excitons in CNTs is neglected since the electric field in the long-channel CNT FETs is low. Since the values of the exciton-ionization coefficient in CNTs are not known, we choose two cases to compare the results. In case C_1, the high value of the exciton-ionization coefficient is chosen and BBN nonradiative recombination is not included, so that all of the recombination of electrons and holes generates excitons. In case C_2, the low value of the exciton-ionization coefficient is chosen and BBN nonradiative recombination *is* included, so that most of the recombination of electrons and holes does not generate excitons. The calculated value of the photocurrent in case C_1 is much bigger than that in case C_2, as expectedly. For case C_1 the profiles of the exciton densities show two parts; one is the exciton generation through photoexcitation, another is the exciton formation through the

recombination of the electrons and holes. However, in case C_2 the majority of the exciton densities are from the exciton generation through photoexcitation, so that the profiles of exciton densities show a flat line for the uniform photoexcitation and a Gaussian for the near-field photoexcitation. In the near-field photoexcitation, we find that the photocurrent is bigger at the photoexcitation position with larger value of the average electric field since both the current gain and the photocurrent are proportional to the average electric field. In addition, for the higher exciton-diffusion coefficient, the profile of the exciton density broadens more and the peak of the exciton density is lower.

8.2 Recommendation for Future Research Work

Based on our model, for photoconductors based on long-channel (L = 60 μm) CNT FETs the photocurrent is much smaller than the dark current since the current gain is proportional to L^{-2}. CNT FETs with channel lengths ranging from 500 nm to 1000 nm were reported in the observed photoconductivity [21, 43], in which the photocurrent is larger than the dark current. Therefore, the short-channel devices are more promising for the photoconductors. Moreover, the observed open-circuit photovoltage and short-circuit photocurrent produced by local illumination at the Schottky contacts of CNT FETs were reported [65, 66, 68, 69]. Internal fields, such as those formed Schottky contacts and those in defect sites, can be used to image such sites and determine the band bending in the open-circuit configuration [68, 69]. The photovoltage images show that the band-bending length near the contacts ranges from hundred nm to microns when the device is depleted. However, in our model for the photoconductors, the incident light is assumed

to illuminate the entire channel but not the contacts, and the effect of the Schottky barriers is simplified to a constant voltage drop across the contact independent of the current. In order to study the incident light exciting near the contacts, the more accurate model for the Schottky barriers is required. Some models including the tunneling and thermionic emission currents through the Schottky barriers were reported in optical emitters based on ambipolar CNT FETs [50, 60]. Moreover, the observed optical emission based on CNT FETs with channel length 1 μm was reported [28]. Since the band-bending length near the contact is comparable with the channel length, the modeling for the short-channel devices of the optical emitters and photoconductors requires the accurate treatment for the Schottky barriers as well.

The calculated value of exciton-ionization rate increases exponentially as the electric field increases [71]. Hence the high internal electric fields forming the Schottky contact can tremendously increase the exciton ionization to e-h pairs to contribute to the photocurrent for the photoconductors. However, in our model for the photoconductors, the effect of the field-dependent ionization of excitons is neglected. In order to calculate the open-circuit photovoltage and short-circuit photocurrent produced by local illumination at the Schottky contacts of CNT FETs, as mentioned above, the effect of the high electric field on the exciton ionization is required to be included.

APPENDIX

PUBLICATIONS

1. **Chi-Ti Hsieh**, D. S. Citrin, and P. P. Ruden, "Recombination-mechanism dependence of transport and light emission of ambipolar long-channel carbon-nanotube field-effect transistors," *Appl. Phys. Lett.*, Vol. 90, pp. 012118, 2007.
2. **Chi-Ti Hsieh**, D. S. Citrin, and P. P. Ruden, "Photoconductivity of ambipolar long-cannel carbon-nanotube field-effect transistors," in *The Conference on Lasers and Electro-Optics/Quantum Electronics and Laser Science Conference 2008 (CLEO/QELS 2008),* San Jose, California, May 4-9, 2008.
3. **C. Hsieh**, D. S. Citrin, and P. P. Ruden, "Light emission from carbon nanotube FETs," in *Optics in the Southeast-2005,* Atlanta, Georgia, October 6-8, 2005.
4. **Chi-Ti Hsieh**, D. S. Citrin, and P. Paul. Ruden, "Carrier transport in carbon nanotube FETs including radiative recombination," in *The 16th International Conference on Electronic Properties of Two-Dimensional Systems (EP2DS-16),* Albuquerque, New Mexico, July 10-15, 2005.

REFERENCES

[1] P. Avouris, J. Chen, M. Freitag, V. Perebeinos, and J. C. Tsang, "Carbon nanotube optoelectronics," *Physica Status Solidi B-Basic Solid State Physics,* vol. 243, pp. 3197-3203, Nov 2006.

[2] M. S. Dresselhaus, G. Dresselhaus, and P. Avouris (Eds.), *Carbon Nanotubes: Synthesis, Structure, Properties, and Applications*: Springer, 2001.

[3] R. Saito, G. Dresselhaus, and M. S. Dresselhaus, *Physical Properties of Carbon Nanotubes*: Imperial College Press, 1998.

[4] P. Avouris, "Carbon nanotube electronics and optoelectronics," *MRS Bulletin,* vol. 29, pp. 403-410, Jun 2004.

[5] P. Avouris, J. Appenzeller, R. Martel, and S. J. Wind, "Carbon nanotube electronics," *Proceedings of the IEEE,* vol. 91, pp. 1772-1784, Nov 2003.

[6] P. Avouris and J. Chen, "Nanotube electronics and optoelectronics," *Materials Today,* vol. 9, pp. 46-54, Oct 2006.

[7] P. Avouris, Z. H. Chen, and V. Perebeinos, "Carbon-based electronics," *Nature Nanotechnology,* vol. 2, pp. 605-615, Oct 2007.

[8] G. Pennington and N. Goldsman, "Semiclassical transport and phonon scattering of electrons in semiconducting carbon nanotubes," *Physical Review B,* vol. 68, p. 045426, Jul 15 2003.

[9] V. Perebeinos, J. Tersoff, and P. Avouris, "Electron-phonon interaction and transport in semiconducting carbon nanotubes," *Physical Review Letters,* vol. 94, p. 086802, Mar 4 2005.

[10] A. Verma, M. Z. Kauser, and P. P. Ruden, "Effects of radial breathing mode phonons on charge transport in semiconducting zigzag carbon nanotubes," *Applied Physics Letters,* vol. 87, p. 123101, Sep 19 2005.

[11] A. Verma, M. Z. Kauser, and P. P. Ruden, "Ensemble Monte Carlo transport simulations for semiconducting carbon nanotubes," *Journal of Applied Physics,* vol. 97, p. 114319, Jun 1 2005.

[12] T. Durkop, S. A. Getty, E. Cobas, and M. S. Fuhrer, "Extraordinary mobility in semiconducting carbon nanotubes," *Nano Letters,* vol. 4, pp. 35-39, Jan 2004.

[13] V. Perebeinos, J. Tersoff, and P. Avouris, "Mobility in semiconducting carbon nanotubes at finite carrier density," *Nano Letters,* vol. 6, pp. 205-208, Feb 2006.

[14] A. Javey, J. Guo, M. Paulsson, Q. Wang, D. Mann, M. Lundstrom, and H. J. Dai, "High-field quasiballistic transport in short carbon nanotubes," *Physical Review Letters,* vol. 92, p. 106804, Mar 12 2004.

[15] J. Y. Park, S. Rosenblatt, Y. Yaish, V. Sazonova, H. Ustunel, S. Braig, T. A. Arias, P. W. Brouwer, and P. L. McEuen, "Electron-phonon scattering in metallic single-walled carbon nanotubes," *Nano Letters,* vol. 4, pp. 517-520, Mar 2004.

[16] Z. Yao, C. L. Kane, and C. Dekker, "High-field electrical transport in single-wall carbon nanotubes," *Physical Review Letters,* vol. 84, pp. 2941-2944, Mar 27 2000.

[17] T. Ando, "Excitons in carbon nanotubes," *Journal of the Physical Society of Japan,* vol. 66, pp. 1066-1073, Apr 1997.

[18] V. Perebeinos, J. Tersoff, and P. Avouris, "Scaling of excitons in carbon nanotubes," *Physical Review Letters,* vol. 92, p. 257402, Jun 25 2004.

[19] C. D. Spataru, S. Ismail-Beigi, L. X. Benedict, and S. G. Louie, "Excitonic effects and optical spectra of single-walled carbon nanotubes," *Physical Review Letters,* vol. 92, p. 077402, Feb 20 2004.

[20] J. Maultzsch, R. Pomraenke, S. Reich, E. Chang, D. Prezzi, A. Ruini, E. Molinari, M. S. Strano, C. Thomsen, and C. Lienau, "Exciton binding energies in carbon nanotubes from two-photon photoluminescence," *Physical Review B,* vol. 72, p. R241402, Dec 2005.

[21] X. H. Qiu, M. Freitag, V. Perebeinos, and P. Avouris, "Photoconductivity spectra of single-carbon nanotubes: Implications on the nature of their excited states," *Nano Letters,* vol. 5, pp. 749-752, Apr 2005.

[22] F. Wang, G. Dukovic, L. E. Brus, and T. F. Heinz, "The optical resonances in carbon nanotubes arise from excitons," *Science,* vol. 308, pp. 838-841, May 6 2005.

[23] V. Perebeinos, J. Tersoff, and P. Avouris, "Radiative lifetime of excitons in carbon nanotubes," *Nano Letters,* vol. 5, pp. 2495-2499, Dec 2005.

[24] C. D. Spataru, S. Ismail-Beigi, R. B. Capaz, and S. G. Louie, "Theory and ab initio calculation of radiative lifetime of excitons in semiconducting carbon nanotubes," *Physical Review Letters,* vol. 95, p. 247402, Dec 9 2005.

[25] R. Martel, T. Schmidt, H. R. Shea, T. Hertel, and P. Avouris, "Single- and multi-wall carbon nanotube field-effect transistors," *Applied Physics Letters,* vol. 73, pp. 2447-2449, Oct 26 1998.

[26] S. J. Tans, A. R. M. Verschueren, and C. Dekker, "Room-temperature transistor based on a single carbon nanotube," *Nature,* vol. 393, pp. 49-52, May 7 1998.

[27] R. Martel, V. Derycke, C. Lavoie, J. Appenzeller, K. K. Chan, J. Tersoff, and P. Avouris, "Ambipolar electrical transport in semiconducting single-wall carbon nanotubes," *Physical Review Letters,* vol. 87, p. 256805, Dec 17 2001.

[28] J. A. Misewich, R. Martel, P. Avouris, J. C. Tsang, S. Heinze, and J. Tersoff, "Electrically induced optical emission from a carbon nanotube FET," *Science,* vol. 300, pp. 783-786, May 2 2003.

[29] A. Javey, J. Guo, D. B. Farmer, Q. Wang, E. Yenilmez, R. G. Gordon, M. Lundstrom, and H. J. Dai, "Self-aligned ballistic molecular transistors and electrically parallel nanotube arrays," *Nano Letters,* vol. 4, pp. 1319-1322, Jul 2004.

[30] S. J. Wind, J. Appenzeller, R. Martel, V. Derycke, and P. Avouris, "Vertical scaling of carbon nanotube field-effect transistors using top gate electrodes," *Applied Physics Letters,* vol. 80, pp. 3817-3819, May 20 2002.

[31] S. Heinze, M. Radosavljevic, J. Tersoff, and P. Avouris, "Unexpected scaling of the performance of carbon nanotube Schottky-barrier transistors," *Physical Review B,* vol. 68, p. 235418, Dec 2003.

[32] S. Heinze, J. Tersoff, R. Martel, V. Derycke, J. Appenzeller, and P. Avouris, "Carbon nanotubes as Schottky barrier transistors," *Physical Review Letters,* vol. 89, p. 106801, Sep 2 2002.

[33] A. Javey, J. Guo, D. B. Farmer, Q. Wang, D. W. Wang, R. G. Gordon, M. Lundstrom, and H. J. Dai, "Carbon nanotube field-effect transistors with integrated ohmic contacts and high-k gate dielectrics," *Nano Letters,* vol. 4, pp. 447-450, Mar 2004.

[34] A. Javey, H. Kim, M. Brink, Q. Wang, A. Ural, J. Guo, P. McIntyre, P. McEuen, M. Lundstrom, and H. J. Dai, "High-kappa dielectrics for advanced carbon-nanotube transistors and logic gates," *Nature Materials,* vol. 1, pp. 241-246, Dec 2002.

[35] Y. M. Lin, J. Appenzeller, and P. Avouris, "Ambipolar-to-unipolar conversion of carbon nanotube transistors by gate structure engineering," *Nano Letters,* vol. 4, pp. 947-950, May 2004.

[36] J. Clifford, D. L. John, and D. L. Pulfrey, "Bipolar conduction and drain-induced barrier thinning in carbon nanotube FETs," *IEEE Transactions on Nanotechnology,* vol. 2, pp. 181-185, Sep 2003.

[37] J. P. Clifford, D. L. John, L. C. Castro, and D. L. Pulfrey, "Electrostatics of partially gated carbon nanotube FETs," *IEEE Transactions on Nanotechnology,* vol. 3, pp. 281-286, Jun 2004.

[38] J. Guo, M. Lundstrom, and S. Datta, "Performance projections for ballistic carbon nanotube field-effect transistors," *Applied Physics Letters,* vol. 80, pp. 3192-3194, Apr 29 2002.

[39] J. Guo, J. Wang, E. Polizzi, S. Datta, and M. Lundstrom, "Electrostatics of nanowire transistors," *IEEE Transactions on Nanotechnology,* vol. 2, pp. 329-334, Dec 2003.

[40] D. L. John, L. C. Castro, J. Clifford, and D. L. Pulfrey, "Electrostatics of coaxial Schottky-barrier nanotube field-effect transistors," *IEEE Transactions on Nanotechnology,* vol. 2, pp. 175-180, Sep 2003.

[41] A. Rahman, J. Guo, S. Datta, and M. S. Lundstrom, "Theory of ballistic nanotransistors," *IEEE Transactions on Electron Devices,* vol. 50, pp. 1853-1864, Sep 2003.

[42] M. Freitag, J. Chen, J. Tersoff, J. C. Tsang, Q. Fu, J. Liu, and P. Avouris, "Mobile ambipolar domain in carbon-nanotube infrared emitters," *Physical Review Letters,* vol. 93, p. 076803, Aug 13 2004.

[43] M. Freitag, Y. Martin, J. A. Misewich, R. Martel, and P. H. Avouris, "Photoconductivity of single carbon nanotubes," *Nano Letters,* vol. 3, pp. 1067-1071, Aug 2003.

[44] M. Freitag, V. Perebeinos, J. Chen, A. Stein, J. C. Tsang, J. A. Misewich, R. Martel, and P. Avouris, "Hot carrier electroluminescence from a single carbon nanotube," *Nano Letters,* vol. 4, pp. 1063-1066, Jun 2004.

[45] A. Javey, J. Guo, Q. Wang, M. Lundstrom, and H. J. Dai, "Ballistic carbon nanotube field-effect transistors," *Nature,* vol. 424, pp. 654-657, Aug 7 2003.

[46] D. Mann, A. Javey, J. Kong, Q. Wang, and H. J. Dai, "Ballistic transport in metallic nanotubes with reliable Pd ohmic contacts," *Nano Letters,* vol. 3, pp. 1541-1544, Nov 2003.

[47] S. J. Wind, J. Appenzeller, and P. Avouris, "Lateral scaling in carbon-nanotube field-effect transistors," *Physical Review Letters,* vol. 91, p. 058301, Aug 1 2003.

[48] P. L. McEuen, M. S. Fuhrer, and H. K. Park, "Single-walled carbon nanotube electronics," *IEEE Transactions on Nanotechnology,* vol. 1, pp. 78-85, Mar 2002.

[49] J. Tersoff, M. Freitag, J. C. Tsang, and P. Avouris, "Device modeling of long-channel nanotube electro-optical emitter," *Applied Physics Letters,* vol. 86, p. 263108, Jun 27 2005.

[50] J. Guo and M. A. Alam, "Carrier transport and light-spot movement in carbon-nanotube infrared emitters," *Applied Physics Letters,* vol. 86, p. 023105, Jan 10 2005.

[51] C.-T. Hsieh, D. S. Citrin, and P. P. Ruden, "Recombination-mechanism dependence of transport and light emission of ambipolar long-channel carbon-nanotube field-effect transistors," *Applied Physics Letters,* vol. 90, p. 012118, Jan 1 2007.

[52] C.-T. Hsieh, D. S. Citrin, and P. P. Ruden, "Photoconductivity of ambipolar long-channel carbon-nanotube field-effect transistors," in *Conference on Lasers and Electro-Optics/Quantum Electronics and Laser Science Conference 2008 (CLEO/QELS 2008)*, San Jose, California, USA, May 4-9, 2008.

[53] J. Appenzeller, J. Knoch, V. Derycke, R. Martel, S. Wind, and P. Avouris, "Field-modulated carrier transport in carbon nanotube transistors," *Physical Review Letters,* vol. 89, p. 126801, Sep 16 2002.

[54] M. Radosavljevic, S. Heinze, J. Tersoff, and P. Avouris, "Drain voltage scaling in carbon nanotube transistors," *Applied Physics Letters,* vol. 83, pp. 2435-2437, Sep 22 2003.

[55] S. Luryi, "QUANTUM CAPACITANCE DEVICES," *Applied Physics Letters,* vol. 52, pp. 501-503, Feb 1988.

[56] J. Guo, S. Goasguen, M. Lundstrom, and S. Datta, "Metal-insulator-semiconductor electrostatics of carbon nanotubes," *Applied Physics Letters,* vol. 81, pp. 1486-1488, Aug 19 2002.

[57] D. L. John, L. C. Castro, and D. L. Pulfrey, "Quantum capacitance in nanoscale device modeling," *Journal of Applied Physics,* vol. 96, pp. 5180-5184, Nov 1 2004.

[58] H. Kroemer, "Einstein relation for degenerate carrier concentrations," *IEEE Transactions on Electron Devices,* vol. 25, pp. 850-850, 1978.

[59] W. B. Joyce and R. W. Dixon, "Analytic approximations for Fermi energy of an ideal Fermi gas," *Applied Physics Letters,* vol. 31, pp. 354-356, 1977.

[60] D. L. McGuire and D. L. Pulfrey, "A multi-scale model for mobile and localized electroluminescence in carbon nanotube field-effect transistors," *Nanotechnology,* vol. 17, pp. 5805-5811, Dec 14 2006.

[61] J. Chen, V. Perebeinos, M. Freitag, J. Tsang, Q. Fu, J. Liu, and P. Avouris, "Bright infrared emission from electrically induced excitons in carbon nanotubes," *Science,* vol. 310, pp. 1171-1174, Nov 18 2005.

[62] V. Perebeinos and P. Avouris, "Impact excitation by hot carriers in carbon nanotubes," *Physical Review B,* vol. 74, p. 121410, Sep 2006.

[63] D. Mann, Y. K. Kato, A. Kinkhabwala, E. Pop, J. Cao, X. R. Wang, L. Zhang, Q. Wang, J. Guo, and H. J. Dai, "Electrically driven thermal light emission from individual single-walled carbon nanotubes," *Nature Nanotechnology,* vol. 2, pp. 33-38, Jan 2007.

[64] Y. J. Ouyang, D. Mann, H. J. Dai, and J. Guo, "Theoretical investigations on thermal light emission from metallic carbon nanotubes," *IEEE Transactions on Nanotechnology,* vol. 6, pp. 682-687, Nov 2007.

[65] K. Balasubramanian and M. Burghard, "Charge transport through carbon nanotubes interacting with light," *Semiconductor Science and Technology,* vol. 21, pp. S22-S32, Nov 2006.

[66] K. Balasubramanian, M. Burghard, K. Kern, M. Scolari, and A. Mews, "Photocurrent imaging of charge transport barriers in carbon nanotube devices," *Nano Letters,* vol. 5, pp. 507-510, Mar 2005.

[67] K. Balasubramanian, Y. W. Fan, M. Burghard, K. Kern, M. Friedrich, U. Wannek, and A. Mews, "Photoelectronic transport imaging of individual semiconducting carbon nanotubes," *Applied Physics Letters,* vol. 84, pp. 2400-2402, Mar 29 2004.

[68] M. Freitag, J. C. Tsang, A. Bol, P. Avouris, D. N. Yuan, and J. Liu, "Scanning photovoltage microscopy of potential modulations in carbon nanotubes," *Applied Physics Letters,* vol. 91, p. 031101, Jul 16 2007.

[69] M. Freitag, J. C. Tsang, A. Bol, D. N. Yuan, J. Liu, and P. Avouris, "Imaging of the schottky barriers and charge depletion in carbon nanotube transistors," *Nano Letters,* vol. 7, pp. 2037-2042, Jul 2007.

[70] J. Guo, M. A. Alam, and Y. Yoon, "Theoretical investigation on photoconductivity of single intrinsic carbon nanotubes," *Applied Physics Letters,* vol. 88, p. 133111, Mar 27 2006.

[71] V. Perebeinos and P. Avouris, "Exciton ionization, Franz-Keldysh, and stark effects in carbon nanotubes," *Nano Letters,* vol. 7, pp. 609-613, Mar 2007.

[72] P. L. Gourley and J. P. Wolfe, "Thermodynamics of excitonic molecules in silicon," *Physical Review B,* vol. 20, pp. 3319-3327, 1979.

[73] P. L. Gourley and J. P. Wolfe, "Experimental-determination of equilibrium-constants for excitonic systems in stressed, ultrapure silicon," *Physical Review B,* vol. 25, pp. 6338-6348, 1982.

[74] J. C. Kim, D. R. Wake, and J. P. Wolfe, "Thermodynamics of biexcitons in a GaAs quantum-well," *Physical Review B,* vol. 50, pp. 15099-15107, Nov 15 1994.

[75] M. F. Islam, D. E. Milkie, C. L. Kane, A. G. Yodh, and J. M. Kikkawa, "Direct measurement of the polarized optical absorption cross section of single-wall carbon nanotubes," *Physical Review Letters,* vol. 93, p. 037404, Jul 16 2004.

[76] V. Perebeinos, J. Tersoff, and P. Avouris, "Effect of exciton-phonon coupling in the calculated optical absorption of carbon nanotubes," *Physical Review Letters,* vol. 94, p. 027402, Jan 21 2005.

[77] S. Ramo, J. R. Whinnery, and T. Van Duzer, *Fields and Waves in Communication Electronics*. New York: Wiley, 1994.

[78] J. Singh, *Quantum Mechanics: Fundamentals & Applications to Technology*: John Wiley & Sons, Inc., 1997.

[79] M. S. Fuhrer, B. M. Kim, T. Durkop, and T. Brintlinger, "High-mobility nanotube transistor memory," *Nano Letters,* vol. 2, pp. 755-759, Jul 2002.

[80] S. Rosenblatt, Y. Yaish, J. Park, J. Gore, V. Sazonova, and P. L. McEuen, "High performance electrolyte gated carbon nanotube transistors," *Nano Letters,* vol. 2, pp. 869-872, Aug 2002.

[81] X. J. Zhou, J. Y. Park, S. M. Huang, J. Liu, and P. L. McEuen, "Band structure, phonon scattering, and the performance limit of single-walled carbon nanotube transistors," *Physical Review Letters,* vol. 95, p. 146805, Sep 30 2005.

[82] Y. F. Chen and M. S. Fuhrer, "Electric-field-dependent charge-carrier velocity in semiconducting carbon nanotubes," *Physical Review Letters,* vol. 95, p. 236803, Dec 2 2005.

[83] J. Guo, S. Datta, and M. Lundstrom, "A numerical study of scaling issues for Schottky-Barrier carbon nanotube transistors," *IEEE Transactions on Electron Devices,* vol. 51, pp. 172-177, Feb 2004.

[84] D. T. Harr, "On the use of grand ensembles in statistical mechanics: a new derivation of Saha's formula," *American Journal of Physics,* vol. 23, p. 326, 1954.

[85] G. H. Nickel, "Elementary derivation of the Saha equation," *American Journal of Physics,* vol. 48, pp. 448-450, 1980.

[86] J. Shumway and D. M. Ceperley, "Quantum Monte Carlo simulations of exciton condensates," *Solid State Communications,* vol. 134, pp. 19-22, Apr 2005.

[87] D. L. Smith and P. P. Ruden, "Analytic device model for light-emitting ambipolar organic semiconductor field-effect transistors," *Applied Physics Letters,* vol. 89, p. 233519, Dec 4 2006.

[88] D. L. Smith and P. P. Ruden, "Device modeling of light-emitting ambipolar organic semiconductor field-effect transistors," *Journal of Applied Physics,* vol. 101, p. 084503, Apr 15 2007.

[89] M. Kemerink, D. S. H. Charrier, E. C. P. Smits, S. G. J. Mathijssen, D. M. de Leeuw, and R. A. J. Janssen, "On the width of the recombination zone in ambipolar organic field effect transistors," *Applied Physics Letters,* vol. 93, p. 033312, Jul 2008.

[90] S. Selberherr, *Analysis and Simulation of Semiconductor Devices*: Springer-Verlag Wien New York, 1984.

[91] A. W. Smith and K. F. Brennan, "Hydrodynamic simulation of semiconductor devices," *Progress in Quantum Electronics,* vol. 21, pp. 293-360, 1997.

[92] D. L. Scharfetter and H. K. Gummel, "LARGE-SIGNAL ANALYSIS OF A SILICON READ DIODE OSCILLATOR," *IEEE Transactions on Electron Devices,* vol. ED16, pp. 64-77, 1969.

[93] W. H. Press, S. A. Teukolsky, W. T. Vetterling, and B. P. Flannery, *Numerical Recipes in C++: The Art of Scientific Computing,* 2nd ed.: Cambridge University Press, 2002.

[94] P. Bhattacharya, *Semiconductor Optoelectronic Devices,* Second ed.: Prentice-Hall, Inc., 1997.

[95] S. M. Sze, *Physics of Semiconductor Devices,* Second ed.: John Wiley and Sons, New York, 1981.

[96] V. Perebeinos and P. Avouris, "Phonon and electronic nonradiative decay mechanisms of excitons in carbon nanotubes," *Physical Review Letters,* vol. 101, p. 057401, Aug 1 2008.

[97] L. Cognet, D. A. Tsyboulski, J. D. R. Rocha, C. D. Doyle, J. M. Tour, and R. B. Weisman, "Stepwise quenching of exciton fluorescence in carbon nanotubes by single-molecule reactions," *Science,* vol. 316, pp. 1465-1468, Jun 8 2007.

[98] O. J. Korovyanko, C. X. Sheng, Z. V. Vardeny, A. B. Dalton, and R. H. Baughman, "Ultrafast spectroscopy of excitons in single-walled carbon nanotubes," *Physical Review Letters,* vol. 92, p. 017403, Jan 9 2004.

[99] C. X. Sheng, Z. V. Vardeny, A. B. Dalton, and R. H. Baughman, "Exciton dynamics in single-walled nanotubes: Transient photoinduced dichroism and polarized emission," *Physical Review B,* vol. 71, p. 125427, Mar 2005.